INVERSION OF CONVERTED-WAVE SEISMIC DATA FOR RESERVOIR CHARACTERIZATION AT RULISON FIELD, COLORADO

by

Alexandre Araman

A thesis submitted to the Faculty and the Board of Trustees of the Colorado School of Mines in partial fulfillment of the requirements for the degree of Master of Science (Geophysics).

Golden, Colorado

Date Nov. 9, 2009

Signed: Alexandre Araman

Alexandre Araman

Approved: Thomas L. Davis

Dr. Thomas L. Davis
Professor of Geophysics
Thesis Advisor

Golden, Colorado

Date Nov. 9, 2009

Terence K Young

Dr. Terence K. Young
Professor and Head,
Department of Geophysics

ABSTRACT

Rulison Field is a basin-centered gas accumulation located in the Piceance Basin of northwest Colorado. The reservoir consists of lenticular fluvial sands, shales, and coals of the Upper Cretaceous Williams Fork Formation. Typical sand body thicknesses are 10−15 ft, an order of magnitude lower than the seismic resolution which is 105 ft. The sandstone reservoirs are the primary target and are typically low porosities (6−12 %) and very low permeabilities (1−10 μD). The best production is dependent on the fracture permeability. The major objectives of the reservoir characterization in Rulison are (1) the imaging of the lenticular sand bodies, (2) the identification of the high quality overpressured productive sandstones, and (3) the determination of the fractured intervals. In order to achieve these goals, a quantification of anisotropy in the reservoir is essential in understanding the seismic amplitude responses.

Converted-wave poststack gathers lead to a successful fault delineation as well as an average shear-wave splitting determination over the entire reservoir section. Assuming vertical transverse isotropy, the Thomsen anisotropy parameters are estimated at the UMV Shale interval from a joint PP/PS traveltime inversion. An anisotropic AVO modeling study based on the elastic parameters extracted at the study well location and on the Thomsen parameters shows that the reflection coefficients in the VTI-over-HTI model of the upper reservoir can be approximated by the small-offset reflection coefficients in isotropic media after application of appropriate scaling factors. This approximation holds for offsets less than 7,000 ft and 5,000 ft for compressional and converted waves, respectively.

Using poststack converted-wave amplitude inversion, pseudo-S-impedance volumes are generated and nine gas-bearing lenticular fluvial sand bodies are imaged in the vicinity of the study well location. The good-quality overpressured sand bodies are identified from high resolution Vp/Vs volumes. Low Vp/Vs intervals correlate

with the best overpressured sandstone reservoirs and high Vp/Vs intervals correlate with shaly or underpressured intervals. These Vp/Vs volumes are generated by first registering the pseudo-S-impedance volumes to the compressional-wave time scale and then by dividing them. Finally, the high fracture density intervals are determined by evaluating the influence of shear-wave splitting on converted-wave reflectivity. Instantaneous anisotropy volumes are generated by subtracting the fast and slow pseudo-S-impedance volumes. The intervals of high anisotropy are related to higher fracture density.

Traveltime and amplitude inversion of converted-wave data leads to a successful anisotropic reservoir characterization. The key to success is the joint analysis and integration of traveltime and amplitude data extracted from compressional and converted waves in order to generate an accurate anisotropic model for the reservoir.

TABLE OF CONTENTS

LIST OF FIGURES

LIST OF TABLES

ACKNOWLEDGMENT

The professors and the students of the Colorado School of Mines made my two years stay in Golden successful and fruitful. Without them, I would not be able to succeed in pursuing my master's degree. They stood by my side all the way through, giving me support, encouragement, and brilliant ideas.

I would first like to thank my committee members: my advisor Thomas Davis, Ilya Tsvankin, Robert Benson, and Lawrence Meckel. I would like to express my sincere appreciation to Tom Davis because he has been an excellent advisor. Without his creativity, flexibility, and great ideas, this thesis would have not been written. He provided me with guidance and gave me enough freedom necessary for my research. His dedication to the RCP and his belief in the importance of converted-wave data for reservoir characterization were the key to success of this thesis. I would also like to express my gratefulness and admiration to Ilya Tsvankin. Not only do we share Russian language in common, we now share the same passion for seismology. Ilya thaught me to understand and appreciate anisotropy and for that I will be forever grateful to him. I am also grateful to Larry Meckel because he taught me important concepts in geology. I will go back home with a broad knowledge and an amazing background in geology. I would also like to thank Bob Benson for helping me with the data processing and seismic interpretation.

I would also like to thank all the professors and the students of the Department of Geophysics. I would like to address a special acknowledgment to John Stockwell. I will definitely be missing John, the great scientist and the wonderful man. I would like to acknowledge Terry Young, head of the Department of Geophysics, and Mike Batzle, head of the Center for Rock Abuse. I would also like to acknowledge my friends who helped and inspired me: Jyoti Behura, Steve Smith, Praj Mazumdar, Cucha López, Paritosh Singh, and Farnoush Forghani-Arani. I would also like to thank all my RCP friends: Ibrahim Mustafayev, Rafael Pinto, Andrew Pomroy, Ayyoub Heris, Dawn Jobe, Aaron Wandler, Mohsen Minaei, Naser Tamimi, Sony Mohammad, Colin Melvin and Mark Wiley. I would finally like to thank Andrey Bakulin, Ivan Vasconcelos, and Rodrigo Fuck for their advice, suggestions, and support.

I am also very grateful to Roel Sneider, head of the Center for Wave Phenomena (CWP), for his support and kindness: I have always been invited to the CWP meetings and I was always given the opportunity to share my research results with the CWP. I would also like to acknowledge the staff of the RCP, the CWP, and the Department of Geophysics: Dawn Umpleby, Susan Venable, Barbara McLenon, Michelle Szobody, and Sara Summers for their willingness to help in any situation.

Here, I would like to address a special acknowledgment to TOTAL S.A.; I am going to join them soon after I leave Colorado. They funded my stay at the RCP and provided me with financial aid. From TOTAL S.A., I would like to thank Paul Williamson, François Audebert, and Jean-Luc Boëlle for their advice and kindness. I would also like to acknowledge Pierre Thore, Wafik Beydoun, and Serge Nicoletis for their guidance and support.

My final acknowledgments belong to my close friends and family. I thank Iryna, my closest friend, for her honest love and great support. I am grateful to her because she created a home for me here in Colorado. I thank her for all the happiness she brought to my life. I would also like to thank the dear friends who stood by my side in the U.S.A: Maksim Avseyev, Nikita Turkin, Natallia Temnikova, Olga Sapozhnikova, Toni Jeitani, and Daniel Haddad. I am also grateful to my dear friends who were always close to me although I was far away from home: James Kairouz, Antoine Kassis, Karim Safieddine, Joe Zarifeh, Salim Yasmine, Frédéric Chavanon, Henri Lecieux, Thomas Volmer, Frédéric Méraux, and Paul Wilczynski.

I would finally like to express my love and my gratefulness to my mother May, my brother Magid, my sisters Daniela and Adriana, and my stepfather Mouhib. I thank all of them because they never stopped supporting me, loving me, and believing in me. I dedicate this thesis to them.

Мороз и солнце, день чудесный!
Ещё ты дремлешь, друг прелестный –
Пора, красавица, проснись:
Открой сомкнуты негой взоры
Навтречу северной Авроры,
Звездою севера явись!
(А. С. Пушкин)

Cold frost and sunshine, day of wonder!
But you, my friend, are still in slumber
Wake up, my beauty, time belies:
You dormant eyes, I beg you, broaden
Toward the northerly Aurora,
As though a northern star arise!
(A. S. Pushkin)

Chapter 1

INTRODUCTION: GEOLOGICAL OVERVIEW, SEISMIC ACQUISITION AND DATA PROCESSING

1.1 Research Objectives

The objectives of my research in the Reservoir Characterization Project (RCP) were (1) the imaging of the elusive lenticular sand bodies, (2) the identification of the best overpressured productive sandstones, and (3) the determination of the fractured intervals.

The first step was to analyze poststack traveltime and amplitude attribute data. I generated shear-wave splitting maps that relate to fractured zones in the reservoir. In the absence of strong P-wave azimuthal anisotropy, shear-wave splitting coefficients can be computed equivalently from pure shear-wave or converted-wave data without having to eliminate the downgoing P-wave traveltime contribution from the total PS-wave traveltime.

I then modeled the UMV Shale Formation as a VTI medium and estimated the Thomsen anisotropy parameters from P- and PS-wave moveout analysis. Using velocity and density values combined with the Thomsen anisotropy parameters, I conducted an elastic anisotropic AVO modeling study to characterize the influence of anisotropy on the reflection coefficients for P- and PS-wave data at the UMV Shale interface.

Finally, I inverted the seismic amplitude data for both pure and converted modes in order to obtain impedance volumes. The output of this operation consisted of a P-impedance volume as well as fast and slow S-impedance volumes derived from both pure shear-wave and converted-wave seismic data. The fluvial sandstones were imaged as high-impedance bodies on S-impedance volumes. The location and the lateral extent of the lenticular sand bodies were thus determined. The P- and S-impedance volumes were then divided in order to give high resolution Vp/Vs volumes. Low Vp/Vs intervals characterize the high quality overpressured gas-bearing sandstones. The fast and slow S-impedance volumes were then jointly analyzed to characterize shear-wave splitting and identify the fractured intervals in the reservoir.

1.2 Reservoir Characterization Project Phase X and XI

The Reservoir Characterization Project (RCP) is an industry-funded research consortium in the Department of Geophysics at Colorado School of Mines. It focuses on the development and application of 4-D multicomponent seismic to enhance static and dynamic characterization of conventional and unconventional hydrocarbon reservoirs. Phase X and XI of the project are related to the study of the tight gas sandstone reservoirs and coals in the Rulison Field, Colorado.

1.3 Rulison Field

Rulison Field, operated by Williams Production RMT Company, is a basin-centered gas accumulation in the Piceance Basin, Colorado (Figure 1.1). The field is considered unconventional since 98% of the gas is being produced from pervasive gas in tight sandstones and coals in the Upper Cretaceous Williams Fork Formation. Although the Williams Fork Formation contains a vast amount of gas, the low permeability and porosity of the formation combined with the strong lateral discontinuity of the stacked sand bodies complicate the tasks of well completion, production, and seismic imaging. It is a challenge for geophysicists to be able to estimate anisotropy and fracture orientation and density using seismic data. Since 4-D multicomponent seismic data have been shot in the Rulison Field by the RCP in 2003, 2004, and 2006, both groundbreaking geophysical techniques and innovative methods can be tested in order to improve reservoir characterization.

1.4 Geological Setting

The Piceance Basin is a Laramide structural basin in northwestern Colorado. It comprises geologic formations from Cambrian to Eocene in age, but the thickest and most productive section is the Upper Cretaceous. The 7,255 mi^2 basin is bounded on the north by the Axial Fold Belt, on the west by the Douglas Creek Arch and the Uncompahgre Uplift, on the east by the White River Uplift, and on the south by the Gunnison Uplift (Figure 1.1). The basin is asymmetric with a synclinal axis near the eastern margin. Rulison Field is located in the eastern part of the basin, in the synclinal axis of the basin, near the town of Rifle.

1.4.1 Stratigraphy of the Upper Cretaceous Mesaverde Group

Iles Formation

The Upper Cretaceous Mesaverde Group comprises the Iles and Williams Fork formations (Figure 1.2). The Iles Formation includes three regressive marine sandstone cycles (the Corcoran, the Cozzette, and the Rollins sandstones) that are separated by tongues of the marine Mancos Shale (Cumella & Scheevel, 2008). These sandstones are continuous and can be correlated across the southern and eastern Piceance Basin. The marine Mancos Shale is a regional source rock in the Piceance Basin. The stratigraphy of the Mesaverde Group is presented in detail in Cole and Cumella (2003).

Williams Fork Formation: main producing unit

Most of the gas production in the Piceance Basin is from the Williams Fork Formation of the Upper Cretaceous Mesaverde Group. The Williams Fork Formation ranges from 1,500 ft to 4,000 ft thick with an average thickness of 2,000 ft. Gas shows are typically sparse in the upper 1,000-1,700 ft of the Mesaverde Group (Hood & Yurewicz, 2008). The stratigraphic section is shown in Figure 1.2 and a type log for the Mesaverde Group is shown in Figure 1.3. The Mesaverde Group is underlain

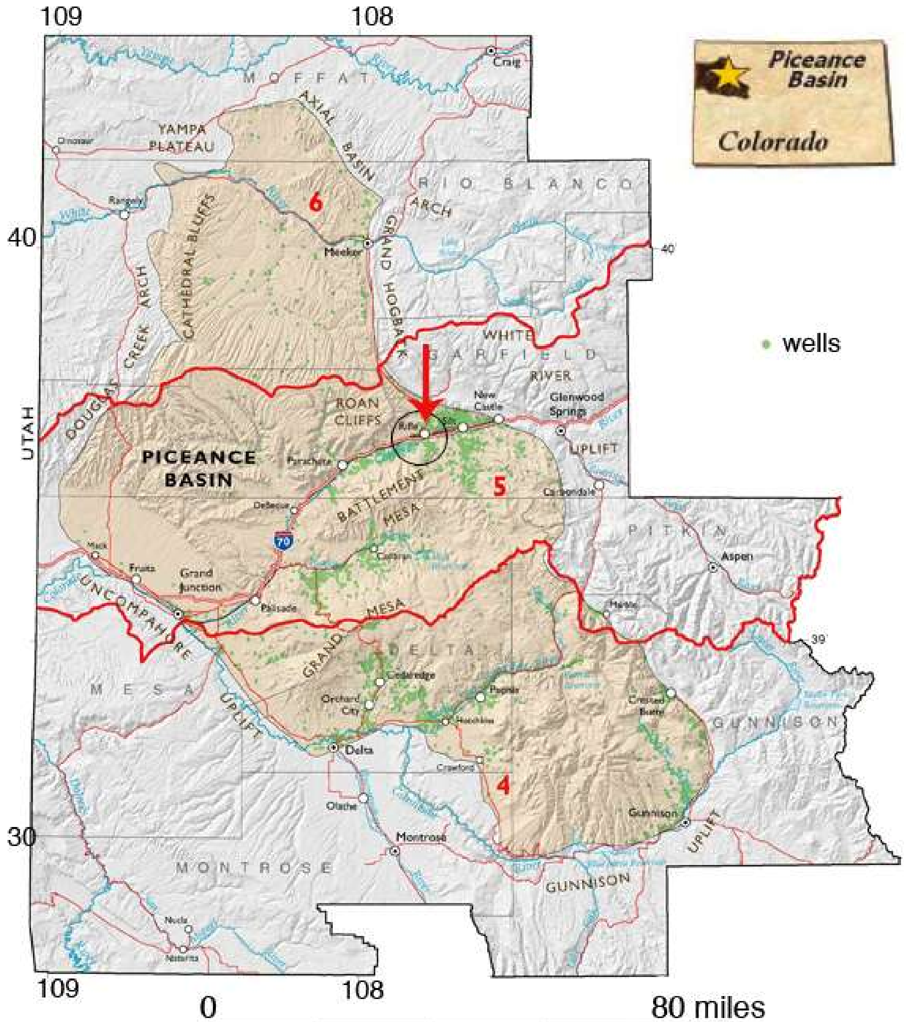

Figure 1.1. Map showing the geographic location and extent of the Piceance Basin in northwestern Colorado. The red arrow indicates the approximate location of the Rulison Field. Adopted from Topper et al. (2003).

by the Mancos Shale and and overlain by the Tertiary Fort Union Formation. The Williams Fork Formation is overlain by the Wasatch Formation and underlain by the Rollins Sandstone (Figure 1.3). The structure map of the Piceance Basin at the top of the Rollins Sandstone is shown in Figure 1.4. The top of the UMV Shale as well as the top and bottom of the Cameo Coal are strong reflectors. These three strong reflectors are the main horizons interpreted from the seismic data.

The Williams Fork Formation has been divided into two different lithofacies. The lower 500 to 700 ft is dominantly shale with some isolated discontinuous lenticular fluvial sand bodies. The upper Williams Fork has less shale, is thicker, and contains more laterally continuous lenticular fluvial sand bodies.

1.4.2 Depositional Facies

The sandstone reservoirs of the Williams Fork Formation were mostly deposited as meandering fluvial systems (Cole and Cumella, 2003). The stacked gas-bearing sandstone intervals are highly lenticular. Field data indicate a range in sand body average thickness from 0.5 to 29 ft, with a mean average of 9.3 ft, and a range in apparent sand body width from 40 to 2,791 ft, with an average of 528.4 ft (Cole, 2005). The cross-plot of thickness and width is shown in Figure 1.5. Because of their small thicknesses, the individual sand bodies are invisible to conventional seismic data that have a typical vertical resolution of approximately 100 ft (see Chapter 2). The exact determination and imaging of the lateral extent of the sand bodies is a major task this thesis will adress. Some 100 ft thick, laterally continuous sandstones do exist in the Williams Fork Formation. These are interpreted as amalgamated channels (Lorenz et al., 1985).

1.4.3 Tectonic Settings

In the Precambrian Period, the Piceance Basin was subject to regional crustal shearing and extension resulting in extensive basement faulting. In the Pennsylvanian Period, the basin experienced a NW trending extension that produced a graben in

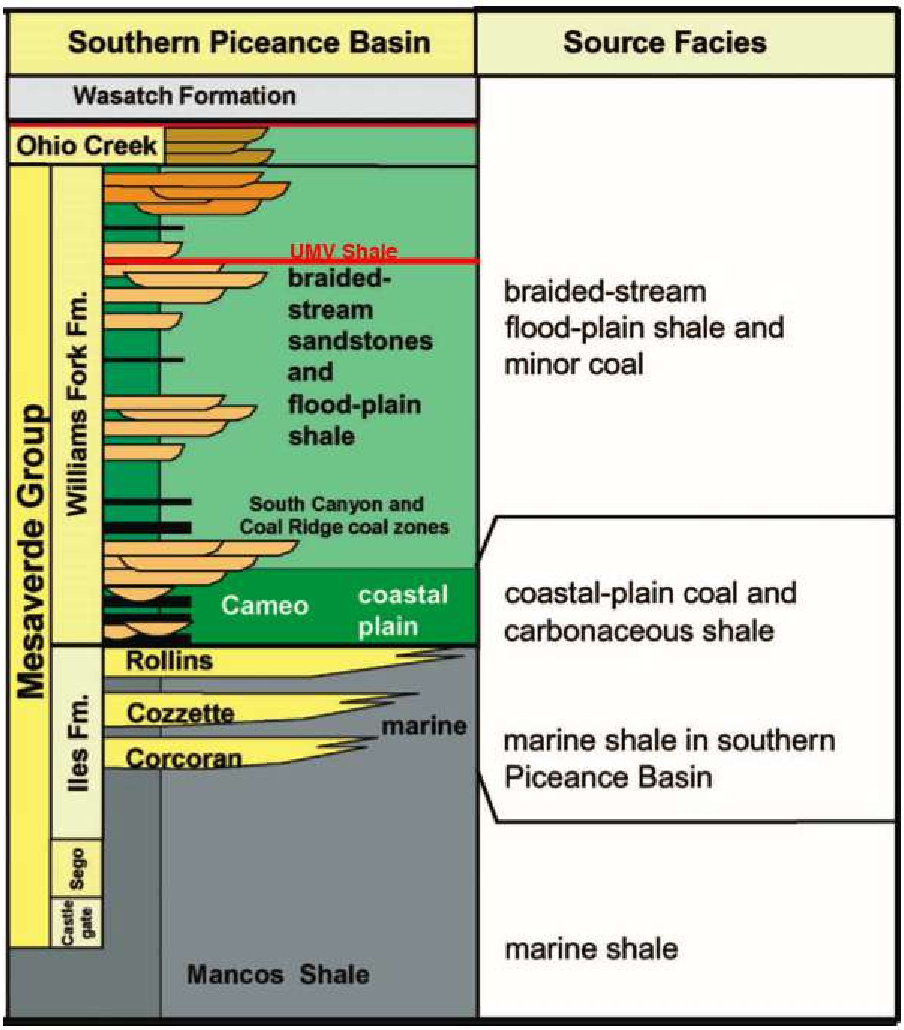

Figure 1.2. Stratigraphic column showing the Williams Fork Formation and the distribution of the main source facies, Southern Piceance Basin. Modified from Yurewicz et al. (2008).

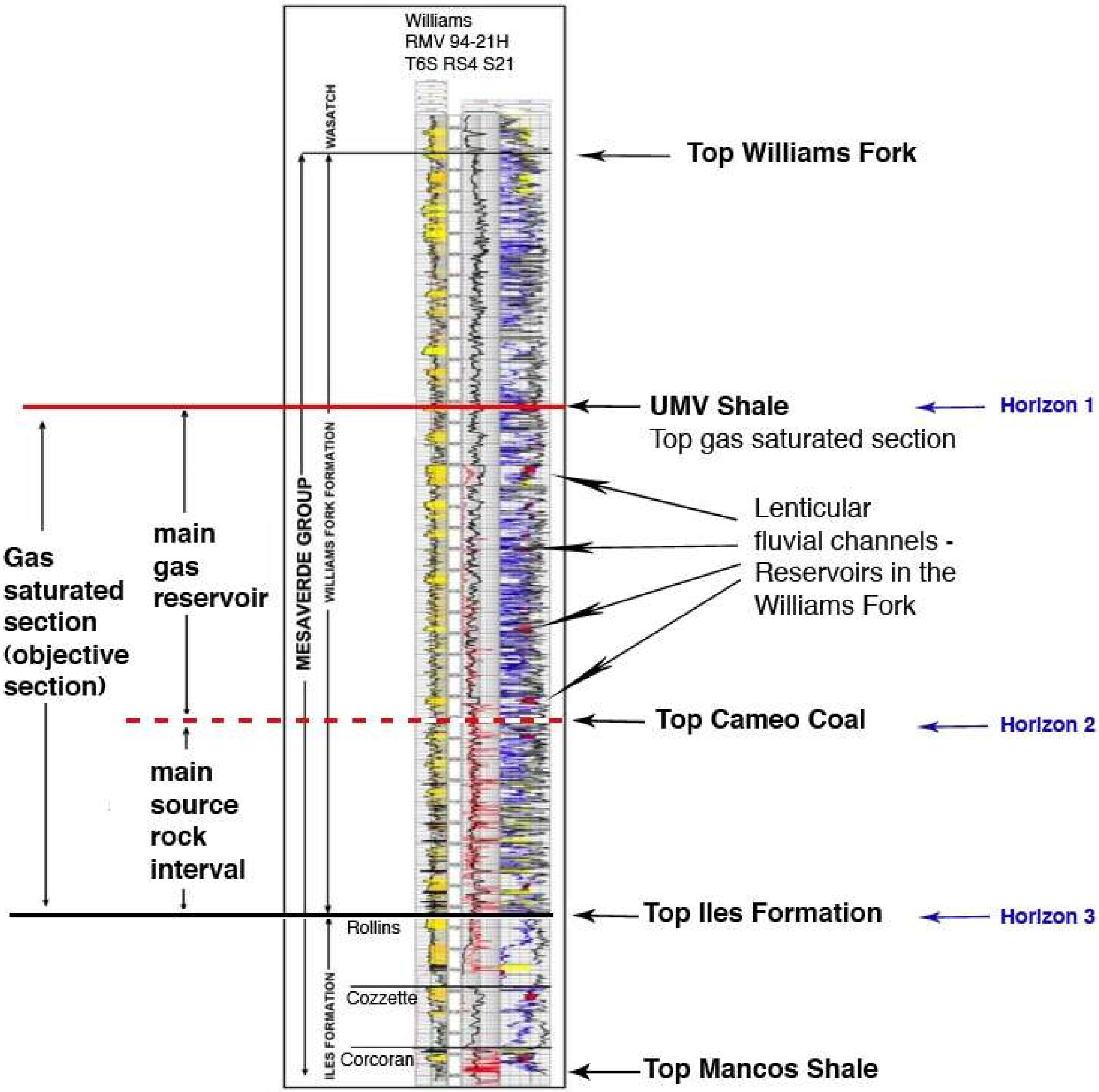

Figure 1.3. Type log for the Mesaverde Group in the Rulison Field study area showing (1) formations, (2) reservoirs, (3) source rocks, (4) gas-saturated section, (5) main seismic horizons, and (6) terminology used in this thesis.

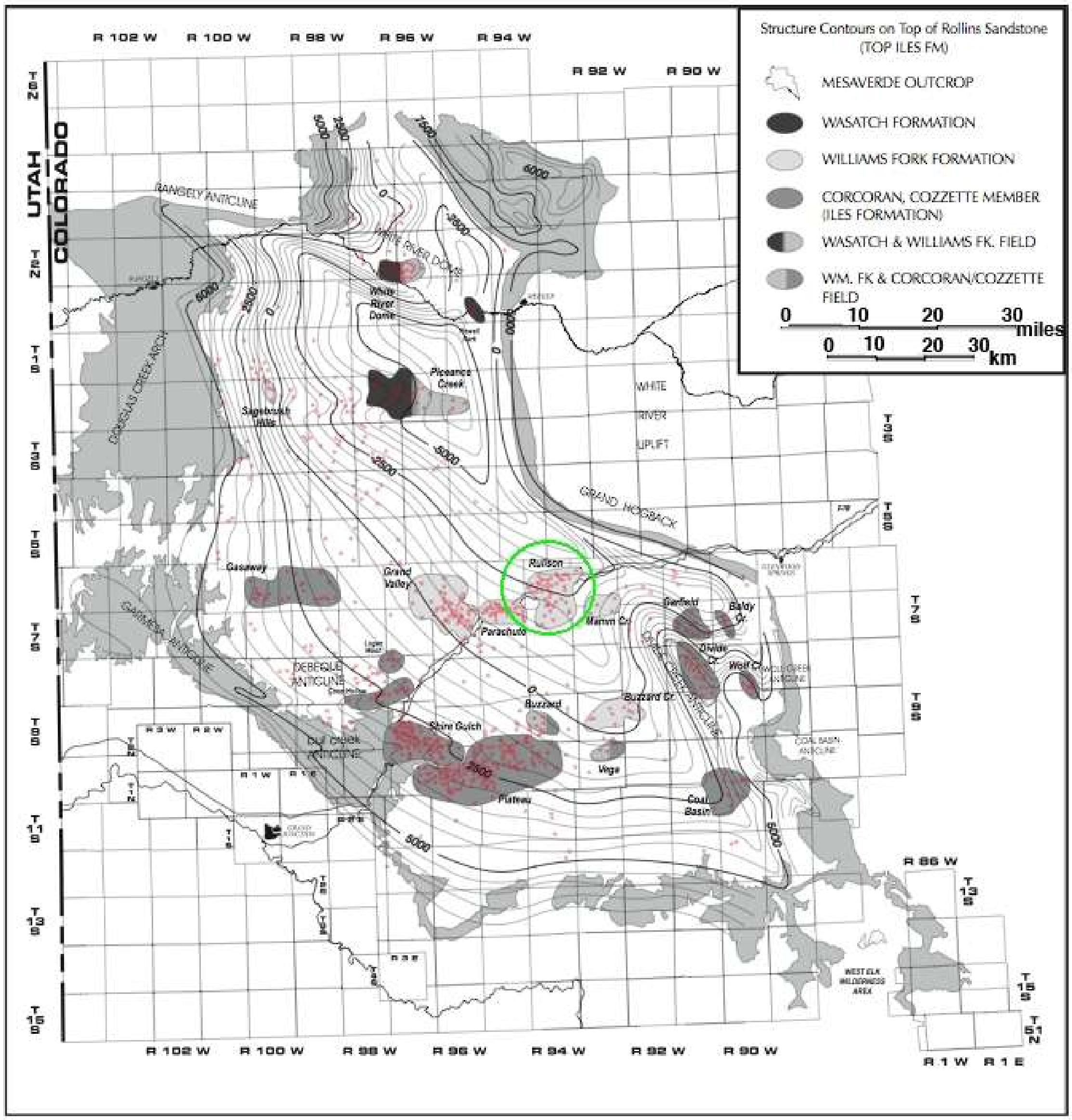

Figure 1.4. Structure map of the Piceance basin at the top of the Rollins Sandstone. The Rulison Field location is indicated by the green circle. Modified from Kuuskraa et al. (1997).

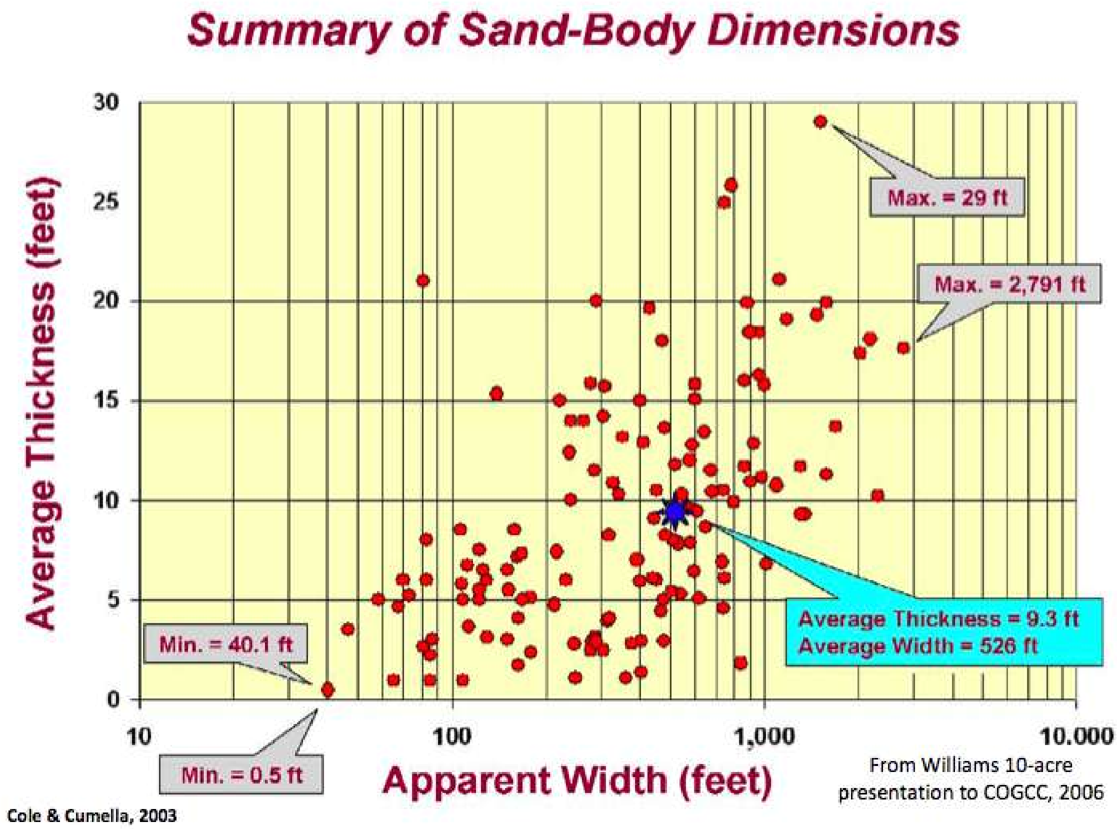

Figure 1.5. Cross-plot of thickness and width of the sand bodies in the William Fork Formation, Piceance Basin. Adapted from Cole and Cumella (2003).

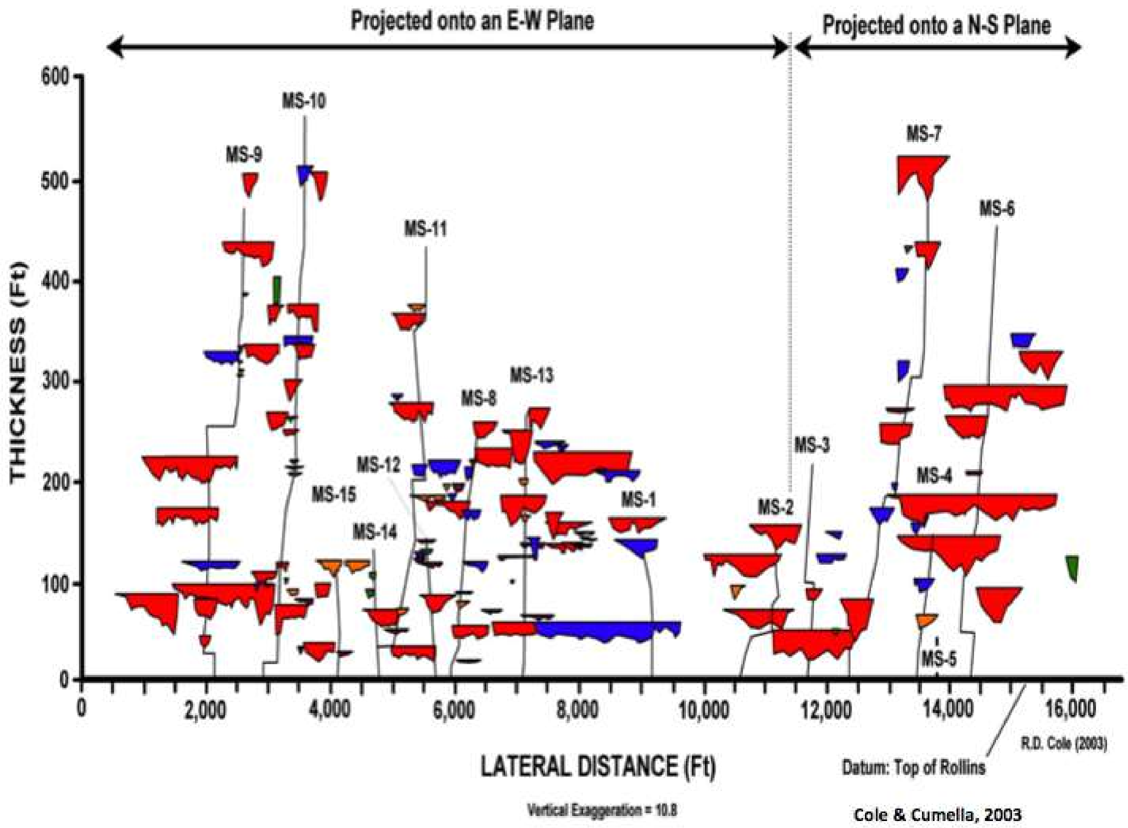

Figure 1.6. Typical channel thickness and width of the sand bodies in the William Forks Formation. Stacked amalgamated sandstone bodies are resolvable using conventional seismic data while individual sand bodies are invisible. Adapted from Cole and Cumella (2003).

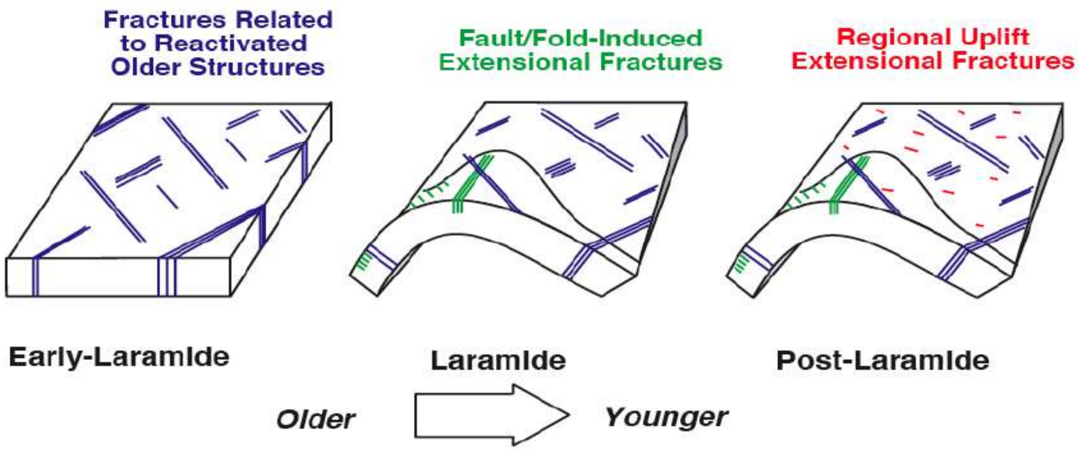

Figure 1.7. Development of the major fractures in Rulison Field. Adopted from Kuuskraa et al. (1997).

the Rulison area. From Cretaceous to Eocene time, the basin was subject to the Laramide compressional tectonics that induced a pronounced SW shortening. This compression created what is now known as the subtle Rulison anticline (Figure 1.4). Both Precambrian to Pennsylvanian extensional tectonics followed by the Cretaceous to Eocene compressional tectonics influenced the state of stress in the Piceance Basin as well as the structural anisotropy and the resulting fault systems in the area. In the Holocene, the basin has been subject to WNW and EW compression and uplift (Kuuskraa et al., 1997). The complex basin tectonic history produced two dominant regional fracture sets. One set trends N30° and the other N60°. The fracture density and orientation as well as the fault zone characteristics have been extensively studied by Jackson (2007).

1.5 Petroleum System and Reservoir Properties

Pervasive gas accumulations are different from conventionally trapped accumulations (Selley, 1982) in several respects. The five elements that characterize a basin-centered gas (BCG) accumulation are: (1) an organic-rich source rock, (2) a high maturity interval, (3) an overpressured compartment, (4) pervasive type I shows, and

(5) low permeability discontinuous reservoir rocks.

The Cameo Coal interval in the lowermost part of the Williams Fork Formation is the primary source rock of gas in the Piceance Basin. The coals from the Piceance Basin are vitrinite-rich coals or type III kerogen (Zhang et al., 2008). Aggregate coal thicknesses in the Lower Williams Forks are typically 20-80 ft, but are commonly greater than 80 ft in the eastern part of the basin (Yurewicz et al., 2008).

Thermal effect from magmatism raised coal rank throughout the Piceance Basin. The thermal history of the basin is hard to reconstruct from coal rank distribution since a short single pulse of heat can yield the same coal rank as would result from a longer, less intense heat-pulse (Yurewicz et al., 2008). The coal rank map of the Cameo Coal Group is shown in Figure 1.8: the darker colors indicate higher coal ranks while the lighter colors indicate lower coal ranks.

Pressure gradients are as high as 0.8 psi/ft in the lower part of the Williams Fork in the structurally deeper part of the basin. Pressure gradients decrease upward to hydrostatic gradients (0.43 psi/ft) near the UMV Shale in the southern part of the basin (see Figure 1.9). Hydrostatic conditions continue upward to the top of the Williams Fork. Therefore, the UMV Shale Formation corresponds to the top of the overpressured compartment in the southern Piceance Basin.

The Williams Forks Formation has continuous gas shows throughout the basin (see Figure 1.10). Due to higher pressure during gas generation in the past, all rock types have been fractured (Yurewicz et al., 2008) and gas migration occurred through a pervasive fracture network resulting in a thick, continuous gas-saturated interval. Regionally, the top of the continuous gas cuts across stratigraphy (see Figure 1.11) and does not appear to be stratigraphically controlled. Although in Rulison Field the top of the continuous gas coincides with the UMV Shale Formation, the continuous gas-saturated section is not sealed.

The matrix permeability in the gas-bearing sand bodies is extremely low ($1-10$ μd) and the porosity is low ($6-10\%$). The presence of authigenic clays, carbonate cement, and quartz overgrowth is responsible for the low porosity observed in the

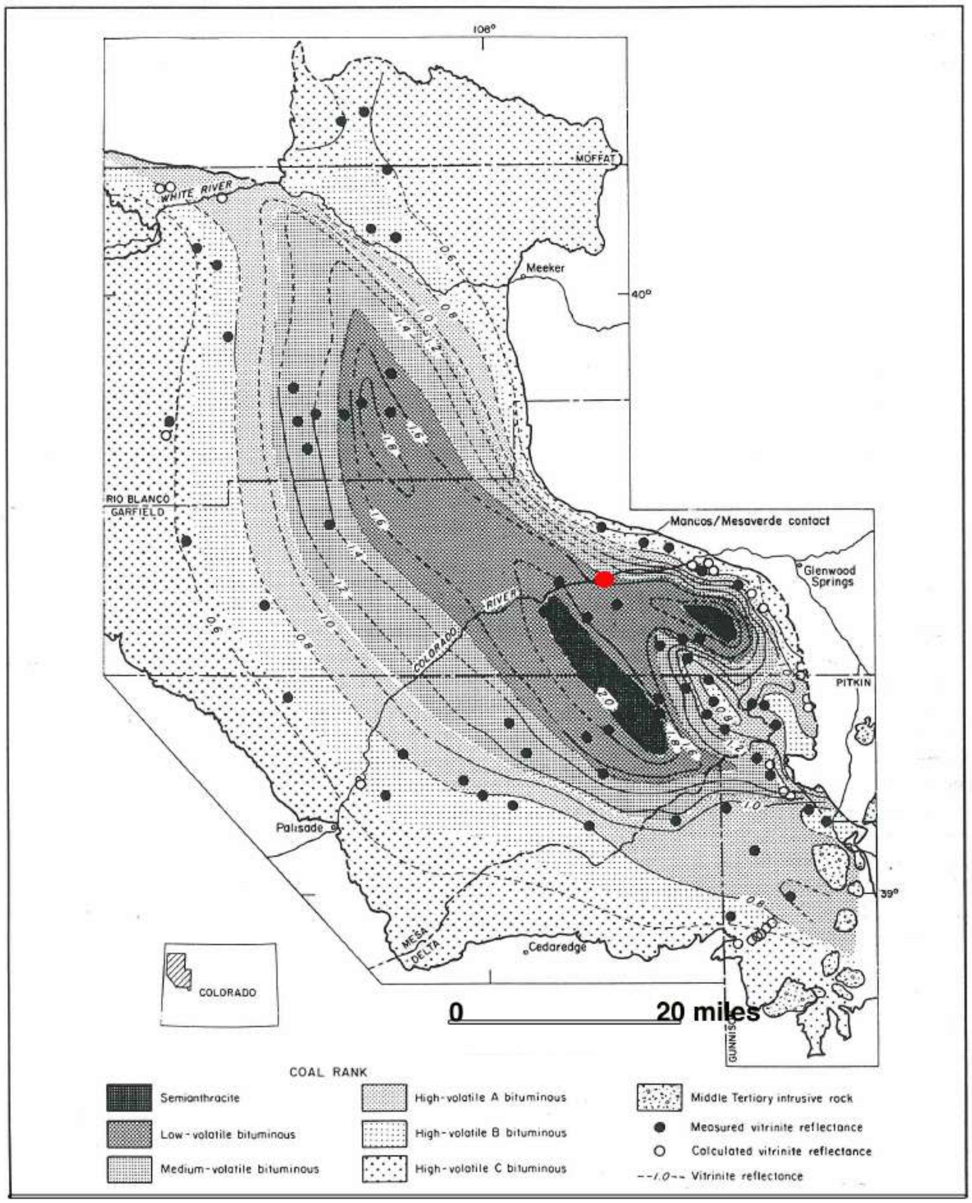

Figure 1.8. Coal rank map of the Cameo Coal Group. The darker colors indicate higher coal ranks while the lighter colors indicate lower coal ranks. The red dot indicates the location of the Rulison Field. Modified from Bostick & Freeman (1984).

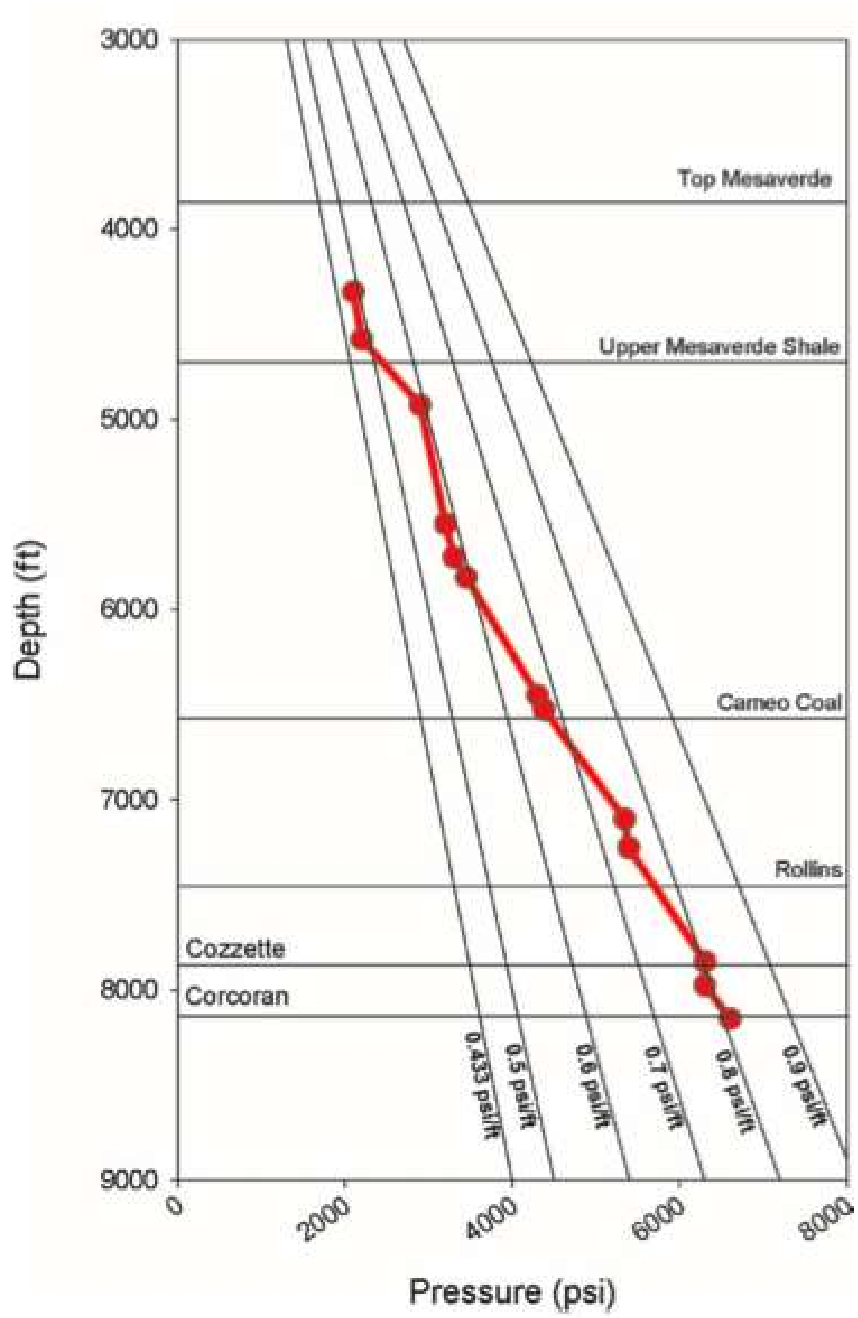

Figure 1.9. Pressure profile in the Piceance Basin. The UMV Shale is the top of the overpressured compartment. Adopted from Cumella & Scheveel (2008).

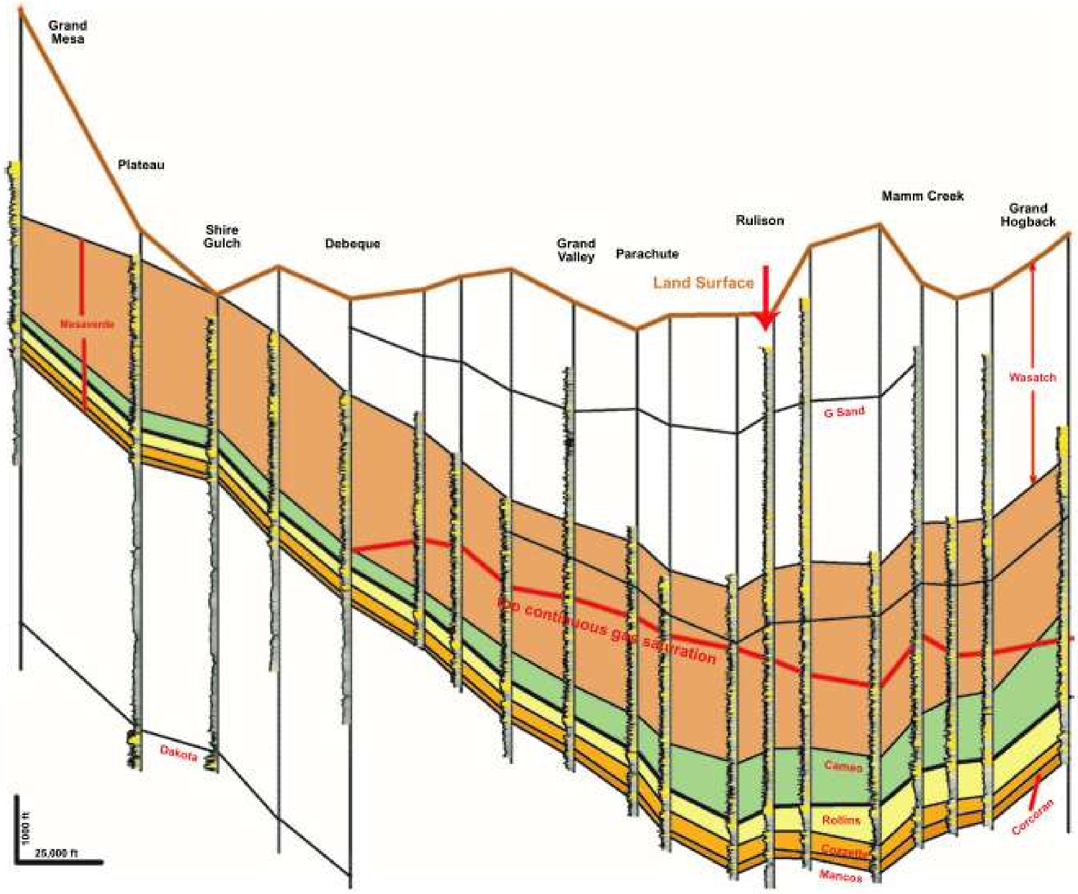

Figure 1.10. Regional east-west cross section of the Mesaverde Group. Color-filled gamma-ray logs are shown (yellow for sandstones and gray for shales). Regionally, the top of the continuous gas cuts across stratigraphy. The red arrow shows the approximate location of Rulison Field. In Rulison Field, the top of continuous gas coincides with the UMV Shale Formation. Adapted from Cumella & Scheveel (2008).

Williams Fork sandstones (Jansen, 2005). Natural fractures significantly enhance the relative permeability to gas and are critical to good production in Rulison. Furthermore, hydraulic fracturing helps connecting the naturally fractured gas-bearing sand bodies to the wellbore and is therefore important for wells productivity and EUR's (Davis & Benson, 2009).

1.6 Production History

The production in Rulison started in the early 1950's. The average annual gas production from 1980 to 1989 was only 32 MMCF. From 1995 to 1999, that average

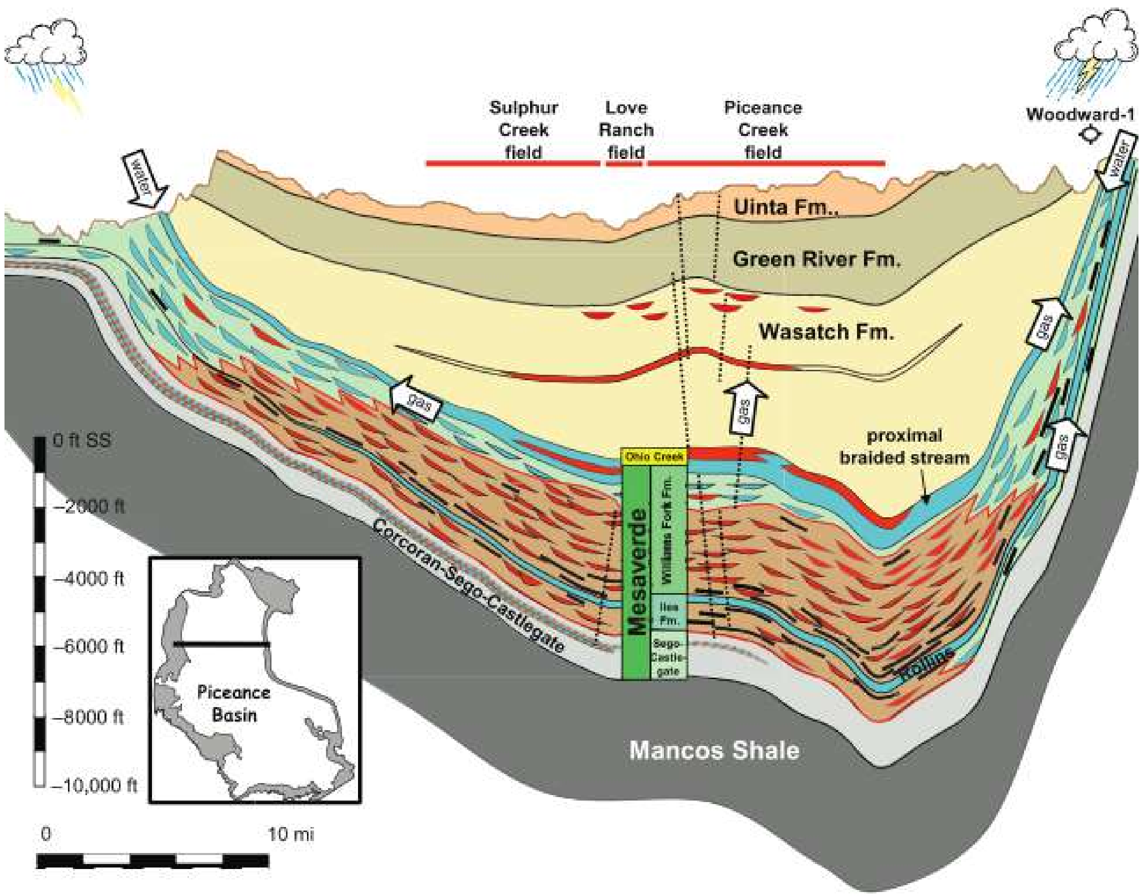

Figure 1.11. Regional east-west cross section through the Piceance Basin depicting the regional distribution of gas (red) and water (blue) within the Mesaverde Group. The Williams Forks Formation has continuous gas shows throughout the basin. Adopted from Yurewicz et al. (2008).

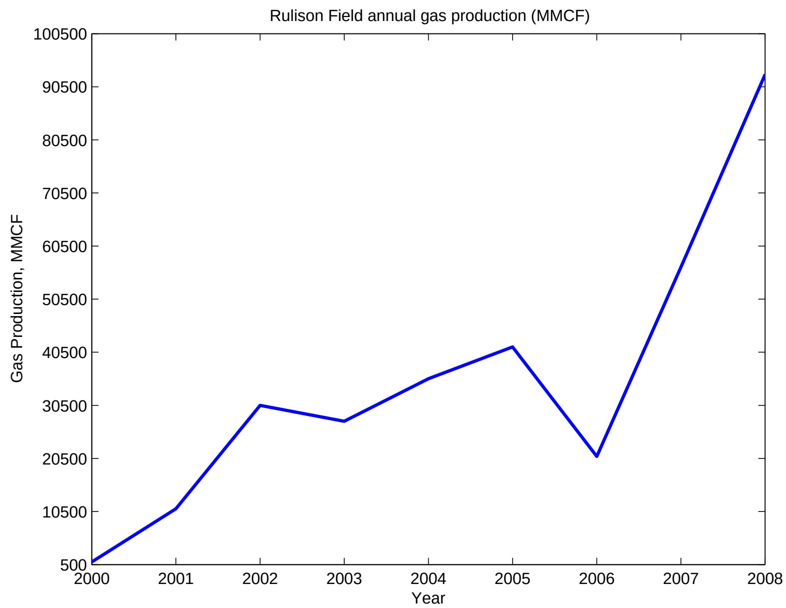

Figure 1.12. Rulison Field annual gas production (in MMCF) from 2000 to 2008. Data from the Colorado Oil and Gas Conservation Commission (COGIS) and from IHS Inc (Douglas County, Colorado).

reached 84 MMCF. In the past decade, the production in Rulison increased exponentially. In 2000, the average gas production was 608 MMCF, while in 2008 the production reached 92,325 MMCF (Figure 1.12). The production data for the time period from 2000 to 2005 were obtained from the Colorado Oil and Gas Conservation Commission (COGIS) and the production data for the time period from 2006 to 2008 were obtained from IHS Inc (Douglas County, Colorado).

1.7 Seismic Acquisition and Borehole Data

The RCP 4-D 9-C seismic surveys cover the area of Rulison Field shown in Figure 1.13. The 2003 survey was recorded in October during very dry conditions. The 2006 survey was recorded in similar conditions. I chose not to work with the 2004 survey because at the time of acquisition the weather conditions were very wet, and therefore, the repeatability of the surveys was affected. Nevertheless, the three surveys were used in different time-lapse studies for dynamic characterizations of the

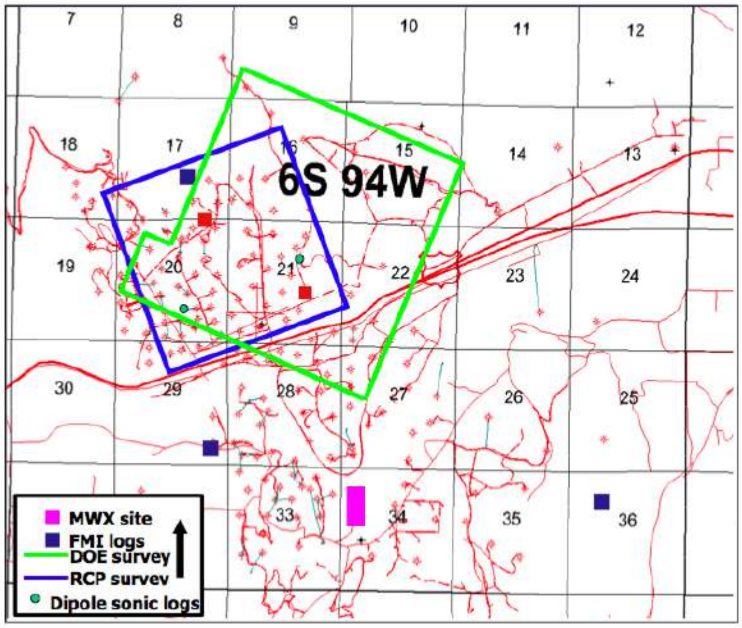

Figure 1.13. Location of the RCP survey (dark blue). Adopted from Franco (2007).

reservoir (Kusuma, 2005; Keighley, 2006; Davis & Benson, 2007; Meza, 2008). The surveys covered an area of two square miles or, more exactly, 7,260 ft by 8,250 ft with 709 source points and approximately 1,500 receivers. Inline receiver spacing was 110 ft and crossline receiver spacing was 330 ft. Source spacing was 110 ft inline and 660 ft crossline with the source lines perpendicular to the receiver lines. This recording geometry was processed into 55 ft by 55 ft bins with 138 inlines and 152 crosslines. The acquisition grid is shown in Figure 1.14.

1.7.1 Seismic Fold and Trace Trimming

All geophones were active for every source location allowing high fold, offset, and azimuthal distribution. The fold is high in the center of the survey with a maximum of 225 for P-waves (Figure 1.15) and a maximum of 65 for PS-waves (Figure 1.16). The edges of the survey were trimmed for S-wave splitting calculations. Twenty lines were trimmed from the east and west edges, thirty lines from the south edge, and forty lines from the north edge. Trimming resulted in a focus on only the high-fold

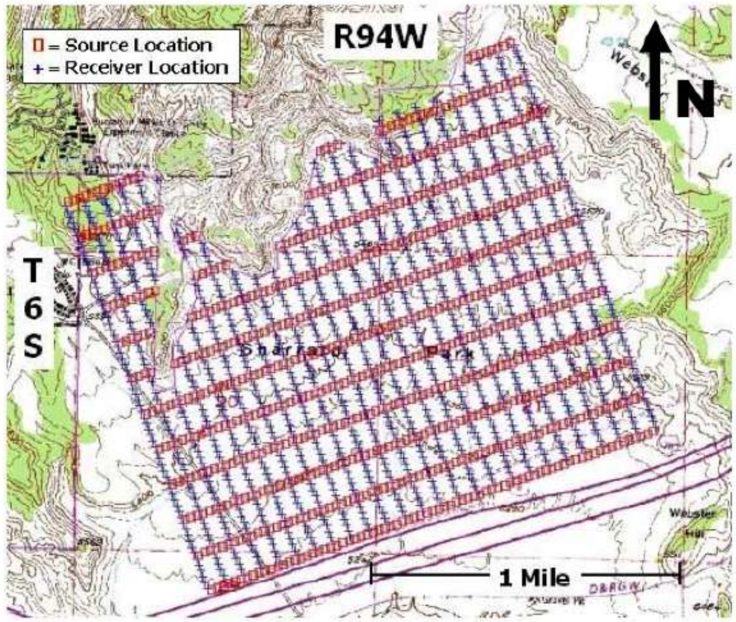

Figure 1.14. The RCP 4-D 9-C acquisition grid. Adopted from LaBarre (2008).

center part of the survey and eliminated much of the error introduced by low fold data. Data were not trimmed for the basic fault interpretations.

1.7.2 Multicomponent Seismic Sources and Receivers

Solid State Geophysical acquired the survey for RCP with vibroseis sources. The P-wave source was an AHV-IV 62,000 lb vibrator which conducted six 5-120 Hz 10 second sweeps at each source point. The S-wave source was a mix of IVI Tri-AX and Mertz 18 shear vibrators with two horizontal sources. The shear vibrators conducted six 5-50 Hz 10 second sweeps at each source location. The receivers were I/O VectorSeis System FourTM single sensor digital (MEMS) receivers. The receivers were GPS surveyed into place to assure maximum repeatability. These receivers were planted singularly at each receiver location and compass oriented into auger drilled holes to assure maximum coupling. The receivers recorded for 16 seconds, and the receiver sampling rate was 2 ms with an instantaneous dynamic range of 118 dB. Table 1.1, based on data given by Winarsky & Kendall (2004b), summarizes the survey acquisition parameters.

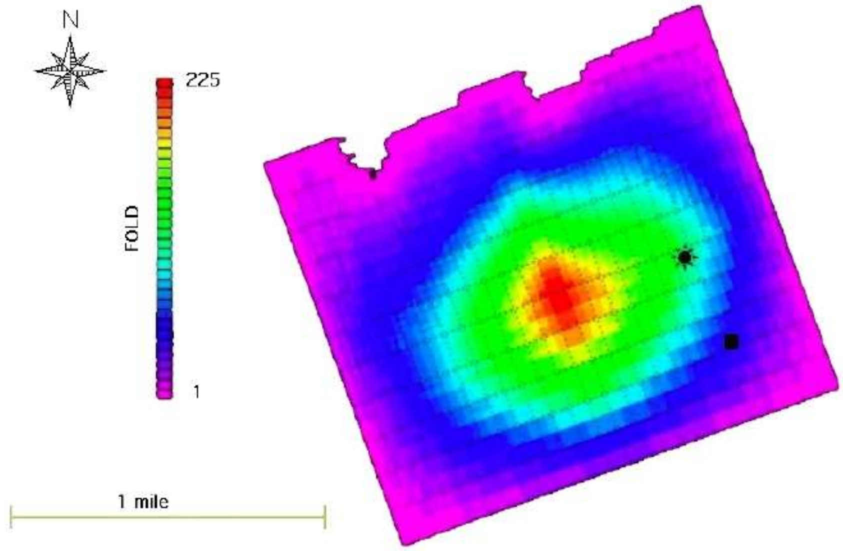

Figure 1.15. Rulison RCP 2003 P-wave fold map for all offsets. The location of the study well RWF 332-21 is indicated by a black square. Modified from Jansen (2005).

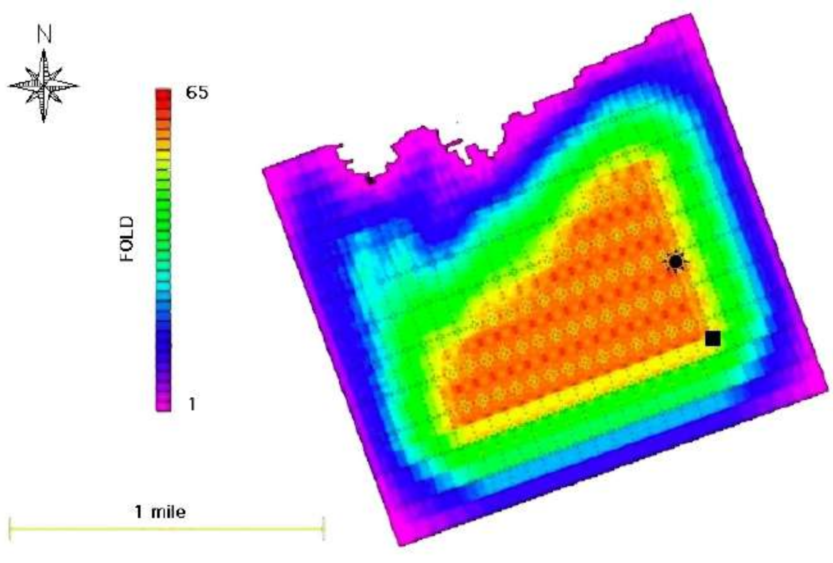

Figure 1.16. Rulison RCP 2003 PS-wave fold map for all offsets. The location of the study well RWF 332-21 is indicated by a black square. Modified from Jansen (2005).

Survey location	Rulison Field, Piceance Basin, Colorado (T6S R94W)
Survey type	4-D, 9-C
Survey size	7260 ft $\times$ 8250 ft (2.15 mi^2)
Nb receiver locations	1500
Nb source locations	700
Receiver grid	110 ft inline spacing, 330 ft between lines
Receiver type	VectorSeis System FourTM digital single sensor (MEMS)
Receiver sampling	2 ms
Source grid	110 ft inline spacing, 660 ft between lines
Source type	Vibroseis
Source P-wave	Mertz 18
Source S-wave	IVI TRI-AX/Mertz
P-wave sweep	6-120 Hz for 10 seconds 6 times per location
S-wave sweep	5-50 Hz for 10 seconds 6 times per location

Table 1.1. The RCP 4-D 9-C survey acquisition parameters. Based on Winarsky & Kendall (2004b).

1.7.3 Wellbore Data

The RCP study area contains more than 70 wells. However only two wells contain cross-dipole sonic logs: well RWF 332-21 (Sec.2, T6S, R94W) located in the lower right corner of the survey (inline 20 and crossline 109 on the seismic grid) and well RWF 441-20 (Sec.20, T6S, R94W) located in the center of the survey (inline 77 and crossline 52 on the seismic grid). The locations of these wells are indicated by red squares on Figure 1.13. Well RWF 332-21 was used as a study and control well since this well contains most of the common log suite: gamma-ray, density, cross-dipole sonic log (rotated for fast and slow shear-wave), P-wave check-shot, resistivity, neutron ...

1.7.4 Seismic Processing

Veritas DGC in Calgary processed the P-wave, S-wave, and converted shear-wave seismic data [for general details on seismic processing, see Yilmaz (2001)]. Table 1.2 shows the processing sequence for the P-wave data, Table 1.3 shows the processing

1. Tilt correction for Vectorseis phone applied in the field
2. Demultiplex/ geometry/ first break picks
3. Refraction tomography statics
4. Manuel trace edits/amplitude recovery - T2
5. Surface consistent amplitude equalization
6. Surface consistent deconvolution
7. Preliminary velocity analysis
8. Preliminary surface consistent statics
9. Final velocity analysis
10. Surface consistent statics
11. First break mutes
12. Trim statics
13. Amplitude equalization and mean scaling
14. Stack
15. Noise attenuation by Fxy deconvolution
16. Kirchhoff migration
17. Filter (5/10-100/110 Hz, 0-1600 ms; 5/10-80/95 Hz 1600-2800 ms)
18. Amplitude equalization - mean scaling

Table 1.2. P-wave seismic processing workflow. Based on Winarsky & Kendall (2004b).

sequence for the S-wave data, and Table 1.4 shows the processing sequence for the converted-wave data (Winarsky & Kendall, 2004b) [for more details on converted-wave processing, see Cary (1994); for more details on converted-wave stacking charts and binning periodicity, see Eaton & Lawton (1992); for more details on converted-wave geometrical spreading correction, see Xu & Tsvankin (2008)]. The most important difference between an S-wave and a P-wave is the direction of particle motion. Because of shear-wave splitting, the processing of shear-wave data involve an extra step known as Alford rotation.

1.7.5 Alford Rotation

The Alford rotation is important in S-wave processing because of a phenomenon known as shear-wave splitting (Alford, 1986). An S-wave will propagate through an isotropic medium with the S-wave velocity of the medium and will maintain the particle motion polarization of which the wave entered the medium. If an S-wave

1. Tilt correction for Vectorseis phone applied in the field
2. Demultiplex
3. Geometry correction
4. Manuel trace edits
5. Polarity correction for receiver and shot
6. Spherical divergence correction
7. Surface consistent amplitude equalization
8. Alford rotation (N45W)
9. Minimum phase correction
10. Surface consistent deconvolution
11. Source/receiver statics - from PS data
12. CDP gather
13. Preliminary velocity analysis
14. Noise attenuation by Radon transform
15. Preliminary surface consistent statics
16. Velocity analysis
17. Surface consistent statics
18. First break mutes
19. Trim statics
20. Amplitude equalization - mean scaling
21. Stack
22. Noise attenuation by Fxy deconvolution
23. Kirchhoff migration
24. Filter (4/8-30/40 Hz, 0-3000 ms; 4/8-25/35 Hz, 3000-6000 ms)
25. Amplitude equalization - mean scaling

Table 1.3. Non converted shear-wave seismic processing workflow. Based on Winarsky & Kendall (2004b).

enters an azimuthally anisotropic medium, it will split into two waves in most cases. A fractured formation is azimuthally anisotropic; therefore, if the initial polarization is not parallel or perpendicular to the fractures, an S-wave will split into a fast and a slow shear-wave. In this thesis, the fast shear wave will be interchangeably denoted by S_{11} or $\grave{S}\acute{S}_1$. The first notation (S_{11}) is based on the Thomsen (1988) notation where the first subscript 1 indicates an inline receiver, and the second subscript 1 indicates an inline source. This notation refers directly to the Alford rotation process. The second notation ($\grave{S}\acute{S}_1$) based on the Aki & Richards (1980) notation clearly indicates that the incident seismic wave is an S-wave and that the reflected seismic-wave is an S-wave as well. In this case, the subscript 1 indicates that the S-wave is a fast shear-wave. In the same way, the slow shear-wave will be interchangeably denoted by S_{22} or $\grave{S}\acute{S}_2$. In the Thomsen (1988) notation, the first subscript 2 indicates a crossline receiver, and the second subscript 2 indicates a crossline source. In the Aki & Richards (1980) notation, the subscript 2 indicates that the S-wave is a slow shear-wave. Figure 1.17 illustrates the splitting phenomenon: an S-wave not parallel or perpendicular to the fractures will split into an S-wave with a polarization parallel to the fractures (S_{11}) propagating with the S-wave velocity of the medium and an S-wave with a polarization perpendicular to the fractures (S_{22}) propagating with a slower velocity. The same analysis and rotation is applied to $\grave{P}\acute{S}$-waves (an incident P- reflected S-wave). The splitting phenomenon will give rise in this case to a *fast* converted-wave denoted as $\grave{P}\acute{S}_1$ and a *slow* converted-wave denoted as $\grave{P}\acute{S}_2$. The notations PS_1 and PS_2 can also be used without ambiguity since we will not be dealing with incident P- transmitted S-waves. The shear-wave splitting phenomenon will be studied, analyzed, and interpreted in Chapters 2, 3, and 5. The reader should also note that the Aki & Richards (1980) notation can also be used for P-waves: an incident P-wave reflected P-wave might be therefore referred to as a $\grave{P}\acute{P}$-wave.

Alford rotation rotates the data recorded on the two orthogonal components in the survey coordinate system to the S_{11} and S_{22} coordinate directions. This creates a matrix of crossline and inline sources and receivers containing energy from both S_{11}

1. Tilt correction for Vectorseis phone applied in the field
2. Demultiplex / geometry (asymptotic binning)
3. Manuel trace edits / amplitude recovery
4. Surface consistent amplitude equalization
5. Rotation of inline and crossline horizontal components using shot and receiver coordinates
6. Surface consistent deconvolution
7. Preliminary velocity analysis
8. Horizon based station drift and long wavelength statics applied
9. Preliminary surface consistent statics suppression
10. Noise attenuation by Radon transform
11. Final velocity analysis
12. Final surface consistent statics suppression
13. First break mutes
14. Trim statics
15. Amplitude equalization - mean scaling
16. Depth variant binning and stack
17. Kirchhoff migration
18. Filter (4/8-50/60 Hz, 0-2400 ms ; 4/8-35/50 Hz, 2400-4000 ms)
19. Amplitude equalization - mean scaling

Table 1.4. Converted shear-wave seismic processing workflow. Based on Winarsky & Kendall (2004b).

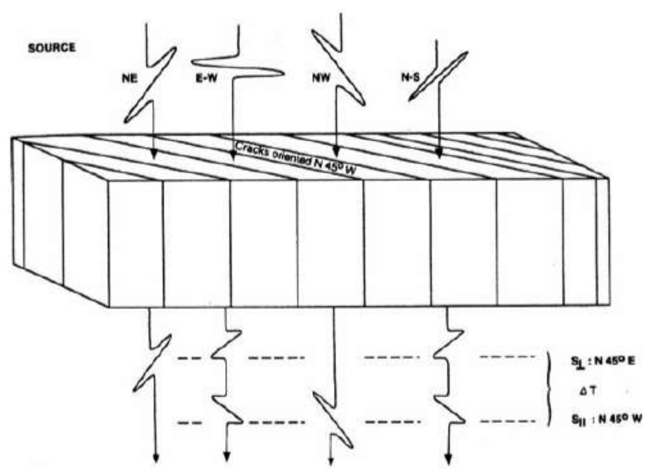

Figure 1.17. Diagram showing S-waves of various polarizations incident on a fractured anisotropic medium. S-waves polarized obliquely to the fractures split into two S-waves. S-waves polarized parallel or perpendicular to the fractures do not split and continue to propagate with their initial polarity. Adopted from LaBarre (2008).

and S_{22} polarizations. The Alford rotation moves the energy to the diagonal principal components of the matrix through a tensor rotation to the direction for which the S_{11} and S_{22} energy is maximized and the energy in the off-diagonal directions is minimized (Alford, 1986). This rotation allows the S_{11} and S_{22} data to separate and shows the principal direction of azimuthal anisotropy (Thomsen, 1988). Based on the processing report from Winarsky & Kendall (2004a), the processing steps of the Alford rotation applied to the Rulison data are the following:

i) The 3D seismic data are sorted into orthogonal pairs (a radial component and a transverse component) within a supergather to create a 2×2 (4C) data matrix.

ii) Each trace in each quadrant represents a 10 degree azimuthal slice of that supergather. Therefore, 36 traces are obtained (0 to 350°, with 10 degrees of increment). The radial component azimuth stack for the $\grave{P}\acute{S}$-wave is shown in Figure 1.18 and the transverse component azimuth stack is shown in Figure 1.19.

iii) Each set of traces is rotated in increments of 10 degrees. The 40°, 50°, and 60° rotations are shown in Figures 1.20, 1.21, and 1.22.

iv) The angle that minimizes the energy on the off-diagonal is the one that corresponds to the fast polarization direction.

v) The time delay between the $\grave{S}\acute{S}_1$ (or $\grave{P}\acute{S}_1$) and $\grave{S}\acute{S}_2$ or ($\grave{P}\acute{S}_2$) sections is related to the degree of anisotropy.

vi) The analysis has only been done in areas of good azimuth distribution.

vii) The data were azimuthally restricted into a fast volume ($\grave{P}\acute{S}_1$- or S_{11}-volume) and a slow volume ($\grave{P}\acute{S}_2$- or S_{22}-volume) and the velocities and statics were recalculated for the new coordinate system.

The Alford rotation to an azimuth of 315° (N45°W) was applied to the Rulison 9-C data (Winarsky & Kendall, 2004a; Mazumdar et al., 2008). This angle resulted in the largest minimization of off-diagonal energy (Figures 1.20, 1.21, and 1.22). This angle is also similar to the polarization angle calculated from the 2003 VSP data obtained in well RMV 30-21 which was N45°W (Figure 1.23).

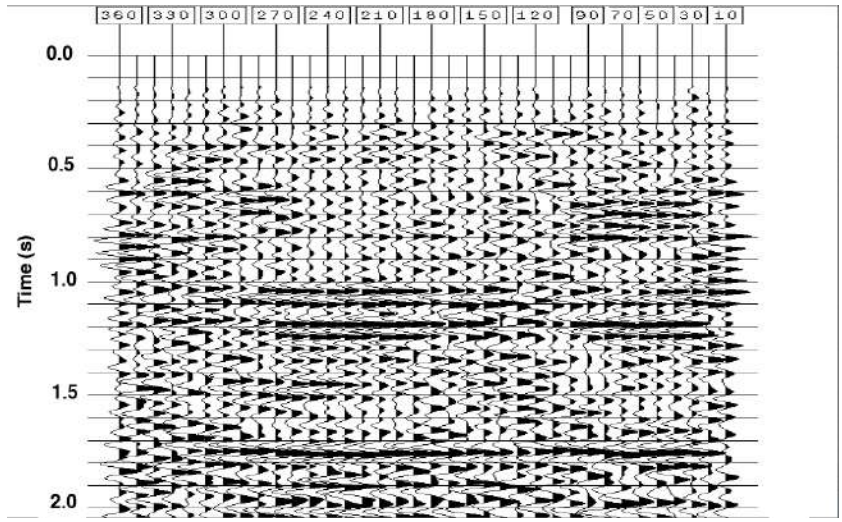

Figure 1.18. The radial component azimuth stack for the P̀Ś-wave corresponding to the 0-350° stack by 10 degree increments for the asymptotic conversion-point (ACP) 9610. Modified from Winarsky & Kendall (2004a).

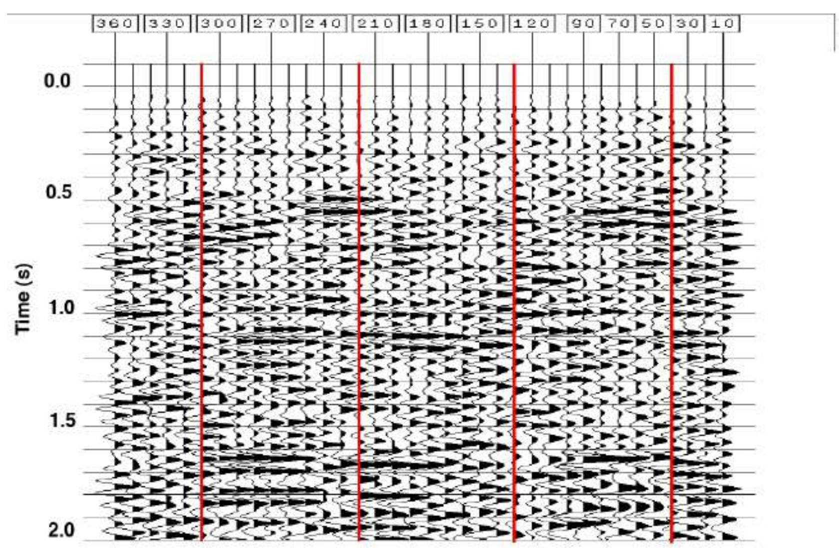

Figure 1.19. The transverse component azimuth stack for the P̀Ś-wave corresponding to the 0-350° stack by 10 degree increments for the asymptotic conversion-point (ACP) 9610. Modified from Winarsky & Kendall (2004a).

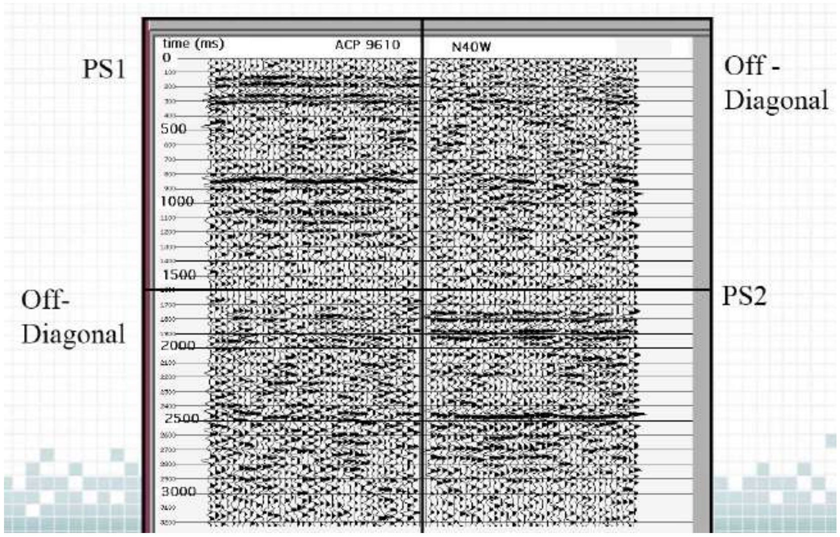

Figure 1.20. The 40° Alford Rotation (N40W) for the asymptotic conversion-point (ACP) 9610. Modified from Winarsky & Kendall (2004a).

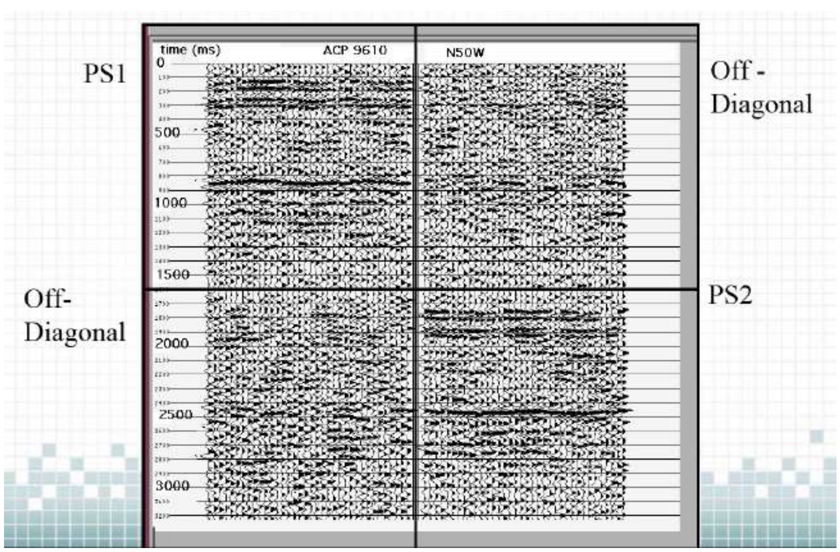

Figure 1.21. The 50° Alford Rotation (N50W) for the asymptotic conversion-point (ACP) 9610. The energy minimization is obtained between the 40° and 50° Alford rotation. Modified from Winarsky & Kendall (2004a).

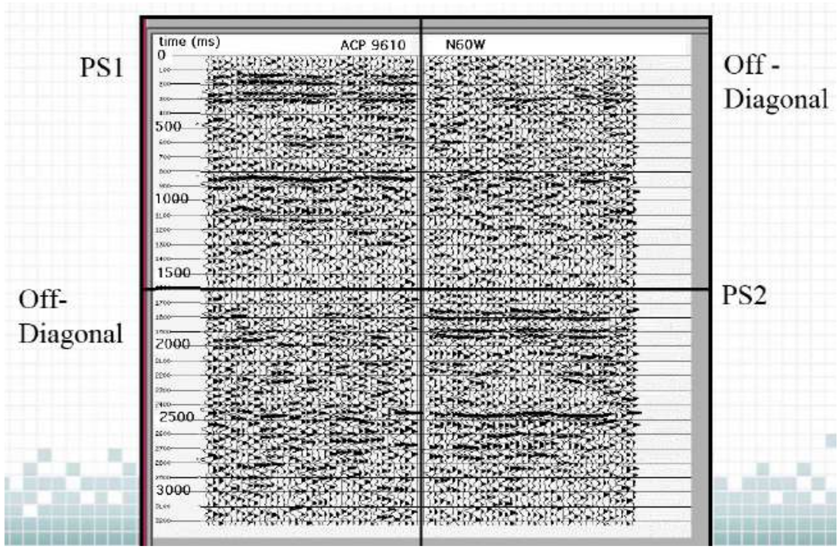

Figure 1.22. The 60° Alford Rotation (N60W) for the asymptotic conversion-point (ACP) 9610. Modified from Winarsky & Kendall (2004a).

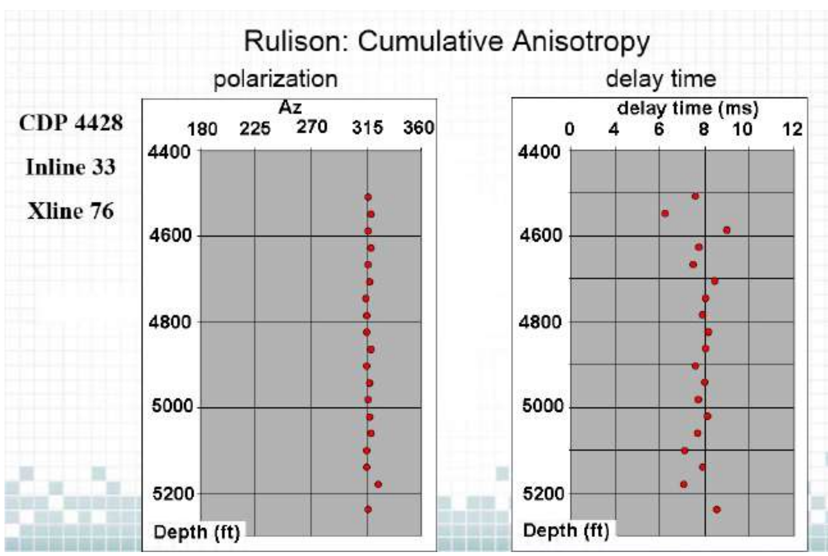

Figure 1.23. The 2003 VSP Alford Rotation in well RMV 30-21. The fast direction for the asymptotic conversion-point (ACP) 4428 (Inline 33, Crossline 76) is found to be 315° (N45°W). Modified from Winarsky & Kendall (2004a).

Chapter 2

SEISMIC ATTRIBUTE ANALYSIS

2.1 Preliminary Data Analysis

As stated in Chapter 1, three 9-C seismic surveys were acquired by the RCP in 2003, 2004, and 2006. At the time of acquisition in 2004, the weather conditions were very wet, while in 2003 and 2006 the weather conditions were dry. Therefore, I chose not to work with the data from the 2004 survey . Henceforth, this study will only use the 2003 and 2006 surveys.

2.1.1 Horizon Interpretation

Figure 2.1 shows for crossline 109 of the processed 2006 survey the fast shear-wave component S_{11} after Kirchhoff migration, and Figure 2.2 shows for that same crossline 109 the corresponding slow shear-wave component S_{22} after Kirchhoff migration. Three horizons have been interpreted for both 2003 and 2006 surveys: (1) the UMV Shale horizon characterized by a strong peak reflection, (2) the top Cameo Coal horizon (often simply designated as Cameo Coal horizon) characterized by a strong trough reflection, and (3) the bottom Cameo Coal characterized by a strong peak reflection. The UMV Shale overlies the top of the gas-saturated section. The top Cameo Coal horizon corresponds to the bottom of the main gas-saturated section producing from the lenticular sand bodies of the Williams Fork Formation; it is also the top of the main source rock interval. The bottom Cameo Coal horizon corresponds to the bottom of the gas-saturated section. It is important to note in these two seismic cross-sections (Figures 2.1 and 2.2) that S_{11} has shorter two-way traveltimes than S_{22}, and therefore, S_{11} is indeed faster than S_{22} as one would expect from the Alford rotation.

On the other hand, Figure 2.3 shows for the crossline 109 of the processed 2006 survey the fast converted-wave component $\grave{\mathrm{P}}\acute{\mathrm{S}}_1$ after Kirchhoff migration and Figure 2.4 shows for that same crossline 109 the slow converted-wave component $\grave{\mathrm{P}}\acute{\mathrm{S}}_2$ after Kirchhoff migration. The same three horizons (UMV Shale, top Cameo Coal, and bottom Cameo Coal) have been interpreted, and the three of them are still characterized respectively by a strong peak reflection, a strong trough reflection, and a strong peak reflection. From Figures 2.3 and 2.4, it seems that $\grave{\mathrm{P}}\acute{\mathrm{S}}_1$ is in deed faster than $\grave{\mathrm{P}}\acute{\mathrm{S}}_2$ since $\grave{\mathrm{P}}\acute{\mathrm{S}}_1$ two-way traveltimes at the top and bottom of the main gas reservoir are slightly smaller than the corresponding $\grave{\mathrm{P}}\acute{\mathrm{S}}_2$ two-way traveltimes.

2.1.2 Repeatability of the Surveys

Figure 2.5 shows the $\grave{\mathrm{P}}\acute{\mathrm{S}}_1$ time-structure maps at the bottom Cameo Coal horizon for the 2003 and 2006 surveys. The two time-structure maps are very similar: the structural high (red and yellow in Figure 2.5) located in the center of the survey has the same shape and dimensions in both surveys, and the structural lows (purple in Figure 2.5) located in the western and northeastern parts of the survey also have similar distributions. Hence, on both 2003 and 2006 surveys, the converted-wave $\grave{\mathrm{P}}\acute{\mathrm{S}}_1$ has similar vertical two-way traveltimes. Therefore, the two surveys have probably been acquired in similar conditions using similar acquisition pattern and processing workflow. In this thesis, I chose to conduct my analysis mainly on the 2006 dataset, but the different attribute studies, traveltime analyses, and amplitude inversions could have also been conducted on the 2003 dataset.

2.1.3 Time-structure Maps and Fault Interpretation

I generated time-structure maps at the bottom Cameo Coal horizon for the 2006 survey based on the pure shear-wave as well as the converted-wave two-way traveltime data in order to (1) understand the information carried in both of these seismic wave modes, and (2) link this information to the geological knowledge of the field.

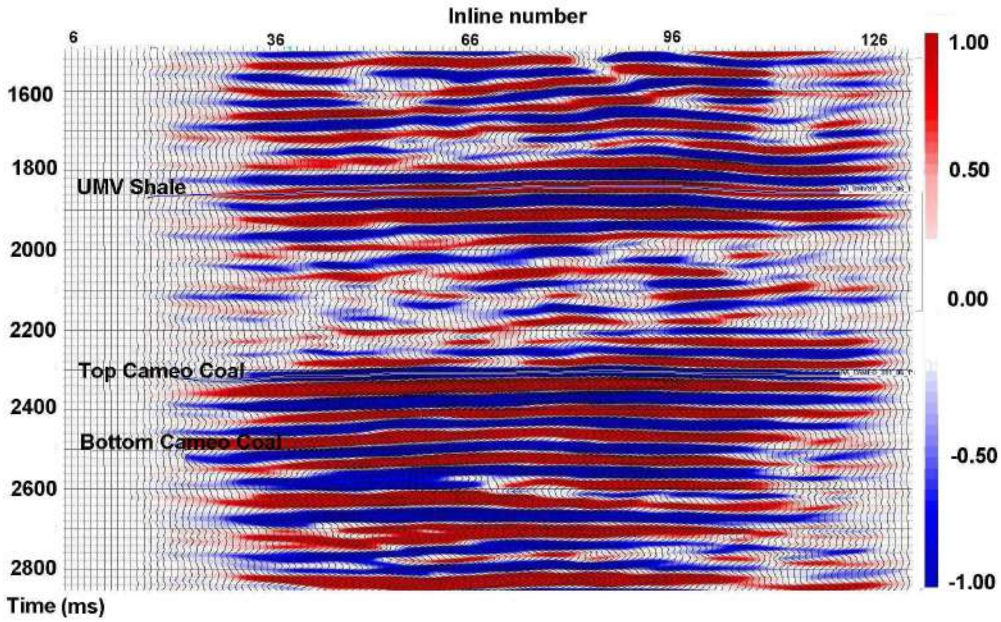

Figure 2.1. Crossline 109 of the Kirchhoff migrated fast shear-wave volume (S_{11}) with the three main reflectors (UMV Shale, top Cameo Coal, and bottom Cameo Coal) indicated.

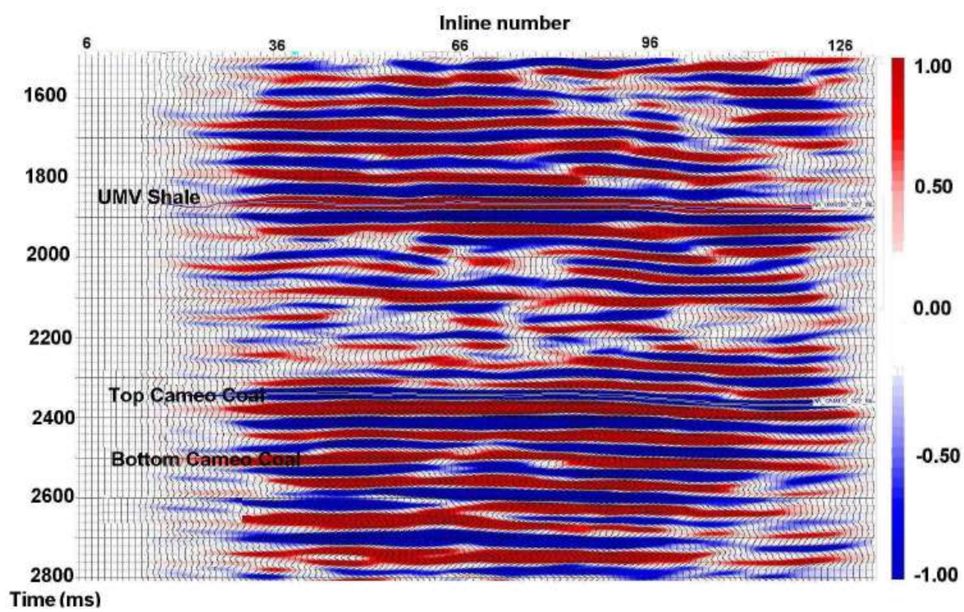

Figure 2.2. Crossline 109 of the Kirchhoff migrated slow shear-wave volume (S_{22}) with the three main reflectors (UMV Shale, top Cameo Coal, and bottom Cameo Coal) indicated.

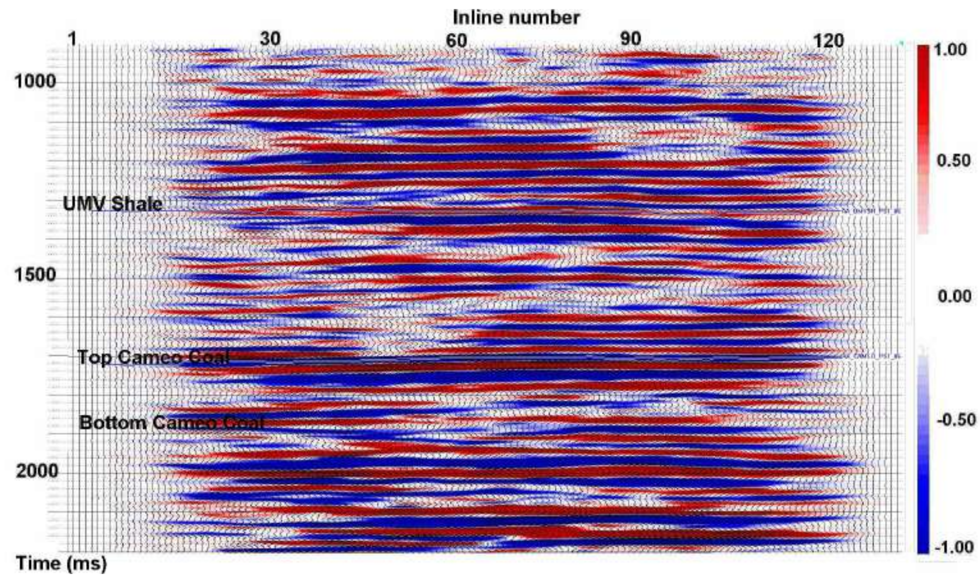

Figure 2.3. Crossline 109 of the Kirchhoff migrated fast component of the converted-wave volume ($\grave{\mathrm{P}}\acute{\mathrm{S}}_1$) with the three main reflectors (UMV Shale, top Cameo Coal, and bottom Cameo Coal) indicated.

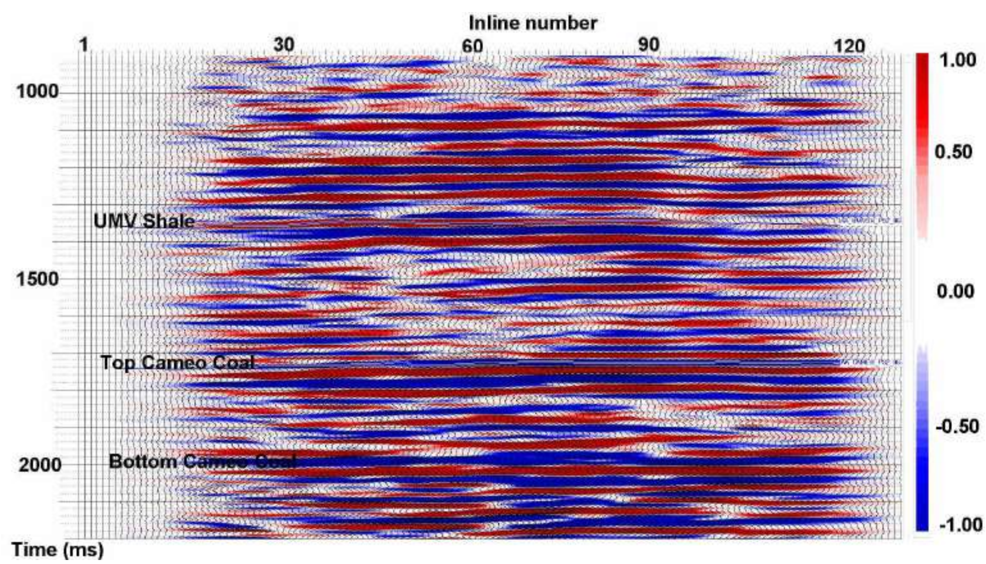

Figure 2.4. Crossline 109 of the Kirchhoff migrated slow component of the converted-wave volume ($\grave{\mathrm{P}}\acute{\mathrm{S}}_2$) with the three main reflectors (UMV Shale, top Cameo Coal, and bottom Cameo Coal) indicated.

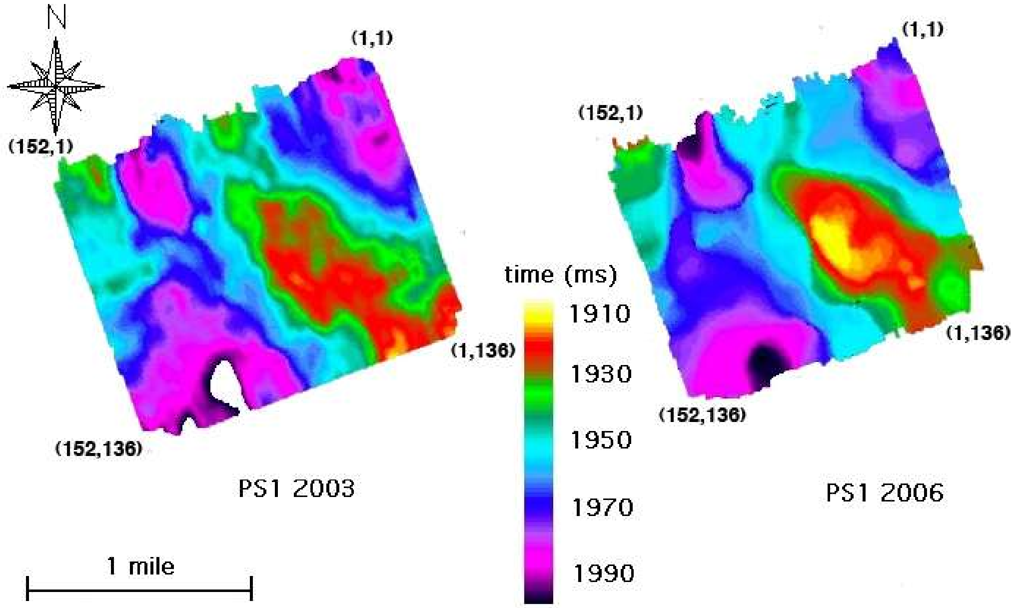

Figure 2.5. Similar time-structure maps at the bottom Cameo Coal horizon for the 2003 and 2006 surveys showing the repeatability of the surveys. The two-way traveltime maps for both surveys are very similar.

Time-structure maps were generated for both fast (Figure 2.6) and slow (Figure 2.7) components of the converted shear-wave and non-converted shear-wave vertical two-way traveltime data. I observed that for both fast and slow components, the converted shear-waves seem to give a better structural image. In fact, from Figure 2.6, one can easily observe a structural high and a structural low, and the separation between these two strucutres is very clear. This separation corresponds to a documented strike-slip fault (Franco, 2007; LaBarre 2008). This fault is visible on the converted-wave data in Figure 2.7 but is not clearly visible on the pure shear-wave data. This was predictable, since the time-structure map corresponds to two-way traveltime; and from converted-wave seismology[1], the vertical two-way $\grave{\mathrm{P}}\acute{\mathrm{S}}$-wave traveltime ($t_{\grave{p}\acute{s},0}$) has a P-wave propagation component (t_{p0}) that is not present in the pure shear-wave kinematics. This vertical P-wave propagation component carries important geological information about structure and faulting, which is commonly absent from the S-wave

[1]For details on converted-wave seismology in multilayer isotropic media, see Chapter 3; for details on converted-wave seismology in layered VTI media, see Appendix A.

propagation component. Therefore, the converted-wave vertical two-way traveltime is useful for mapping geological structures and faulting. This information is not embedded in the pure shear-wave vertical two-way traveltime that has downgoing and upgoing S-wave propagation components. On the other hand, for converted-waves propagating in isotropic media, the parameter $\kappa_0 = \overline{V_p}/\overline{V_s}$ is the physical parameter that determines the offset to the image point, while for P- and S-waves, the offset to the image point is only determine by the acquisition geometry [for more details, see Chapter 3]. Furthermore, the physical parameter κ_0 is determined by the geology and lithology of the medium. Therefore, the geological and lithological information of the medium is embedded in the physical parameter κ_0 that governs the $\grave{\mathrm{P}}\acute{\mathrm{S}}$-wave kinematics in isotropic media.

It is also important to note that since converted-waves have also an S-wave propagation component, when the splitting occurs at a given interface in a fractured or faulted interval, the P-wave will convert into two shear-waves: a fast shear-wave polarized in a direction parallel to the fracture set (or to the fault strike) and a slow shear-wave polarized in a direction orthogonal to the fracture set (or to the fault strike). The first type is rotated and displayed as $\grave{\mathrm{P}}\acute{\mathrm{S}}_1$-data and the second type is rotated and displayed as $\grave{\mathrm{P}}\acute{\mathrm{S}}_2$-data. Since $\grave{\mathrm{P}}\acute{\mathrm{S}}_2$ is the wave that has a shear-component polarized in a direction orthogonal to the fault strike, we would expect to see a sharp discontinuity in traveltime for $\grave{\mathrm{P}}\acute{\mathrm{S}}_2$-wave at the fault location because the presence of the fault perturbes the propagation at this location. This explains why the fault is very well imaged in the $\grave{\mathrm{P}}\acute{\mathrm{S}}_2$ cross-section (Figure 2.7) compared to the $\grave{\mathrm{P}}\acute{\mathrm{S}}_1$ cross-section (Figure 2.6).

The work of LaBarre (2008) supports my identification and location of the main fault at the bottom of the Cameo Coal Formation. Figure 2.8 shows a depth slice below the top Cameo Coal horizon from the S_{11} and S_{22} similarity volumes. The S_{11} similarity volume is displayed with a blue-white scale, and the S_{22} volume is displayed with a red-white scale. The red or blue areas are where the similarity algorithm detected dissimilar traces. Where these areas create semi-linear features

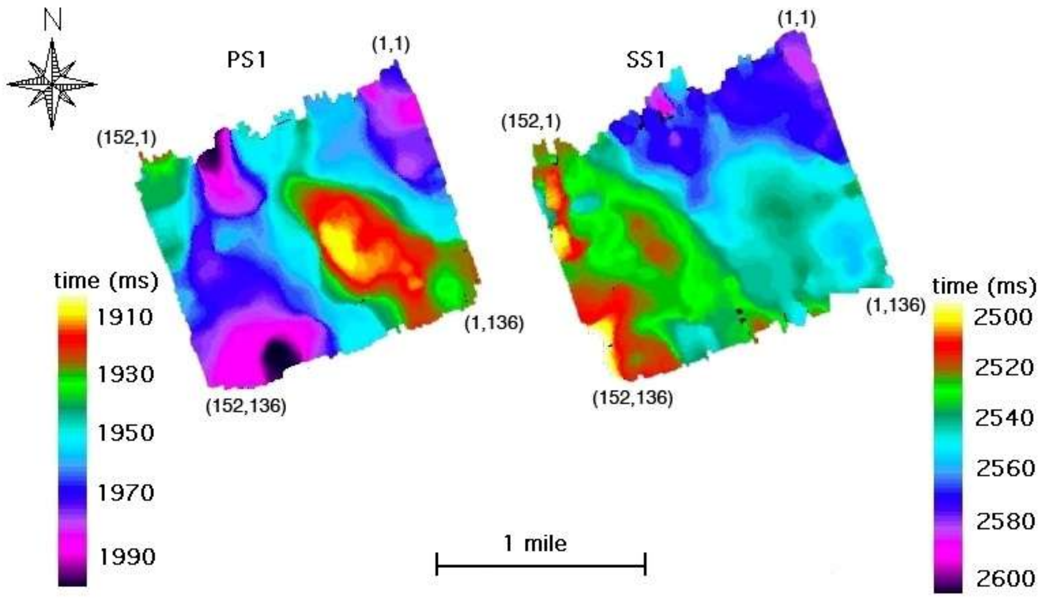

Figure 2.6. Time-structure maps at the bottom Cameo Coal horizon for the 2006 survey for $\grave{P}\acute{S}_1$ and S_{11} seismic components.

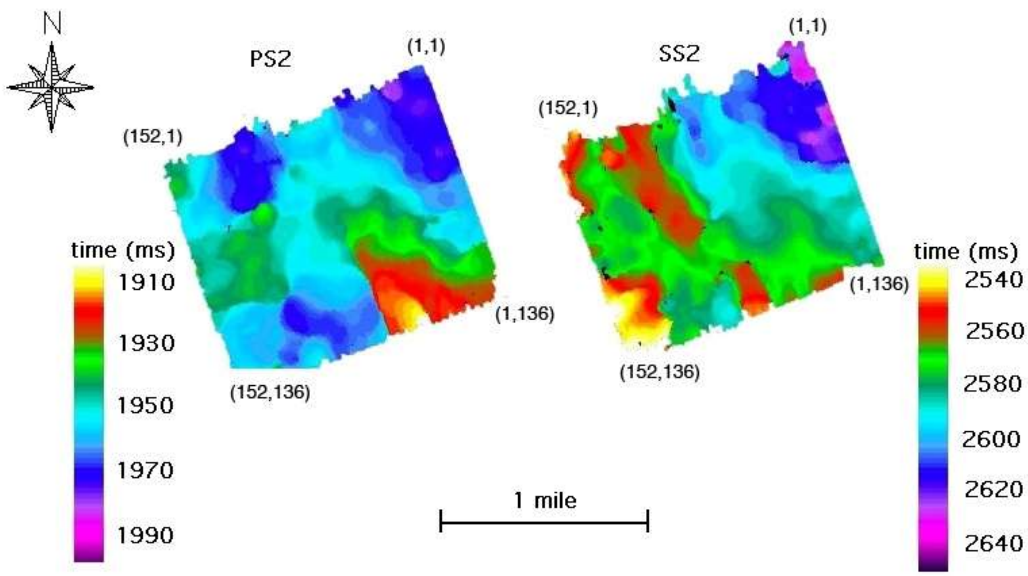

Figure 2.7. Time-structure maps at the bottom Cameo Coal horizon for the 2006 survey for $\grave{P}\acute{S}_2$ and S_{22} seismic components.

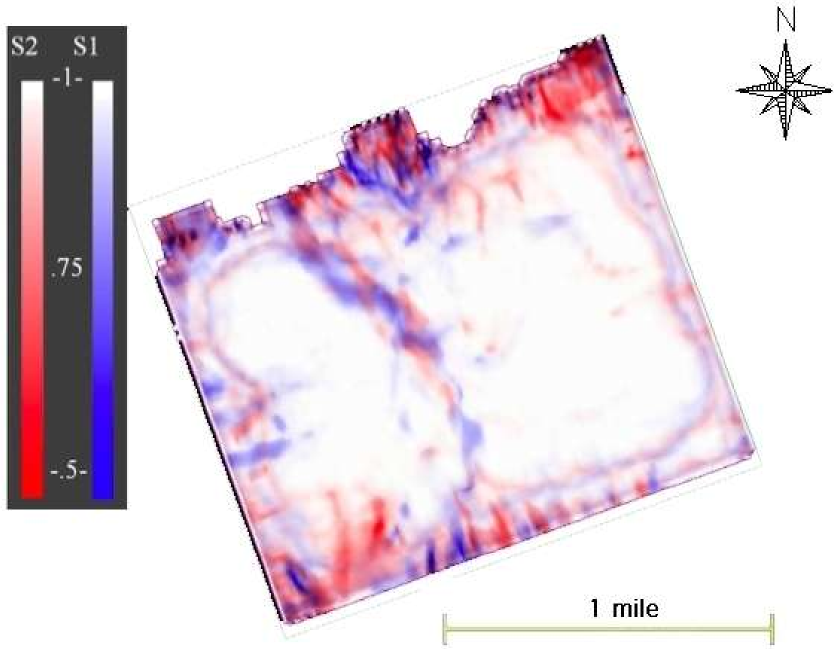

Figure 2.8. Co-rendered depth slice of the S_{11} and S_{22} similarity volumes slightly below the Cameo Coal horizon. S_{11} is displayed with a red scale, and S_{22} is displayed with a blue scale. Modified from LaBarre (2008).

that coincide with discontinuities in the vertical seismic displays, LaBarre (2008) interpreted a fault. Figure 2.9 shows the interpreted fault traces on the same depth slice as on Figure 2.8 .

2.2 Shear-wave Splitting from Pure Shear-wave and Converted-wave Data in the Gas-saturated Section

After having used the converted-wave to obtain information about the strucure and the faulting, our next step is to characterize the fracture density in the objective section. To achieve this goal, shear-wave splitting will be estimated from pure shear-wave data and from converted-wave data. The strict definition of orthorhombic media and the relation between shear-wave splitting, anisotropy, and fracture density are the subject of Section 3.5. In this current chapter, we will only quantify, interpret, and compare the shear-wave splitting from pure shear-wave data and from converted-wave data.

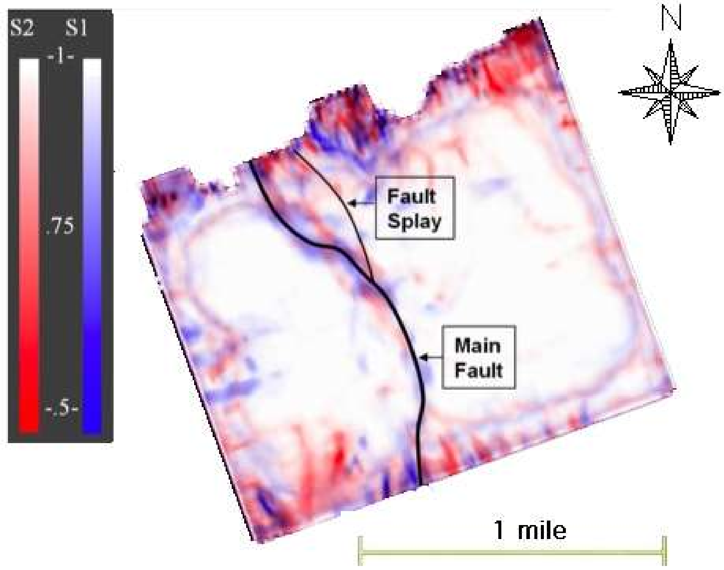

Figure 2.9. The same depth slice shown in Figure 2.8 with the interpreted fault overlaid on the similarity volume slice. Modified from LaBarre (2008).

Pure shear-wave splitting in Rulison Field has been the topic of many theses in RCP (Rumon, 2006; Gulyiev, 2007; Meza, 2008). Pure shear-wave splitting is characterized by the traveltime difference between pure seismic shear-wave components S_{11} and S_{22}. In fact, if the formation was isotropic, there would be no traveltime difference between shear-waves propagating horizontally in two orthogonal directions within the formation. On the other hand, if the formation is anisotropic, there would be a traveltime difference between the S-waves polarized in orthogonal directions. The percentage of two-way traveltime difference is a practical measure of the shear-wave splitting parameter $\gamma^{(S)}$ [for more details, see Section 3.5]. In this chapter only, when referred to anisotropy, the reader should keep in mind that we will be talking about the specific shear-wave splitting parameter $\gamma^{(S)}$ defined in Section 3.5.

Figures 2.1 and 2.2 show the crossline 109 of the S_{11} and the S_{22} poststack gathers from the 2006 survey respectively . We are first interested in an analysis of the gas-saturated section. Therefore, we will first study the objective section included between the UMV Shale horizon and the bottom Cameo Coal horizon. The first step will be to use these two time horizons to try to find a general anisotropy trend for

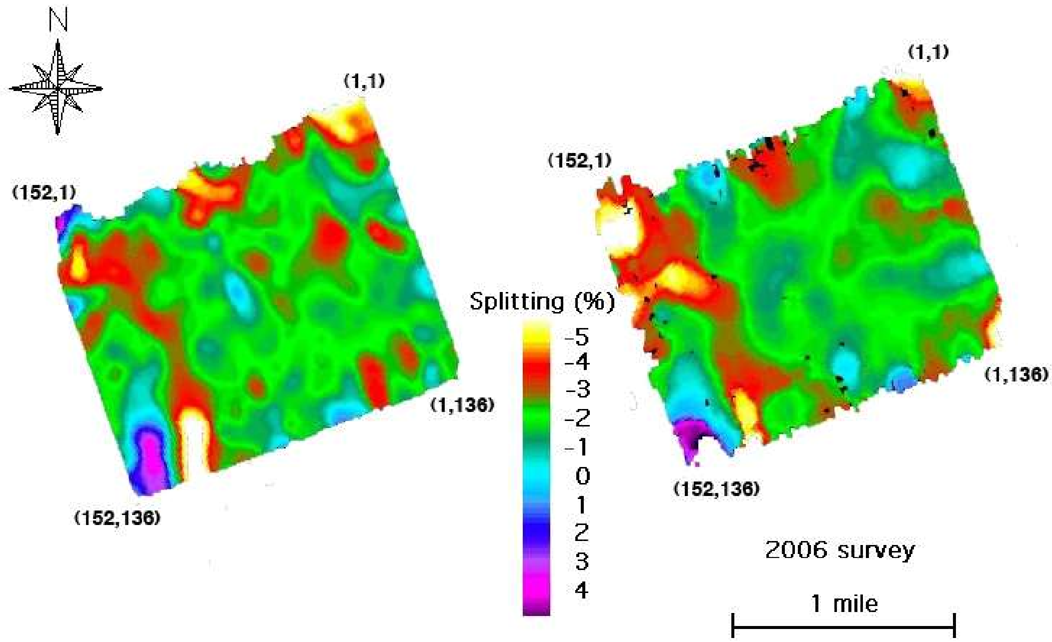

Figure 2.10. Shear-wave splitting parameter $\gamma_{ss}^{(S)}$ computed from non-converted shear-wave data across the gas-saturated section (UMV Shale to bottom Cameo Coal) for the 2003 and 2006 surveys.

the gas-saturated section. This is done by subtracting S_{11} two-way traveltime data from S_{22} two-way traveltime data between the UMV shale and the bottom Cameo Coal horizons and by normalizing this difference (Araman et al., 2008a; Araman et al., 2008b). The practical equation used for the computation of the pure shear-wave splitting parameter $\gamma_{ss}^{(S)}$ in the gas-saturated section is:

$$\gamma_{ss}^{(S)} = \frac{(t_{s1}^{(U)} - t_{s1}^{(C)}) - (t_{s2}^{(U)} - t_{s2}^{(C)})}{t_{s2}^{(U)} - t_{s2}^{(C)}}, \tag{2.1}$$

where $t_{s1}^{(U)}$ is the two-way traveltime to the UMV Shale reflector for the S_{11}-wave, $t_{s2}^{(U)}$ is the two-way traveltime to the UMV Shale reflector for the S_{22}-wave, $t_{s1}^{(C)}$ is the two-way traveltime to the bottom Cameo Coal reflector for S_{11} shear-wave, and $t_{s2}^{(C)}$ is the two-way traveltime to the bottom Cameo Coal reflector for S_{22} shear-wave. The result for the $\gamma_{ss}^{(S)}$ computation is shown in Figure 2.10.

The very high amplitude differences seen on the SW corner of the map are due to edge effects. The pure shear-wave data volumes are noisy, especially on the edges of the survey. Therefore, the horizon picking process in these areas is inaccurate. The western part of the survey has high values of anisotropy, while the eastern part has lower values. This leads us to divide the survey in terms of anisotropy into two parts: a western part, located west of the main fault imaged in the previous section using converted-wave data, that has large values of seismic anisotropy, and that could be related to high fracture density; and an eastern part, located east of the main fault, that has low values of seismic anisotropy.

The same shear-wave splitting analysis was reproduced using converted-wave data. Equation (2.2) is the practical equation used for the computation of the converted-wave splitting parameter $\gamma_{ps}^{(S)}$ in the gas-saturated section (Araman et al., 2008a; Araman et al., 2008b):

$$\gamma_{ps}^{(S)} = \frac{(t_{ps1}^{(U)} - t_{ps1}^{(C)}) - (t_{ps2}^{(U)} - t_{ps2}^{(C)})}{t_{ps2}^{(U)} - t_{ps2}^{(C)}}, \tag{2.2}$$

where $t_{ps1}^{(U)}$ is the two-way traveltime until the UMV Shale reflector for $\grave{\mathrm{P}}\acute{\mathrm{S}}_1$-wave, $t_{ps2}^{(U)}$ is the two-way traveltime until the UMV Shale reflector for $\grave{\mathrm{P}}\acute{\mathrm{S}}_2$-wave, $t_{ps1}^{(C)}$ is the two-way traveltime until the Cameo Coal reflector for $\grave{\mathrm{P}}\acute{\mathrm{S}}_1$-wave, and $t_{ps2}^{(C)}$ is the two-way traveltime until the Cameo Coal reflector for $\grave{\mathrm{P}}\acute{\mathrm{S}}_2$-wave. The result for the $\gamma_{ps}^{(S)}$ computation is shown in Figure 2.11.

The subtraction of $\grave{\mathrm{P}}\acute{\mathrm{S}}$-wave traveltimes in equation (2.2) eliminated the downgoing P-wave traveltime contribution from the numerator. Nevertheless, equation (2.2) has still a P-wave traveltime component in its denominator. Therefore, unlike $\gamma_{ss}^{(S)}$, $\gamma_{ps}^{(S)}$ will be biased by P-wave traveltime. A pure shear-wave splitting parameter could have been defined from $\grave{\mathrm{P}}\acute{\mathrm{S}}$-wave by canceling downgoing P-wave traveltime contributions from the numerator and the denominator.

The results of the $\grave{\mathrm{P}}\acute{\mathrm{S}}$-wave traveltime analysis are fundamentally different from the ones reproduced using non-converted shear-wave traveltime analysis. In other words, $\gamma_{ss}^{(S)}$ and $\gamma_{ps}^{(S)}$ computed over the gas-saturated section (UMV Shale to bottom Cameo Coal) are very different. Figure 2.11 shows that the values of $\gamma_{ps}^{(S)}$ in the

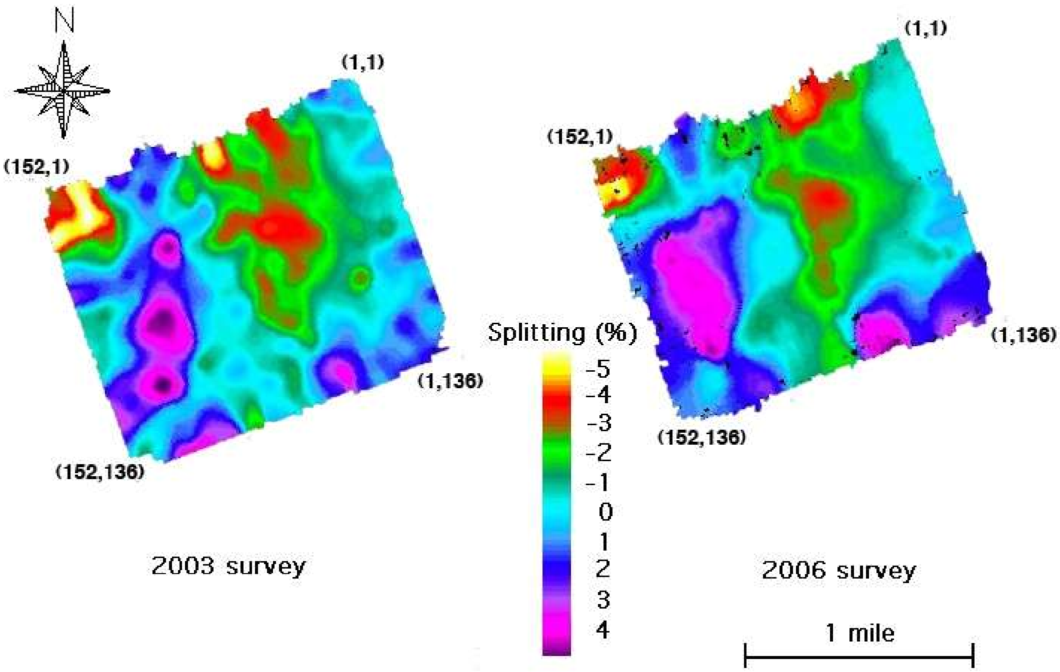

Figure 2.11. Shear-wave splitting parameter $\gamma_{ps}^{(S)}$ computed from converted-wave data across the gas-saturated section (UMV Shale to bottom Cameo Coal) for the 2003 and 2006 surveys.

eastern part of the survey are negative as expected, while in the western part of the survey, the values of $\gamma_{ps}^{(S)}$ are postive. This counter-intuitive result should be analyzed carefully.

As we saw previously, the shear-wave propagation across the entire field seems to behave as expected: S_{11}-waves propagate faster than S_{22}-waves. The parameter $\gamma_{ss}^{(S)}$ is negative over the entire survey area. Hence, there are probably no changes in the horizontal stress orientation across the survey area, and there are probably no significant changes in the fracture orientation that could affect the shear-wave splitting and lead to an improper Alford rotation. Therefore, the anomaly in the time-anisotropy map derived from converted-wave data is not due to a shear-wave polarization anomaly, and might be due to P-wave azimuthal anisotropy (Araman & Davis, 2009a).

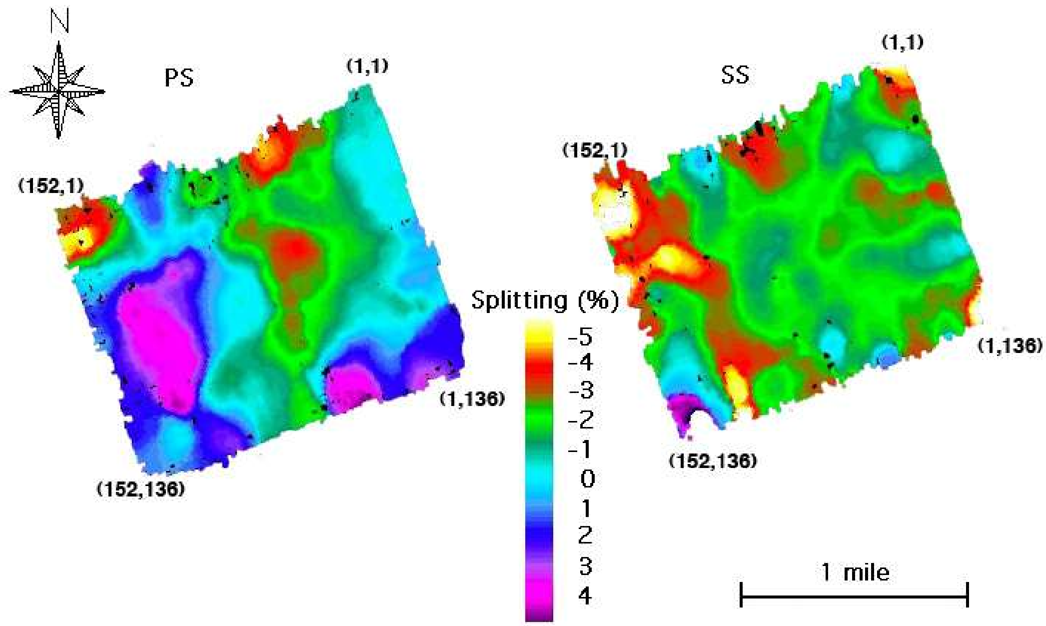

Figure 2.12. Comparison between shear-wave splitting for pure shear-waves and converted-waves (comparison between $\gamma_{ss}^{(S)}$ and $\gamma_{ps}^{(S)}$) based on the 2006 survey.

2.3 P-wave Azimuthal Anisotropy

Azimuthal dependence of the seismic properties (velocity, amplitude, phase, frequency...) can affect the properties of P-waves. A P-wave azimuthal anisotropy analysis was conducted by Franco (2007) to estimate the fracture density and its correlation to production data. These results will be presented and correlated with the results obtained in this chapter from converted-wave data in order to differentiate between azimuthal P-wave anisotropy and shear-wave splitting as computed from converted-waves.

2.3.1 Quality Control of Surface Seismic Data

Low signal-to-noise ratio, low fold on the border of the survey, extreme topography, statics correction in the presence of complex weathering layers, and low P-wave reflectivity at the main gas reservoir level (between the UMV Shale and the top Cameo Coal) are some of the difficulties that had to be dealt with during the azimuthal NMO analysis of the prestack P-wave data (Franco, 2007).

On the other hand, it is important to estimate the vertical and lateral resolution of the P-wave seismic data at the main gas reservoir level. P-wave seismic frequency at main gas reservoir level is equal to 30 Hz and the P-wave vertical velocity approches 13,000 ft/s. The vertical resolution (R_V) is obtained using equation (2.3) and the spacial resolution (R_F) is obtained from the Fresnel zone using equation (2.4). A more detailed discussion of multicomponent seismic resolution is presented in Section 5.3.

$$R_V = \frac{\lambda_p}{4} = \frac{1}{4}\frac{V_{p0}}{f} = 108ft, \tag{2.3}$$

$$R_{F_P} = \frac{V_{p0}}{2}\sqrt{\frac{t}{f}} = 1,100ft, \tag{2.4}$$

where λ_p is the P-wave seismic wavelength, V_{p0} is the P-wave velocity, f is the P-wave seismic frequency, and t is the P-wave two-way traveltime.

2.3.2 Processing Sequence

The first important processing step applied by Veritas after the filtering and denoising of the data is the selection of the offset range to reduce the survey design azimuthal bias. Offset ranges were selected using an azimuth versus offset crossplot. Full azimuth coverage was acheived using a maximum offset of 5,500 ft. The next step is the selection of the data in azimuth bins (4 bins of 45°). The P-wave velocity variations are fitted at each time sample to the ellipse following equation (2.5). Since equation (2.5) involves three unknowns, one should use at least three independent azimuths to obtain a unique solution for the fracture density and orientation. Then, a Kirchhoff prestack time migration is performed for every bin. This operation gives four azimuth-limited volumes migrated with the same velocity field. The last steps are the picking of high density interval velocity, the stacking of every azimuth bin followed by an RMS velocity to interval velocity conversion for every azimuth bin. Finally the fractograms are generated (Franco, 2007). P-wave NMO ellipses were also generated by Xu & Tsvankin (2007).

2.3.3 P-wave Azimuthal Anisotropy Analysis Using Fractograms

The processing sequence includes P-wave NMO ellipse analysis. The orientation and eccentricity of the ellipse reflect the fractures direction and spacing frequency in the subsurface. The P-wave velocity variations are fitted at each time sample to the ellipse using the $f(\phi)$ function defined as:

$$f(\phi) = A + B\cos[2(\phi - \phi_0)], \tag{2.5}$$

where ϕ is the source-receiver azimuth, ϕ_0 is the orientation of major axis of ellipse, A is the average value of the property, and B is the modulus value or ellipticity (Franco, 2007).

Four volumes of 45° azimuth were selected and a prestack time migration of each individual azimuth bin was carried out. After the prestack processing and migration, a high density velocity analysis was produced and interpreted using data from each of the volumes independently. The interval velocity volumes were fitted to the NMO ellipse equation to obtain the fractograms. Finally, the volume of percent anisotropy β is defined by the eccentricity of the NMO ellipse as:

$$\beta = \frac{2B}{A + B}. \tag{2.6}$$

The parameter β indicates areas with high azimuthal anisotropy. In fractured zones, there is a P-wave azimuthal dependence on amplitude and velocity, and hence a high amplitude of azimuthal anisotropy will be detected. Therefore, P-wave azimuthal anisotropy can be used as a fracture detection and estimation tool. Qian et al. (2007) suggested that both amplitudes and interval traveltimes of radial components of converted-waves may also be used to obtain fracture information through elliptical anisotropy analysis; they also argued that the azimuthal amplitudes of the radial

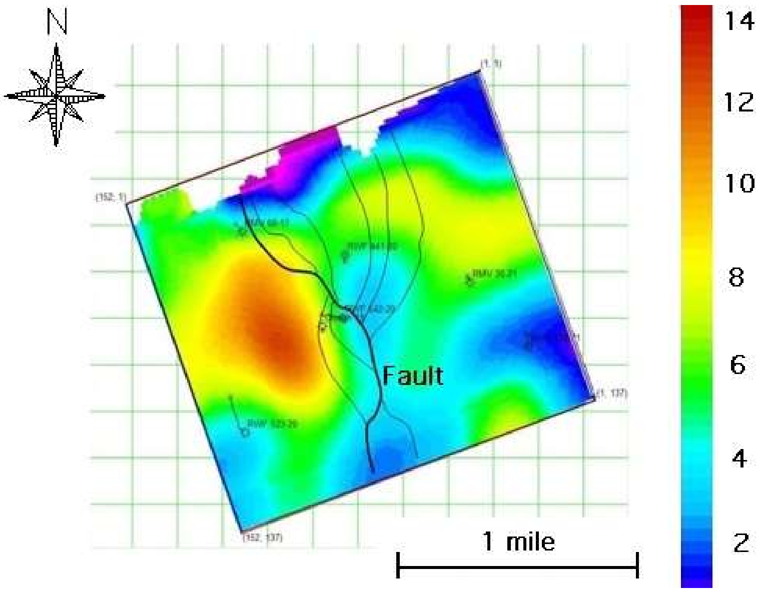

Figure 2.13. Percent of P-wave azimuthal anisotropy over the gas-saturated section (UMV Shale to bottom Cameo Coal). Modified from Franco (2007).

components of P̀Ś-waves display more elliptical variation than that of the P-waves, and that the offset range suitable for azimuthal amplitude analysis is larger for P̀Ś-waves. This method should be tested on the Rulison data set.

The P-wave azimuthal anisotropy parameter β computed for the objective section (UMV Shale to bottom Cameo Coal) is shown in Figure 2.13. We observe 11% of azimuthal anisotropy west of the main fault. This anomaly probably relates to the crest of the low relief Rulison structure on top of the Iles Formation (see Figure 1.4) that could be responsible for a high incidence of fractures. This hypothesis will be investigated in a later paragraph. The anomaly is located in the exact same area as the anomaly detected on the anisotropy maps based on the converted-wave splitting analysis (Figure 2.14). This observation supports my previous statement that the anomaly observed on the converted-wave data is due to P-wave azimuthal anisotropy. The Estimated Ultimate Recovery (EUR) from wells is overlapped over the percentage of azimuthal anisotropy map as shown in Figure 2.15. Some of the good wells have been drilled where that anomaly is present. This observation also confirms that the

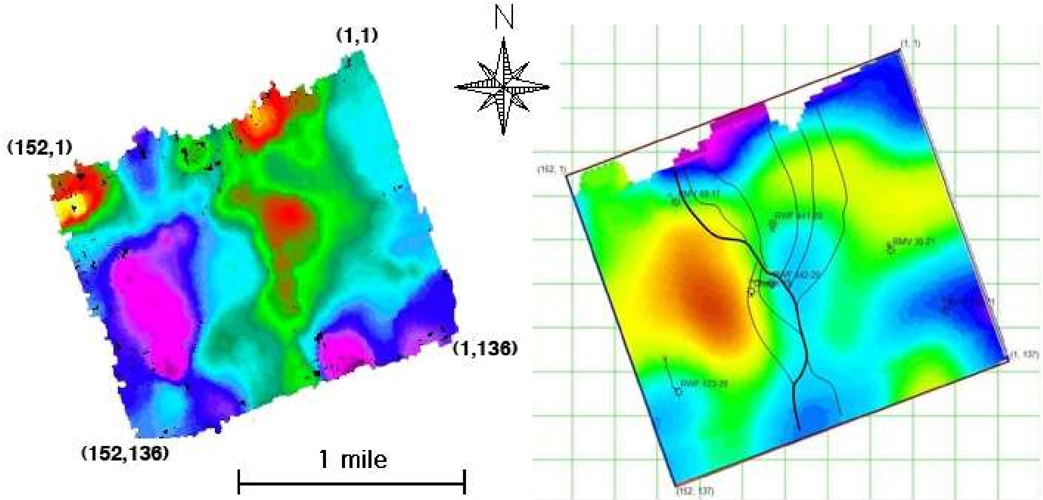

Figure 2.14. Comparison between the P-wave azimuthal anisotropy parameter β (right panel) and the shear-wave splitting parameter $\gamma_{ps}^{(S)}$computed for converted-wave traveltime data (left panel).

observed anomaly is due to a high density of fractures.

In order to prove that the observed anomaly is due to fractures in the Cameo Coal Formation, the parameters $\gamma_{ps}^{(S)}$ and $\gamma_{ss}^{(S)}$ were computed for the main gas reservoir section (top UMV Shale to top Cameo Coal) that does not include the Cameo Coal interval. These results, displayed in Figures 2.16 and 2.17, confirm our previous interpretation. In the main gas reservoir, there are neither $\gamma_{ps}^{(S)}$ nor $\gamma_{ss}^{(S)}$ anomalies. The previously observed P-wave anomaly is hence occurring in the Cameo Coal Formation and is thus probably due to intense fracturing in the western part of the survey caused by the low relief Rulison anticline and the wrench faulting at the base of the coal. On the other hand, in the main gas reservoir, both $\gamma_{ps}^{(S)}$ and $\gamma_{ss}^{(S)}$ give similar results. This correlates with the absence of P-wave azimuthal anomalies. Therefore, $\gamma_{ps}^{(S)} \approx \gamma_{ss}^{(S)} \approx \gamma^{(S)}$ with $\gamma^{(S)}$ being the theoretical shear-wave splitting parameter defined for orthorhombic media by Tsvankin (1997a; 2001) and computed as a combination of the stiffness coefficient c_{44} and c_{55} [for more details, see Section 3.5].

In conclusion, pure-shear wave data are not needed in order to measure the shear-

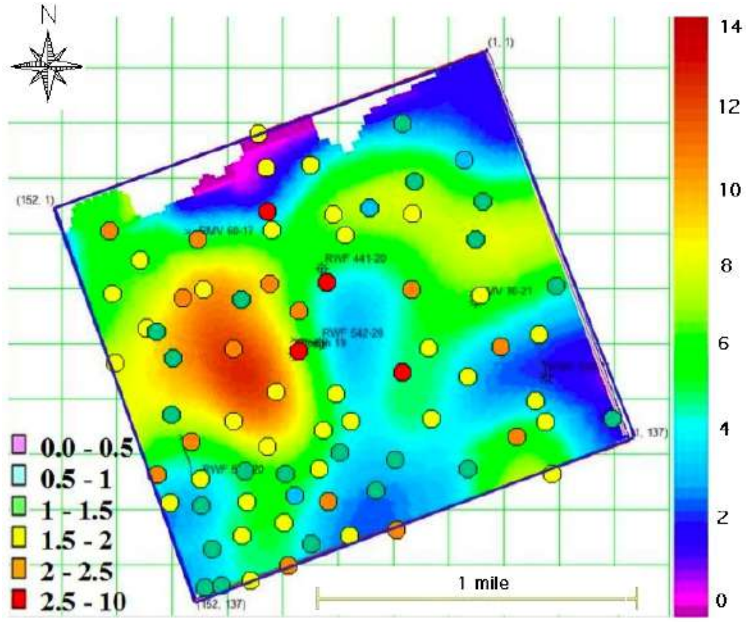

Figure 2.15. Percent of P-wave azimuthal anisotropy over the gas-saturated section (UMV Shale to bottom Cameo Coal) with the EUR from wells in BCF overlapped. Modified from Franco (2007).

wave splitting that can often be related to fracture density (Davis, 2006; Davis, 2007), since the estimation of the $\gamma^{(S)}$ parameter can be done by using exclusively converted-wave data. In the presence of P-wave anisotropy, $\gamma_{ps}^{(S)}$ should be redefined so that the P-wave traveltime is eliminated from the denominator (see equation (2.2)). Some of the minor differences observed between $\gamma_{ps}^{(S)}$ and $\gamma_{ss}^{(S)}$ are probably due to the manual horizon picking process of corresponding seismic events on converted shear-wave and non-converted shear-wave poststack volumes.

The reader will notice a difference between the definition of the $\gamma^{(S)}$ parameter in this chapter and in Chapter 3. The roles of $\grave{\mathrm{P}}\acute{\mathrm{S}}_1$ and $\grave{\mathrm{P}}\acute{\mathrm{S}}_2$ are reversed in both definitions. Therefore, in this chapter, according to the proposed definition, the shear-wave splitting parameter has negative values, and in Chapter 3, $\gamma^{(S)}$ will normally be positive. Except this flip in sign, there is no fundamental difference between the shear-wave splitting parameters defined in both chapters.

For completeness, it is to be mentioned that Mazumdar et al. (2008) computed shear-wave splitting from virtual sources in Rulison by implementing a multicom-

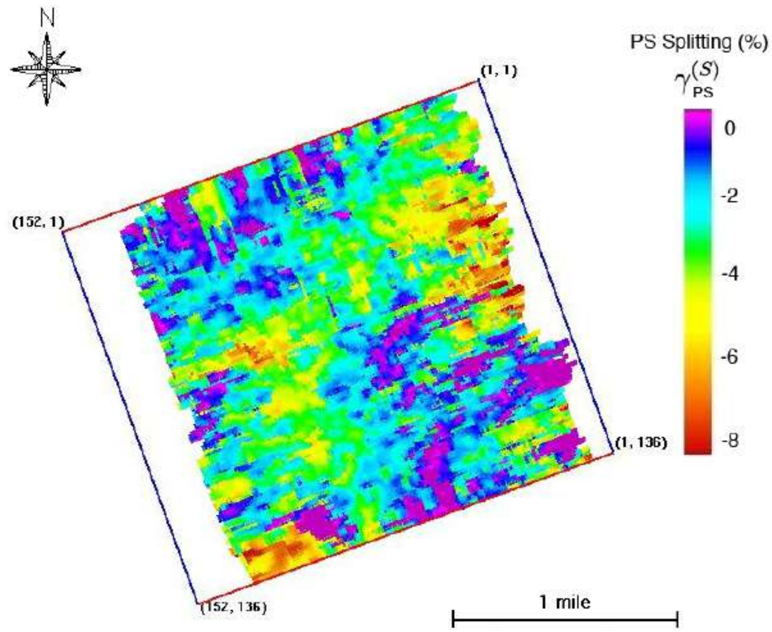

Figure 2.16. Shear-wave splitting $\gamma_{ps}^{(S)}$ computed from converted-wave data across the main gas reservoir section (UMV Shale to top Cameo Coal).

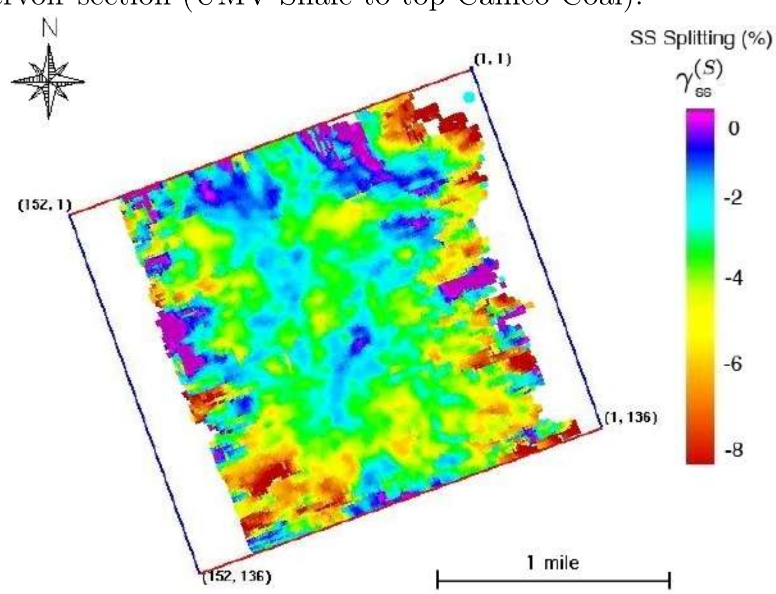

Figure 2.17. Shear-wave splitting $\gamma_{ss}^{(S)}$ computed from pure shear-wave data across the main gas reservoir section (UMV Shale to top Cameo Coal).

ponent version of the virtual source method (Korneev & Bakulin, 2006; Bakulin & Calvert, 2006) in which 3 component VSP geophones are turned into virtual shear sources. They succeeded in measuring shear-wave splitting of less than 1% under anisotropic overburden and inferred a predominant fracture orientation in the main gas reservoir of 75°-85°. This estimation was off by approximately 15° from the 60° fracture orientation calculated from the FMI logs. This inaccuracy is due to the small measured $\gamma^{(S)}$ values.

2.4 Anisotropy Determination from RMS Seismic Amplitudes

Another estimation of anisotropy is based on the RMS amplitude difference between the pure shear-wave components S_{11} and S_{22}. This technique is believed to give higher resolution measurements and was already applied to Weyburn Field in Saskatchewan by Araman et al. (2008a; 2008b). Equation (2.7) shows how this amplitude difference is computed from S-waves, and Figure 2.18 shows the result of this computation over a 50 ms window below the UMV Shale horizon. The maps of Figure 2.18 were not trimmed to remove the low-fold effect. Therefore, the edge values should be discarded.

$$\Delta RMS^{(SS)} = \frac{RMS_{S1} - RMS_{S2}}{RMS_{S2}}, \tag{2.7}$$

where RMS_{S1} is the RMS amplitude computed from S_{11}-wave data over a given window length in the gas-saturated section (between the UMV Shale horizon and the top Cameo Coal horizon) and RMS_{S2} is the RMS amplitude computed from S_{22}-wave data over a given window length in the gas-saturated section. $\Delta RMS^{(SS)}$ is often referred to as the *RMS amplitude anisotropy.*

From Figure 2.18, there is no general anisotropy trend related to a dominant set of fractures having a given orientation. On the other hand, in terms of pure shear-wave amplitudes, the two surveys (2003 and 2006) seem not to have good repeatability since the RMS amplitudes observed for the same interval are fundamentally

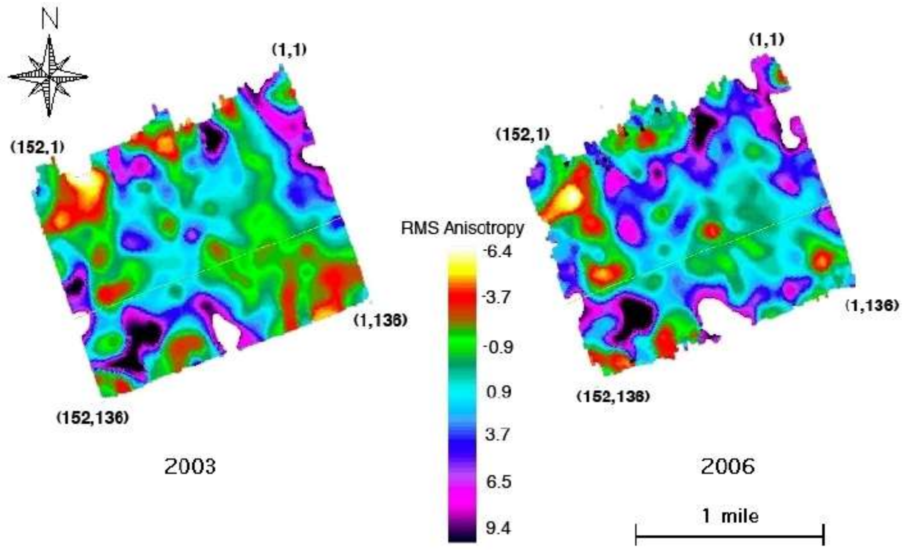

Figure 2.18. RMS amplitude anisotropy $\Delta RMS^{(SS)}$ from pure shear-wave amplitude data over a 50 ms window below the UMV Shale horizon for both 2003 and 2006 surveys.

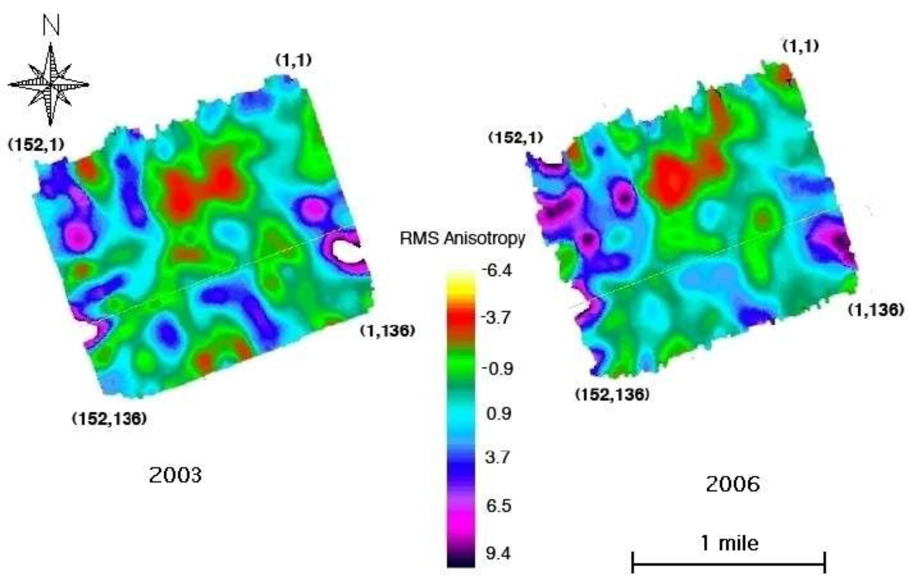

Figure 2.19. RMS amplitude anisotropy $\Delta RMS^{(PS)}$ from converted-wave amplitude data over a 50 ms window below the UMV Shale horizon for both 2003 and 2006 surveys.

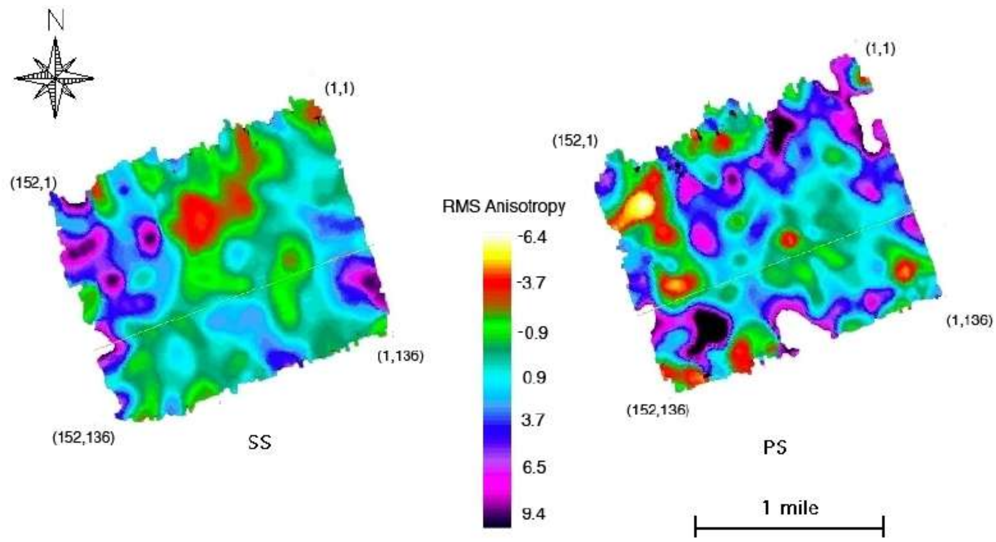

Figure 2.20. Comparison between RMS amplitude anisotropy computed from pure shear- and converted-wave data over a 50 ms window below the UMV Shale horizon for the 2006 survey.

different. Although time-lapse anisotropy change is expected when fractured media are produced, such dramatic changes in RMS amplitudes cannot be due to reservoir depletion.

Anisotropy based on the RMS amplitude difference between the converted-wave components $\grave{\mathrm{P}}\acute{\mathrm{S}}_1$ and $\grave{\mathrm{P}}\acute{\mathrm{S}}_2$ has also been computed. Equation (2.8) shows how this estimation of anisotropy is computed, and Figure 2.19 shows the result of this computation over a 50 ms window below the UMV Shale horizon. As in Figure 2.18, the maps of Figure 2.19 were not trimmed to remove the low-fold effect.

$$\Delta RMS^{(PS)} = \frac{RMS_{PS1} - RMS_{PS2}}{RMS_{PS2}}, \tag{2.8}$$

where RMS_{PS1} is the RMS amplitude computed on $\grave{\mathrm{P}}\acute{\mathrm{S}}_1$ converted-wave data over a given window length in the gas-saturated section and RMS_{PS2} is the RMS amplitude computed on PS_2 converted-wave data over a given window length in the gas-saturated section. $\Delta RMS^{(PS)}$ can also be referred to as the *RMS amplitude anisotropy*.

From Figure 2.19, there is also no general anisotropy trend related to a dominant set of fractures having a given orientation. But, in terms of converted-wave amplitudes, the two surveys (2003 and 2006) seem to have a good repeatability since the RMS amplitudes observed for the same interval are similar. Therefore, in terms of RMS amplitudes over relatively small window lengths (5 to 50 ms), converted-wave data might be more robust and more suitable for time-lapse amplitude analysis than pure shear-wave data.

Furthermore, from Figures 2.18 and 2.19, the amplitude anisotropy maps generated from converted-wave and pure shear-wave amplitude data are significantly different. One of the reasons is that the converted-wave reflection coefficient depends on the P-wave velocity, while the pure shear-wave reflection coefficient is independent of the P-wave velocity [for pure shear-wave and converted-wave reflection coefficient expressions in isotropic media, see equations (5.32) and (5.33)]. The converted-wave reflection coefficients in VTI and HTI media and the impact of the Thomsen (1986) anisotropy parameters on these reflection coefficients are dealt with in Chapter 4.

In conclusion, the interpretation of amplitude anisotropy maps generated from converted-wave data is not straightforward, and a study in depth of the converted-wave reflection coefficients in transversely isotropic media is conducted in Chapters 4 and 5.

Chapter 3

CONVERTED-WAVE MOVEOUT ANALYSIS AND ANISOTROPY PARAMETER ESTIMATION

3.1 Introduction

A P-wave incident upon an elastic discontinuity converts some of its energy to transmitted and reflected S-waves. If it is an incident P-wave that generates a reflected S-wave, this mode is referred to as converted shear-wave. We should note that the conversion from an incident S-wave to a reflected P-wave (referred to as S̀Ṕ-wave) exists as well. This type of conversion is not dealt with in this thesis. Generally, determining that a recorded shear-wave has been converted from a P-wave at a particular horizon instead of another is non-trivial. The analysis of conversion points is one of the objectives of this chapter. The UMV Shale layer will be modeled as transversely isotropic media with a vertical symmetry axis (VTI). This choice will be justified and the Thomsen anisotropy parameters will be estimated using multicomponent surface seismic data.

3.2 Single-layer Homogeneous Isotropic Model

Figure 3.1 shows a homogeneous isotropic layer. A ray emitted as a P-wave with an incident angle θ_p from a source S at the surface reflects from the bottom of the layer as an S-wave at an angle θ_s and is recorded at a position x. The conversion occurs at a position x_c. The two angles θ_p and θ_s are related by Snell's law:

$$\frac{\sin\,\theta_p}{V_p} = \frac{\sin\,\theta_s}{V_s} = p = \frac{\partial t_{\grave{p}\acute{s}}}{\partial x}, \tag{3.1}$$

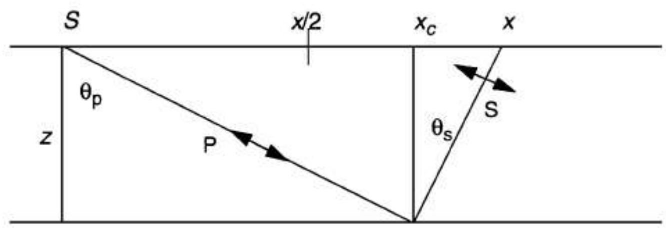

Figure 3.1. Canonical converted-wave schematic in a single-layer isotropic medium. Adopted from Thomsen (1999).

where p is the ray parameter (constant along the ray path) and $t_{\grave{p}\acute{s}}$ is the arrival time of the P̀Ś-wave at the position x. The offset x_c to the image point at depth in the subsurface is different from the midpoint. This difference depends upon the ratio of V_p over V_s that is henceforth denoted κ_0 ($\kappa_0 = V_p/V_s$). If one considers this same geometry (Figure 3.1), the midpoint $x/2$ is determined geometrically, while the offset x_c to the image point is determined geometrically and physically through the parameter κ_0. The determination of the conversion point is one of the fundamental differences in processing techniques between pure-mode and converted-mode seismic data (Thomsen, 1999). Since the physical parameter κ_0 controls the source-receiver offset, or equivalently the conversion depth, the heterogeneity and anisotropy of the velocity model play a crucial role in converted-wave seismology.

The parameter κ_0 is always greater than unity and, therefore, the S-wave leg comes up always more steeply than the P-wave leg goes down. On the other hand, the P̀Ś-wave arrival is polarized transversely. Hence, a horizontally polarized receiver is preferred over a vertically polarized receiver (Thomsen, 1999). In the isotropic, single-layer homogeneous model, the energy appears only on the vertical and inline horizontal components. The first step will be to study the conversion point equations given by Tessmer & Behle (1988) and Tsvankin & Thomsen (1994) for the simple isotropic homogeneous case. The conversion point issue in VTI media will be dealt with in later sections.

3.2.1 Traveltimes and Velocities for a Single Homogeneous Isotropic Layer

The homogeneous isotropic single-layer model shown in Figure 3.1 is the simplest elastic model possible. Even in this case, the moveout of the P̀Ś-wave is not hyperbolic. Using simple trigonometry, one can derive the exact P̀Ś-wave traveltime $t_{\grave{p}\acute{s}}$:

$$t_{\grave{p}\acute{s}}(x) = t_p(x) + t_s(x) = \frac{z}{V_p \cos\theta_p(x)} + \frac{z}{V_s \cos\theta_s(x)}, \tag{3.2}$$

where t_p is the downward propagating P-wave traveltime and t_s is the corresponding upward propagating S-wave traveltime. The offset x can be written as:

$$x = V_p\, t_p \sin\theta_p + V_s\, t_s \sin\theta_s = p\, V_p^2\, t_p + p\, V_s^2\, t_s. \tag{3.3}$$

The Taylor series expansion of t^2 in x^2 gives the following expression for $t_{\grave{p}\acute{s}}$:

$$t_{\grave{p}\acute{s}}^2 = t_{\grave{p}\acute{s},0}^2 + \frac{x^2}{V_{\grave{p}\acute{s},2}^2} + A_4\, x^4 + \cdots, \tag{3.4}$$

where $t_{\grave{p}\acute{s},0}$ is the vertical two-way P̀Ś-wave traveltime, $V_{\grave{p}\acute{s},2}$ is the P̀Ś-wave short-spread moveout velocity, and A_4 is the quartic moveout parameter.

The vertical two-way P̀Ś-wave traveltime can be rewritten in terms of one-way P-wave traveltime (t_{p0}) and one-way S-wave traveltime (t_{s0}) as:

$$t_{\grave{p}\acute{s},0} = t_{p0} + t_{s0} = t_{p0}(1 + t_{s0}/t_{p0}) = t_{p0}(1 + \kappa_0), \tag{3.5}$$

since

$$\kappa_0 = V_p/V_s = \frac{z/t_{p0}}{z/t_{s0}} = t_{s0}/t_{p0}. \tag{3.6}$$

The amplitude of the converted-wave at vertical-incidence is zero in an isotropic medium (Aki & Richards, 1980). However, one can still compute the vertical P̀Ś-wave traveltime $t_{\grave{p}\acute{s},0}$ by NMO-correcting and then stacking the non-zero offset traces. This procedure is explained in detail in Chapter 4. Computing t_{p0} requires a prestack or poststack P-wave propagation study and a correspondence between P- and P̀Ś-wave arrivals. The latter operation is closely related to the conversion point determination.

For the simple single-layer homogeneous isotropic model, the P̀Ś-wave moveout velocity $V_{\grave{p}\acute{s},2}$ is computed as follows:

$$V_{\grave{p}\acute{s},2}^2 = \frac{V_p^2\,t_{p0} + V_s^2\,t_{s0}}{t_{p0} + t_{s0}} = \frac{V_p^2}{1+\kappa_0} + \frac{V_s^2}{1+1/\kappa_0} = \frac{V_{p2}^2}{\kappa_0}. \tag{3.7}$$

Furthermore, the quartic moveout parameter A_4 derived by Tsvankin & Thomsen (1994) is given by:

$$A_4 = \frac{-(\kappa_0 - 1)^2}{4\,(\kappa_0 + 1)\,t_{\grave{P}\acute{S},0}^2\,V_{\grave{P}\acute{S},2}^4}. \tag{3.8}$$

In Rulison Field, the maximum available offset is approximatively 10,000 ft. If $\kappa_0 \approx 2$, then the quartic term is at worse -5% of the hyperbolic term for a reflector located at a depth of 6,000 ft.

The problem with the Taylor series expansion is that for $x \rightarrow \infty$, t^2 should be increasing as x^4. This cannot be true since t^2 should be increasing as x^2 with the correct velocity coefficient. Tsvankin (2001) corrected the previous Taylor series expansion for converted-waves by modifying the quartic term. Hence, equation (3.4) has been replaced by equation (3.9):

$$t_{\grave{p}\acute{s}}^2 = t_{\grave{p}\acute{s},0}^2 + \frac{x^2}{V_{\grave{p}\acute{s},2}^2} + \frac{A_4\,x^4}{1 + A_5\,x^2} + \cdots\,, \tag{3.9}$$

with

$$A_5 = \frac{-A_4\,V_{\grave{p}\acute{s},2}^2}{(1 - \frac{V_{\grave{p}\acute{s},2}^2}{V_{p2}^2})}. \tag{3.10}$$

As expected, for small offsets, equation (3.9) approximates equation (3.4). A_5 is not an independent parameter, and its value can be derived from the values of the parameters A_4, V_{p2}, and $V_{\grave{p}\acute{s},2}$.

3.2.2 Conversion Point Offset for Single-layer Homogeneous Isotropic Media

The source-receiver offset x_c for the $\grave{\text{P}}\acute{\text{S}}$-wave satisfies the following equality:

$$x_c = V_p \, t_p \, \sin \, \theta_p = p \, V_p^2 \, t_p, \tag{3.11}$$

which is also equivalent to:

$$\frac{x_c}{x} = \frac{1}{1 + \frac{V_s^2 \, t_s}{V_p^2 \, t_p}} = \frac{1}{1 + \frac{t_s(x)}{\kappa_0^2 \, t_p(x)}}. \tag{3.12}$$

For small offsets,

$$\frac{t_s(x)}{t_p(x)} \approx \frac{t_s(0)}{t_p(0)} = \frac{V_p}{V_s} = \kappa_0. \tag{3.13}$$

Therefore,

$$x_{c0} = \frac{x \, \kappa_0}{1 + \kappa_0}, \tag{3.14}$$

where x_{c0} is the small offset approximation of the conversion point, more currently known as the asymptotic conversion point (ACP).

For large offsets, the asymptotic conversion point given by equation (3.14) is no longer valid, and the following equation derived by Tessmer & Behle (1988) should be used instead:

$$\left[\frac{x_c \, (x - x_c)}{z}\right]^2 + \left[(x_c^2 - \frac{2 \, \kappa_0^2}{\kappa_0^2 - 1} x \, (x_c - x/2))\right] = 0. \tag{3.15}$$

An analytic solution for equation (3.15) has been derived by Thomsen (1999) using a Taylor series expansion based approximation (for small but finite values of x/z):

$$x_c(x, z) \approx x \left[c_0 + c_2 \frac{(x/z)^2}{(1 + c_3 (x/z)^2)}\right], \tag{3.16}$$

where

$$c_0 = \frac{\kappa_0}{1+\kappa_0}, \qquad c_2(\kappa_0) = \frac{\kappa_0}{2}\frac{(\kappa_0-1)}{(\kappa_0+1)^3}, \qquad c_3 = \frac{c_2}{1-c_0}. \tag{3.17}$$

Thomsen (1999) studied the differences between the asymptotic conversion point (equation (3.14)), the exact Tessmer & Behle (1988) solution (equation (3.15)), the regular Taylor series expansion of the Tessmer & Behle (1988) equation (equation (3.16) with c_3=0), and the analytic solution of the Tessmer & Behle (1988) equation based on the Taylor series expansion (equation (3.16)). The results are displayed and interpreted in Figures 3.2 and 3.3 adapted from Thomsen (1999).

From Figure 3.2, it is clear that the analytic solution of the Tessmer and Behle (1988) equation based on the Taylor series expansion is always valid except for very shallow depths or very large offsets. The regular Taylor series approximation (equation (3.16) with c_3=0) is accurate for offset-to-depth ratios as large as 1.25 but fails for larger offsets or shallower depths (the dot-dashed curve in Figure 3.2). The ACP solution seems to be accurate only for offset-to-depth ratios smaller than 1/2. Therefore, for large offset traces or for shallow depth reflections, the ACP differs greatly from equation (3.16). The latter should be therefore used to position the conversion points. On the other hand, from Figure 3.3, it is clear that for increasing source-receiver offsets, the asymmetry of the P̀Ś-wave raypath increases: the conversion occurs closer to the receiver and farther away from the mid point x/2.

What is the actual displacement of the conversion point (x_c) from the asymptotic conversion point (x_{c0}) at the top and bottom of the reservoir in Rulison Field assuming the very simple single-layer single-reflector homogeneous isotropic model? Let us assume that the top of the gas-saturated section (UMV Shale) in Rulison is located at 6,000 ft of depth and the bottom of the gas-saturated is located at 8,000 ft of depth. Let us suppose the maximum offset equal to 6,000 ft (this is close to the maximum offset value used in the stacking process). Hence, x/z=1 for the top of the reservoir and x/z=6/8 for the bottom of the reservoir. We suppose the physical parameter κ_0 equal to 1.9 in the objective section [for more details, see Section 3.3 and Figure 3.4].

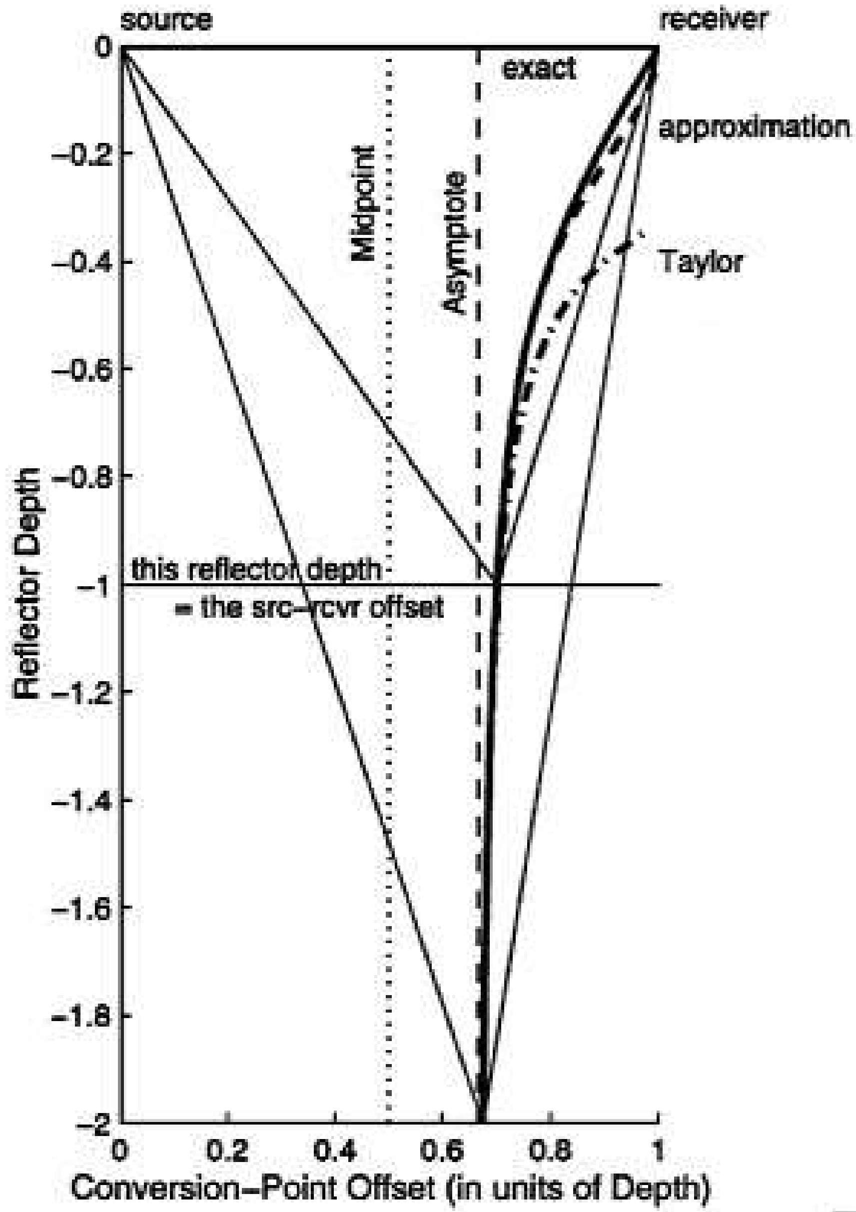

Figure 3.2. Conversion point offset as a function of the reflector depth for a fixed source-receiver offset and for κ_0=2. The asymptotic conversion point (ACP) is noted by the dashed curve, the solution of the regular Taylor series expansion is noted by the dot-dashed curve, the solution of the approximation of the Tessmer & Behle (1988) equation is noted by the bold dashed curve, and the exact solution of the Tessmer & Behle (1988) equation (equation (3.15)) is represented by the full black curve. Adapted from Thomsen (1999).

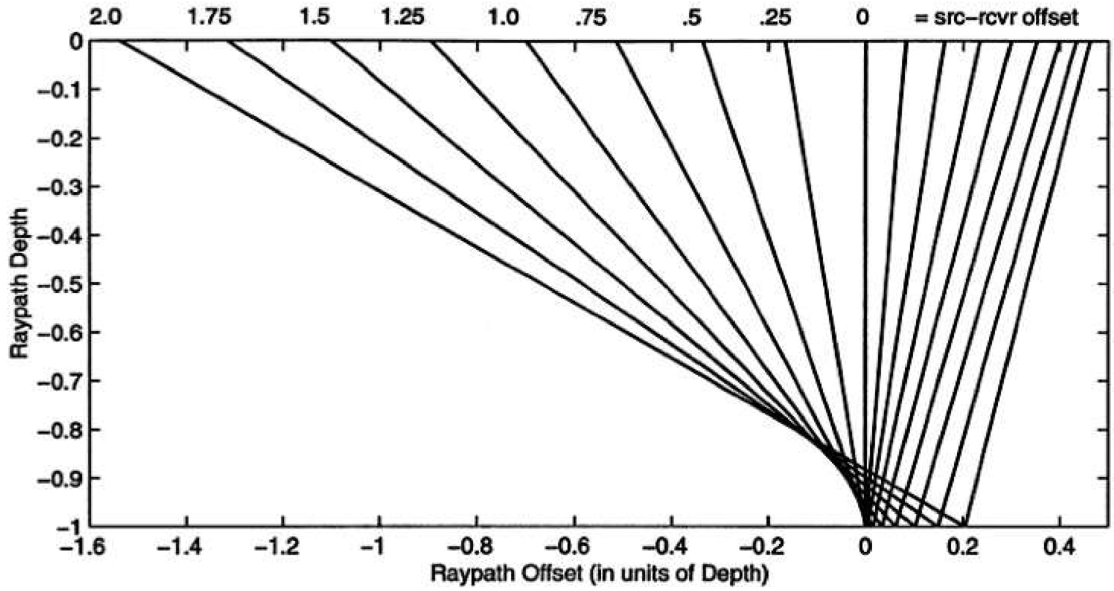

Figure 3.3. Schematic raypaths for a single reflection within a common asymptotic conversion point (CACP) gather as a function of the source-receiver offset. Adapted from Thomsen (1999).

Therefore, at the top of the gas-saturated section, x_{c0}=3,931 ft (equation (3.14)) and x_c=4,122 ft (equation (3.16)). We have hence a displacement $x_c - x_{c0}$ of the actual conversion point from the asymptotic solution of 191 ft for receivers that are 6,000 ft away from the source! In other words, if we were to image arrivals corresponding to the conversion at the top of the reservoir and received by far offset receivers using the ACP x_{c0} instead of the actual conversion point x_c, we would misplace the energy by many bins and obtain a smeared image. For the bottom of the gas-saturated section located at 8,000 ft of depth, x_{c0} is always equal to 3,931 ft. On the other hand, given a receiver at 6,000 ft of offset and κ_0=1.9, x_c is now equal to 4,043 ft. This gives a displacement $x_c - x_{c0}$ equal to 112 ft. As expected from the previous analysis, the displacement for the bottom of the objective section is now less than for the top of the reservoir (x_{c0} is now closer to x_c), but this displacement is still important enough to create smearing if one had to use x_{c0} instead of the actual conversion point x_c.

In conclusion, for the gas-saturated section in Rulison Field (∼2,000 ft of section), and for fairly large offsets, the conversion point determination should not be based on the ACP solution but on the analytic approximation of the Tessmer & Behle (1988) solution.

3.3 Multilayer Homogeneous Isotropic Model

Let us now discuss the more realistic case of multiple layers. Two physical parameters now control the kinematics of the $\grave{P}\acute{S}$-waves: the vertical velocity ratio function (κ_0) (where the bar indicates the average velocity) and the moveout velocity ratio function (κ_2):

$$\kappa_0 = \overline{V_p}/\overline{V_s} = t_{s0}/t_{p0}, \tag{3.18}$$

$$\kappa_2 = V_{p2}/V_{s2}, \tag{3.19}$$

where V_{p2} is the rms P-wave moveout velocity and V_{s2} is the rms S-wave moveout velocity.

3.3.1 Traveltimes and Velocities for Multilayer Homogeneous Isotropic Media

The Taylor series expansion (equation (3.2)) is still valid for the multilayer case, and the vertical two-way $\grave{P}\acute{S}$-wave traveltime $t_{\grave{p}\acute{s},0}$ is now generalized as:

$$t_{\grave{p}\acute{s},0} = t_{p0} + t_{s0} = t_{p0}(1 + \kappa_0). \tag{3.20}$$

On the other hand, Thomsen (1999) showed that the $\grave{P}\acute{S}$-wave moveout velocity generalizes as:

$$V^2_{\grave{p}\acute{s},2} = \frac{V^2_{p2}}{1+\kappa_0} + \frac{V^2_{s2}}{1+1/\kappa_0} = \frac{V^2_{p2}}{1+\kappa_0}(1 + 1/\kappa_{eff}), \tag{3.21}$$

where

$$\kappa_{eff} = \kappa_2^2/\kappa_0. \tag{3.22}$$

Finally, the quartic Taylor series coefficient A_4 and the correction coefficient A_5 are usually nonnegligible, and can be derived as special cases of the general anisotropic

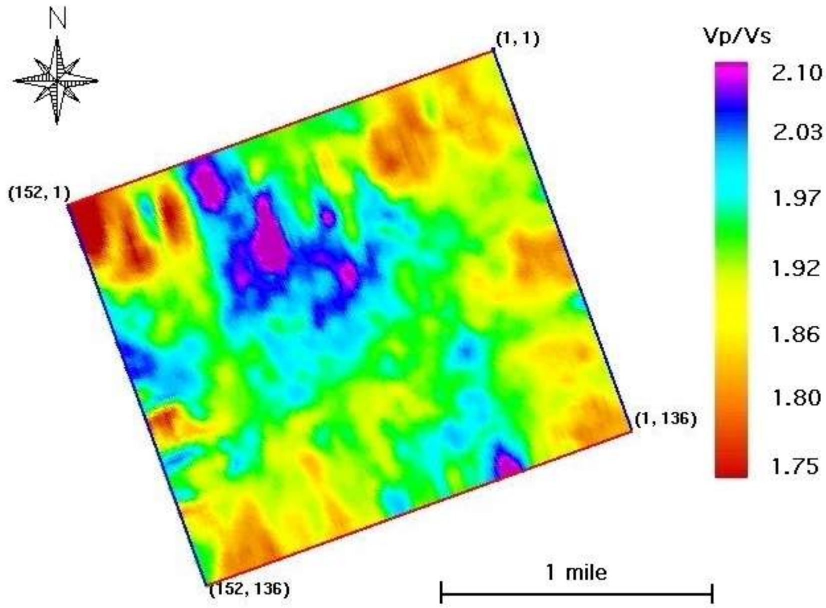

Figure 3.4. The vertical velocity ratio $\kappa_0 = V_{p0}/V_{s0}$ in the reservoir computed from poststack gathers based on equation (3.23).

expressions given by Tsvankin & Thomsen (1994). These coefficients derived for the more general layered VTI model are presented in Appendix A.

The velocity ratios presented above can be derived directly from P- and P̀Ś-wave data once the corresponding events have been identified on both P- and P̀Ś-wave seismic volumes. The parameter κ_0 is found directly from poststack gathers as the ratio of corresponding P- and P̀Ś-wave vertical traveltimes (Figure 3.4) using the following formulae:

$$\kappa_0 = \frac{\overline{V_p}}{\overline{V_s}} = \frac{2\Delta t_{ps} - \Delta t_{pp}}{\Delta t_{pp}}. \tag{3.23}$$

The parameter κ_2 can be computed using velocity moveout analysis that should be performed on both P- and P̀Ś-wave traveltime data independently. To determine the V_{p2}/V_{s2} ratio without any S̀Ś-wave moveout analysis, one should first invert equation (3.21) in order to find κ_{eff}:

$$\kappa_{eff} = [(1 + \kappa_0)(V^2_{\grave{p}\acute{s},2}/V^2_{p2}) - 1]^{-1}. \tag{3.24}$$

The parameter κ_2 is then computed from equation (3.22). The advantage of this approach is that $V_{\grave{p}\acute{s},2}$ is determined independently of any P-wave analysis, making it more robust than if a joint pure-mode inversion (PP-SS inversion) was performed. From the data available, the parameter κ_2 could not be computed using the above method based on a joint PP-PS inversion, because there was no velocity moveout analysis performed on P̀Ś-wave data and the prestack data were not available for processing. Therefore, a joint analysis of pure-modes (PP-SS) had to be performed. NMO analysis was performed independently on P-wave data and on S-wave data generating a P-wave NMO velocity volume (Figure 3.5) and an S-wave NMO velocity volume (Figure 3.6). The processing was performed under the supervision of Steve Roche at Veritas. The parameter κ_2 is then obtained directly from equation (3.19) using P- and S-wave NMO velocities. For completeness, an accurate technique for converted-wave velocity analysis based on the pseudo-offset migration[1] (POM) technique is presented by Wang & Tsingas (2002a; 2002b).

3.3.2 Conversion Point Offset for Multilayer Homogeneous Isotropic Media

Following the work of Thomsen (1999), the P̀Ś-wave conversion point can be generalized as:

$$x_c(x, t_{\grave{p}\acute{s},0}) \approx x \left[c_0 + c_2 \frac{x/(t_{\grave{p}\acute{s},0}\, V_{\grave{p}\acute{s},2})^2}{(1 + c_3(x/t_{\grave{p}\acute{s},0}\, V_{\grave{p}\acute{s},2})^2)} \right], \tag{3.25}$$

with

$$c_0 = \frac{\kappa_{eff}}{1+\kappa_{eff}}, \qquad c_2 = \frac{\kappa_{eff}}{2\kappa_0} \frac{(\kappa_{eff}\,\kappa_0 - 1)(1+\kappa_0)}{(1+\kappa_{eff})^3}, \qquad c_3 = \frac{c_2}{1-c_0}. \tag{3.26}$$

The asymptotic term c_o for the multiple-layer medium is very similar to the

[1]For more details on the implementation and the advantages of the POM technique, see Bancroft et al. (1998) and Wang & Tsingas (2002a; 2002b).

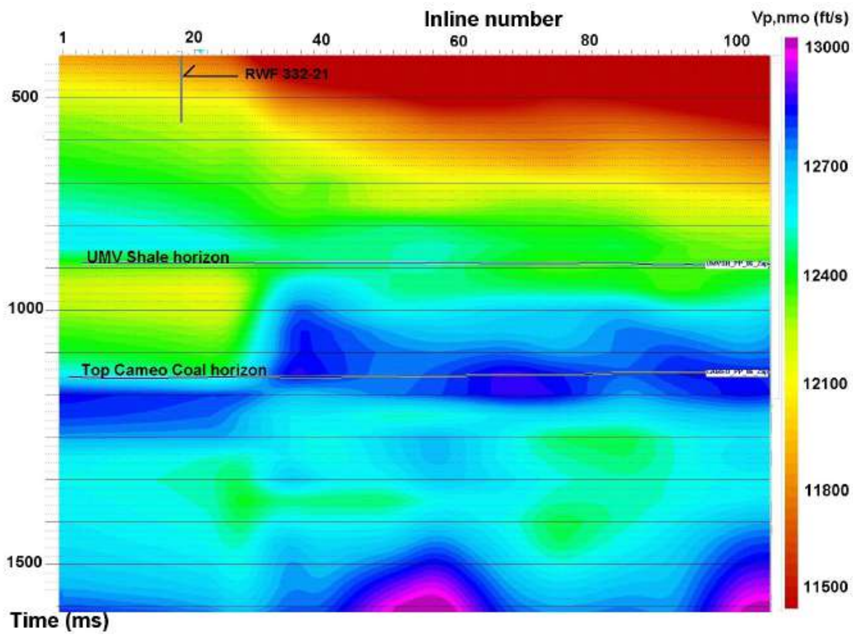

Figure 3.5. Crossline 109 of the P-wave NMO velocity volume. The UMV Shale and the Cameo Coal horizons are shown.

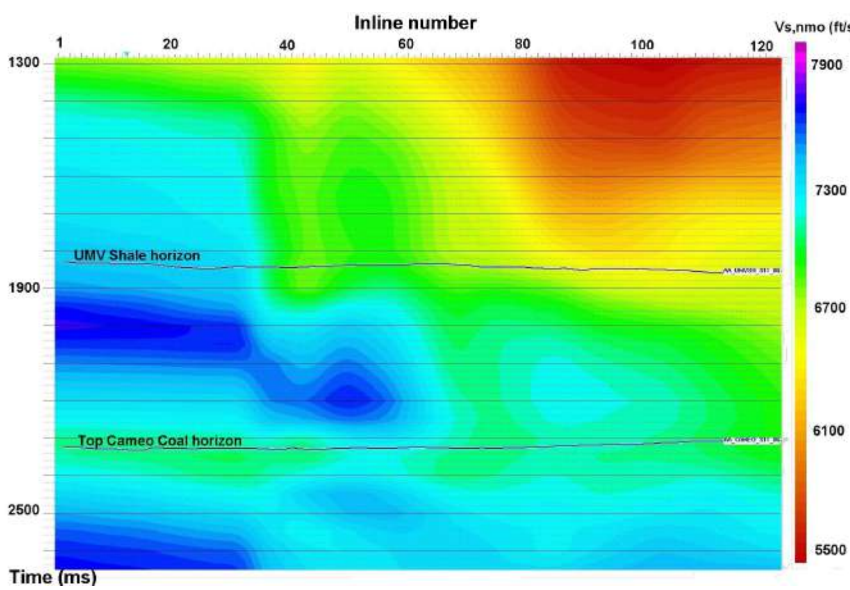

Figure 3.6. Crossline 109 of the S-wave NMO velocity volume. The UMV Shale and the Cameo Coal horizons are shown.

ACP of the single-layer medium expect that the physical parameter κ_0 has been replaced with κ_{eff}. This result can be used to check if a medium is single-layered or multilayered.

For the main gas reservoir, the vertical velocity ratio computed at the study well location using equation (3.23) is $\kappa_0 = 1.86$ (Figure 3.4):

$$\kappa_0 = 2\,\frac{\Delta t_{PS}}{\Delta t_{PP}} - 1 = 1.86. \tag{3.27}$$

On the other hand, at that location for the UMV Shale layer, the P- and S-wave moveout velocities are $V_{p2} = 12,360$ ft/s (Figure 3.5) and $V_{s2} = 7,400$ ft/s (Figure 3.6). Therefore, the ratio of the moveout velocities is $\kappa_2 = 1.73$ (equation (3.19)); and hence $\kappa_{eff} = 1.6$ (equation (3.22)).

The reader should not forget that the parameters κ_{eff} and κ_2 could have been computed using exclusively $\grave{\text{P}}\acute{\text{P}}$- and $\grave{\text{P}}\acute{\text{S}}$-wave data. The way to do it is to compute first κ_{eff} from the inversion formulae given by equation (3.24) and then to compute κ_2 from equation (3.22). Nevertheless, although the $\grave{\text{S}}\acute{\text{S}}$-wave traveltime data are not theoretically needed for the computation of the different velocity ratios, they can still be reconstructed from the $\grave{\text{P}}\acute{\text{P}}$- and $\grave{\text{P}}\acute{\text{S}}$-wave traveltime data using the PP+PS=SS method (Grechka & Tsvankin, 2002; Grechka et al. 2002a; Grechka et al., 2002b).

Different asymptotic conversion points are computed by using the velocity ratios obtained at the study well location for the UMV Shale. First, by using the vertical velocity ratio κ_0, the following conversion-to-offset ratio is obtained:

$$\frac{x_{c0}}{x} = \frac{\kappa_0}{1+\kappa_0} = 0.64. \tag{3.28}$$

On the other hand, using the moveout velocity ratio κ_2:

$$\frac{x_{c0}}{x} = \frac{\kappa_2}{1+\kappa_2} = 0.63. \tag{3.29}$$

Finally, using the effective ratio κ_{eff}, the conversion-to-offset ratio becomes :

$$\frac{x_{c0}}{x} = \frac{\kappa_{eff}}{1+\kappa_{eff}} = 0.61. \tag{3.30}$$

For large offsets, a significant difference is observed when the conversion-to-offset ratio (x_{c0}/x) is properly computed using κ_{eff} compared to the calculation based on κ_0. In fact, for 6,000 ft of offset, using the parameter κ_0, x_{c0} is found to be equal to 3,840 ft, while using the parameter κ_{eff}, x_{c0} is equal to 3,660 ft, leading to a difference of 180 ft between both cases. This difference is probably due to polar anisotropy and layering.

3.4 VTI Model for the UMV Shale

Since most shale layers are horizontally layered, and because of the aligned plate-shaped clay particles that describe the structure of shales, the VTI model is an appropriate model for horizontally layered shale formations.

3.4.1 Transversely Isotropic Media

A transversely isotropic medium has a single axis of rotational symmetry. Seismic signatures in such a model depend only on the angle between the direction of propagation and the symmetry-axis. Any plane that contains the axis of symmetry is a plane of symmetry. The plane perpendicular to the symmetry axis is also a symmetry plane. It is called the isotropy plane since the phase velocities of all three waves in that plane are independent of the propagation direction because the angle between the slowness vector and the symmetry axis remains constant in that plane and is always equal to 90° (Tsvankin, 2001). Nevertheless, SV- and SH-waves are kinematically decoupled in the isotropy plane. If the symmetry axis is vertical, then the medium is a vertical transversely isotropic (VTI) medium. The stiffness tensor for VTI media is given by equation (3.31). Following the work of Thomsen (1986), the stiffness tensor for a VTI medium can be written as:

$$\mathbf{c} = \begin{pmatrix} c_{11} & c_{11}-2c_{66} & c_{13} & 0 & 0 & 0 \\ c_{11}-2c_{66} & c_{11} & c_{13} & 0 & 0 & 0 \\ c_{13} & c_{13} & c_{33} & 0 & 0 & 0 \\ 0 & 0 & 0 & c_{55} & 0 & 0 \\ 0 & 0 & 0 & 0 & c_{55} & 0 \\ 0 & 0 & 0 & 0 & 0 & c_{66} \end{pmatrix}. \tag{3.31}$$

The five independent stiffness coefficients in VTI media can be replaced by the vertical velocities of P- and S-waves and by three anisotropy parameters (δ, ϵ and γ) introduced by Thomsen (1986):

$$V_{p0} = \sqrt{\frac{c_{33}}{\rho}}, \tag{3.32}$$

$$V_{s0} = \sqrt{\frac{c_{55}}{\rho}}, \tag{3.33}$$

$$\epsilon = \frac{c_{11}-c_{33}}{2c_{33}}, \tag{3.34}$$

$$\delta = \frac{(c_{13}+c_{55})^2-(c_{33}-c_{55})^2}{2c_{33}(c_{33}-c_{55})}, \tag{3.35}$$

$$\gamma = \frac{c_{66}-c_{55}}{2c_{55}}. \tag{3.36}$$

In Chapter 1, it has been shown that the UMV Shale interval corresponds to (1) the top of the gas-saturated section (see Figure 1.3), (2) the top of the overpressured compartment (see Figure 1.9), and (3) one of the three main seismic reflectors in the RCP survey area. Therefore, an accurate modeling of the UMV Shale interval is important for the reservoir characterization in Rulison Field.

In the previous section, the UMV Shale Formation was shown to be layered. Furthermore, in a study by Xu and Tsvankin (2007), the AVO and NMO ellipses of P-wave data were estimated for the UMV Shale layer. The NMO ellipticity was found to be negligible except for a couple of spots in the eastern part of the survey (see Figure 3.7). One of the conclusions drown by this study is that the UMV Shale Formation is probably azimuthally isotropic. Therefore, the UMV Shale Formation is a layered azimuthally isotropic shale layer. The VTI model is therefore an appropriate model for this formation. On the other hand, the only AVO gradient anomaly in the UMV Shale is located in the eastern part of the survey between inlines 40 and 50 (see Figure 3.7). Since the UMV Shale is probably vertically isotropic with a vertical symmetry axis, this anomaly could be caused by a "soft spot" of high fracture density in the upper reservoir (Xu and Tsvankin, 2007).

For completeness, it is to note that a more realistic and complicated model is the multilayer VTI medium. Although this model will not be used in Rulison because of its complexity compared to the available data in the RCP, the P̀Ś-wave kinematics in such media are dealt with in Appendix A.

3.4.2 Estimating Thomsen Parameters at the Study Well Location

Velocity analysis and anisotropy parameter estimation in transversely isotropic media have been extensively used for more than a decade now and many case studies have been published in the literature (Alkhalifah & Tsvankin, 1995; Alkhalifah et al., 1996; Contreras et al., 1999; Li et al, 2008). Following the work of Alkhalifah & Tsvankin (1995), the moveout velocities in a VTI medium are affected by anisotropy in the following way:

$$V_{p2}^2 = V_{p0}^2(1 + 2\delta), \tag{3.37}$$

$$V_{s2}^2 = V_{s0}^2(1 + 2\sigma), \tag{3.38}$$

where σ is defined by the following combination of Thomsen parameters:

$$\sigma = \kappa_0^2(\epsilon - \delta), \tag{3.39}$$

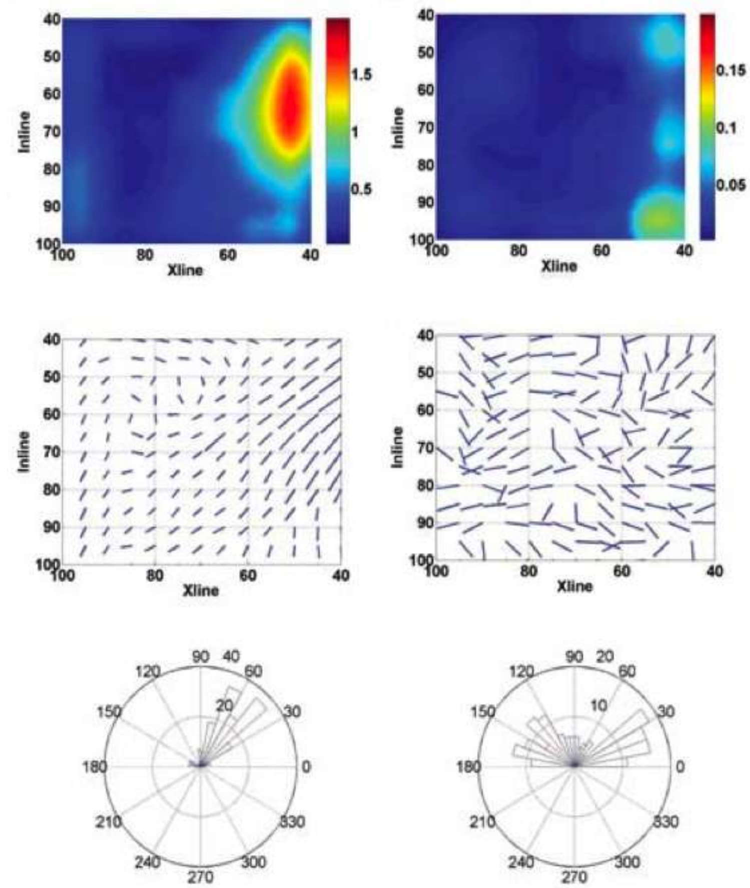

Figure 3.7. P-wave AVO ellipses and interval NMO ellipses in the UMV Shale Formation. The left column shows the AVO ellipses computed using the conventional t^2 gain. The right column shows the effective NMO ellipses. The top row is the eccentricity of the ellipses calculated by subtracting unity from the ratio of the semi-major and semi-minor axes. The middle row is the azimuth of the semi-major axis, the length of the ticks being proportional to the eccentricity. The bottom row is the rose diagram of the azimuths from the middle row. The azimuths are computed with respect to the north. Adapted from Xu & Tsvankin (2007).

V_{p0} and V_{p2} are respectively the vertical and the NMO P-wave velocities, V_{s0} and V_{s2} are respectively the vertical and the NMO S-wave velocities, δ and ϵ are the Thomsen (1986) anisotropy parameters defined by equations (3.34) and (3.35). The parameter δ determines the second derivative of the P-wave phase-velocity function at vertical incidence, while ϵ is close to the fractional difference between the horizontal and vertical P-wave velocities (Tsvankin, 2001). The effective ratio can be now written as:

$$\kappa_{eff} = \frac{\kappa_2^2}{\kappa_0} = \kappa_0 \frac{1+2\delta}{1+2\sigma}. \tag{3.40}$$

The anisotropy parameter estimation for the UMV Shale Formation in the vicinity of the study well location has been already published by Araman & Davis (2009b). Using equation (3.37) with $V_{p0} = 14,000$ ft/s and $V_{p2} = 12,360$ ft/s, they obtained $\delta = -0.11$ at the study well location. From equation (3.40) they directly obtained $\sigma = 0.62$ at the study well location. Equation (3.39) leads to $\epsilon = 0.07$.

Finally, at the study well location, the anellipticity coefficient defined by Alkhalifah & Tsvankin (1995) is:

$$\eta = \frac{\epsilon - \delta}{1+2\delta} = 0.23. \tag{3.41}$$

3.4.3 Thomsen Anisotropy Parameters in the UMV Shale Formation

The Thomsen anisotropy parameters in the UMV Shale Formation will now be estimated across the entire srvey. This procedure will lead to a full spatial characterization of anisotropy in the UMV Shale.

The first step is to build vertical and NMO velocity models for both P- and SV-waves. The moveout velocities for P- and SV-waves have been extracted at the UMV Shale horizon from respectively the NMO velocity volume for P-waves (Figure 3.5) and the NMO velocity volume for SV-waves (Figure 3.6). The NMO velocities for P- and S-waves in the UMV Shale Formation are shown respectively in the upper right and lower right corners of Figure 3.8.

On the other side, the vertical velocity model building requires an additional step. The vertical velocity is known from the well logs at the RWF 332-21 location. What is needed is not a single value for vertical P- and S-wave velocities, but P- and S-wave velocities as a function of the spatial coordinates in the UMV Shale Formation. That is achieved based on P- and S-wave impedance inversions. These inversions are one of the main topics of Chapter 5 where the procedures are discussed and explained in detail. For now, we are just going to use the results of Chapter 5 that consist in two impedance volumes: a P-impedance volume denoted as Z_p and an S-impedance volume denoted as Z_s. The reader will notice that in Chapter 5 two S-impedance volumes have been inverted for: a fast-S-impedance volume denoted as Z_{s1} and a slow-S-impedance volume denoted as Z_{s2}. In the VTI UMV Shale Formation, these two volumes are identical [for more details, the reader can refer to the discussion about anisotropy in Section 5.4]. Therefore, for the following discussion, it does not matter which one of these two volumes is taken to be the S-impedance volume.

Since $Z_p = V_{p0}/\rho$ and $Z_s = V_{s0}/\rho$ with ρ being the density, the knowledge of the density is needed in order to derive the P-wave vertical velocity $V_{p0}^{(t)}$ and the S-wave vertical velocity $V_{s0}^{(t)}$ in the UMV Shale from the inverted impedance data. The impedance values extracted at the UMV Shale level will be referred to as $Z_p^{(t)}$ and $Z_s^{(t)}$. Unfortunately, no density model is available for the UMV Shale. Nevertheless, almost all wells having edited density logs indicate a more or less constant density interval value in the UMV Shale Formation equal to 2.57 g/cc. This is the value that is going to be used everywhere in the UMV Shale as being equal to the density. Therefore, $V_{p0}^{(t)}$ and $V_{s0}^{(t)}$ are obtained as follows:

$$V_{p0}^{(t)} = \frac{Z_p^{(t)}}{\rho^{(t)}} = \frac{Z_p^{(t)}}{2.57}, \tag{3.42}$$

$$V_{s0}^{(t)} = \frac{Z_s^{(t)}}{\rho^{(t)}} = \frac{Z_s^{(t)}}{2.57}. \tag{3.43}$$

The vertical velocity models for P- and S-waves in the UMV Shale are shown respectively in the upper left and lower left panels of Figure 3.8.

The last step is to use equations (3.37), (3.40), and (3.39) with the derived vertical and NMO velocities in order to invert for the anisotropy parameters δ, σ, and ϵ. The result of this inversion is shown in Figure 3.9.

The values obtained for δ in the UMV Shale range from -0.05 to -0.15, while the values obtained for ϵ range from 0 to 0.12. Since δ is negative, the main physical reason for anisotropy in the UMV Shale is fine layering rather than intrinsic anisotropy of clay particles. The anellipticity parameter η ranges from 0 to 0.28 with a mean value of 0.22. The UMV Shale is thus highly anelliptical. These results are close to those obtained by Xu & Tsvankin (2007). This gives us an additional confidence concerning the validity of the obtained results.

It is important to note that the values obtained for the vertical shear-wave velocity V_{s0} are unrealistically high in the northwestern part of the survey. This could be due to variations in the density in this part of the survey. The density was assumed to be constant. This assumption was based on some measurements from the lower part of the survey. Therefore, important errors in the density values could have induced unrealistically high values for the vertical shear-wave velocity that has been directly computed from the inverted shear-impedance.

Another possible explanation for the erroneous vertical S-velocities is the inversion itself. As discussed in Chapter 5, the inversion was constrained by the study well RWF 332-21 located in the southeaster part of the survey. Therefore, the inversion is weakly constrained in the northwestern part of the survey leading to erroneous values for the S-impedance and V_{s0}. This induced unrealistically low values for σ, and thereby erroneous values for the Thomsen parameter ϵ in that part of the survey.

Finally, an additional probable source of error is the low shear-wave fold in the northwestern part of the survey. Therefore, the parameters ϵ and η have been only estimated for a small area near the study well location. This area is indicated by a red square in the top left panel of Figure 3.9.

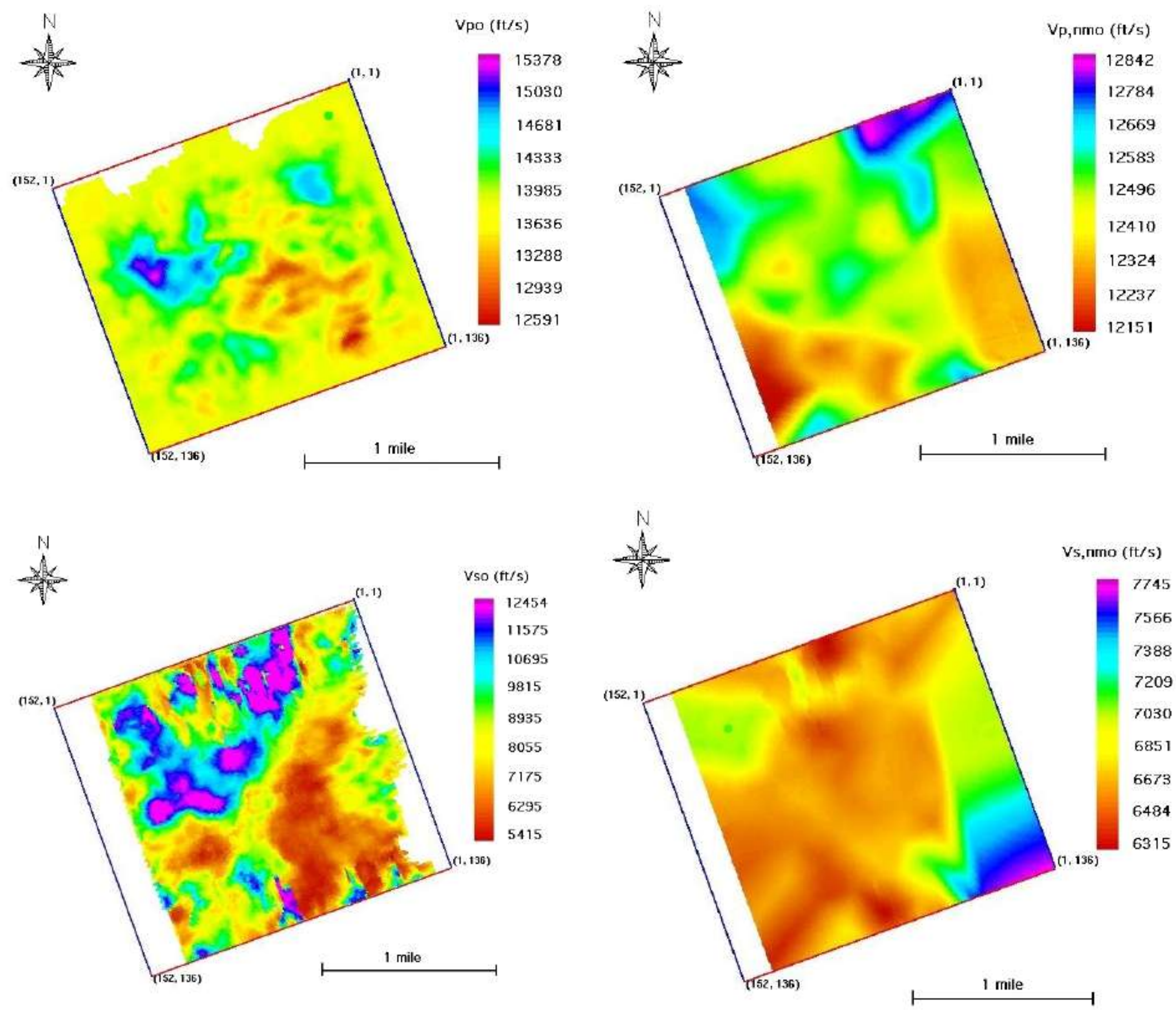

Figure 3.8. The velocity models for the UMV Shale Formation. The vertical P-wave velocity V_{p0} is shown in the upper left panel, the NMO P-wave velocity V_{p2} is shown in the upper right panel, the vertical S-wave velocity V_{s0} is shown in the bottom left panel, and the NMO S-wave velocity V_{s2} is shown in the bottom right panel.

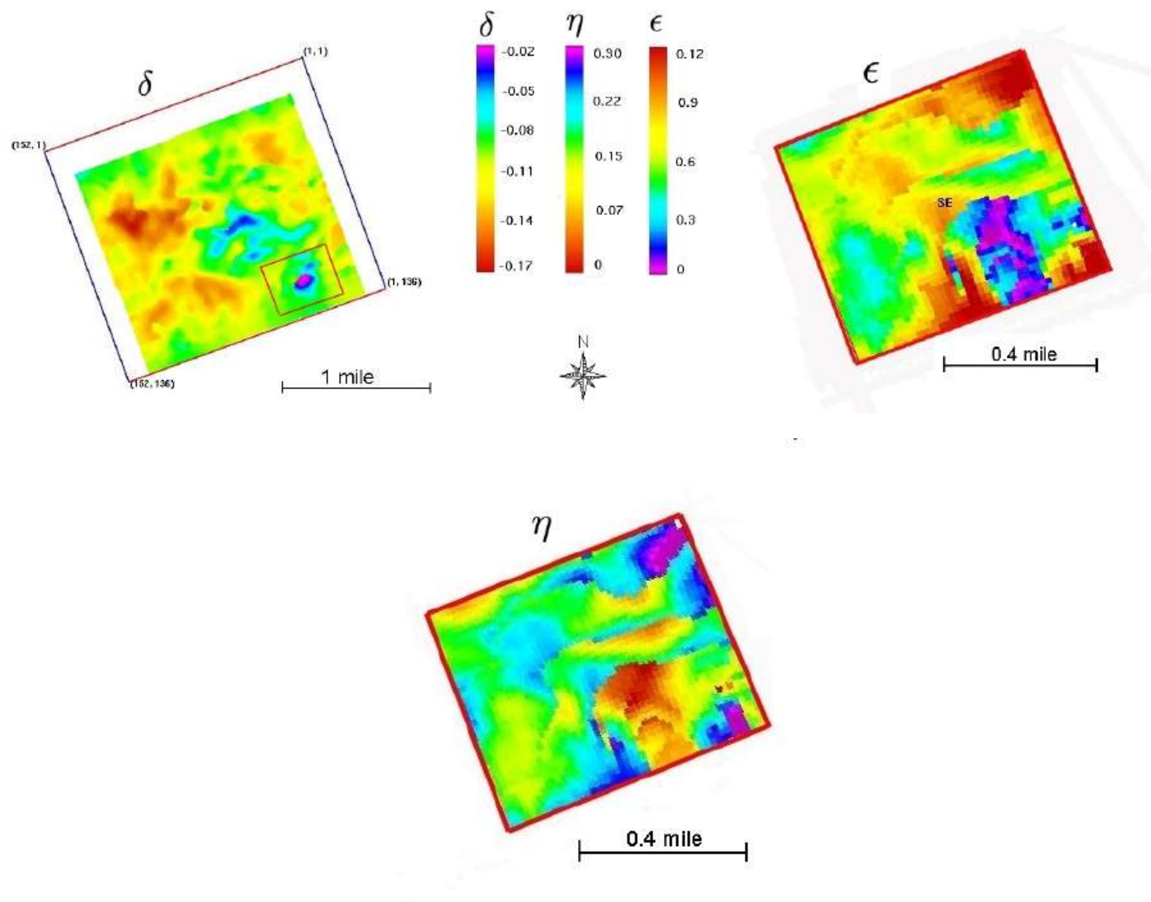

Figure 3.9. The anisotropy parameters δ, ϵ and η in the UMV Shale Formation. The inversion for these parameters is based on the velocity models shown in Figure 3.8 and on equations (3.37), (3.40), and (3.39). The parameters ϵ and η have only been estimated for a small area near the study well location. This area is indicated by a red square in the top left panel.

3.5 Orthorhombic Model and Shear-wave Splitting

The UMV Shale was modeled as a VTI medium. On the other hand, the gas saturated section is orthorhombic and might even be of a lower order symmetry.

3.5.1 Orthorhombic Media

Orthorhombic media are characterized by three mutually orthogonal planes of symmetry (Figure 3.10). In the Cartesian coordinate system associated with the symmetry planes, orthorhombic media have nine independent stiffness coefficients (Tsvankin, 1997a; Tsvankin, 2001) and the stiffness tensor can be written as:

$$\mathbf{c}^{(\mathbf{ort})} = \begin{pmatrix} c_{11} & c_{12} & c_{13} & 0 & 0 & 0 \\ c_{12} & c_{22} & c_{23} & 0 & 0 & 0 \\ c_{13} & c_{23} & c_{33} & 0 & 0 & 0 \\ 0 & 0 & 0 & c_{44} & 0 & 0 \\ 0 & 0 & 0 & 0 & c_{55} & 0 \\ 0 & 0 & 0 & 0 & 0 & c_{66} \end{pmatrix}. \tag{3.44}$$

Following the analysis conducted for VTI media, two vertical velocities (for P- and S-waves) are defined for the reference isotropic model. For orthorhombic media, one can choose either of the two shear-wave velocities to be the reference shear velocity (Tsvankin, 2001). We will chose the velocity of the S-wave polarized in the x_1-direction in order to define notations that are similar to those of the VTI media.

Tsvankin (1997a) showed that it is possible to define two sets of Thomsen-style parameters (δ, ϵ, and γ) each set being similar in one of the symmetry planes to the Thomsen parameters for VTI media. We will here present these Thomsen-style parameters that fully characterize anisotropy in orthorhombic media, but the inversion and analysis of all these parameters is outside the scope of this thesis. For more details about orthorhombic models, see Tsvankin (1997a; 2001); for details on the derivation of the Green's function in orthorhombic media, see Pšenčík (1998) and

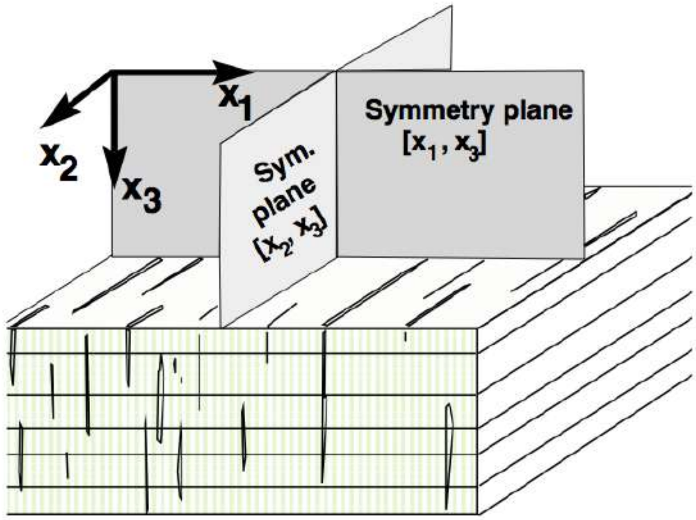

Figure 3.10. Orthorhombic model caused by a parallel vertical set of fractures embedded in a layered medium. One symmetry plane is in this case horizontal and parallel to the bedding, and the two others are parallel and orthogonal to the fracture set. Adapted from Tsvankin (2001).

Tsvankin (2005, chapter 2); for an actual joint PP/PS inversion in multilayered arbitrary anisotropic media above a plane dipping reflector, see Tsvankin & Grechka (2002).

The complete list of the Thomsen-style parameters is:

$$V_{p0} = \sqrt{\frac{c_{33}}{\rho}}, \tag{3.45}$$

$$V_{s0} = \sqrt{\frac{c_{55}}{\rho}}, \tag{3.46}$$

$$\epsilon^{(2)} = \frac{c_{11} - c_{33}}{2\,c_{33}}, \qquad \epsilon^{(1)} = \frac{c_{22} - c_{33}}{2\,c_{33}}, \tag{3.47}$$

$$\delta^{(2)} = \frac{(c_{13} + c_{55})^2 - (c_{33} - c_{55})^2}{2\,c_{33}(c_{33} - c_{55})}, \qquad \delta^{(1)} = \frac{(c_{23} + c_{44})^2 - (c_{33} - c_{44})^2}{2\,c_{33}(c_{33} - c_{44})}, \tag{3.48}$$

$$\gamma^{(2)} = \frac{c_{66} - c_{44}}{2\,c_{44}}, \qquad \gamma^{(1)} = \frac{c_{66} - c_{55}}{2\,c_{55}}, \tag{3.49}$$

$$\delta^{(3)} = \frac{(c_{12} + c_{66})^2 - (c_{11} - c_{66})^2}{2\,c_{11}(c_{11} - c_{66})}. \tag{3.50}$$

It is important to note that P-wave kinematics[2] are controlled by the following set of parameters: V_{p0}, $\epsilon^{(2)}$, $\delta^{(2)}$, $\epsilon^{(1)}$, $\delta^{(1)}$, and $\delta^{(3)}$ (Grechka & Tsvankin, 1998).

3.5.2 P̀Ś-wave Splitting in the Main Gas Reservoir

The computation of the nine Thomsen-style parameters requires an azimuthal NMO study on the long-offset prestack data. Since such a study has not been conducted in the RCP, a full characterization of the orthorhombic model for the reservoir will not be achievable as a part of this thesis. On the other hand, shear-wave splitting at vertical-incidence can be described by the fractional difference between the stiffness coefficients c_{44} and c_{55}:

$$\gamma^{(S)} = \frac{c_{44} - c_{55}}{2\,c_{55}} = \frac{\gamma^{(1)} - \gamma^{(2)}}{1 + 2\,\gamma^{(2)}} \approx \frac{V_{s1} - V_{s2}}{V_{s2}} = -\frac{\Delta t_{\grave{P}\acute{S}1} - \Delta t_{\grave{P}\acute{S}2}}{\Delta t_{\grave{P}\acute{S}1}}, \tag{3.51}$$

where $V_{s1} = \sqrt{c_{44}/\rho}$ is the vertical fast shear-wave velocity and $V_{s2} = \sqrt{c_{55}/\rho}$ is the vertical slow shear-wave velocity. $\Delta t_{\grave{P}\acute{S}1}$ represents the $\grave{\mathrm{P}}\acute{\mathrm{S}}_1$ traveltime in the reservoir, while $\Delta t_{\grave{P}\acute{S}2}$ represents the $\grave{\mathrm{P}}\acute{\mathrm{S}}_2$ traveltime in the reservoir.

The parameter $\gamma^{(S)}$ is a combination of the Thomsen-style parameters and is a direct measure of the time delay between the fast and slow shear-waves. This parameter $\gamma^{(S)}$ has been studied and referred to in many theses written about Rulison (Rumon, 2006; Gulyiev, 2007; Meza, 2008) as the *degree of anisotropy*. A slightly different version of the parameter $\gamma^{(S)}$ has been studied in Chapter 2. For an orthorhombic model defined by two sets of orthogonal fractures embedded in an isotropic background,

[2] For details on the nonhyperbolic reflection moveout for orthorhombic media, see Al-Dajani & Tsvankin (1998b); for details on the relations between NMO and vertical velocities and the anisotropic coefficients, see Grechka et al. (1999b).

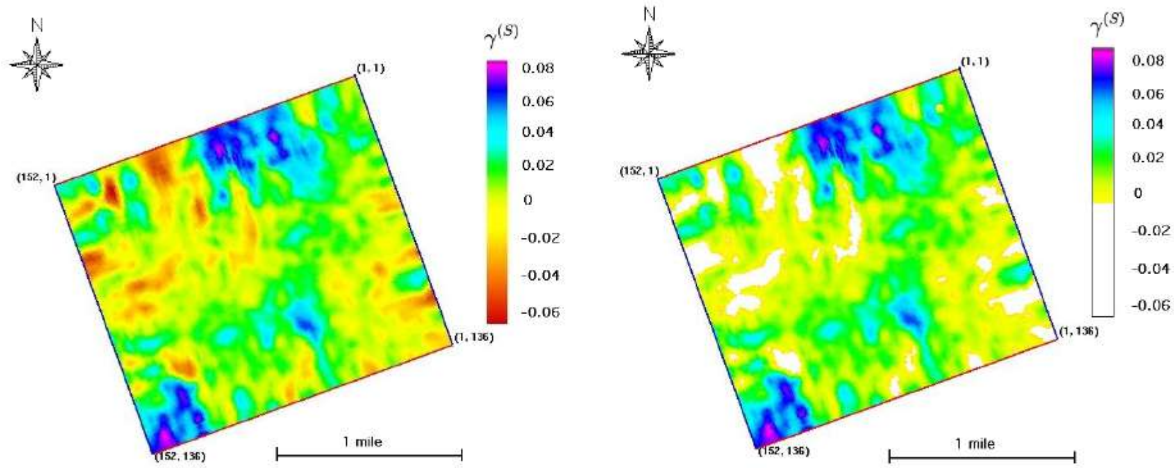

Figure 3.11. P̀Ś-wave splitting ($\gamma^{(S)}$) in the main gas reservoir section. On the left figure a classical colorbar is used, while on the right figure the anomalous values (the negative $\gamma^{(S)}$ values that correspond to a fast shear-wave slower than the slow shear-wave) are highlighted in white.

the parameter $\gamma^{(S)}$ depends on the difference between the crack densities (Stewart et al., 1999; Gaiser, 2004). Furthermore, multiple sets of differently oriented, irregularly shaped, and partially closed fractures appear as two orthogonal sets for long seismic waves (Vasconcelos & Grechka, 2007). This explains why the orthorhombic model based on two sets of orthogonal fractures embedded in an isotropic background has been a successful model for the Rulison reservoir (Jansen, 2005; Rumon, 2006; Vasconcelos & Grechka, 2007). The splitting parameter $\gamma^{(S)}$ has been computed for the main gas reservoir in Rulison (UMV Shale to top Cameo Coal horizon) based on equation (3.51) (Figure 3.11).

The $\gamma^{(S)}$ values range from 0 to 6% with the large majority of values being less than 2%. For an orthorhombic model characterized by one set of fractures embedded in a VTI background, the source of azimuthal anisotropy in the reservoir is exclusively due to the fractures, and $\gamma^{(S)}$ can be interpreted as a fracture detection parameter (Davis, 2006; Davis, 2007; LaBarre et al., 2008). The $\gamma^{(S)}$ map (Figure 3.11) can be then viewed as a fracture map (Jianming et al., 2009). On the other hand, if the orthorhombic model is characterized by two sets of orthogonal fractures, then $\gamma^{(S)}$

depends on the difference between the cracks densities. In other words, if the two crack densities are equal, $\gamma^{(S)}$ will be equal to zero. Therefore, $\gamma^{(S)}$ will no longer be a direct indicator of fracturing in the formation. If the reservoir has only one dominant set of fractures, the yellowish parts of Figure 3.11 would represent the unfractured zones, while the bluish parts of this same figure would represent the fractured zones.

In some restricted areas, $\gamma^{(S)}$ is found to be negative. These areas are colored in white in the right panel of Figure 3.11. These anomalies are probably due to changes of stress orientation in the reservoir or simply to a suboptimal Alford rotation of the two recorded horizontal components. There are also edge effects affecting the accuracy of the $\gamma^{(S)}$ values at the boundaries of the survey. Some of the values in the northwestern part of the survey might also be erroneous because of the low fold in that area.

Finally, it is important to note that the $\gamma^{(S)}$ map might indicate the location of the average high fractured zones in the 2,000 ft thick reservoir but does not indicate where in depth (or equivalently in vertical two-way traveltime) the fractures occur. This is due to the fact that $\gamma^{(S)}$ has been computed based on the fractional difference between the fast and slow shear-wave traveltimes over the entire reservoir section. In Chapter 5, we will determine the exact location of the fractured intervals in depth (or, equivalently, in two-way P-wave traveltime) based on a joint PP-PS amplitude inversion.

Chapter 4

ELASTIC ANISOTROPIC AVO MODELING IN TI MEDIA

4.1 Elastic AVO Modeling in VTI Media

The first section of this chapter will focus on elastic AVO modeling in transversely isotropic media with a vertical symmetry axis (VTI).

4.1.1 The Theoretical Model

Let us consider two elastic VTI halfspaces separated by a welded contact. The physical properties of the upper-halfspace denoted by $\rho^{(1)}$, $V_p^{(1)}$, and $V_s^{(1)}$ correspond respectively to the density, the P-wave velocity, and the S-wave velocity of that upper medium. The physical properties of the lower-halfspace denoted by $\rho^{(2)}$, $V_p^{(2)}$, and $V_s^{(2)}$ correspond respectively to the density, the P-wave velocity, and the S-wave velocity of that lower medium. $\epsilon^{(1)}$, $\delta^{(1)}$, and $\gamma^{(1)}$ correspond to the Thomsen anisotropy parameters in the upper-halfspace, while $\epsilon^{(2)}$, $\delta^{(2)}$, and $\gamma^{(2)}$ correspond to the Thomsen anisotropy parameters in the lower-halfspace. The contrast in density between the two halfspaces is denoted by $\Delta\rho$, while the contrasts in P-wave velocity and S-wave velocity across the interface are respectively denoted by ΔV_p and ΔV_s. On the other hand, the arithmetic mean of the densities across the interfaces is denoted by $\overline{\rho}$ and the arithmetic mean of the P- and S-wave velocities are respectively denoted by $\overline{V_p}$ and $\overline{V_s}$. The arithmetic mean of a given physical property can be seen as the physical property of a background medium, with the actual values of the physical properties in the upper and lower media being perturbations of the physical value for that background medium. Finally, the contrasts in the Thomsen parameters ϵ, δ, and γ across the interface are respectivelly denoted by $\Delta\epsilon$, $\Delta\delta$, and $\Delta\gamma$. Each elastic VTI halfspace (upper halfspace 1 and lower halfspace 2) is fully characterized by the set of six parameters: $\rho^{(i)}$, $V_p^{(i)}$, $V_s^{(i)}$, $\epsilon^{(i)}$, $\delta^{(i)}$, and $\gamma^{(i)}$, with $i \in \{1, 2\}$.

4.1.2 P̀Ṕ-wave Reflection Coefficient in VTI Media

Following the work of Rüger (1996; 1997; 2001) and Behura and Tsvankin (2008), the linearized P̀Ṕ-wave reflection coefficient at a horizontal interface between two VTI media has the following form:

$$R_{\grave{P}\acute{P}} = R_{\grave{P}\acute{P}}(0) + G_{\grave{P}\acute{P}} \sin^2 \theta_p + C_{\grave{P}\acute{P}} \sin^4 \theta_p, \tag{4.1}$$

with

$$R_{\grave{P}\acute{P}}(0) = \frac{\Delta\rho}{2\overline{\rho}} + \frac{\Delta V_p}{2\overline{V_p}}, \tag{4.2}$$

$$G_{\grave{P}\acute{P}} = \frac{-2}{\kappa_0^2}\frac{\Delta\rho}{\overline{\rho}} + \frac{\Delta V_p}{2\overline{V_p}} - \frac{4}{\kappa_0^2}\frac{\Delta V_s}{\overline{V_s}} + \frac{\Delta\delta}{2}, \tag{4.3}$$

$$C_{\grave{P}\acute{P}} = \frac{\Delta V_p}{2\overline{V_p}} + \frac{\Delta\epsilon}{2}, \tag{4.4}$$

were $\kappa_0 = \overline{V_p}/\overline{V_s}$ is the velocity ratio for the background medium, and θ_p is the incidence angle. Equation (4.1) is a Shuey-type approximation for the P̀Ṕ-wave reflection coefficient with $G_{\grave{P}\acute{S}}$ and $C_{\grave{P}\acute{S}}$ the AVO gradient and the curvature terms, respectively.

The zero-offset reflection coefficient is given by:

$$R_{\grave{P}\acute{P}} \approx R_{\grave{P}\acute{P}}(0) = \frac{\Delta\rho}{2\overline{\rho}} + \frac{\Delta V_p}{2\overline{V_p}}. \tag{4.5}$$

The contribution of the contrast in δ across the interface ($\Delta\delta$) is scaled by $\sin^2 \theta_p$, while the contrast in ϵ across the interface ($\Delta\epsilon$) is scaled by $\sin^4 \theta_p$. Therefore, for small incidence angles, the contribution of $\Delta\delta$ within the $R_{\grave{P}\acute{P}}$ coefficient is larger than the contribution of $\Delta\epsilon$. This result will be discussed in more details in this subsection.

Finally, the P-wave reflection coefficient in VTI media is independent of the Thomsen anisotropy parameter γ. This was expected since the Thomsen parameter

γ governs the SH-wave propagation in VTI media. Therefore, the linearized P-wave reflection coefficient in VTI media is governed by two sets of five physical parameters each: $\rho^{(i)}$, $V_p^{(i)}$, $V_s^{(i)}$, $\epsilon^{(i)}$, and $\delta^{(i)}$, with $i \in \{1, 2\}$.

Let us now consider a two-layered VTI medium defined by the set of elastic parameters shown in Table 4.1. This model is a particular case (n=2) of the multilayer VTI model presented in Appendix A. The isotropic version of this model ($\epsilon^{(1)} = \epsilon^{(2)} = \delta^{(1)} = \delta^{(2)} = 0$) has been studied by Stewart et al. (1998).

	P-velocity (m/s)	S-velocity (m/s)	Density (g/cc)	δ	ϵ
Layer 1	3,562	1,837	2.512	0.036	0.074
Layer 2	3,862	2,011	2.528	0.062	0.104

Table 4.1. Elastic parameters for a two-layer VTI model. The upper VTI halfsapce is referred to as Layer 1 and the lower VTI halfspace is referred to as Layer 2. The interface between the two VTI media is flat and horizontal. The P- and PSV-wave propagation in VTI media is characterized by two sets of 5 parameters each: $\rho^{(i)}$, $V_p^{(i)}$, $V_s^{(i)}$, $\epsilon^{(i)}$, and $\delta^{(i)}$, with $i \in \{1, 2\}$.

A linearized form of the P-wave reflection coefficient $R_{\grave{P}\acute{P}}$ in isotropic media can be derived from the more general linearized P-wave reflection coefficient in VTI media (equation (4.1)) by setting both $\Delta\delta$ and $\Delta\epsilon$ to zero. The exact expression for the $R_{\grave{P}\acute{P}}$ coefficient in isotropic media is given by Aki & Richards (1980). The exact reflection coefficient function of incidence angle in isotropic media is plotted as a solid black curve on Figure 4.1. The linearized P-wave reflection coefficient is plotted as a dashed black curve on Figure 4.1. On the other hand, the linearized $R_{\grave{P}\acute{P}}$ coefficient in VTI media based on equation (4.1) is plotted as a solid red curve in Figure 4.1, while the small offset approximation of the P-wave refelctivity computed by taking $\sin^4 \theta_p \approx 0$ in equation (4.1) is plotted as a dashed red curve in Figure 4.1.

The first observation made from Figure 4.1 is that the small-offset approximation is valid in the isotropic medium up to an incidence angle of 18°, and in the VTI medium up to an incidence angle of 14°. Another observation is that up to an

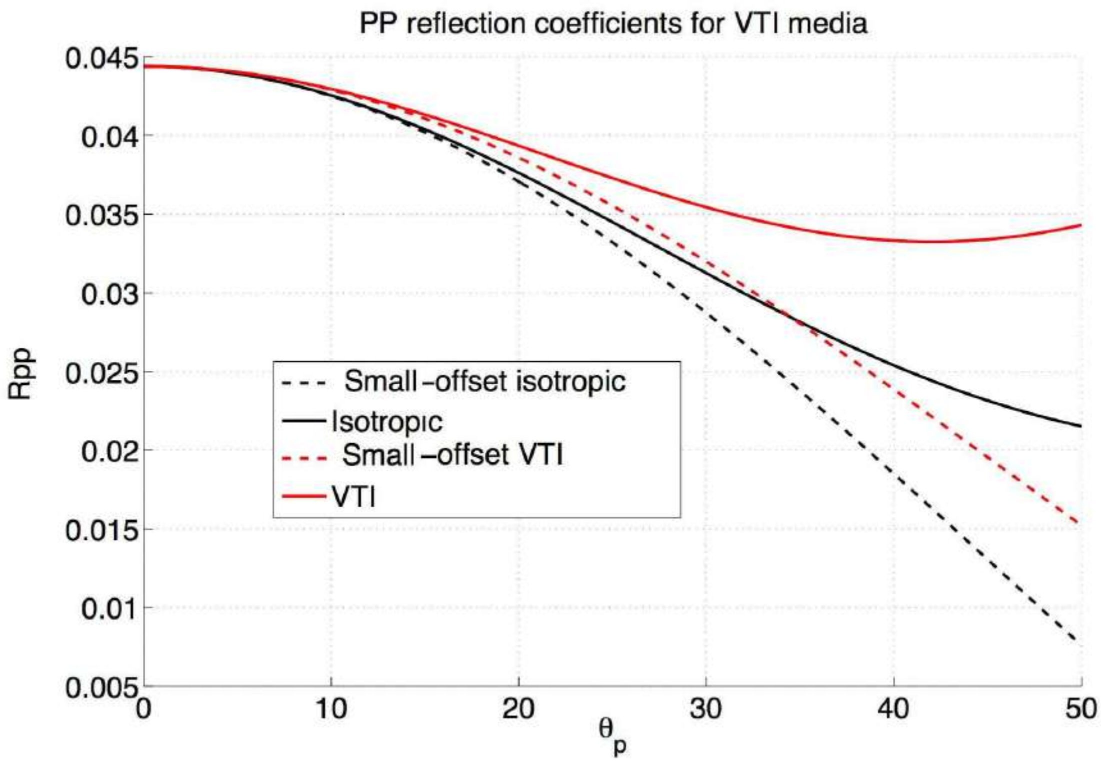

Figure 4.1. The exact P-wave reflection coefficient in the isotropic model is represented by the solid black curve, the linearized P-wave reflection coefficient in the isotropic model is represented by the black dashed curve, the linerized P-wave reflection coefficient in the VTI model is represented by the solid red curve, and the small-offset P-wave reflection coefficient in the VTI model is represented by the red dashed curve. The models used to plot these curves are based on a two-halfspace medium with the elastic parameters given by Table 4.1.

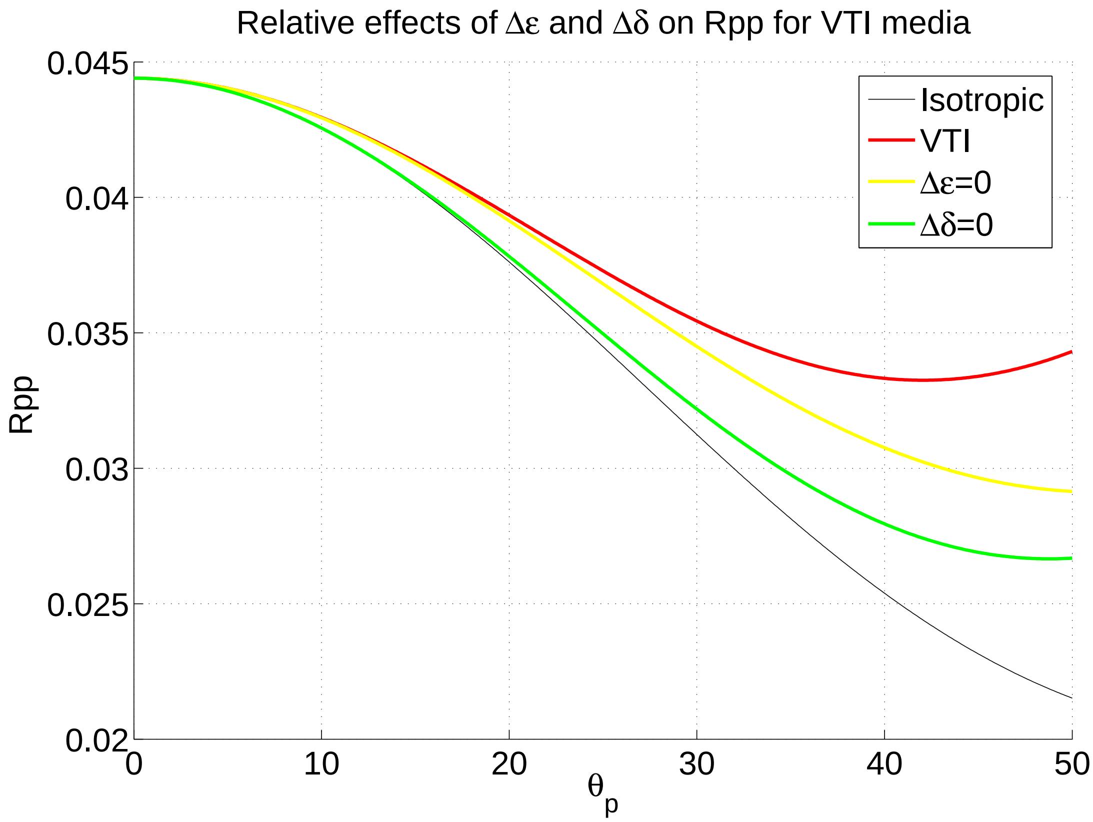

Figure 4.2. Relative effects of $\Delta\delta$ and $\Delta\epsilon$ on the $R_{\grave{P}\acute{P}}$ coefficient. The models used to plot these curves are based on a two-halfspace medium with the elastic parameters given by Table 4.1. The P-wave reflectivity in isotropic media is plotted in gray, and the P-wave reflectivity in VTI media is plotted in red. The P-wave reflectivity in VTI media with no contrast in the Thomsen parameter ϵ is plotted in yellow, while the P-wave reflectivity in VTI media with no contrast in the Thomsen parameter δ is plotted in green.

incidence angle of 8°, the VTI model can be approximated by the isotropic model. This result is directly predictable from equation (4.1): for small offsets, $\sin\theta_p \approx 0$ and, therefore, $R_{\grave{P}\acute{P}} \approx R_{\grave{P}\acute{P}}(0)$. For a layer at 6,000 ft of depth, a P-wave incidence angle of 8° corresponds roughly to 1,685 ft of offset, and hence the isotropic model will be a good approximation of the VTI model for the P-wave reflection coefficient up to 1,685 ft of offset.

The relative influence of the contrast in the Thomsen parameters δ and ϵ on the P-wave reflection coefficient is shown in Figure 4.2. The P-wave reflection coefficient in isotropic media is shown in gray, and the P-wave reflection coefficient in VTI media with the elastic parameters of Table 4.1 is shown in red. In yellow is shown the P-wave reflection coefficient in that same VTI model but with $\Delta\epsilon$ set to zero, and in green is the P-wave reflection coefficient in the same VTI model but with $\Delta\delta$ set to zero. The conclusion is that up to an incidence angle of 25°, only $\Delta\delta$ has a contribution to the P-wave reflection coefficient (the red and yellow curves coincide up to an incidence angle of 25°, and equivalently the gray and green curves coincide up to an incidence angle of 25° as well). The contribution of $\Delta\epsilon$ starts only above an incidence angle of 25°, or equivalently above 5,600 ft of offset for a layer at 6,000 ft of depth. In other words, for a layer at 6,000 ft of depth and considering the realistic elastic parameters given by Table 4.1, the Thomsen anisotropy parameter ϵ will have an influence on the P-wave reflection coefficient only above 5,600 ft of offset while the influence of the Thomsen parameter δ is noticeable above 1,685 ft of offset.

4.1.3 ṔŚ-wave Reflection Coefficient in VTI Media

Multicomponent AVO analysis has already been the subject of different theoretical and practical case studies (Rüger, 1996; Bryan et al., 2002; Behura & Tsvankin, 2006). Following the work of Rüger (1996; 2001), Jílek (2002a; 2002b), and Behura and Tsvankin (2008), the linearized P̀Ś-wave reflection coefficient on a horizontal interface between two VTI media is:

$$R_{\grave{P}\acute{S}} = B_{\grave{P}\acute{S}} \sin\theta_p + K_{\grave{P}\acute{S}} \sin^3\theta_p, \tag{4.6}$$

where $B_{\grave{P}\acute{S}}$ and $K_{\grave{P}\acute{S}}$ are the AVO gradient and curvature terms, respectively:

$$B_{\grave{P}\acute{S}} = -\frac{2}{\kappa_0}\left[\left(\frac{\kappa_0}{4}+\frac{1}{2}\right)\frac{\Delta\rho}{\overline{\rho}} + \frac{\Delta V_s}{\overline{V_s}} - \frac{\kappa_0^2}{4\,(1+\kappa_0)}\Delta\delta\right], \tag{4.7}$$

$$K_{\grave{P}\acute{S}} = \frac{3+2\,\kappa_0}{4\,\kappa_0^2}\frac{\Delta\rho}{\overline{\rho}} + \frac{2+\kappa_0}{\kappa_0^2}\frac{\Delta V_s}{\overline{V_s}} + \frac{1-4\,\kappa_0}{2\,(1+\kappa_0)}\Delta\delta + \frac{\kappa_0}{1+\kappa_0}\Delta\epsilon, \tag{4.8}$$

$\kappa_0 = \overline{V_p}/\overline{V_s}$ is the velocity ratio for the background medium, and θ_p is the incidence angle. The $R_{\grave{P}\acute{S}}$ coefficient is independent of the Thomsen anisotropy parameter γ.

Thus, the linearized PSV-wave reflection coefficient in VTI media is governed by two sets of five physical parameters each: $\rho^{(i)}$, $V_p^{(i)}$, $V_s^{(i)}$, $\epsilon^{(i)}$, and $\delta^{(i)}$, with $i \in \{1, 2\}$.

In isotropic media, $\Delta\delta = 0$ and $\Delta\epsilon = 0$; and in the small-offset approximation $\sin^3\,\theta_p \approx 0$. Therefore, the isotropic small-offset P̀Ś-wave reflection coefficient can be written as:

$$R_{\grave{P}\acute{S}} \approx -\frac{2}{\kappa_0} \sin\,\theta_p \left[\left(\frac{\kappa_0}{4} + \frac{1}{2} \right) \frac{\Delta\rho}{\overline{\rho}} + \frac{\Delta V_s}{\overline{V_s}} \right]. \tag{4.9}$$

Furthermore, for converted-waves, Snell's law can be written as:

$$\frac{\sin\,\theta_p}{V_p} = \frac{\sin\,\theta_s}{V_s} = p, \tag{4.10}$$

where θ_s is the reflected angle. Therefore equation (4.9) can also be written as:

$$R_{\grave{P}\acute{S}} \approx -2 \sin\,\theta_s \left[\left(\frac{\kappa_0}{4} + \frac{1}{2} \right) \frac{\Delta\rho}{\overline{\rho}} + \frac{\Delta V_s}{\overline{V_s}} \right]. \tag{4.11}$$

Equation (4.11) is equal to the linearized P̀Ś-wave reflection coefficient in isotropic media presented by Valenciano & Michelena (2000).

It is now important to explain the notion of a P̀Ś zero-offset section. Equation (4.6) shows that the converted-wave reflection coefficient for VTI media is zero at normal incidence. In fact, the P̀Ś-wave zero-offset section is the NMO-corrected and stacked set of traces. In other word, the P̀Ś-wave zero-offset section is the average reflectivity (which is not zero) across the set of source-receiver offsets for each common conversion point (Stewart et al., 1998).

Figure 4.3 shows the P̀Ś-wave reflection coefficient as a function of incidence angle for different media with the elastic parameters of Table 4.1. The P̀Ś-wave reflection coefficient in isotropic media based on equation (4.11) is plotted as a solid black curve, and the small-offset approximation of the P̀Ś-wave reflection coefficient in isotropic media based on equation (4.11) is plotted as a dashed black curve on Figure 4.3. On the other hand, the P̀Ś-wave reflection in VTI media based on equation (4.6) is plotted as a solid red curve, and the small-offset approximation based on that same

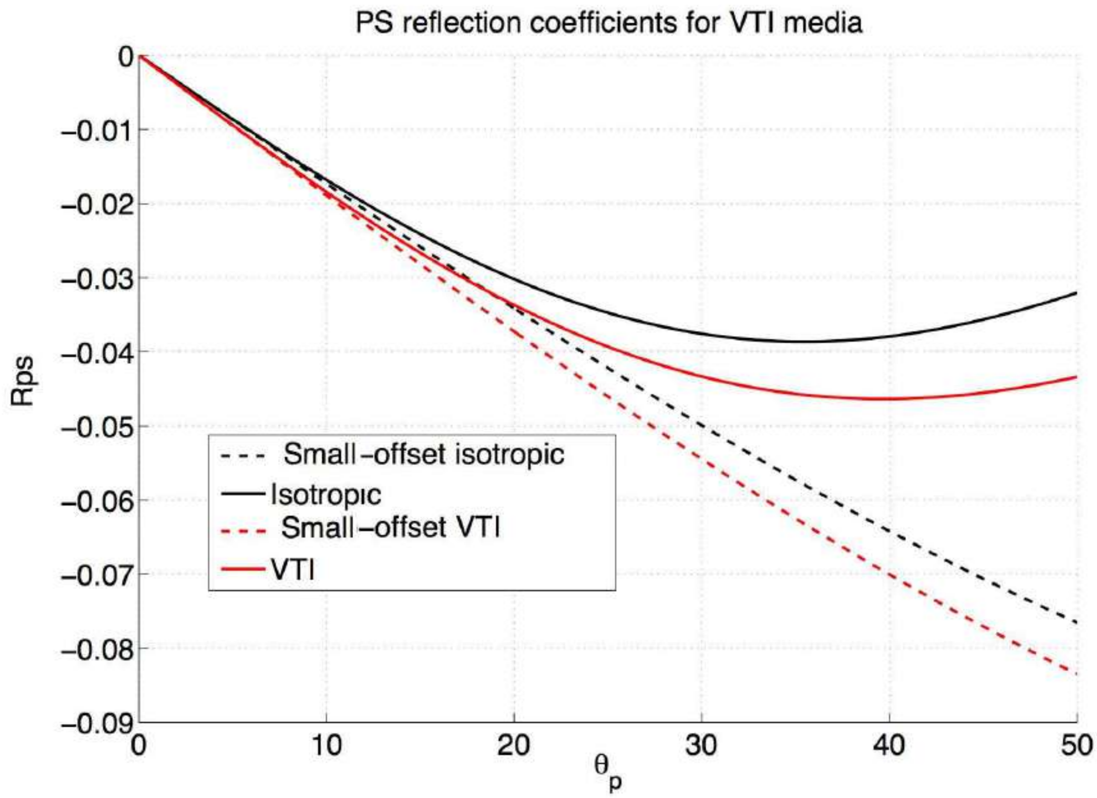

Figure 4.3. The P̀Ś-wave reflection coefficient in isotropic media is represented by the solid black curve, the small-offset P̀Ś-wave reflection coefficient in isotropic media is represented by the black dashed curve, the exact P̀Ś-wave reflection coefficient in VTI media is represented by the solid red curve, and the small-offset P̀Ś-wave reflection coefficient in VTI media is represented by the red dashed curve. The models used to plot these curves are based on a two-halfspace medium with the elastic parameters given by Table 4.1.

equation (4.6) and on the approximation $\sin^3 \theta_p \approx 0$ is plotted as a dashed red curve on Figure 4.3.

The first observation is that for both isotropic and VTI models, the absolute value of the $R_{\grave{P}\acute{S}}$ coefficient reaches a global maximum for a certain angle (in the isotropic model, this angle is close to 32°, and in the VTI model, this angle is close to 38°). The second observation is that the small offset approximation is valid in both isotropic and VTI models up to an incidence angle of 10°. In other words, up to an incidence angle of 10°, we can ignore the term of order $\sin^3 \theta_p$. From Snell's law, and with $\kappa_0 = 1.9$, a 10° incidence angle corresponds to a reflection angle of

5.24°. Therefore, for a layer at 6,000 ft of depth, the 10° incidence angle corresponds to roughly 1,600 ft of offset. Hence, for less than 1,600 ft of offset, the small-offset approximation is valid and the $\grave{P}\acute{S}$-wave reflectivity can be computed to the first order in $\sin\theta_p$. A last observation is that up to an incidence angle of 7°, given the elastic parameters of Table 4.1, the isotropic model approximates very well the VTI model. From Snell's law, and with $\kappa_0 = 1.9$, a 7° incidence angle corresponds to a reflected angle of 3.68°. Therefore, for a layer at 6,000 ft of depth, the 7° incidence angle corresponds to roughly 1,120 ft of offset. Hence, for less than 1,120 ft of offset there is no influence of anisotropy on the $\grave{P}\acute{S}$-wave reflection coefficient, and thus, the $\grave{P}\acute{S}$-wave reflectivity in VTI media can be approximated by the $\grave{P}\acute{S}$-wave reflectivity in isotropic media.

The relative influence of the contrast in the Thomsen parameters δ and ϵ on the $\grave{P}\acute{S}$-wave reflection coefficient is shown in Figure 4.4. The isotropic $\grave{P}\acute{S}$-wave reflectivity is shown in gray, and the $\grave{P}\acute{S}$-wave reflectivity in VTI media with the elastic parameters of Table 4.1 is shown in red. In yellow is shown the $\grave{P}\acute{S}$-wave reflection coefficient in that same VTI model but with $\Delta\epsilon = 0$, and in green is shown the $\grave{P}\acute{S}$ reflectivity in the same VTI model but with $\Delta\delta = 0$. The conclusion is that up to an incidence angle of 17°, only $\Delta\delta$ has a contribution to the $\grave{P}\acute{S}$-wave reflection coefficient (the red and yellow curves coincide up to an incidence angle of 17°, and equivalently the gray and green curves coincide for that same range of incidence angles). The contribution of $\Delta\epsilon$ starts only above an incidence angle of 17° or equivalently above 2,770 ft of offset for a layer at 6,000 ft of depth. In other words, for a layer at 6,000 ft of depth and considering the realistic elastic parameters given by Table 4.1, the Thomsen anisotropy parameter ϵ will have an influence on the $\grave{P}\acute{S}$-wave reflection coefficient at offsets greater than 2,770 ft, while the influence of the Thomsen parameter δ is noticeable at offsets greater than 1,120 ft. The last observation is that the relative influence of $\Delta\delta$ and $\Delta\epsilon$ on both $\grave{P}\acute{P}$- and $\grave{P}\acute{S}$-wave reflectivities is different. In the case of P-waves, both $\Delta\delta$ and $\Delta\epsilon$ tend to increase the reflectivity compared to the P-wave reflectivity in isotropic media. For $\grave{P}\acute{S}$-waves, in

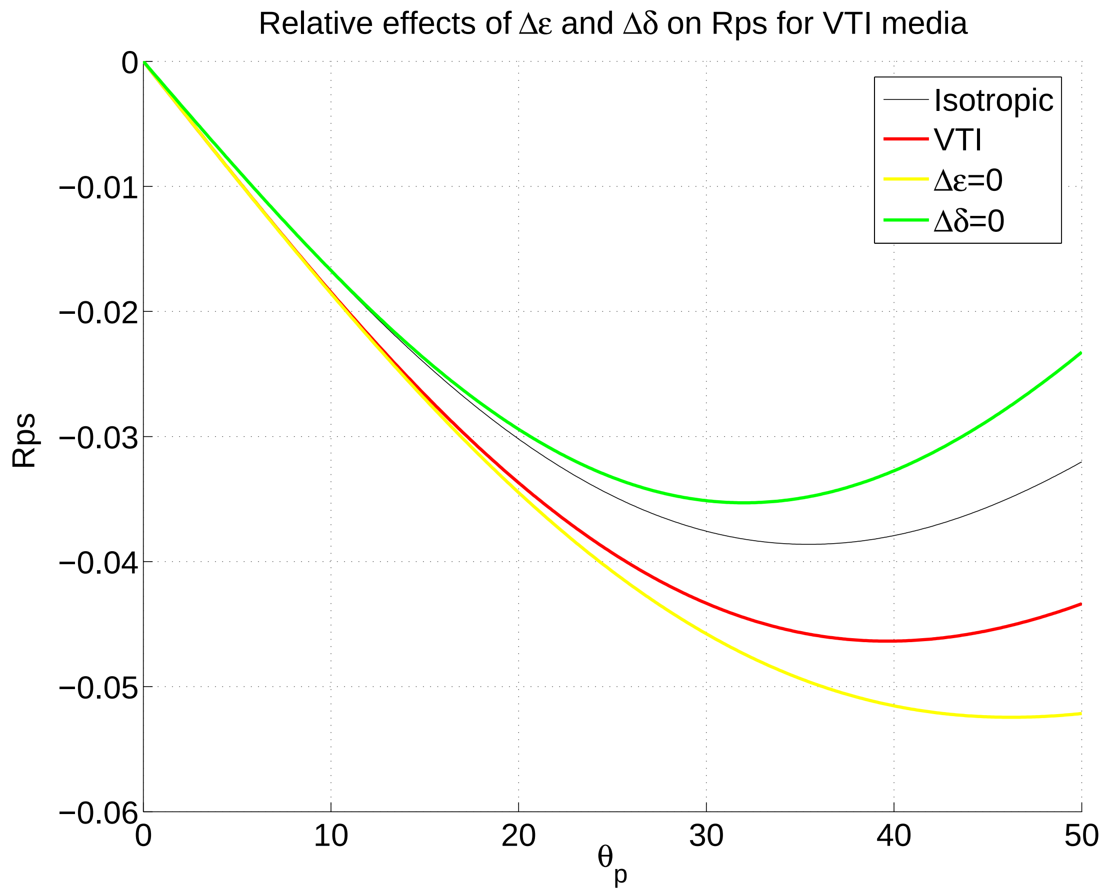

Figure 4.4. Relative effects of $\Delta\delta$ and $\Delta\epsilon$ on the $R_{\grave{P}\acute{S}}$ coefficient. The models used to plot these curves are based on a two-halfspace medium with the elastic parameters given by Table 4.1. The P̀Ś-wave reflectivity in isotropic media is plotted in gray, and the P̀Ś-wave reflectivity in VTI media is plotted in red. The P̀Ś-wave reflectivity in VTI media with no contrast in the Thomsen parameter ϵ is plotted in yellow, while the P̀Ś-wave reflectivity in VTI media with no contrast in the Thomsen parameter δ is plotted in green.

terms of absolute values, $\Delta\epsilon$ tends to reduce the reflectivity, while $\Delta\delta$ tends to increase the reflectivity compared to the $\grave{P}\acute{S}$-wave reflectivity in isotropic media. Therefore, the absolute value of the $\grave{P}\acute{S}$-wave reflectivity is significantly higher when $\Delta\epsilon = 0$. The comparison of the $\grave{P}\acute{S}$-wave reflectivity results with the $\grave{P}\acute{P}$-wave reflectivity results obtained previously is the object of the next subsection.

4.1.4 Joint Analysis of $R_{\grave{P}\acute{P}}$ and $R_{\grave{P}\acute{S}}$ Coefficients

Based on the elastic parameters given by Table 4.1, both $\grave{P}\acute{P}$- and $\grave{P}\acute{S}$-wave reflection coefficients in isotropic and VTI media and their small-offset approximations are plotted on Figure 4.5. For the current study model, the $\grave{P}\acute{S}$-wave reflectivity has larger variations with offset compared to the $\grave{P}\acute{P}$-wave reflectivity that has a constant behavior up to an incidence angle of 15° and then diminishes slowly with increasing incidence angle. On the other hand, in both isotropic and VTI media, the small-offset approximation is valid for larger incidence angles in the case of compressional-waves compared to converted-waves. Finally, $\grave{P}\acute{P}$-wave reflectivities in both isotropic and VTI media remain very close up to an incidence angle of 10° (or equivalently 2,115 ft of offset for a layer at 6,000 ft of depth), whereas $\grave{P}\acute{S}$-wave reflectivity in VTI media is close to the isotropic $\grave{P}\acute{P}$-wave reflectivity only up to an incidence angle of 7° (or equivalently 1,120 ft of offset for a layer at 6,000 ft of depth).

Based on Figure 4.6, some conclusions about the relative influence of $\Delta\epsilon$ and $\Delta\delta$ were derived. For P-waves, the reflectivity with respect to offset in isotropic media is the lowest. Both contrasts in δ and ϵ increase P-wave reflectivity. The contribution of δ starts for midrange offsets (for incidence angles larger than 15°) while the contribution of ϵ is noticeable only for large offsets (for incidence angles larger than 25°). On the other hand, for $\grave{P}\acute{S}$-waves, the reflectivity with respect to offset in isotropic media is not the lowest in terms of absolute values. The $\grave{P}\acute{S}$-wave reflectivity in VTI media with no contrast in δ is the lowest, with the influence of ϵ being noticeable for incidence angles larger than 20°. The contrast in δ has an important influence on converted-wave reflectivity even for relatively small offsets

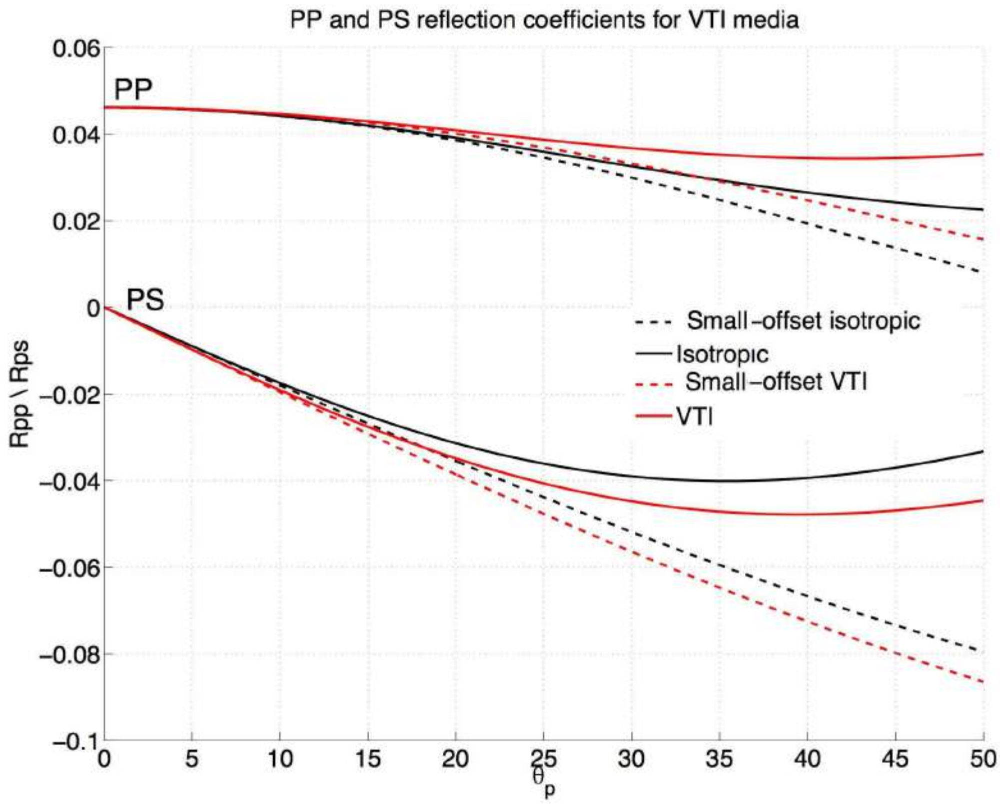

Figure 4.5. P̀Ṕ- and P̀Ś-wave reflection coefficients in VTI and isotropic media and their small-offset approximations. The models used to plot these curves are based on a two-halfspace medium with the elastic parameters given by Table 4.1. There are two models represented on this figure: the reflection coefficients related to the first model, which consists of an upper and lower isotropic halfspaces separated by a flat horizontal interface, are represented in black; the reflection coefficients of the second model, which consists of an upper and lower VTI halfspaces separated by the same flat horizontal interface, are represented in red. The small-offset approximations are plotted as dashed curves.

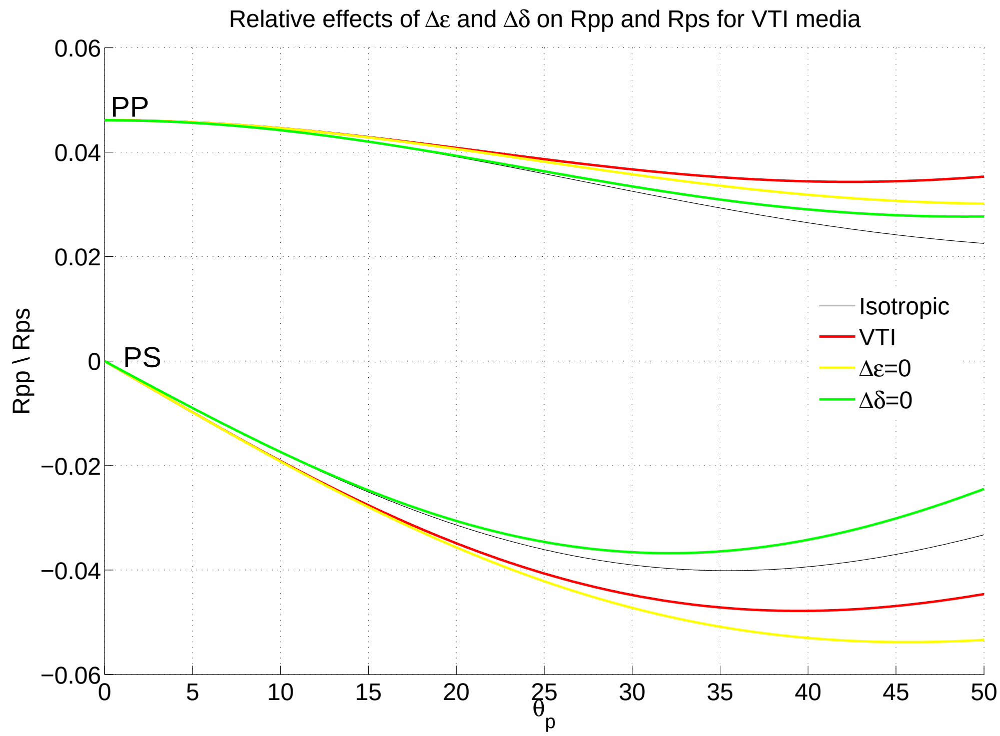

Figure 4.6. Relative effects of $\Delta\delta$ and $\Delta\epsilon$ on the $R_{\grave{P}\acute{P}}$ and $R_{\grave{P}\acute{S}}$ coefficients. The models used to plot these curves are based on a two-halfspace medium with the elastic parameters given by Table 4.1. The ÈṔ- and ÈŚ-wave reflectivities in isotropic media are plotted in gray, and the reflectivities in VTI media are plotted in red. The reflectivities in VTI with no contrast in the Thomsen parameter ϵ are plotted in yellow, while the reflectivities in VTI media with no contrast in the Thomsen parameter δ are plotted in green.

(for incidence angles larger than 7°). Above incidence angles of 20°, the influence of ϵ is noticeable, and the P̀Ś-wave reflectivity in general VTI media tends to be lower than the P̀Ś-wave reflectivity in VTI media with no contrast in the Thomsen parameter ϵ. The complex dependence of the P̀Ś-wave reflection coefficient on $\Delta\epsilon$ and $\Delta\delta$ will be analyzed in the next subsection.

4.1.5 $\mathbf{R_{\grave{P}\acute{S}}}$ Coefficient in VTI Media Function of $\Delta\delta$ and $\Delta\epsilon$

For a given incidence angle θ_p and in terms of absolute values, the P̀Ś-wave reflection coefficient increases linearly with an increasing positive contrast in the Thomsen parameter δ across the interface (Figure 4.7). Furthermore, for larger incidence angles, the increase in P̀Ś-wave reflectivity as a function of $\Delta\delta$ is steeper: the slope of the straight line that describes the $R_{\grave{P}\acute{S}}$ coefficient as a function of $\Delta\delta$ increases with larger incidence angles. Also, given that $\Delta\epsilon = 0$, the P̀Ś-wave reflectivity remains negative for all incidence angles and all positive contrasts in the Thomsen parameter δ.

On the other hand, the P̀Ś-wave reflectivity dependence on increasing positive contrasts in the Thomsen parameter ϵ across the interface exists only for incidence angles larger than 25°. Up to an incidence angle of 45°, and with increasing positive contrasts in ϵ, the $R_{\grave{P}\acute{S}}$ coefficient diminishes linearly in terms of absolute values and gets close to zero (Figure 4.8). For incidence angles larger than 45°, the $R_{\grave{P}\acute{S}}$ coefficient first diminishes linearly (in terms of absolute values), then reaches zero for a given value of $\Delta\epsilon$, and finally starts increasing linearly. In other terms, the $R_{\grave{P}\acute{S}}$ coefficient increases linearly from initially negative values to positive values with increasing $\Delta\epsilon$: for small values of $\Delta\epsilon$, $R_{\grave{P}\acute{S}}$ is negative and increases linearly (in terms of absolute values the $R_{\grave{P}\acute{S}}$ coefficient decreases); then for a given value of $\Delta\epsilon$, the $R_{\grave{P}\acute{S}}$ coefficient is equal to zero, this means that there exists a value of $\Delta\epsilon$ for which there is no mode conversion; finally, for larger values of $\Delta\epsilon$, the $R_{\grave{P}\acute{S}}$ coefficient is positive and continue increasing linearly with increasing contrast in ϵ at the interface. It is also important to note that just like the P̀Ś-wave reflectivity dependence on

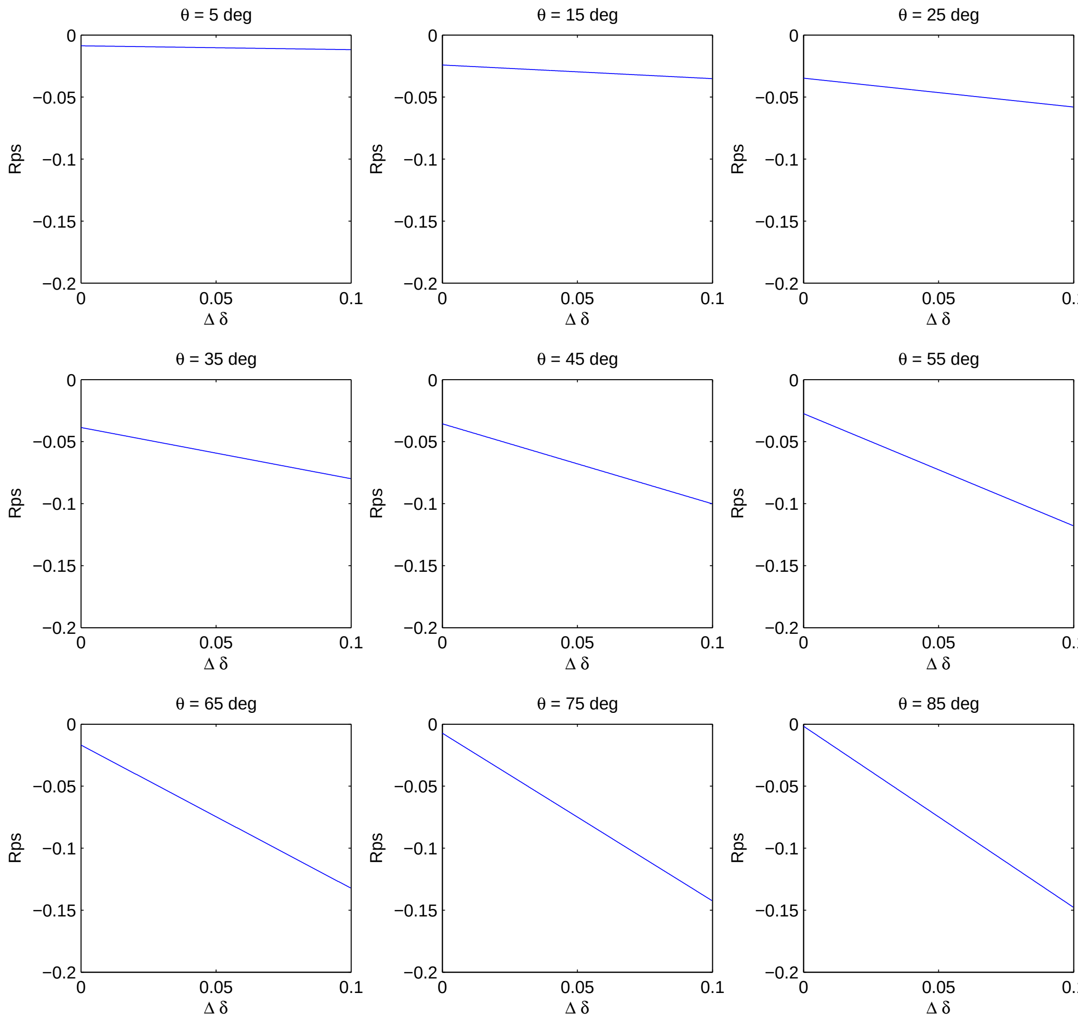

Figure 4.7. $R_{\grave{P}\acute{S}}$ coefficient in VTI media as a function of positive contrasts in the Thomsen parameter δ and no contrast in the Thomsen parameter ϵ ($\Delta\epsilon = 0$) across the interface. The different plots correspond to different values of the incidence angle. The model used to plot these curves is based on a two-halfspace VTI media (an upper VTI medium and a lower VTI medium separated by a flat horizontal interface) with the density and velocity values given by Table 4.1.

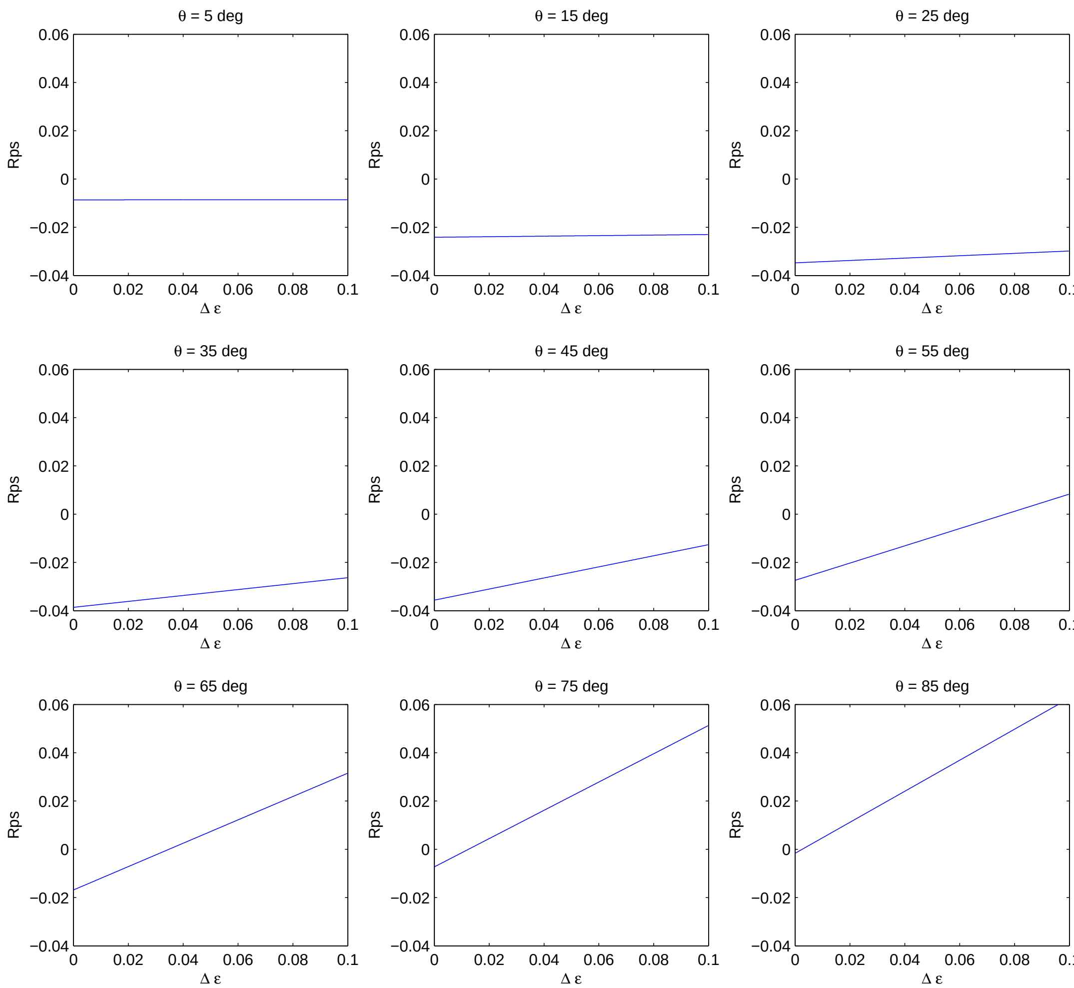

Figure 4.8. $R_{\grave{P}\acute{S}}$ coefficient in VTI media as a function of positive contrasts in the Thomsen parameter ϵ and no contrast in the Thomsen parameter δ ($\Delta\delta = 0$) across the interface. Same model and display as in Figure 4.7.

$\Delta\delta$, the P̀Ś-wave reflectivity dependence on $\Delta\epsilon$ gets steeper for increasing incidence angles. This is shown on Figure 4.8 by the increasing slope of the $R_{\grave{P}\acute{S}}$ coefficient straight line function of $\Delta\epsilon$ with increasing incidence angles. A last observation is that for very large incidence angles (larger than 85° for the considered model), the P̀Ś-wave reflection coefficient is always positive for all positive contrasts in the Thomsen parameter ϵ.

For negative contrasts in the Thomsen parameter δ, the $R_{\grave{P}\acute{S}}$ coefficient can have positive values (Figure 4.9). Furthermore, the $R_{\grave{P}\acute{S}}$ coefficient will increase linearly for increasing negative contrasts in the Thomsen parameter δ. The larger the incidence angle is, the steeper the increase of the $R_{\grave{P}\acute{S}}$ coefficient will be with respect to the negatively increasing $\Delta\delta$. It is important to note that there exists a negative value of $\Delta\delta$ for which the $R_{\grave{P}\acute{S}}$ coefficient is equal to zero. This means that for this given value of $\Delta\delta$ there is no mode conversion.

On the other hand, in terms of absolute values, the P̀Ś-wave reflection coefficient increases linearly with increasing negative contrasts in the Thomsen parameter ϵ across the interface for incidence angles larger than 25° (Figure 4.10). For incidence angles less than 25°, there is no noticeable influence of $\Delta\epsilon$ on the $R_{\grave{P}\acute{S}}$ coefficient. Furthermore, for increasing incidence angles, the increase in P̀Ś-wave reflectivity as a function of $\Delta\epsilon$ gets steeper: the slope of the $R_{\grave{P}\acute{S}}$ straight line function of $\Delta\epsilon$ increases with larger incidence angles. Also, given that $\Delta\delta = 0$, the P̀Ś-wave reflectivity remains negative for all incidence angles and for all negative contrasts in the Thomsen parameter ϵ across the interface.

4.2 AVO Modeling in Rulison VTI-over-HTI Model

Now that the dependence of the P̀Ṕ- and P̀Ś-wave reflection coefficient on the Thomsen parameters δ and ϵ in VTI media has been studied, a similar analysis will be applied on a simplified model for the upper part of the reservoir in Rulison Field.

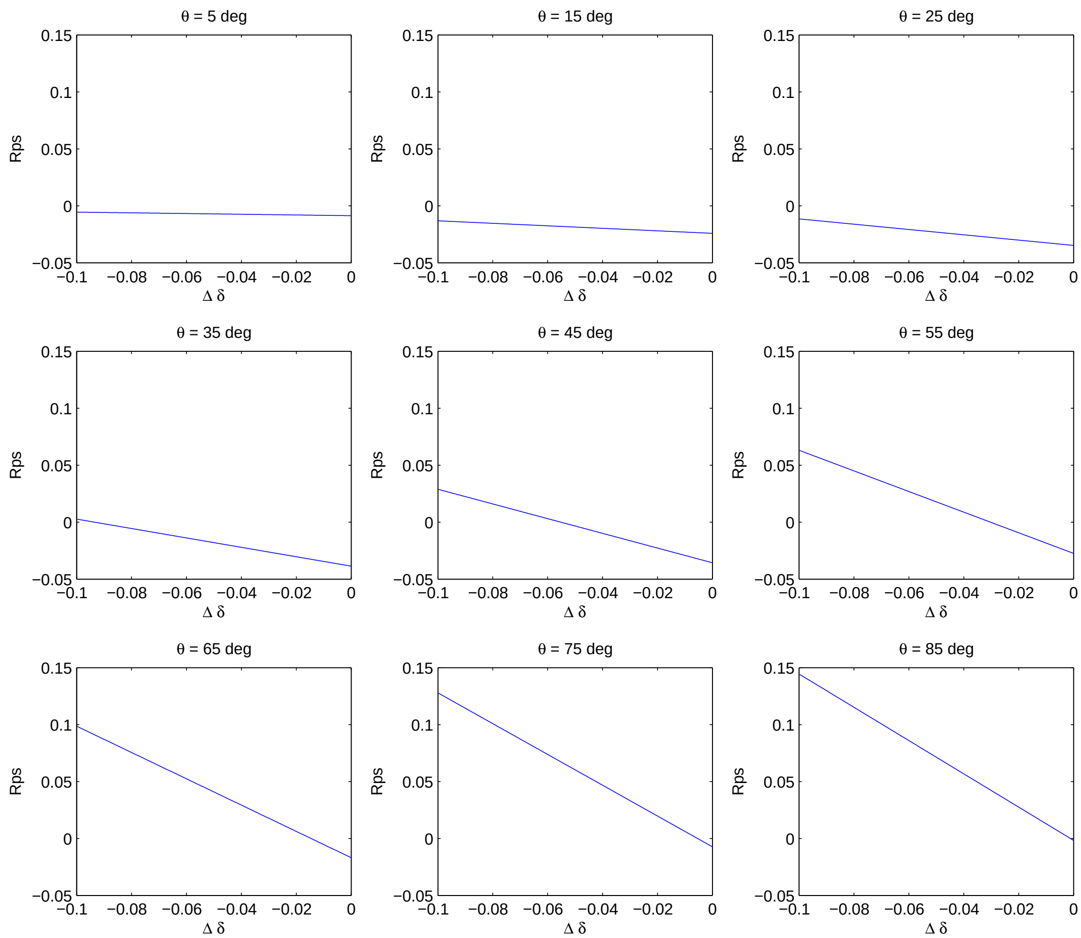

Figure 4.9. $R_{\grave{P}\acute{S}}$ coefficient in VTI media as a function of negative contrasts in the Thomsen parameter δ and no contrast in the Thomsen parameter ϵ ($\Delta\epsilon = 0$) across the interface. Same model and display as in Figure 4.7.

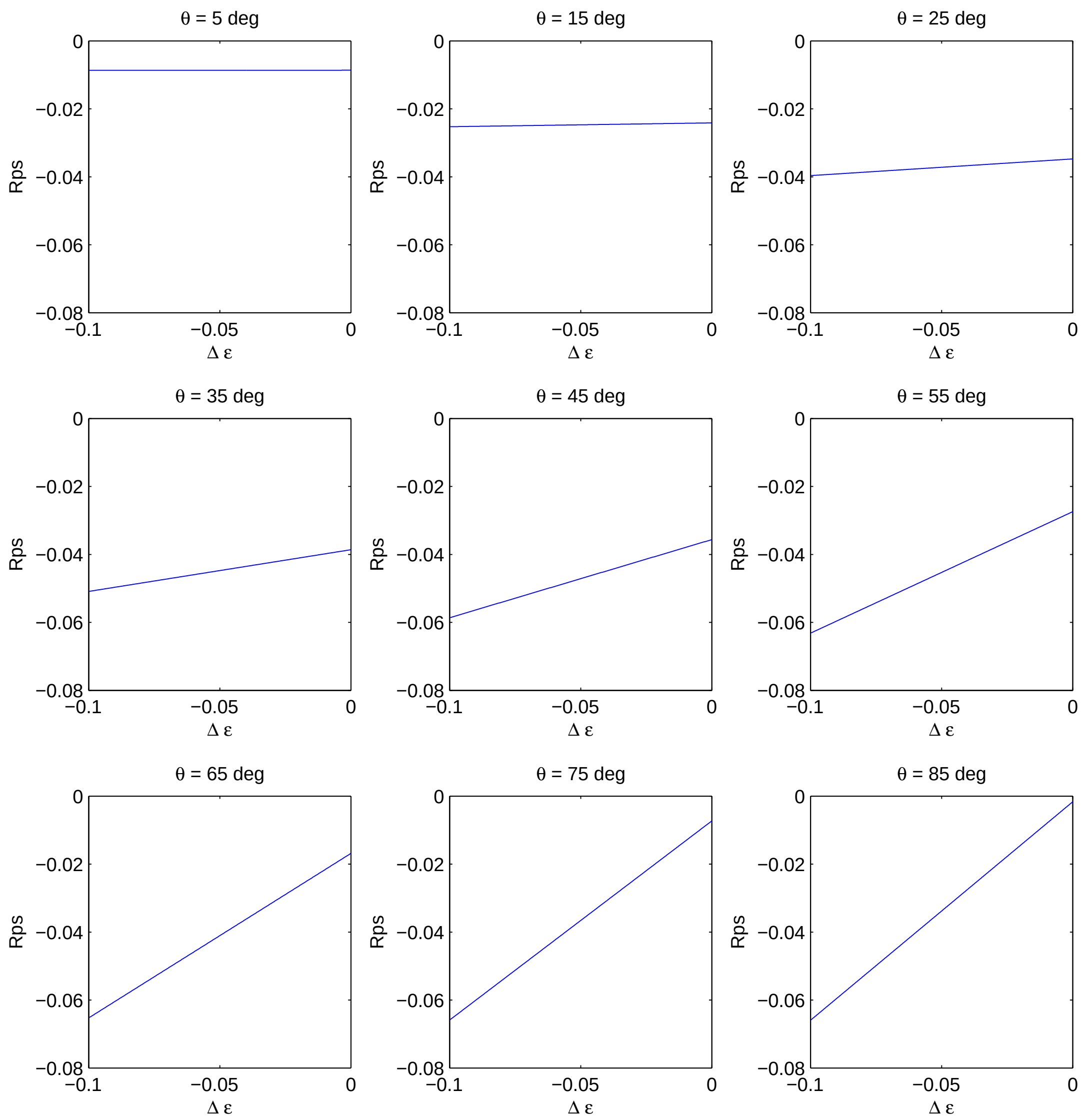

Figure 4.10. $R_{\grave{P}\acute{S}}$ coefficient in VTI media as a function of negative contrasts in the Thomsen parameter ϵ and no contrast in the Thomsen parameter δ ($\Delta\delta = 0$) across the interface. Same model and display as in Figure 4.7.

4.2.1 HTI Model for the Main Gas Reservoir

The UMV Shale Formation has been modeled as a VTI medium in Chapter 3 and the Thomsen parameters have been estimated (see Figure 3.9). The main gas reservoir has been studied by Vasconcelos & Grechka (2007) and modeled as an orthorhombic medium characterized by two sets of orthogonal fractures embedded in an isotropic background. This point was discussed in section 3.5. For such a model, Vasconcelos & Grechka (2007) inverted for the set of Thomsen-style parameters in both vertical symmetry planes. The Thomsen-style parameters for orthorhombic media were already introduced in Section 3.5. The seven Thomsen-style parameters $\epsilon^{(1)}$, $\delta^{(1)}$, $\gamma^{(1)}$, $\epsilon^{(2)}$, $\delta^{(2)}$, $\gamma^{(2)}$, and $\delta^{(3)}$ fully characterize anisotropy in orthorhombic media (Tsvankin, 1997a). The computation was done first by estimating P-, S_{11}-, and S_{22}-wave velocities and the NMO ellipses for the top and the bottom of the main gas reservoir over the entire survey, and then by computing the interval ellipses with the Dix-type differentiation (Grechka & Tsvankin, 1999; Grechka et al., 1999a).

From Figures 4.11 and 4.12 it is clear that the anisotropy parameters $\epsilon^{(1)}$ and $\delta^{(1)}$, corresponding to one of the two vertical symmetry planes, are close to zero near the study well location (in the lower right corner of the survey). Therefore, in the vicinity of the study well location, we will make the assumption that $\epsilon^{(1)} \approx \delta^{(1)} \approx 0$. Thus, near the study well location, the main gas reservoir can be modeled locally as an HTI medium. The kinematics and dynamics of $\grave{\text{P}}\acute{\text{S}}$-waves in this HTI medium will be governed by the six parameters V_{p0}, V_{s0}, ρ, $\epsilon^{(2)}$, $\delta^{(2)}$, and $\gamma^{(2)}$. The anisotropy parameters $\epsilon^{(2)}$ and $\delta^{(2)}$ are shown respectively in Figures 4.11 and 4.12.

It is important to note that the anisotropy parameters given by Vasconcelos & Grechka (2007) for the Rulison reservoir are not accurate. This is due to the fact that after ground roll suppression and shear-wave rotation, Vasconcelos & Grechka (2007) sorted the data back to CMP geometry creating 9 $\times$ 9 (135 m $\times$ 135 m) superbins and extracted the NMO ellipses over the survey area. Xu & Tsvankin (2007) showed that the 9 $\times$ 9 super-binning was suboptimal and that the optimal super-binning

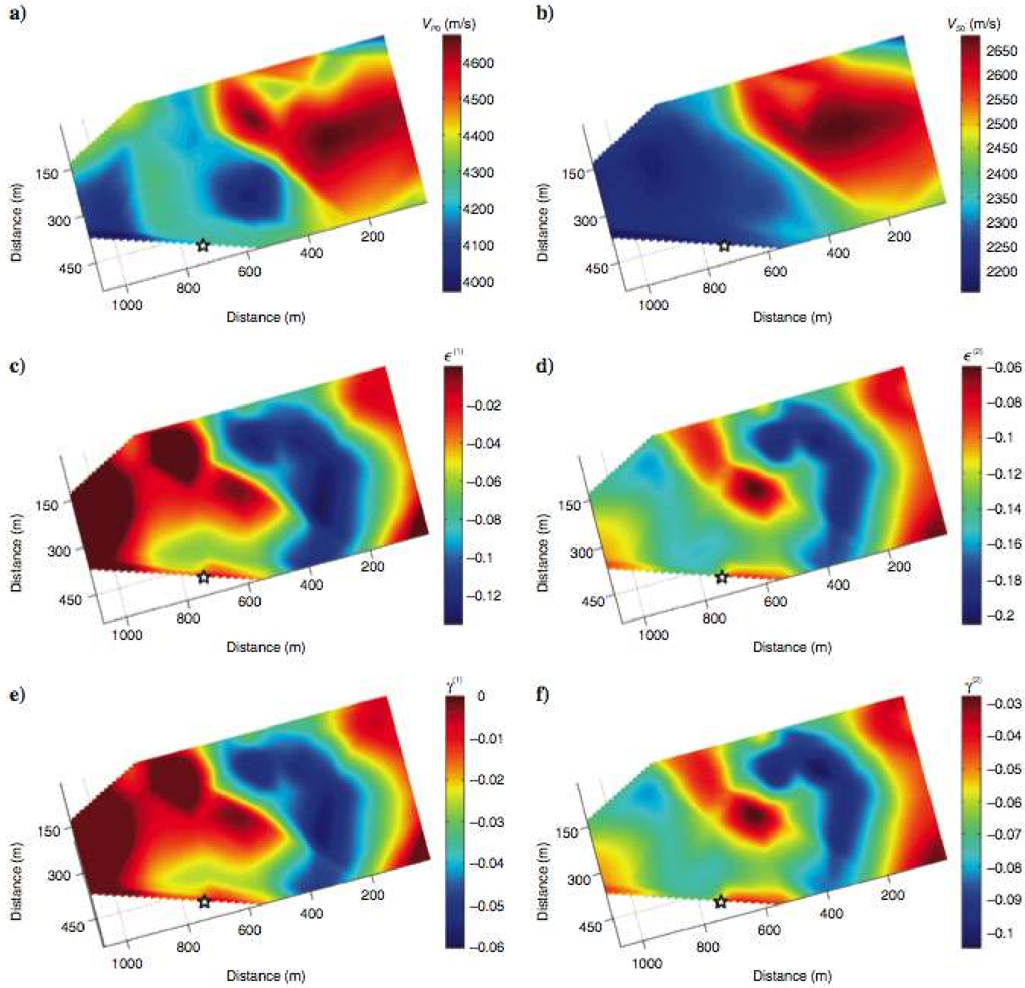

Figure 4.11. Vertical velocities V_{p0} (a), V_{s0} (b) and the anisotropy coefficient $\epsilon^{(1)}$ (c), $\epsilon^{(2)}$ (d), $\gamma^{(1)}$ (e), and $\gamma^{(2)}$ (f) at the main gas reservoir level. The inversion used exclusively surface reflection data. This was done by assuming crack-induced orthotropy based on a model with two sets of orthogonal fractures embedded in an isotropic background. Adopted from Vasconcelos & Grechka (2007).

was 5 × 5. Nevertheless, although the results from Vasconcelos & Grechka (2007) are not optimal, they can still be used for the anisotropic AVO modeling: as long as the incidence angle is less than 35°, small inaccuracies in $\Delta\delta$ and $\Delta\epsilon$ will have insignificant influence on the reflection coefficients.

Therefore, the simplified dynamic model for the upper part of the main gas reservoir will consist of a VTI medium (the UMV Shale) over an HTI medium (the upper part of the main gas reservoir). This model remains valid for any shale-sand

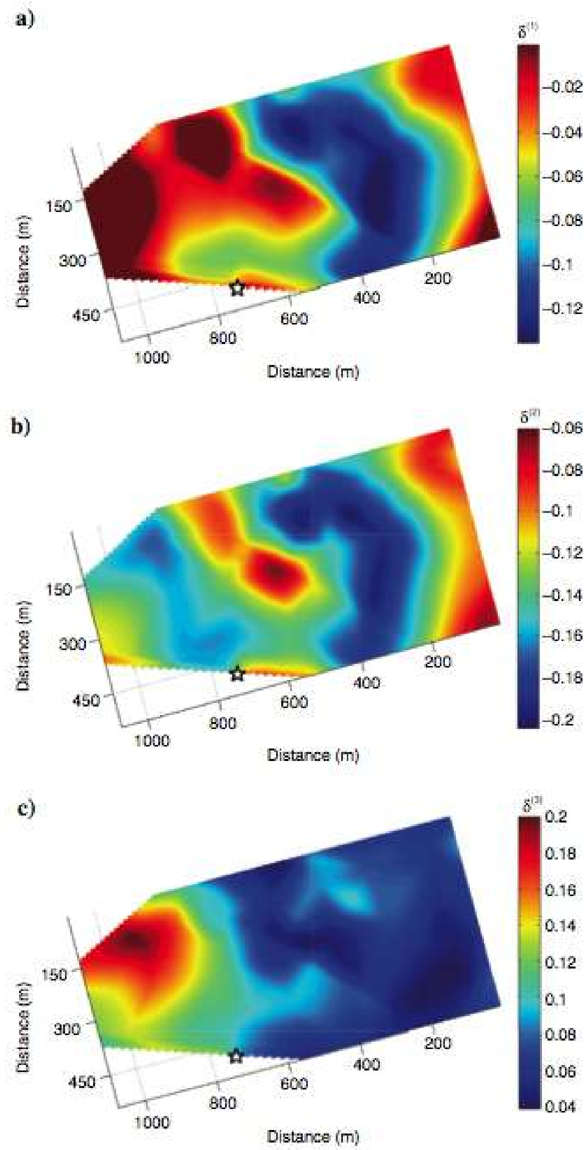

Figure 4.12. The anisotropy parameters $\delta^{(1)}$ (a), $\delta^{(2)}$ (b), and $\delta^{(3)}$ (c) at Rulison reservoir. Adopted from Vasconcelos & Grechka (2007).

interface in the gas-saturated section. The model that we studied in the previous section was a VTI-over-VTI model. In order for our Rulison model to be similar to a VTI-over-VTI model, one more processing step is thus required: the transformation of the HTI medium into its equivalent VTI medium. This equivalence is only valid in the symmetry-axis plane.

4.2.2 Thomsen Anisotropy Parameters for Rulison HTI Gas Reservoir

The general azimuthally dependent $\grave{\text{P}}\acute{\text{P}}$- and $\grave{\text{P}}\acute{\text{S}}$-wave reflection coefficients for HTI media have been derived by Rüger (1997), Jílek (2002a; 2002b), Shaw & Sen (2004), and Qiankin et al. (2008). But in our case we would like to use the results for VTI media that we already analyzed. As suggested by Tsvankin (1997b), Rüger (2001), and Jílek (2002b), for any HTI medium there is an equivalent VTI medium that has the same kinematic properties and polarizations for P- and P-SV-waves in the symmetry-axis plane. Therefore, the P- and P-SV-wave propagation in the symmetry plane of an HTI medium can be described by the known VTI equations using the modified Thomsen parameters $\epsilon^{(V)}$ and $\delta^{(V)}$ defined with respect to vertical as in a regular VTI medium:

$$\epsilon^{(V)} = \frac{c_{11} - c_{33}}{2\, c_{33}}, \tag{4.12}$$

$$\delta^{(V)} = \frac{(c_{11} + c_{55})^2 - (c_{33} - c_{55})^2}{2\, c_{33}(c_{33} - c_{55})}. \tag{4.13}$$

The parameters $\epsilon^{(V)}$ and $\delta^{(V)}$ of the equivalent VTI medium are different from the generic coefficients ϵ and δ for HTI media (denoted as $\epsilon^{(2)}$ and $\delta^{(2)}$ in our model) defined with respect to the HTI horizontal symmetry-axis. The VTI and HTI anisotropy parameters are related in the following way:

$$\epsilon^{(V)} = -\frac{\epsilon}{1 + 2\,\epsilon}, \tag{4.14}$$

$$\delta^{(V)} = \frac{\delta - 2\,\epsilon\,(1 + \frac{\epsilon}{f})}{(1 + 2\,\epsilon)(1 + \frac{\epsilon}{f})}, \tag{4.15}$$

where

$$f = 1 - (V_{s0}/V_{p0})^2. \tag{4.16}$$

Thanks to the newly introduced parameters $\epsilon^{(V)}$ and $\delta^{(V)}$ that are now defined with respect to the vertical axis, all the kinematics and dynamics of $\grave{\mathrm{P}}\acute{\mathrm{P}}$- and $\grave{\mathrm{P}}\acute{\mathrm{S}}$-waves in the symmetry-axis plane of an HTI medium can now be described using the already known VTI equations (Rüger, 2001). Therefore, an HTI medium with the generic Thomsen parameters ϵ and δ is kinematically and dynamically equivalent to a VTI medium with the anisotropy parameters $\epsilon^{(V)}$ and $\delta^{(V)}$ defined in equations (4.14) and (4.15). This equivalence holds for reflection coefficients but nor for geometrical spreading.

For completeness, it should be mentioned that azimuthally dependent $\grave{\mathrm{P}}\acute{\mathrm{S}}$-wave kinematics and dynamics will depend on an extra parameter $\gamma^{(V)}$ (Al-Dajani et al., 1996; Tsvankin, 1997b; Rüger, 1997; Al-Dajani & Tsvankin, 1998a; Jílek, 2001; Qiankin et al., 2008) defined as:

$$\gamma^{(V)} = \frac{c_{55} - c_{44}}{2\, c_{44}} = -\frac{\gamma}{1 + 2\,\gamma}, \tag{4.17}$$

where $\gamma^{(V)}$ is the shear-wave splitting parameter denoting the traveltime difference between fast and slow shear-wave velocities, and γ is the generic Thomsen (1986) anisotropy coefficient for VTI media. In the symmetry-axis plane, there is no dependence on $\gamma^{(V)}$, and the $\grave{\mathrm{P}}\acute{\mathrm{S}}$-wave reflection coefficient only depends on $\epsilon^{(V)}$ and $\delta^{(V)}$ just like in the VTI case.

4.2.3 AVO Modeling for the VTI-over-HTI Model

$\grave{\mathrm{P}}\acute{\mathrm{P}}$- and $\grave{\mathrm{P}}\acute{\mathrm{S}}$-wave reflection coefficients in the HTI symmetry-axis plane

From Figures 4.11 and 4.12, we extracted the values of the Thomsen parameters in the symmetry-axis plane $\epsilon^{(2)} \approx -0.09$ and $\delta^{(2)} \approx -0.09$ for the HTI approximative

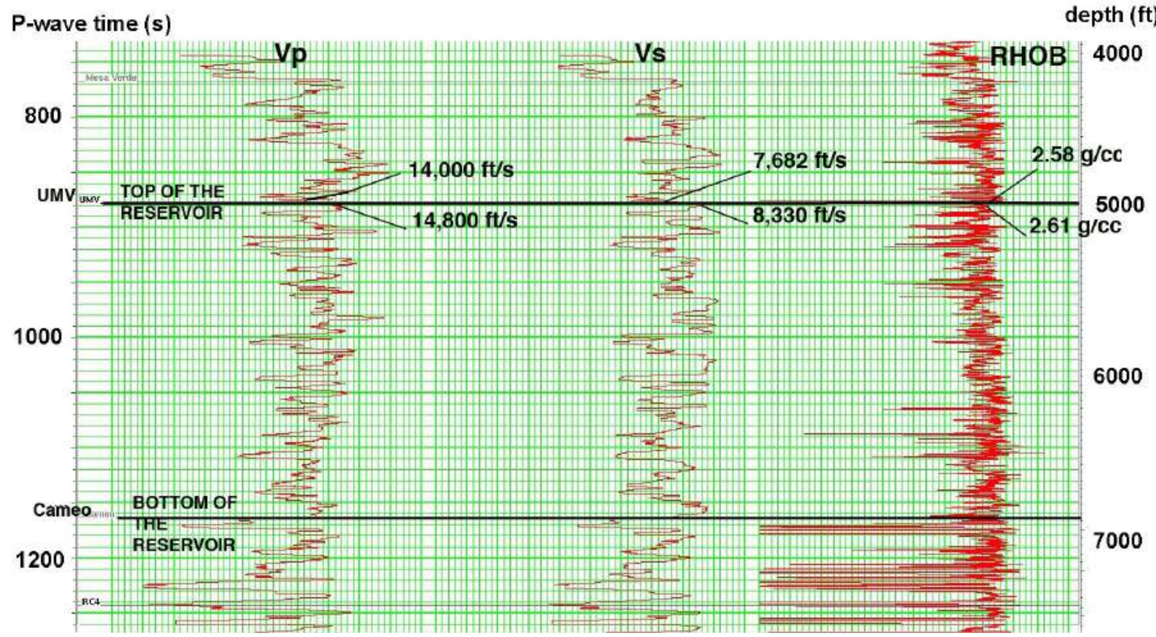

Figure 4.13. Sonic and density logs at the study well RWF 332-21. The vertical velocities V_{p0} and V_{s0} for the UMV Shale Formation were found from the sonic logs to be respectively equal to 14,000 ft/s and 7,682 ft/s. V_{p0} and V_{s0} for the upper part of the main gas reservoir were found from the sonic logs to be respectively equal to 14,800 ft/s and 8,830 ft/s. The density values were found from the RHOB log to be respectively equal respectively to 2.58 g/cc (in the UMV Shale) and 2.61 g/cc (in the reservoir). The top and bottom of the main gas reservoir are marked by black lines.

model in the vicinity of the study well (in the lower right corner of the survey). The VTI equivalent anisotropy parameters $\epsilon^{(V)}$ and $\delta^{(V)}$ are computed from equations (4.14) and (4.15). We obtained $\epsilon^{(V)} \approx 0.11$ and $\delta^{(V)} \approx 0.11$. The VTI equivalent medium is thus elliptical. This is usually the case in sandstone formations.

On the other hand, for the UMV Shale layer, the VTI Thomsen parameters were inverted for in Chapter 3 and the results were shown in Figure 3.9. In the vicinity of the study well, we had $\epsilon \approx 0.07$ and $\delta \approx -0.11$.

Finally, the vertical velocities V_{p0} and V_{s0} and the densities for the upper VTI halfspace (corresponding to the UMV Shale) and the lower HTI lowerspace (corresponding to the upper part of the main gas reservoir) were derived from log data at the study well location (Figure 4.13). All the elastic parameters for the VTI-over-HTI model (denoted by VTI/HTI) are shown in Table 4.2.

	P-velocity (ft/s)	S-velocity (ft/s)	Density (g/cc)	δ	ϵ
VTI	14,000	7,680	2.58	-0.11	0.07
	P-velocity (ft/s)	S-velocity (ft/s)	Density (g/cc)	$\delta^{(V)}$	$\epsilon^{(V)}$
HTI	14,800	8,330	2.61	0.11	0.11

Table 4.2. Elastic parameters for the HTI symmetry-axis plane of the two-layer VTI-over-HTI model for Rulison. The P-wave and P-SV-wave propagation in the symmetry-axis plane is characterized by two sets of 5 parameters each: $\rho^{(i)}$, $V_p^{(i)}$, $V_s^{(i)}$, $\epsilon^{(i)}$, and $\delta^{(i)}$, with $i \in \{1, 2\}$.

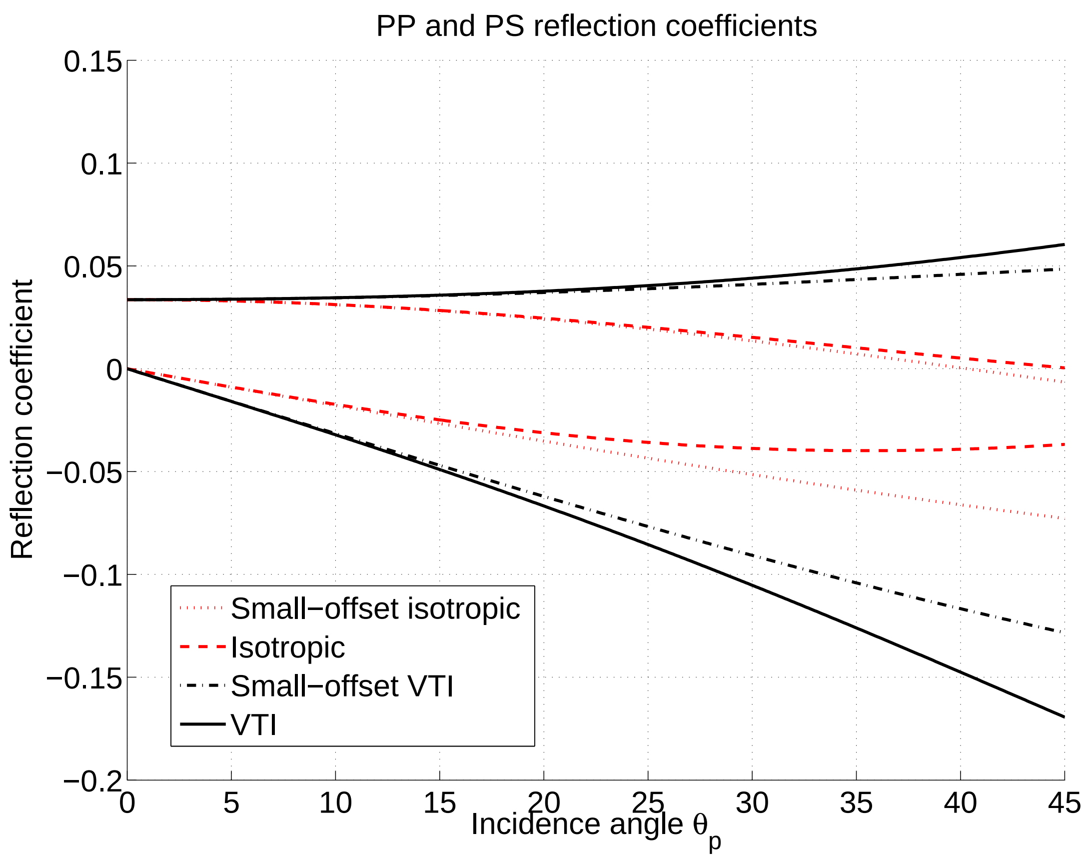

Figure 4.14. $\grave{\text{P}}\acute{\text{P}}$- and $\grave{\text{P}}\acute{\text{S}}_2$-wave reflection coefficients in the symmetry-axis plane of the Rulison VTI-over-HTI model and in isotropic media, and their small-offset approximations. The reflection coefficients related to the first model, which consists of an upper and lower isotropic halfspaces separated by a flat horizontal interface, are represented in red; the reflection coefficients of the second model, which consists of an upper VTI and lower HTI halfspaces separated by the same flat horizontal interface, are represented in black. The elastic parameters are given by Table 4.2. The $R_{\grave{P}\acute{P}}$ coefficients have positive values, while the $R_{\grave{P}\acute{S}}$ coefficients have negative values.

Based on the elastic parameters given in Table 4.2, the $R_{\grave{P}\acute{P}}$ and $R_{\grave{P}\acute{S}}$ coefficients in isotropic and VTI/HTI media and their small-offset approximations are plotted on Figure 4.14. For P-waves, the small-offset approximation is based on $\sin^4 \theta_p \approx 0$. The vertical-incidence reflection coefficient is equal to 0.38 (Figure 4.14). For P̀Ṕ-wave reflectivity, the small-offset approximation is valid up to an incidence angle of 40° in the isotropic model and up to an incidence angle of 30° in the VTI/HTI model. For the upper part of the main gas reservoir located at 6,000 ft of depth, this corresponds to more than 10,000 ft of offset in the isotropic model, and roughly 7,000 ft of offset in the VTI/HTI model. Therefore, for the upper part of the main gas reservoir and up to 7,000 ft of offset, the small-offset approximation for P̀Ṕ-wave reflectivity is always valid. Furthermore, the isotropic P̀Ṕ-wave reflectivity is a good approximation of the P̀Ṕ-wave reflectivity in the VTI/HTI model up to an incidence angle of 10°, or roughly 2,100 ft of offset for the top of the reservoir. Above 2,100 ft of offset, an amplitude correction should be done if we want to use an inversion software based on isotropic vertical-incidence impedance-based inversion. For the upper part of the main gas reservoir at Rulison and for large offsets (≈ 6,500 ft) the relative difference between the vertical-incidence P-wave reflection coefficient (0.38) and the reflection coefficient in the VTI/HTI model (0.43) is around 10%. Therefore, the largest offsets should have a slight amplitude correction before stacking.

For P̀Ś-wave reflectivity, the small-offset approximation is valid in the VTI/HTI case even for very long offsets (≈ 10,000 ft). The small-offset approximation is valid in the isotropic model up to an incidence angle of 30° or roughly 5,000 ft of offset for the upper part of the main gas reservoir. Therefore, one can always approximate the P̀Ś-wave reflectivity in Rulison by its small-offset approximation. The isotropic $R_{\grave{P}\acute{S}}$ coefficient is different from that for the VTI/HTI model for all offsets. But on the other hand, the small-offset approximations in both models are linear functions, and the ratio of the slopes of these two coefficients is close to 1/2 (Figure 4.14). Therefore, in order to use the small-offset isotropic inversion algorithm presented by Valenciano & Michelena (2000) (equation (4.11), the amplitudes of all P̀Ś$_2$-wave traces should be scale by a factor of 1/2. This scaling factor is added to all other scaling factors needed to perform the inversion [for more details, see Section 5.1].

The conclusions about the relative influence of $\Delta\epsilon$ and $\Delta\delta$ are similar to those derived for the model in the previous section. This was predictable since the contrast in the elastic parameters across the interface are similar for both cases except that for the Rulison model the contrast in the anisotropy parameter δ (although positive as well) is significantly more important. The contrasts in both δ and ϵ increase the P-wave reflectivity (Figure 4.15). The contribution of δ becomes substantial for midrange offsets (for incidence angles larger than 10°, or roughly 2,100 ft of offset for the top of the main gas reservoir), while the contribution of ϵ is noticeable only for very large offsets (for incidence angles larger than 40°).

For $\grave{\mathrm{P}}\acute{\mathrm{S}}$-waves, the contrast in δ has a substantial contribution on reflectivity in VTI/HTI media for all offsets. The influence of ϵ becomes noticeable for incidence angles larger than 25°. The contrast in δ has an important influence on the converted-wave reflectivity for all offsets. Above an incidence angle of 25°, the influence of ϵ is noticeable, and the $\grave{\mathrm{P}}\acute{\mathrm{S}}$-wave reflectivity in VTI/HTI media tends to be lower than the $\grave{\mathrm{P}}\acute{\mathrm{S}}$-wave reflectivity in VTI/HTI media with no contrast in the Thomsen parameter ϵ. The relative dependence of the $\grave{\mathrm{P}}\acute{\mathrm{S}}$-wave reflection coefficient on $\Delta\epsilon$ and $\Delta\delta$ for increasing incidence angles is similar to that presented in the previous section (for positive contrasts in ϵ and δ at the interface).

$\grave{\mathbf{P}}\acute{\mathbf{P}}$- and $\grave{\mathbf{P}}\acute{\mathbf{S}}$-wave reflection coefficients in the HTI isotropy plane

In the HTI isotropy plane, the Thomsen anisotropy parameters are equal to zero. The elastic parameters for this VTI-over-HTI model are shown in Table 4.3. The results are similar to those obtained in the symmetry-axis plane. The only difference is that the slopes of the $\grave{\mathrm{P}}\acute{\mathrm{S}}$-wave reflection coefficient small-offset approximations in isotropic and VTI/HTI media have a ratio of 5/7. Therefore, in order to use the small-offset isotropic inversion algorithm presented by Valenciano & Michelena (2000) (equation (4.11), the amplitudes of all $\grave{\mathrm{P}}\acute{\mathrm{S}}_1$-wave traces should be scale by a factor of

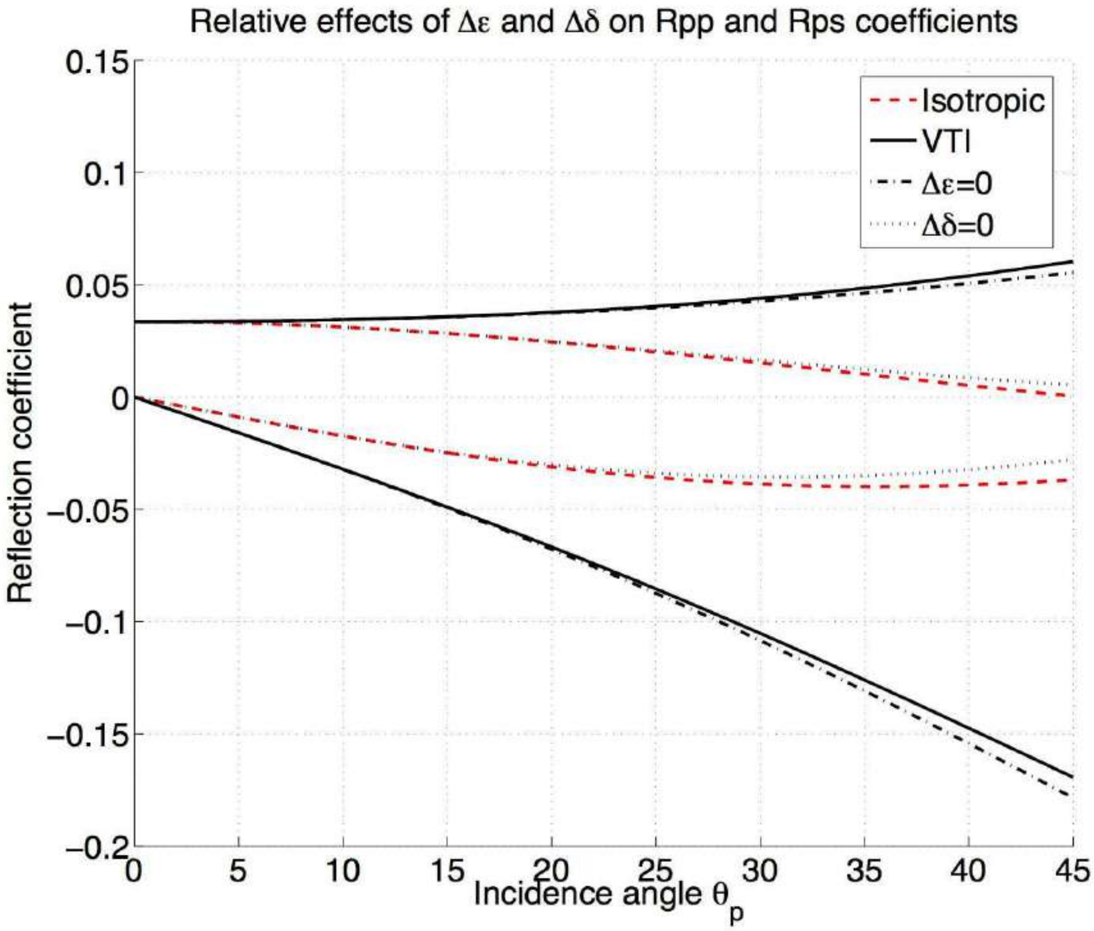

Figure 4.15. Relative effects of $\Delta\delta$ and $\Delta\epsilon$ on the $R_{\grave{P}\acute{P}}$ and $R_{\grave{P}\acute{S}2}$ coefficients at the top of the main gas reservoir in Rulison. The models used to plot these curves are based on a two-halfspace medium with the elastic parameters given by Table 4.2. The P̀Ṕ- and P̀Ś- reflectivities in isotropic media are plotted in red, and the reflectivities in Rulison VTI-over-HTI media are plotted in black. The reflectivities in VTI media with no contrast in the Thomsen parameter ϵ are plotted as dash-dot curves, while the reflectivities in VTI media with no contrast in the Thomsen parameter δ are plotted as dot curves. On these plots, the $R_{\grave{P}\acute{P}}$ coefficients have positive values, while the $R_{\grave{P}\acute{S}2}$ coefficients have negative values.

	P-velocity (ft/s)	S-velocity (ft/s)	Density (g/cc)	δ	ϵ
VTI	14,000	7,680	2.58	-0.11	0.07
	P-velocity (ft/s)	S-velocity (ft/s)	Density (g/cc)	δ	ϵ
HTI	14,800	8,330	2.61	0	0

Table 4.3. Elastic parameters for the HTI isotropy plane of the two-layer VTI-over-HTI model for Rulison.

5/7. This scaling factor is added to all other scaling factors needed to perform the inversion.

For $\grave{P}\acute{P}$- and $\grave{P}\acute{S}$-wave reflectivity, the small-offset approximation is valid in the VTI/HTI case even for incident angles as large as 35° (see Figure 4.16). Therefore, one can always approximate $\grave{P}\acute{P}$- and $\grave{P}\acute{S}$-wave reflectivities in Rulison by their small-offset approximations. For $\grave{P}\acute{P}$- and $\grave{P}\acute{S}$-waves, the VTI parameter δ has a substantial contribution on reflectivity in the HTI isotropy plane of VTI/HTI media for all offsets, while the VTI parameter ϵ has a very small contribution even for large incident angles (see Figure 4.17).

4.2.4 Non-converted Shear-wave AVO Modeling

Following the work of Rüger (1996; 1997; 2001), the linearized SV-wave reflection coefficient at a horizontal interface between two VTI media has the following form:

$$R_{SV}^{VTI} = -\frac{1}{2}\frac{\Delta Z^S}{\overline{Z^S}} + \left(\frac{7}{2}\frac{\Delta V_s}{\overline{V_s}} + 2\frac{\Delta\rho}{\overline{\rho}} + \frac{1}{2}\frac{\Delta V_p}{\overline{V_s}}\left(\Delta\epsilon - \Delta\delta\right)\right)\sin^2\theta_s - \frac{1}{2}\frac{\Delta V_s}{\overline{V_s}}\sin^2\theta_s\tan^2\theta_s, \tag{4.18}$$

where Z^S is the shear impedance, ΔZ^S the contrast in shear impedances across the interface, and $\overline{Z^S}$ the arithmetic mean of shear impedances in the two halfspaces.

Based on the Rulison Field elastic parameters for the upper main gas reservoir given in Tables 4.2 and 4.3, the SV-wave reflection coefficients in isotropic and VTI/HTI media have been modeled in both the isotropy plane and the symmetry-axis

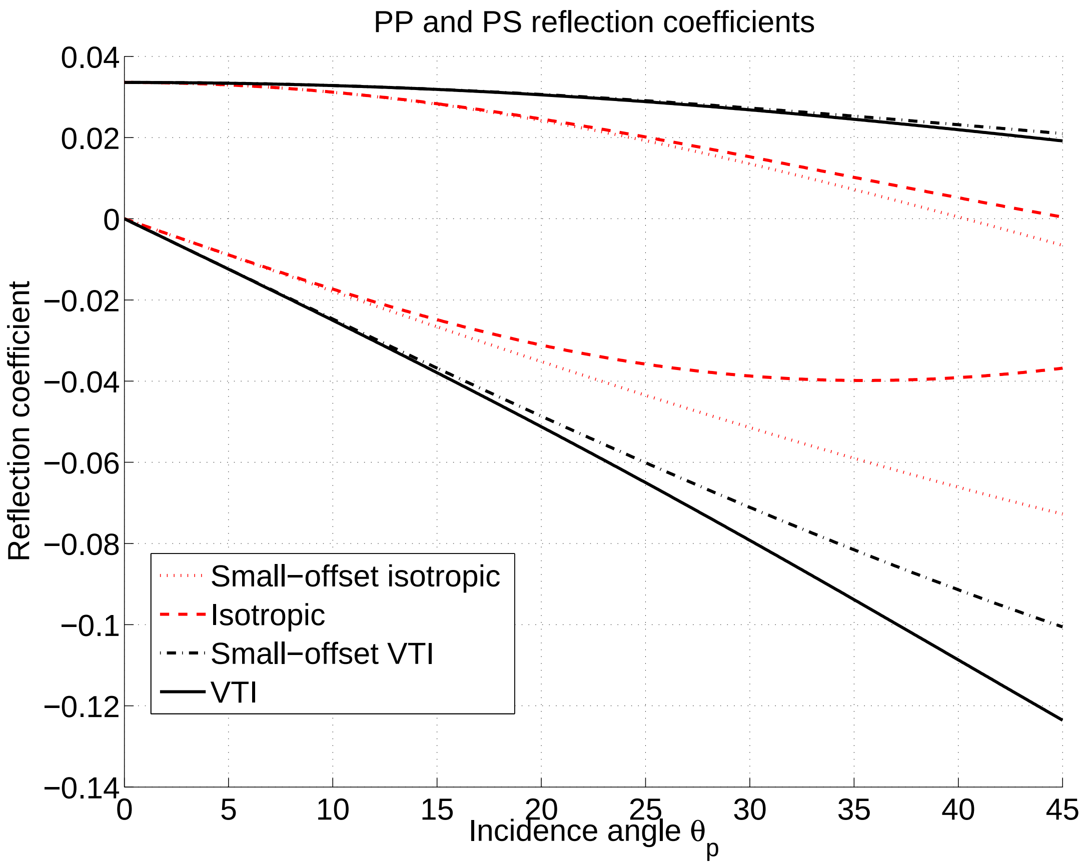

Figure 4.16. $\grave{\mathrm{P}}\acute{\mathrm{P}}$-wave and $\grave{\mathrm{P}}\acute{\mathrm{S}}_1$-wave reflection coefficients in the isotropy plane of the Rulison VTI-over-HTI model and in isotropic media, and their small-offset approximations. Same display as in Figure 4.14.

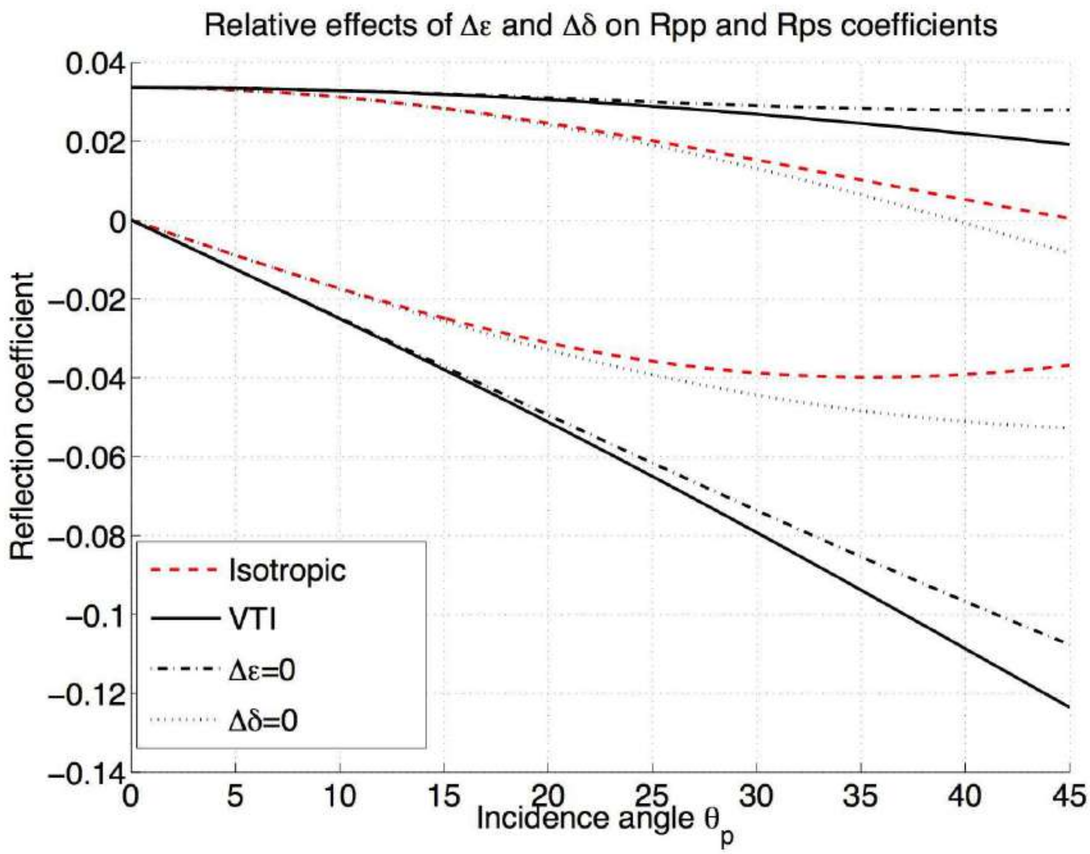

Figure 4.17. Relative effects of $\Delta\delta$ and $\Delta\epsilon$ on the $R_{\grave{P}\acute{P}}$ and $R_{\grave{P}\acute{S}1}$ coefficients in the HTI isotropy plane. The models used to plot these curves are based on a two-halfspace medium with the elastic parameters given by Table 4.3. Same display as in Figure 4.15.

plane. The SV-wave reflection coefficient in isotropic media is plotted as a dashed curve on both panels of Figure 4.18 and the SV-wave reflection coefficients in both the isotropy and the symmetry-axis planes of VTI/HTI media are plotted as solid curves on Figure 4.18. The isotropic model shows that the SV-wave reflection coefficient increases with higher incidence angles starting with negative values and reaching positive values for larger incidence angles. The change in polarity occurs at an incidence angle close to 20°. The anisotropic model shows a constant reflection coefficient for offsets up to 40° in both the HTI isotropy and symmetry-axis planes.

The AVO response of the VSP prestack Kirchhoff depth migrated image gathers (Mazumdar, 2009) has been studied. The obliquity factor correction was applied, and the anisotropic geometrical spreading was ignored since the ray trajectories from the source to the shallowest and deepest receivers are not very different. A VSP prestack Kirchhoff depth migrated image gather for a maximum offset of 4,600 ft (which corresponds to an incidence angle of 40° in the VSP geometry (Mazumdar, 2009)) in both the HTI isotropy and symmetry-axis planes is shown in Figure 4.19. The VSP AVO response shows constant amplitudes for all offsets as predicted by the VTI/HTI model. This confirms the validity of the VTI/HTI model and the accuracy of the estimated Thomsen parameters.

Finally, a sensitivity test was conducted in order to study the effects of the variation in the Thomsen parameters of the upper VTI medium on the AVO response in the HTI symmetry-axis plane of the VTI/HTI model. δ was first set to -0.05 (left panel on Figure 4.20) and ϵ was kept unchanged, and then ϵ was set to 0.15 (right panel on Figure 4.20) and δ was kept unchanged. In both cases, the AVO response changed with increasing incidence angles.

In conclusion, the VTI/HTI model is an accurate dynamic model for sand/shale interfaces in the Rulison main gas reservoir, and the estimated Thomsen parameters for the UMV Shale are accurate since the AVO response matched perfectly with the modeling results.

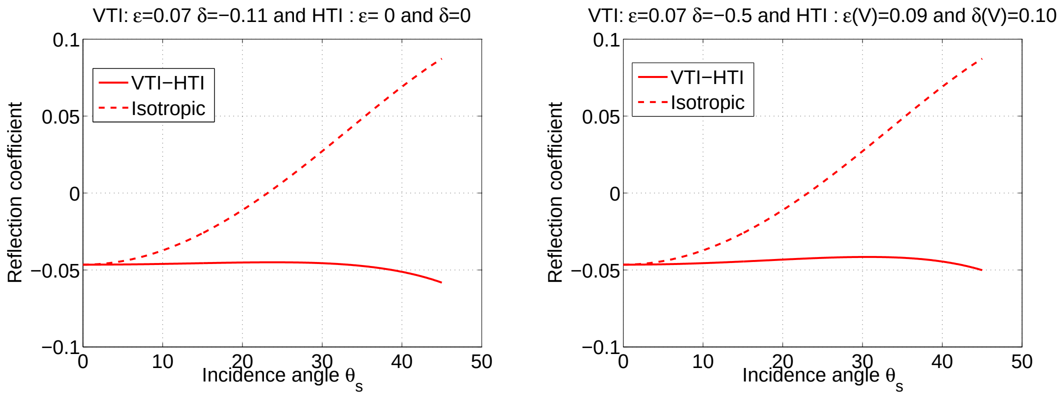

Figure 4.18. SV-wave reflection coefficients in isotropic media (dashed curves) and in VTI/HTI media (solid curves) based on the elastic parameters given in Tables 4.2 and 4.3 in both the HTI isotropy plane (left panel) and symmetry-axis plane (right panel).

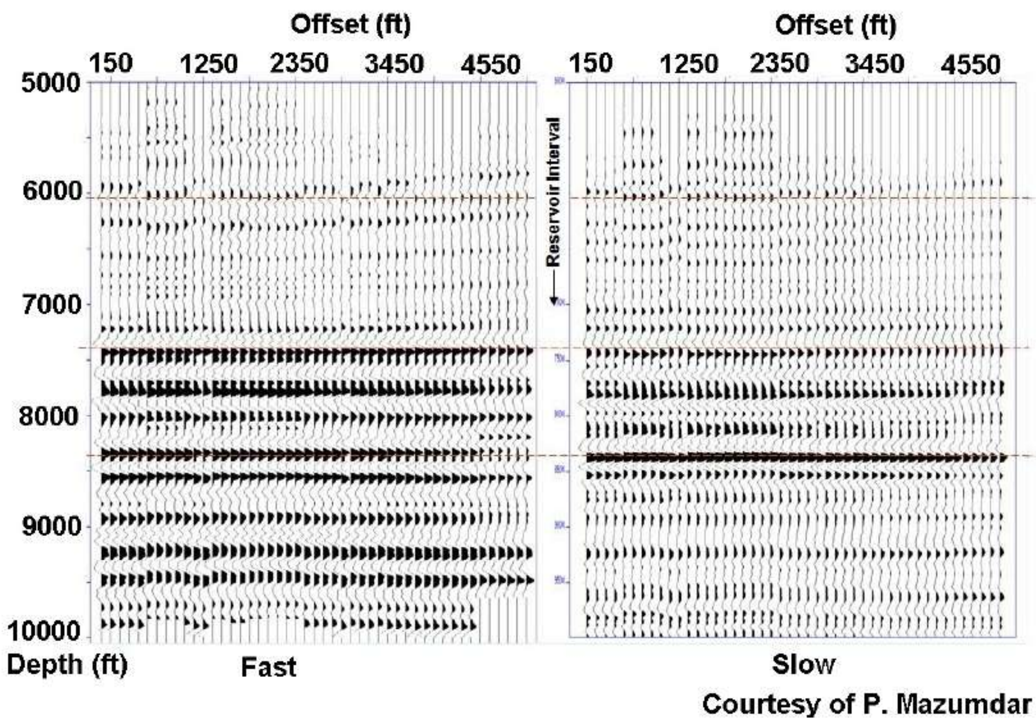

Figure 4.19. VSP prestack Kirchhoff depth migrated common image gather in both the HTI isotropy plane (left panel) and symmetry-axis plane (right panel). Adapted from Mazumdar (2009).

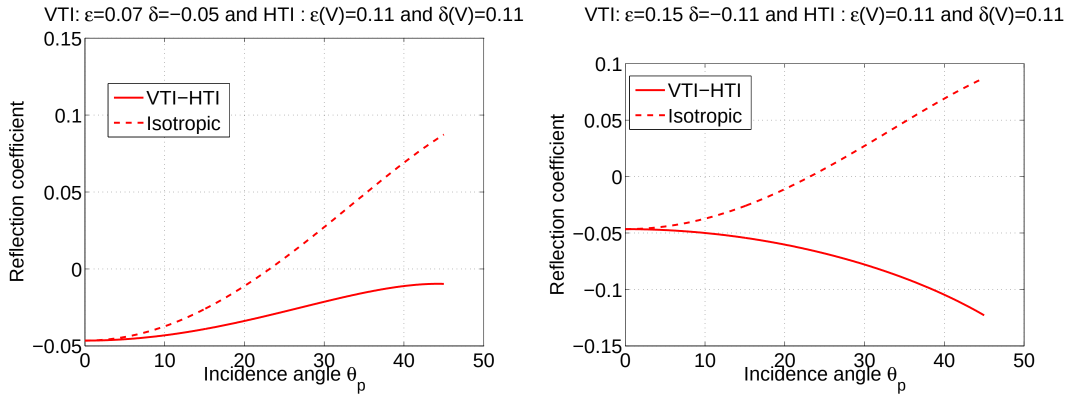

Figure 4.20. Sensitivity test in order to study the effects of the variation in the Thomsen parameters of the upper VTI medium on the AVO response in the HTI symmetry-axis plane of the VTI/HTI model. δ was first set to -0.05 (left panel) and ϵ was kept unchanged and then ϵ was set to 0.15 (right panel on Figure) and δ was kept unchanged.

4.2.5 Conclusion

In conclusion, the $R_{\grave{P}\acute{P}}$ coefficient in the symmetry-axis plane in the upper part of the main gas reservoir has a small dependence on anisotropy up to 7,000 ft of offset. The maximum amplitude variation with offset in the isotropic model is close to 10% for offsets as large as 6,500 ft. Therefore, the effect of anisotropy on the P-wave reflectivity will be ignored, and the P-wave inversion will be performed as if the medium was isotropic. On the other hand, for small offsets, the $R_{\grave{P}\acute{S}}$ coefficient is only dependent on the Thomsen parameter δ and is independent of the Thomsen parameter ϵ. For larger offsets, and up to 5,000 ft of offset, the contribution of ϵ is very small compared to the contribution of δ. This is good news, since the inversion for ϵ was subject to more errors than the inversion for δ [see Chapter 3]. The inversion for δ in VTI media requires just the vertical and NMO P-wave velocities, while the inversion for ϵ requires the P-wave and S-wave vertical and NMO velocities. Furthermore, the inaccuracies as well as the small aerial extent related to the estimation of ϵ in Chapter 3 will practically have no influence on the amplitude response of $\grave{P}\acute{S}$-waves function of offset. In order to handle the variation of the $\grave{P}\acute{S}$-wave amplitude response due to the anisotropy parameter δ, a simple scaling by a factor of 1/2 for $\grave{P}\acute{S}_2$-waves and 5/7 for $\grave{\text{P}}\acute{\text{S}}_1$-waves is sufficient. Henceforth, after the scaling, the $\grave{\text{P}}\acute{\text{S}}$-wave amplitudes and impedance inversion will be dealt with as if the medium was isotropic.

Chapter 5

IMPEDANCE INVERSION OF MULTICOMPONENT POSTSTACK SEISMIC DATA

5.1 Small-offset Approximation of Reflection Coefficients in Isotropic Media

Chapter 4 discusses linearized reflection coefficients in TI media. This chapter focuses on the small-angle elastic AVO response in isotropic media and its applications for impedance inversion.

5.1.1 Small-offset Approximation of Pure-mode Reflection Coefficients in Isotropic Media

As stated in Chapter 4, the linearized $\grave{\mathrm{P}}\acute{\mathrm{P}}$-wave reflection coefficient in VTI media has the following form:

$$R_{\grave{P}\acute{P}} = R_{\grave{P}\acute{P}}(0) + G_{\grave{P}\acute{P}} \sin^2 \theta_p + C_{\grave{P}\acute{P}} \sin^4 \theta_p, \tag{5.1}$$

where $G_{\grave{P}\acute{S}}$ and $C_{\grave{P}\acute{S}}$ are the AVO gradient and the curvature terms, respectively:

$$R_{\grave{P}\acute{P}}(0) = \frac{\Delta\rho}{2\,\overline{\rho}} + \frac{\Delta V_p}{2\,\overline{V_p}}, \tag{5.2}$$

$$G_{\grave{P}\acute{P}} = \frac{-2}{\kappa_0^2}\frac{\Delta\rho}{\overline{\rho}} + \frac{\Delta V_p}{2\,\overline{V_p}} - \frac{4}{\kappa_0^2}\frac{\Delta V_s}{\overline{V_s}} + \frac{\Delta\delta}{2}, \tag{5.3}$$

$$C_{\grave{P}\acute{P}} = \frac{\Delta V_p}{2\,\overline{V_p}} + \frac{\Delta\epsilon}{2}. \tag{5.4}$$

In isotropic media, δ and ϵ are equal to zero and, therefore, $\Delta\delta$ and $\Delta\epsilon$ are also equal to zero.

At small incidence angles,

$$R_{\grave{P}\acute{P}} \approx R_{\grave{P}\acute{P}}(0) = \frac{\Delta\rho}{2\,\overline{\rho}} + \frac{\Delta V_p}{2\,\overline{V_p}}. \tag{5.5}$$

The above equation is the well-known normal-incidence reflection coefficient for P-waves. This expression can also be written as:

$$R_{\grave{P}\acute{P}} \approx \frac{1}{2}\frac{Z_{p2} - Z_{p1}}{Z_{p2} + Z_{p1}}, \tag{5.6}$$

where $Z_{p1} = \rho_1 V_{p1}$ is the acoustic impedance in the upper halfspace, and $Z_{p2} = \rho_2 V_{p2}$ is the acoustic impedance in the lower halfspace.

Similarly, the normal-incidence S-wave reflection coefficient can be written as:

$$R_{\grave{S}\acute{S}} \approx -\frac{1}{2}\frac{Z_{s2} - Z_{s1}}{Z_{s2} + Z_{s1}}, \tag{5.7}$$

where $Z_{s1} = \rho_1 V_{s1}$ is the shear impedance in the upper halfspace, and $Z_{s2} = \rho_2 V_{s2}$ is the shear impedance in the lower halfspace.

5.1.2 Small-offset Approximation of Converted-wave Reflection Coefficient in Isotropic Media

As already shown in Chapter 4, the linearized PSV-wave reflection coefficient in VTI media has the following form:

$$R_{\grave{P}\acute{S}} = B_{\grave{P}\acute{S}} \sin\theta_p + K_{\grave{P}\acute{S}} \sin^3\theta_p, \tag{5.8}$$

where $B_{\grave{P}\acute{S}}$ and $K_{\grave{P}\acute{S}}$ are the AVO gradient and curvature terms, respectively:

$$B_{\grave{P}\acute{S}} = -\frac{2}{\kappa_0}\left[\left(\frac{\kappa_0}{4} + \frac{1}{2}\right)\frac{\Delta\rho}{\overline{\rho}} + \frac{\Delta V_s}{\overline{V_s}} - \frac{\kappa_0^2}{4\,(1+\kappa_0)}\Delta\delta\right], \tag{5.9}$$

$$K_{\grave{P}\acute{S}} = \frac{3 + 2\,\kappa_0}{4\,\kappa_0^2}\frac{\Delta\rho}{\overline{\rho}} + \frac{2+\kappa_0}{\kappa_0^2}\frac{\Delta V_s}{\overline{V_s}} + \frac{1 - 4\,\kappa_0}{2\,(1+\kappa_0)}\Delta\delta + \frac{\kappa_0}{1+\kappa_0}\Delta\epsilon. \tag{5.10}$$

In isotropic media, $\Delta\delta = 0$ and $\Delta\epsilon = 0$. The isotropic small-offset $\grave{P}\acute{S}$-wave reflection coefficient depends on the AVO gradient $B_{\grave{P}\acute{S}}$:

$$R_{\grave{P}\acute{S}} \approx -\frac{2}{\kappa_0} \sin\,\theta_p \left[\left(\frac{\kappa_0}{4} + \frac{1}{2} \right) \frac{\Delta\rho}{\overline{\rho}} + \frac{\Delta V_s}{\overline{V_s}} \right]. \tag{5.11}$$

Snell's law for mode conversions can be written as:

$$\frac{\sin\,\theta_p}{V_p} = \frac{\sin\,\theta_s}{V_s} = p. \tag{5.12}$$

Using Snell's law, equation (5.11) can be finally rewritten as:

$$R_{\grave{P}\acute{S}} \approx -2\,\sin\theta_s \left[\left(\frac{\kappa_0}{4} + \frac{1}{2} \right) \frac{\Delta\rho}{\overline{\rho}} + \frac{\Delta V_s}{\overline{V_s}} \right]. \tag{5.13}$$

Most of the available software deal exclusively with pure-mode impedance inversion under the small-offset assumption. The acoustic impedance inversion is based on equation (5.6). The problem with equations (5.11) and (5.13) is that they cannot be written as a normalized difference of the impedances in the two halfspaces. In order to use the available pure-mode impedance inversion algorithms for converted-wave inversion, equations (5.11) and (5.13) should be modified accordingly. From Chapter 4 we know that the isotropic small-offset assumption is valid for the converted-mode data in the upper part of the main gas reservoir up to 6,500 ft of offset if the data are properly scaled. Above 6,500 ft of offset, neither the small-offset assumption nor the isotropic assumption are valid.

5.1.3 Pseudo-impedance Concept for $\grave{P}\acute{S}$-waves

To represent the isotropic small-offset $\grave{P}\acute{S}$-wave reflection coefficient as a normalized difference of impedances, Valenciano & Michelena (2000) defined the "pseudo-density $\widehat{\rho}$" as:

$$\frac{\Delta\widehat{\rho}}{\widehat{\rho}} = \left(\frac{1}{4}\frac{V_p}{V_s} + \frac{1}{2} \right) \frac{\Delta\rho}{\overline{\rho}}. \tag{5.14}$$

Since

$$\frac{\Delta\rho}{\rho} \approx \Delta ln(\rho), \tag{5.15}$$

$$\widehat{\rho} = \rho^{\left(\frac{1}{4}\kappa_0 + \frac{1}{2}\right)}, \tag{5.16}$$

with $\kappa_0 = Vp/Vs$. Equation (5.16) relates the pseudo-density $\widehat{\rho}$ to the density ρ and the velocity ratio κ_0.

The P̀Ś-wave small-offset reflection coefficient in isotropic media can now be written as:

$$R_{\grave{P}\acute{S}}(\theta_s) \approx -2\,\sin\theta_s\left[\frac{\Delta\widehat{\rho}}{\widehat{\rho}} + \frac{\Delta V_s}{\overline{V_s}}\right], \tag{5.17}$$

where $\Delta\widehat{\rho}$ is the pseudo-density contrast between the two halfspaces, $\widehat{\rho}$ is the arithmetic average of the pseudo-densities, ΔV_s is the shear-wave velocity contrast, and $\overline{V_s}$ is the arithmetic average of the shear-wave velocities.

As shown in Sheriff and Geldart (1982), equation (5.17) can be rewritten as:

$$R_{\grave{P}\acute{S}}(\theta_s) \approx -2\,\sin\,\theta_s\frac{\widehat{\rho_2}V_{s2} - \widehat{\rho_1}V_{s1}}{\widehat{\rho_2}V_{s2} + \widehat{\rho_1}V_{s1}}, \tag{5.18}$$

where $\widehat{\rho_1}$ and V_{s1} are respectively the pseudo-density and the shear-wave velocity of the upper halfspace, and $\widehat{\rho_2}$ and V_{s2} are respectively the pseudo-density and the shear-wave velocity of the lower halfspace.

The above expression is also the normalized difference of pseudo-impedances between two halfspaces:

$$R_{\grave{P}\acute{S}}(\theta_s) \approx -2\,\sin\theta_s\frac{\widehat{Z}_{S2} - \widehat{Z}_{S1}}{\widehat{Z}_{S2} + \widehat{Z_{S1}}}, \tag{5.19}$$

with $\widehat{Z}_{Si} = \widehat{\rho}_i V_{si}$ defined as the pseudo-impedance.

For positive contrasts of the medium properties across the interface, the P̀Ś-wave reflection coefficient at small offsets is negative. This differs from the P̀Ṕ-wave normal-incidence reflection coefficient, which is positive. Another important difference is the scaling factor $-2\,\sin\theta_s$ that depends of the reflection angle. For pure-mode seismic waves, the scaling factor is independent of the offset and equal to ± 0.5.

5.1.4 P̀Ś-wave Reflectivity and Stacking

The small-offset P̀Ś-wave reflectivity as a function of the propagation time for isotropic media can be written as:

$$r_{\grave{P}\acute{S}}(t) = \sum_{i}^{N} R_{\grave{P}\acute{S}_i}(\theta_s)\,\delta(t - \tau_{\grave{P}\acute{S}i}), \tag{5.20}$$

where δ represents the delta function, N is the total number of interfaces, θ_s is the reflected angle, and $\tau_{\grave{P}\acute{S}i}$ is the position in P̀Ś-time of the i^{th} interface.

Let us now consider a wavelet $W_{\grave{P}\acute{S}}$. One can then write the P̀Ś-wave trace as:

$$t_{\grave{P}\acute{S}}(t) \approx r_{\grave{P}\acute{S}}(t) * W_{\grave{P}\acute{S}}(t). \tag{5.21}$$

The P̀Ś-wave stacked trace is obtain after integrating the previous equation from zero to the converted-wave angle $\theta_{s,max}$ that corresponds to the farthest trace in the NMO corrected CCP gather. The P̀Ś-wave stacked trace is hence given by the following equation:

$$R_{\grave{P}\acute{S}_{stack}} \approx -2\int_0^{\theta s,max} \sum_{i}^{N} \sin(\theta_s, i)\left[\frac{\Delta\widehat{\rho}}{\widehat{\rho}} + \frac{\Delta V_s}{\overline{V_s}}\right]\delta(t - \tau_{\grave{P}\acute{S}i}) * W_{\grave{P}\acute{S}}(t)\, d\theta_s, \tag{5.22}$$

where $W_{\grave{P}\acute{S}}$ is the extracted wavelet, and $\tau_{\grave{P}\acute{S}i}$ is the position in time of the i^{th} interface as already defined.

Now, for the P̀Ś-wave scaling factor to be equal to the P̀Ṕ-wave scaling factor (1/2), the following equation should be satisfied:

$$-2 \times \int_0^{\theta s,max} \sin(\theta_s, i)\, di = \frac{1}{2}. \tag{5.23}$$

Using Snell's law, the above equality can be rewritten in term of the incidence angle θ_p:

$$-2 \times \int_0^{\theta p,max} \frac{\sin(\theta_p, i)}{\kappa_0} \, di = \frac{1}{2}, \tag{5.24}$$

where $\theta_{p,max}$ is the incidence angle corresponding to the farthest trace in the NMO corrected CCP gather.

Let us suppose $\kappa_0 \approx 2$. This is generally true in the Rulison main reservoir where $1.85 \leq \kappa_0 \leq 2.1$ (Figure 3.4). Then

$$\int_0^{\theta p,max} \sin(\theta_p, i) \, di = -\frac{1}{2}. \tag{5.25}$$

Hence, $\sin \theta_{p,max} = 60°$. Using Snell's law and assuming $\kappa_0 = 2$, one finds that the maximum reflected angle is $\theta_{s,max} \approx 25.66°$. If the top of the reservoir is at approximately 6,000 ft, the maximum offset from the source to the conversion point should be approximately equal to 10,400 ft and the offset from the conversion point to the receiver is consequently equal to 2,900 ft. Therefore, in order to obtain the same scaling factor for converted-mode and pure-mode seismic waves at the top of the reservoir, the available offset should be equal to 13,300 ft. In Rulison, the maximum offsets available for converted-waves are slightly larger than 10,000 ft. Therefore, in order to use the pure-mode algorithms for the converted-mode inversion, one should correct for the polar angle dependance. Furthermore, from the analysis of Chapter 4, all PS_2 traces should be scaled by an additional factor of 1/2 and all PS_1 traces should be scaled by an additional factor of 5/7 [see Section 4.2]. Thus, the corrections X_1 and X_2 to be respectively applied to the amplitudes of PS_1- and PS_2-waves are:

$$X_1 = -\frac{5}{28} \times \left(\int_0^{\theta p,max} \frac{\sin(\theta_p, i)}{\kappa_0} \, di \right)^{-1}, \tag{5.26}$$

$$X_2 = -\frac{1}{8} \times \left(\int_0^{\theta p,max} \frac{\sin(\theta_p, i)}{\kappa_0} \, di \right)^{-1}. \tag{5.27}$$

Instead of being applied to the seismic traces on a trace-to-trace basis, the scaling is applied to the wavelets $W_{\grave{P}\acute{S}1}(t)$ and $W_{\grave{P}\acute{S}2}(t)$:

$$\widehat{W}_{\grave{P}\acute{S}i}(t) = X_i \times W_{\grave{P}\acute{S}}(t), \text{ with i} = 1, 2. \tag{5.28}$$

Therefore,

$$R_{\grave{P}\acute{S}i_{stack}} \approx \int_0^{\theta s,max} \sum_j^N \left[\frac{\Delta\widehat{\rho}}{\widehat{\rho}} + \frac{\Delta V_s}{\overline{V_s}} \right] \delta(t - \tau_{\grave{P}\acute{S}(j)}) * \widehat{W}_{\grave{P}\acute{S}i}(t)\, d\theta_s, \text{ with i} = 1, 2. \tag{5.29}$$

5.2 Impedance Inversion of Multicomponent Seismic Data

Impedance volumes are important because they integrate seismic and well log data which lead to an accurate structural and stratigraphical interpretation of the reservoir on a finer scale (Atkins et al., 2001). In order to constrain the result of an inversion, seismic data alone are not sufficient. The industry generally uses log data such as sonic logs and density logs in order to constrain the inversion result. In this study I used the data from well RWF 332-21. This well has dipole sonic data (P-wave and S-wave sonic data) as well as density data. The location of the well is indicated by a red square in the lower right corner of the RCP survey on Figure 1.13. The inversion scheme used in this study is a model-based inversion. The model-based inversion perturbs an initial guess usually based on low-frequency log data. At each iteration, the difference between the observed data and the data based on forward modeling is computed. The algorithm stops when the difference between the observed and the modeled data gets under a certain specified threshold. Accurate knowledge of the seismic wavelet is necessary in order to perform the forward modeling at each iteration. I inverted the 2006 pure-mode (P-, S_{11}-, and S_{22}-waves) data and for the 2006 converted-mode ($\grave{P}\acute{S}_1$- and $\grave{P}\acute{S}_2$-waves) data using an initial model based on the density and velocity estimated in the well. For every inversion I followed the following workflow proposed by Guliyev (2007) and Meza (2008):

i) building the synthetic seismogram using the RWF 332-21 well data,

ii) horizon picking of the top (UMV Shale) and the bottom (Cameo Coal) of the main

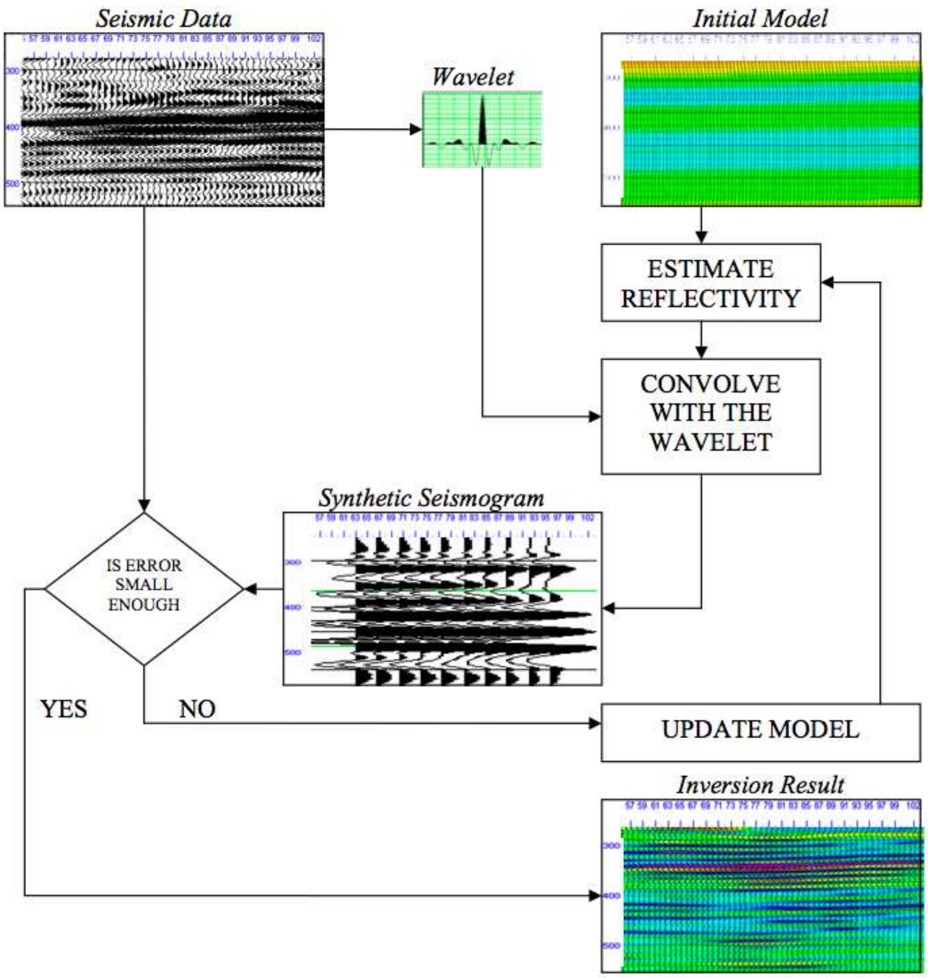

Figure 5.1. Model-based inversion workflow. After Guliyev (2007).

gas reservoir,

iii) initial model building,

iv) determination of the optimal parameters for the model-based inversion,

v) minimizing the difference between the observed and the modeled data.

This workflow is illustrated in Figure 5.1.

5.2.1 Inversion of the P-wave Data

Wavelet extraction and P-wave synthetic seismogram

The first step is to pick the horizons that correspond to prominent geological boundaries on the seismic data. The top and bottom of the main gas reservoir cor-

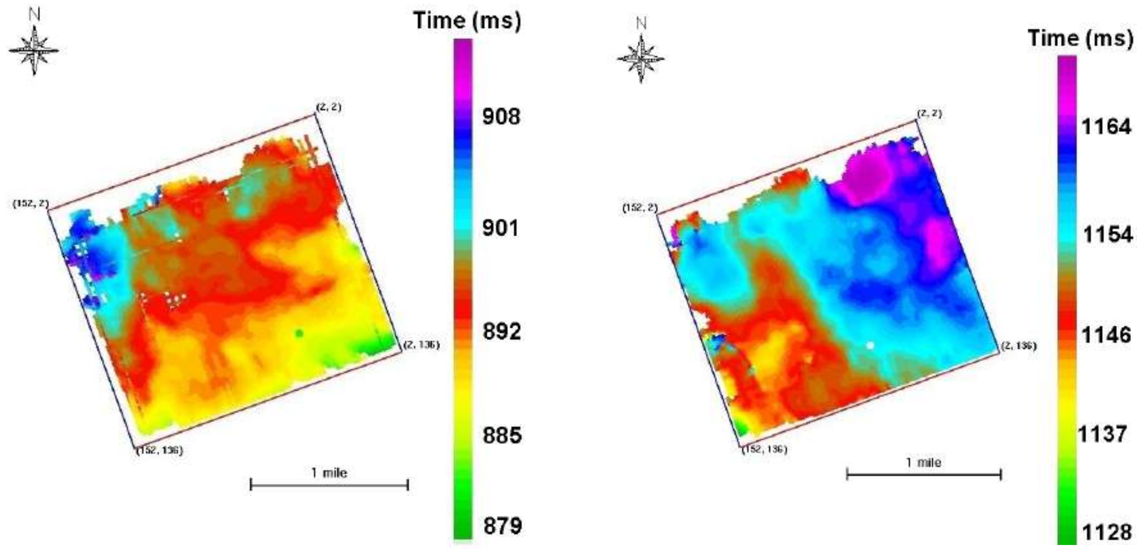

Figure 5.2. P-wave time-structure maps for the UMV Shale horizon (left) and top Cameo Coal horizon (right).

respond to the UMV Shale and top Cameo Coal, respectively. These horizons were used in order to extrapolate the well-log impedance over the whole seismic volume in order to build the initial model for the inversion. The time-structure maps are shown in Figure 5.2. The second step is to extract the seismic wavelet from the data. The extraction is performed statistically on all traces for the main gas reservoir section. The wavelet time and frequency response are shown in Figure 5.3. The third step is to compute the acoustic impedance at the well location by multiplying the density log by the P-wave velocity log (the inverse of the sonic log). The result is convolved with the extracted wavelet to produce the synthetic seismogram.

Building the initial model

The initial acoustic impedance model was built by extrapolating the initial acoustic impedance (computed at the well location) for the UMV Shale and top Cameo Coal horizons. The acoustic impedance log computed using the sonic and density logs has been low-pass filtered with a high-cut frequency of 10 Hz. The initial acoustic impedance model is shown in Figure 5.4.

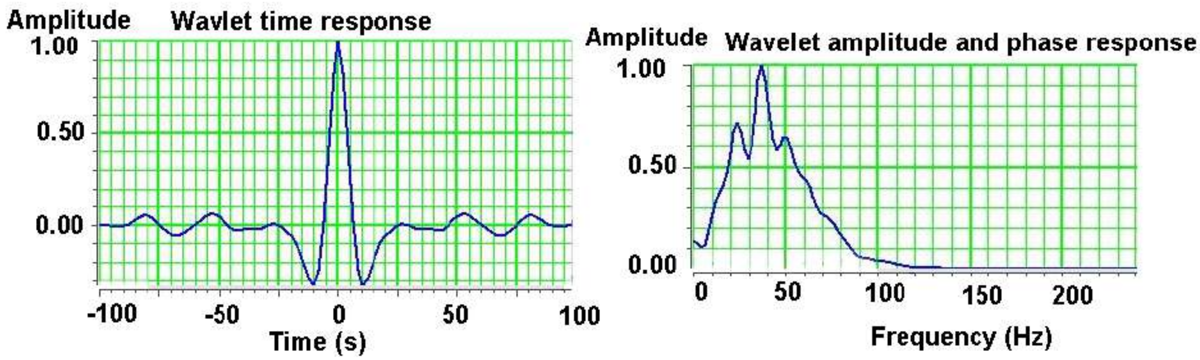

Figure 5.3. Extracted P-wave wavelet time response (left) and frequency response (right).

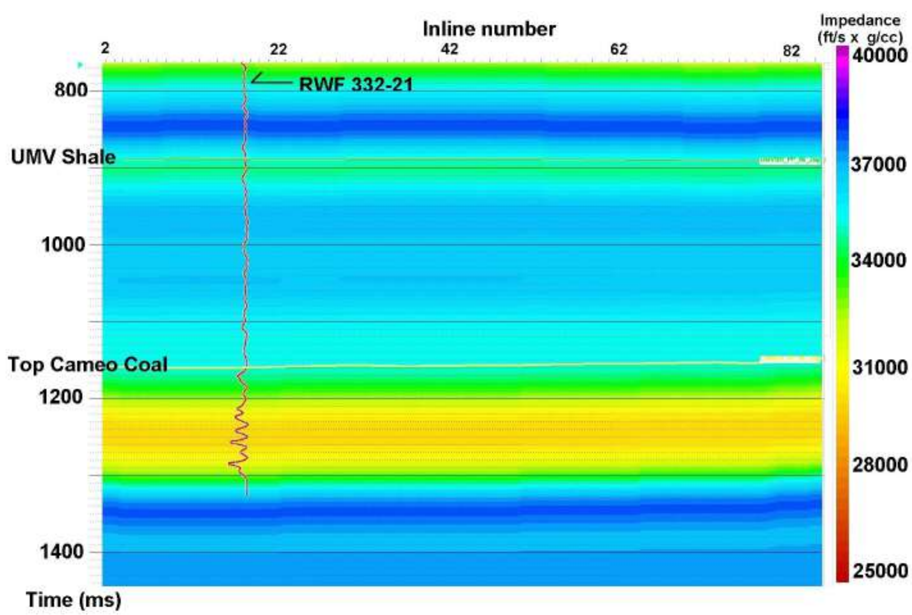

Figure 5.4. Crossline 109 of the initial low-pass filtered (high-cut frequency of 10 Hz) acoustic impedance model with the study well RWF 332-21 low-pass impedance log superposed (in red).

P-wave amplitude inversion

The initial acoustic impedance model was used to test different inversion parameters at the study well location. Once the optimum set of parameters is found, the P-wave amplitude inversion is performed. The optimum parameter set is:
i) number of iterations: 5,
ii) pre-whitening filter: 1%,
iii) maximum impedance variation from the initial model: $\pm$ 50 %,
iv) scalar adjustment factor: 0.6.

The P-wave amplitude inversion successfully generated an impedance model that matches the impedance log at the study well location RWF 332-21 (inline 20, crossline 109) at 0-65 Hz bandwidth (see Figure 5.6). Crossline 109 of the acoustic impedance volume is shown on Figure 5.5. Coals are characterized by low impedance values and are therefore well imaged as low-impedance bodies. The UMV Shale and top Cameo Coal are clearly visible in the impedance volume. However, the fluvial sand bodies in the main gas reservoir are not imaged adequately. Except for a couple of high-impedance intervals that probably correspond to fluvial sand bodies (these high-impedance intervals match with low gamma ray values on Figure 5.5), the acoustic impedance inversion was not able to image laterally the producing sand bodies in the reservoir because the fluvial sand bodies have very low acoustic impedance contrasts with the adjacent non-marine shales. On the other hand, the contrast in shear impedance is larger (Rojas, 2005), which justifies the use of pure shear-wave inversion as well as converted-wave inversion for the main gas reservoir interval.

P-wave inversion analysis

Before starting the shear-wave inversion, the results of the P-wave inversion should be analyzed. At the study well location, both the original acoustic impedance log and the inverted impedance curve extracted from the inverted impedance volume are represented in track 1 of Figure 5.6. We clearly see that the inverted impedance

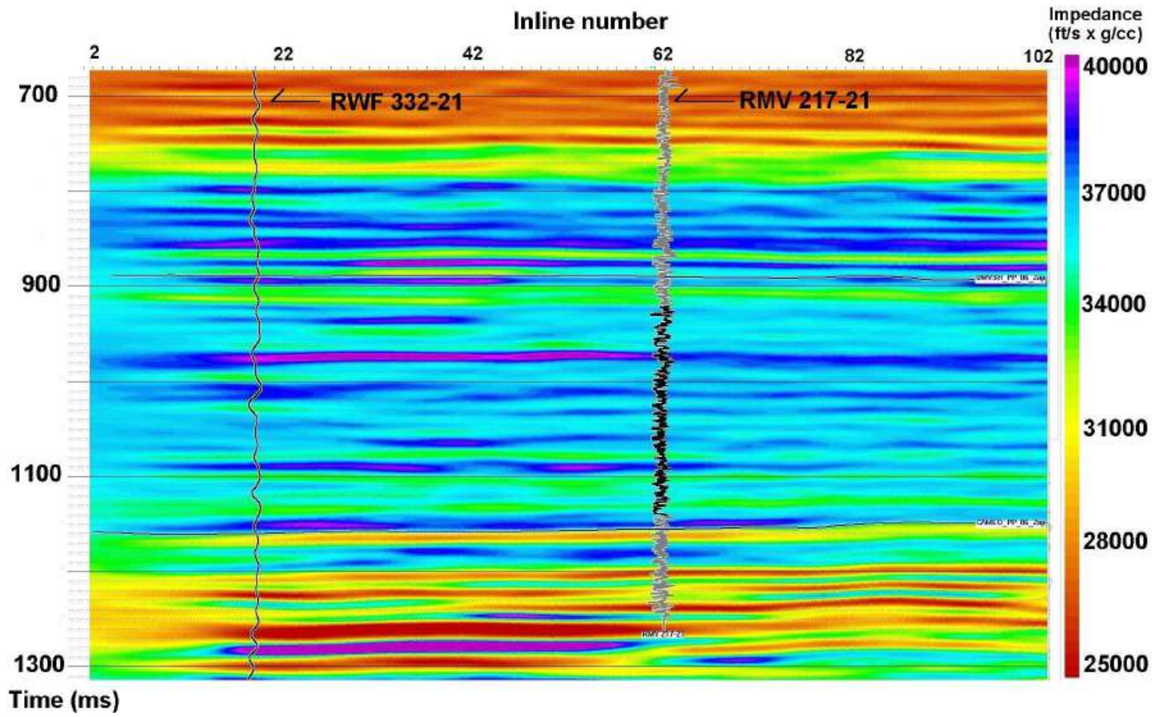

Figure 5.5. Crossline 109 of the acoustic impedance inversion result. The study well RWF 332-21 low-pass filtered gamma-ray log is displayed on the left and the well RWV 217-21 (inline 63 and crossline 107 in the seismic grid) gamma-ray log is displayed on the right.

corresponds to a low-pass filtered version of the original impedance log. The correlation coefficient between the observed seismic data and the synthetic seismogram at the well location (track 2 on Figure 5.6) is equal to 98 %. Then, from the result of the P-wave inversion, a synthetic seismic model for inline 20 was created (Figure 5.7). In the main gas reservoir interval, most of the events have been successfully modeled in term of traveltimes and amplitudes. The correlation coefficient between the field seismic data and the synthetic seismic data for inline 20 is equal to 90% in the reservoir interval.

5.2.2 Inversion of the S-wave Data

Time-depth relationship

The inversion of both pure shear-wave data (S_{11}- and S_{22}-waves) requires a correlation of the relative events in respectively S_{11}-time and S_{22}-time in order to build

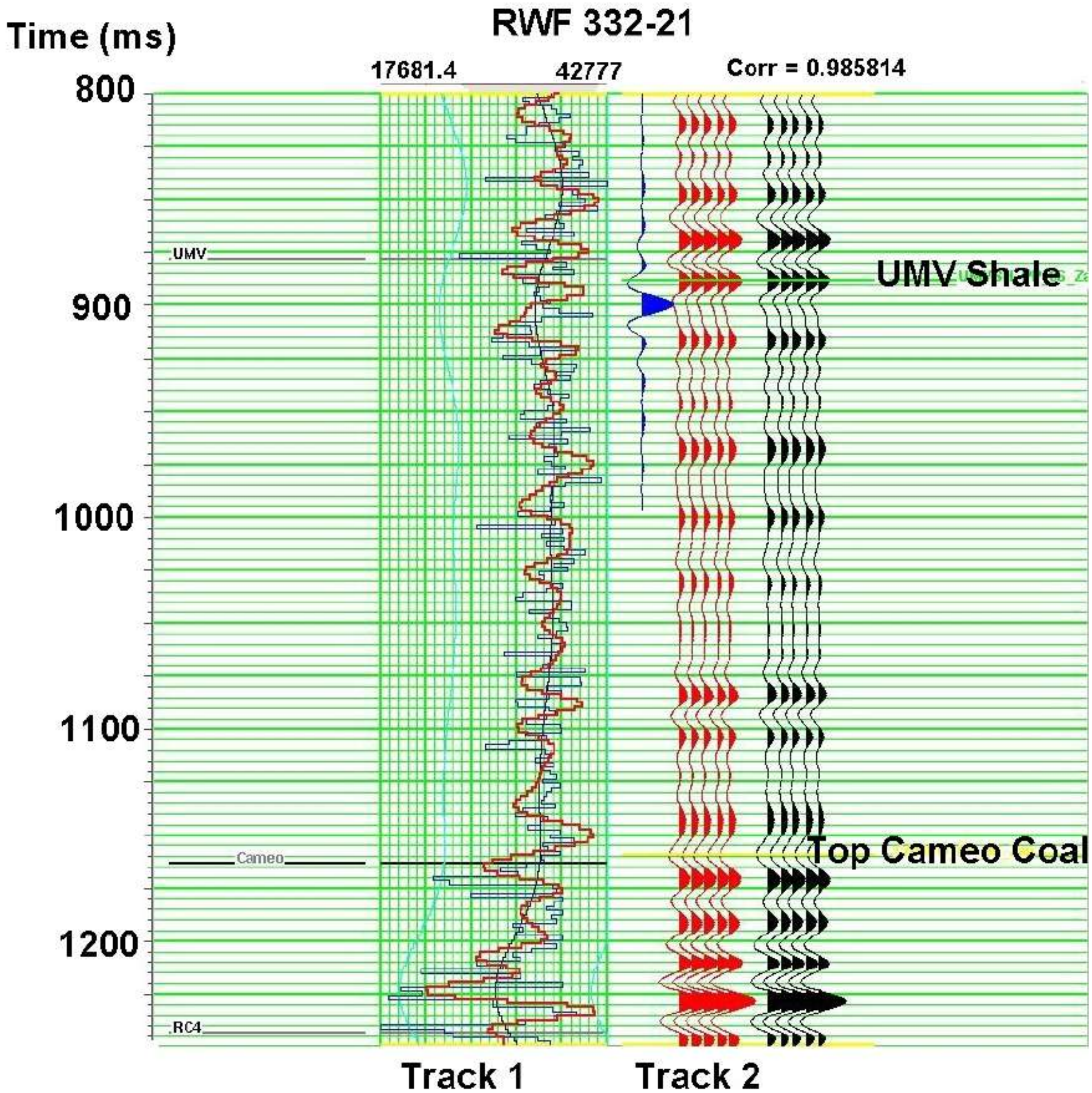

Figure 5.6. P-wave inversion analysis. The original acoustic impedance log (in blue), the inverted acoustic impedance at the study well location (in red), and the initial low frequency model (in black) are represented in track 1. The synthetic P-wave seismogram (in red) and the recorded P-wave seismic data (in black) at the study well location are represented in track 2; their correlation coefficient is equal to 98%.

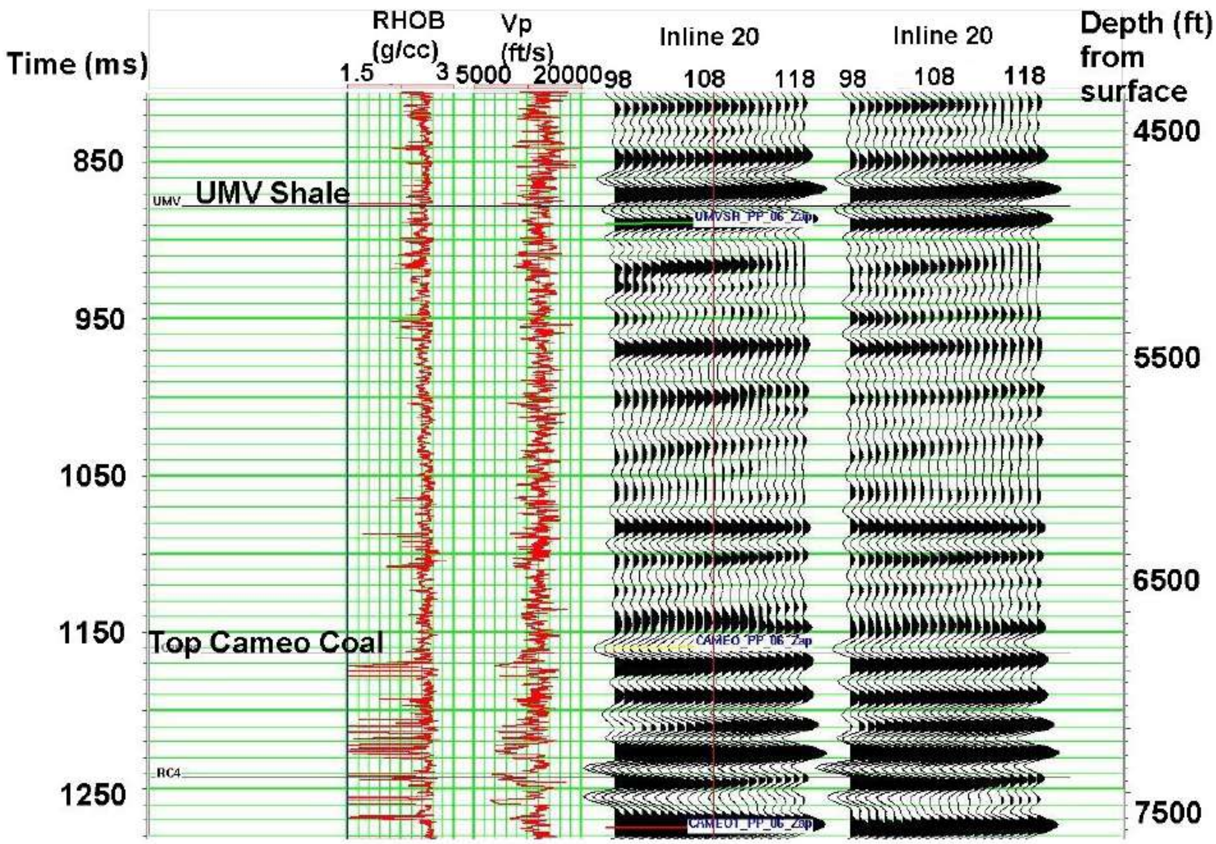

Figure 5.7. From left to right: density log at the study well location, P-wave sonic log at the study well location, observed seismic data for inline 20, modeled seismic data for inline 20 based on the results of the inversion.

a synthetic seismogram. This is done by building a time-depth function for both S_{11}- and S_{22}-waves. The initial guess for this function is a Vp/Vs ratio equal to two. Then, a visual correlation of seismic events is performed for each mode that modifies the initial time-depth function. The well-seismic tie of events on the natural domains of both shear-modes can then be performed. The result of this operation is a more accurate time-depth function.

Wavelet extraction and S-wave synthetic seismogram

The first step is to pick the horizons that correspond to visible geological boundaries on both S_{11}- and S_{22}-seismic volumes. The UMV Shale and top Cameo Coal horizons were picked as already done for P-wave data. The time-structure maps for both modes are shown in Figures 5.8 and Figures 5.9, respectively. These horizons were used in order to extrapolate the well-log impedances over the entire seismic volume in order to build the initial models for the non-converted shear-wave amplitude inversions. The second step is to extract the seismic wavelets from both S_{11}- and S_{22}- seismic volumes. The extraction is performed statistically on all traces for the main gas reservoir interval for both S_{11}- and S_{22}-wave data. The wavelet time and frequency responses for both shear volumes are shown in Figure 5.10. The third step is to compute the fast and slow shear impedances at the study well location by multiplying the density log with the fast and slow shear-wave velocities. For non-converted shear-waves, the reflection coefficient for small-offset traces depends only on the contrast in shear impedance (equation (5.7)). This result is similar to P-wave inversion for small-offset traces in isotropic media. The computed shear impedance results are then respectively convolved with the corresponding extracted wavelet to give two synthetic seismograms: a fast shear-wave synthetic seismogram and a slow shear-wave synthetic seismogram.

Building the pure shear impedance initial models

Both fast and slow initial shear impedance models were built by extrapolating

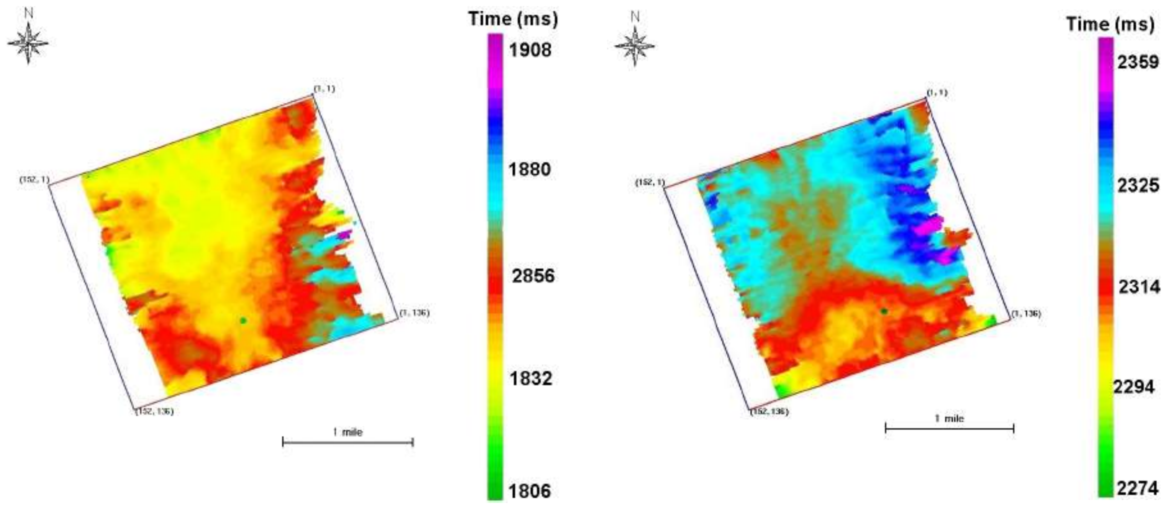

Figure 5.8. S_{11}-wave time-structure maps for the UMV Shale horizon (left) and Cameo Coal horizon (right).

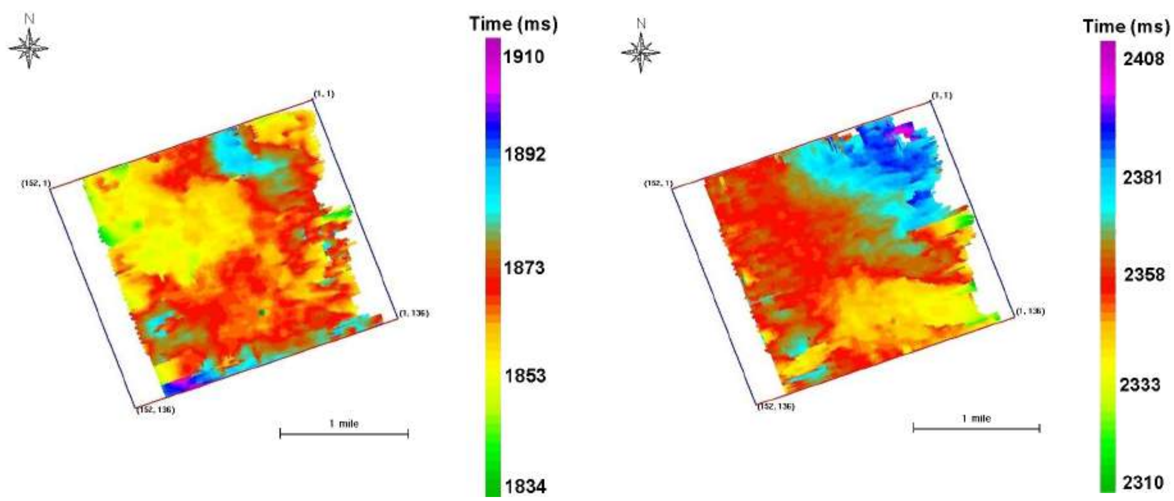

Figure 5.9. S_{22}-wave time-structure maps for the UMV Shale horizon (left) and Cameo Coal horizon (right).

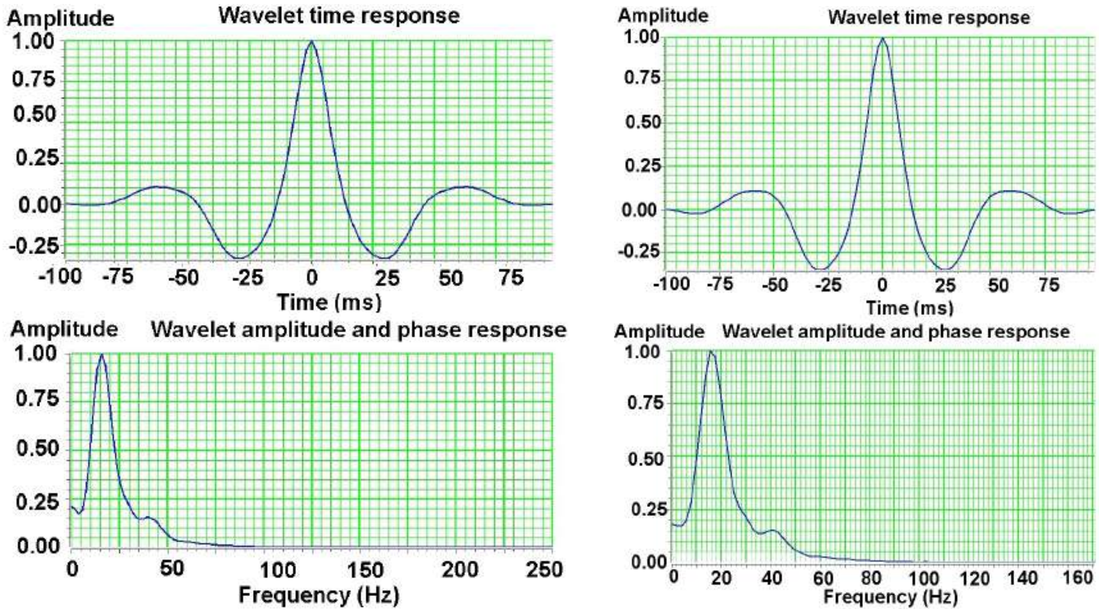

Figure 5.10. Extracted S_{11}-wavelet time response (upper left panel) and frequency response (lower left panel) and S_{22}-wavelet time response (upper right panel) and frequency response (lower right panel).

the initial shear impedance logs (computed at the study well RWF 332-21 location) for the UMV Shale and top Cameo Coal horizons. Both S_{11}- and S_{22}-impedance logs computed using the sonic and density logs were low-pass filtered with a high-cut frequency of 5 Hz. The S_{11}-impedance initial model is shown in Figure 5.11 and the S_{22}-impedance initial model is shown in Figure 5.12 .

Non-converted shear-wave amplitude inversion

Both initial shear impedance volumes were used to test different inversion parameters at the study well RWF 332-21 location. The optimum parameter set given hereafter was found to be identical for both S_{11}- and S_{22}-wave inversions:

i) number of iterations: 5,

ii) pre-whitening filter: 1%,

iii) maximum impedance variation from the initial model: ± 50 %,

iv) scalar adjustment factor: 0.5.

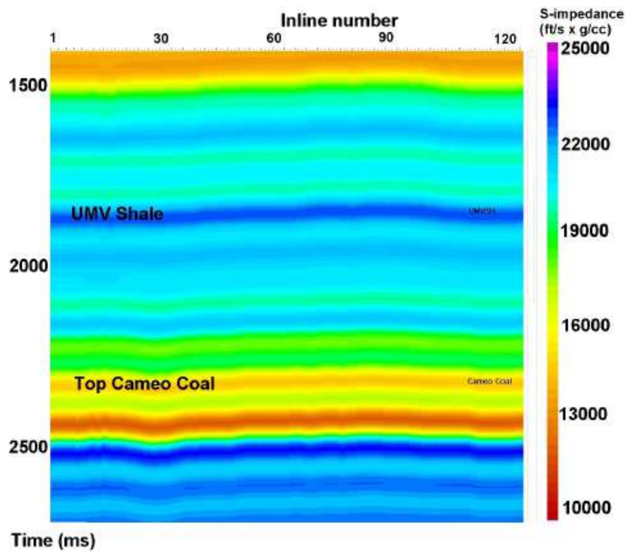

Figure 5.11. Crossline 109 of the low-pass filtered initial S_{11}-impedance model with a high-cut frequency of 5 Hz.

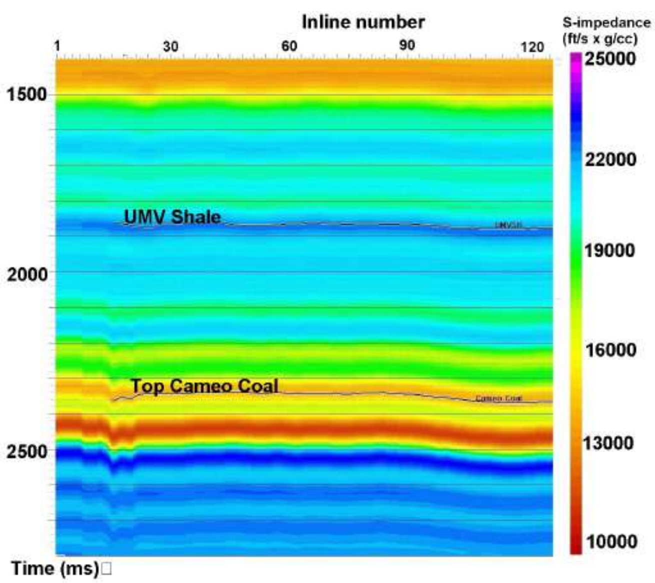

Figure 5.12. Crossline 109 of the low-pass filtered initial S_{22}-impedance model with a high cut frequency of 5 Hz.

The S_{11}- and S_{22}-wave amplitude inversions successfully generated impedance models that match respectively the S_{11}- and S_{22}-impedance logs at the study well location (inline 20, crossline 109) at 0-30 Hz bandwidth (see Figures 5.15 and 5.16). The crossline 109 of the S_{11}-impedance volume result is shown in Figure 5.13 and the crossline 109 of the S_{22}-impedance volume result is shown in Figure 5.14. The top and bottom of the main gas reservoir are clearly visible on both volumes. Compared to the acoustic impedance inversion, the reservoir is no longer invisible. Several high impedance intervals that correspond to fluvial sand bodies (these high impedance intervals match with low gamma ray intervals on Figure 5.13) are now clearly identifiable and, therefore, the lateral extent of these producing sand bodies is now imaged using shear impedances. As already mentioned, shear impedance is the key to successful sand delineation in the Rulison Field.

Pure shear-wave inversion analysis

The last step is to analyze the results of the both shear-wave inversions. At the study well location, the original low-pass filtered S_{11}-impedance log and the inverted S_{11}-impedance curve extracted from the inverted S_{11}-impedance volume are represented in track 1 on Figure 5.15, while the original low-pass filtered S_{22}-impedance log and the inverted S_{22}-impedance curve extracted from the inverted S_{22}-impedance volume are represented in track 1 on Figure 5.16. Both figures show that for S_{11}- and S_{22}-waves, the inverted impedance and the low-pass filtered impedance computed from logs at the well location match well. The correlation coefficient between the inverted impedances and the original impedances is higher than 80% for both pure shear-modes. On the other hand, the correlation coefficient between the observed S_{11}-wave data and the synthetic S_{11}-seismogram at the well location (track 2 on Figure 5.15) is equal to 93 %, and the correlation coefficient between the observed S_{22}-wave data and the synthetic S_{22}-seismogram at the well location (track 2 on Figure 5.16) is equal to 96 %.

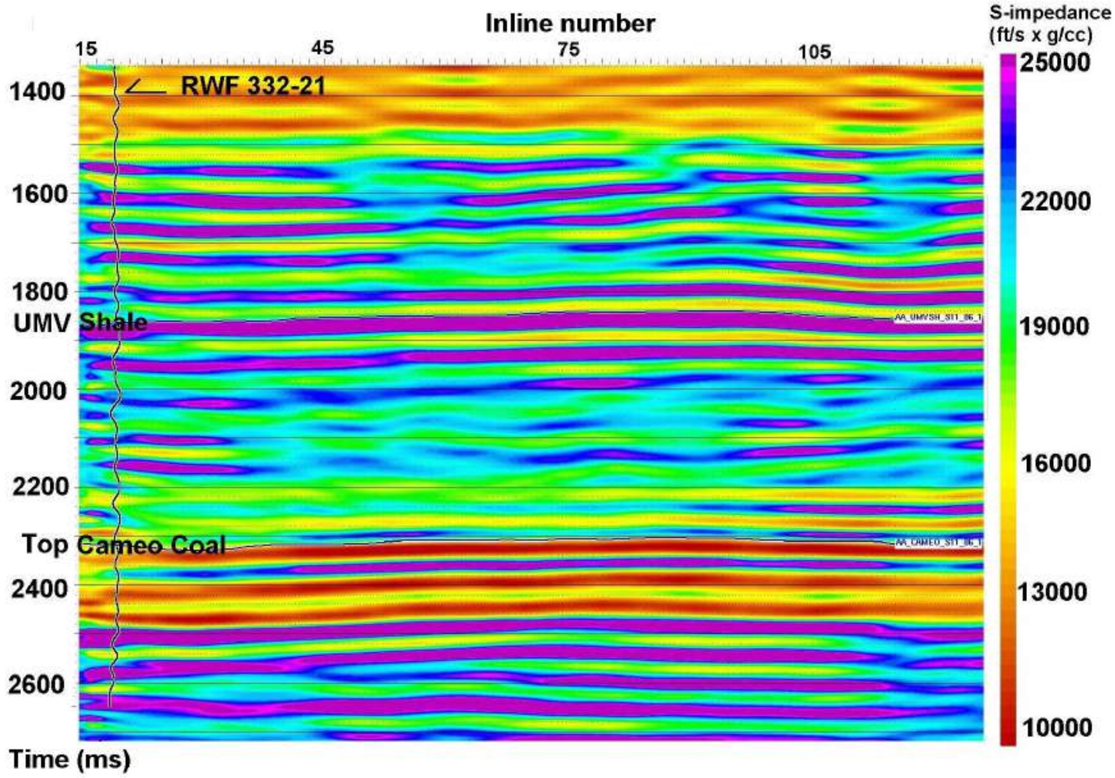

Figure 5.13. Crossline 109 of the fast shear-wave (S_{11}-wave) inversion result with the low-pass filtered gamma ray log (black curve) displayed at the study well location.

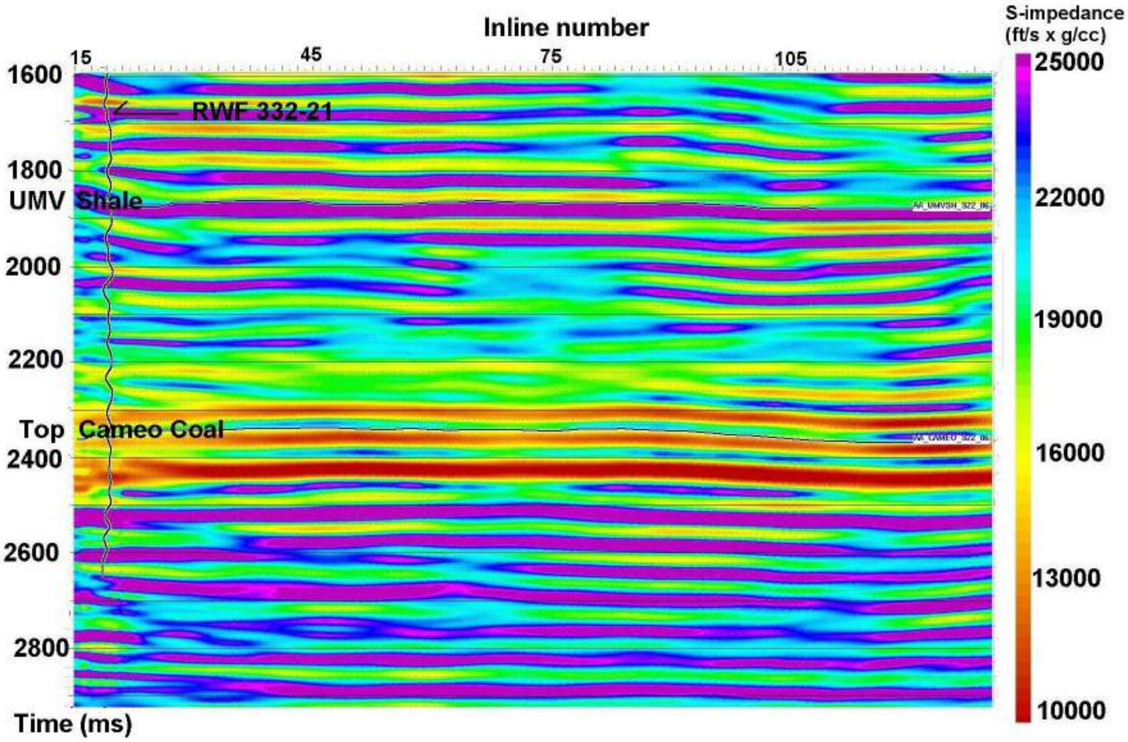

Figure 5.14. Crossline 109 of the slow shear-wave (S_{22}-wave) inversion result with the low-pass filtered gamma ray log (black curve) displayed at the study well location.

5.2.3 Inversion of the $\grave{P}\acute{S}$-wave Data

Now that the pure shear-wave inversion was successfully performed and analyzed, the next step is to invert the converted-wave data. Different studies proposed a workflow for $\grave{P}\acute{S}$-wave amplitude inversion (Carazzone, 1986; Stewart, 1991; Valenciano & Michelena, 2000). The method proposed in this subsection is based on the anisotropic elastic AVO modeling of Chapter 4, is the closest to the pure-mode amplitude inversion, and makes use of the existing small-offset pure-mode inversion algorithms.

Building the pseudo-density model and the time-depth relationship

As already seen in the first section of this chapter, for small offsets and for isotropic media, the $\grave{P}\acute{S}$-wave reflection coefficient is dependent on the contrast in pseudo-impedances between two halfspaces (equation (5.19)). We also studied how

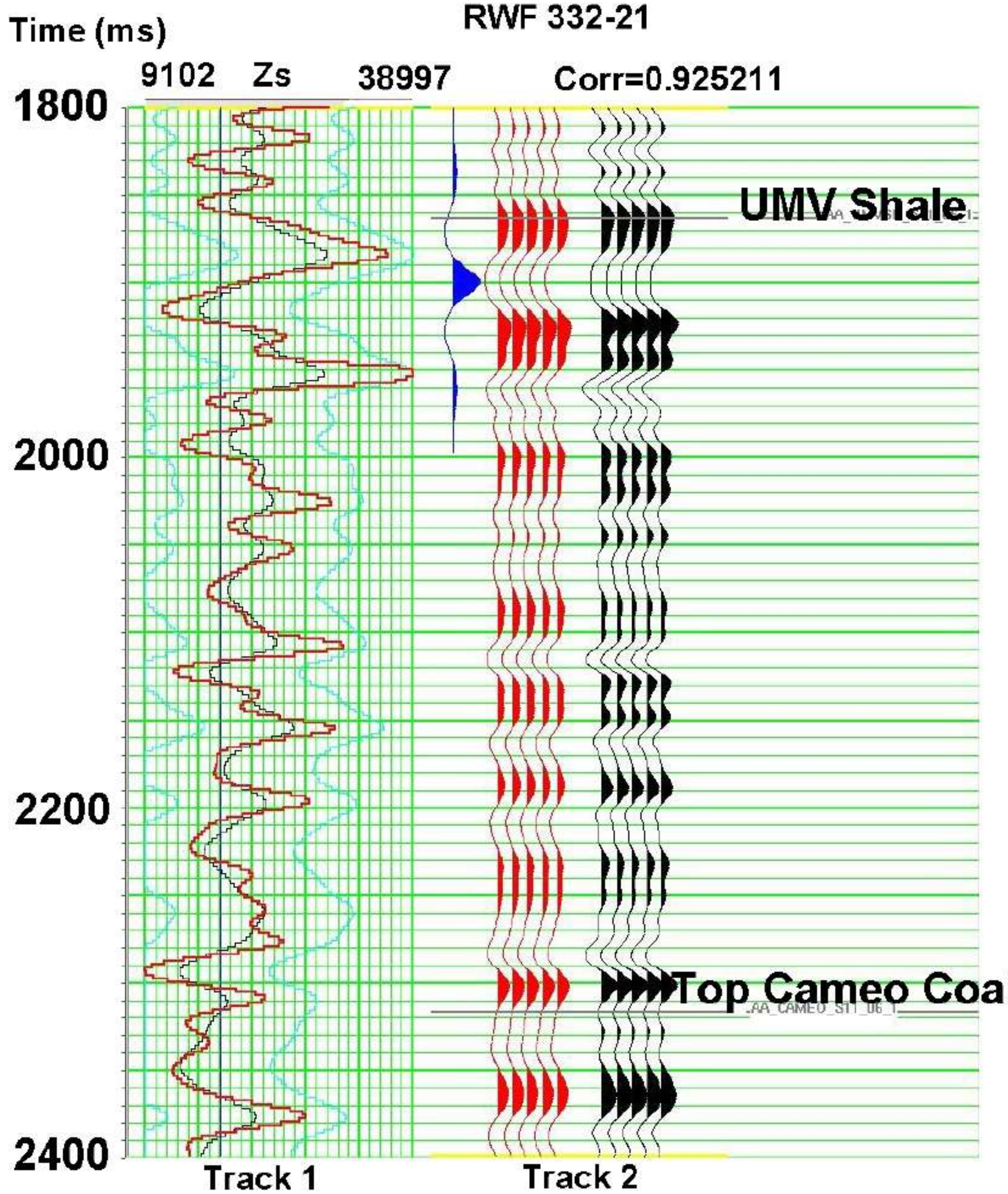

Figure 5.15. S_{11}-wave inversion analysis. The original low-pass filtered S_{11}-impedance log (in blue) and the inverted S_{11}-impedance at the study well location (in red) are represented in track 1. The synthetic S_{11}-seismogram (in red) and the observed S_{11}-seismic data (in black) at the study well location are represented in track 2; their correlation coefficient is equal to 93%.

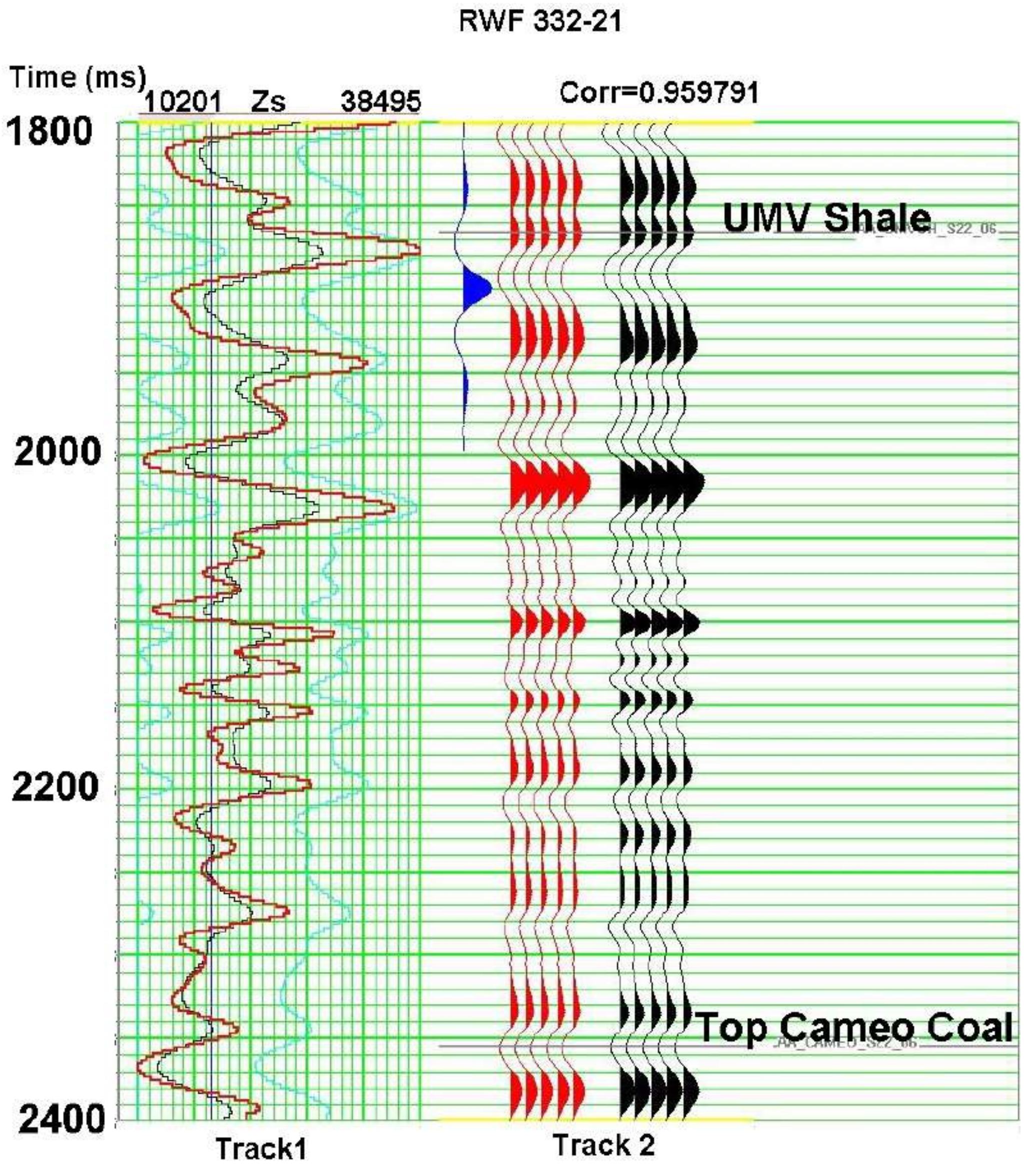

Figure 5.16. S_{22}-wave inversion analysis. The original low-pass filtered S_{22}-impedance log (in blue) and the inverted S_{22}-impedance at the study well location (in red) are represented in track 1. The synthetic S_{22}-seismogram (in red) and the observed S_{22}-seismic data (in black) at the study well location are represented in track 2; their correlation coefficient is equal to 96%.

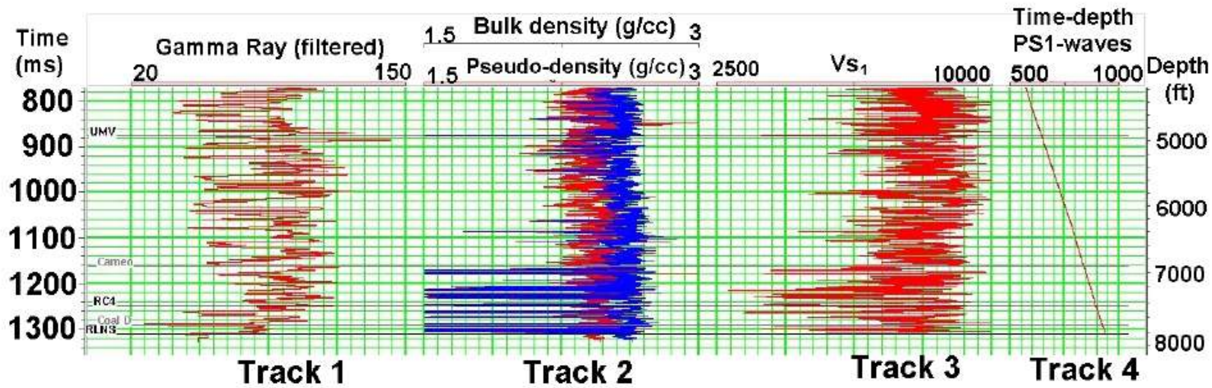

Figure 5.17. Well logs and computed logs at the main reservoir level at the study well RWF 332-21. The gamma-ray is represented at the far left (track 1). Track 2 shows the density log (in blue) and the pseudo-density log related to the fast converted-wave ($\widehat{\rho}^{(1)}$). Track 3 shows the fast shear-wave velocity V_{s1}. Track 4 shows the time-depth conversion function for the $\grave{\text{P}}\acute{\text{S}}_1$-wave.

to correct for polar angle dependance and anisotropy (see Chapter 4) by scaling the extracted wavelet by a factor proportional to the maximum stacking offset used to generate the poststack gathers.

The first step will be to generate the pseudo-density logs from the density and dipole sonic logs. Since pseudo-density is dependent on the Vp/Vs ratio, and since we have two shear-wave velocities measured at the study well, one should build two pseudo-densities logs. The first pseudo-density will be related to the fast converted-wave ($\grave{\text{P}}\acute{\text{S}}_1$-wave) and will be denoted $\widehat{\rho}^{(1)}$,while the second pseudo-density will be related to the slow converted-wave ($\grave{\text{P}}\acute{\text{S}}_2$-wave) and will be denoted $\widehat{\rho}^{(2)}$. $\widehat{\rho}^{(1)}$ and $\widehat{\rho}^{(2)}$ are computed according to equations (5.30) and (5.31) and are represented on Figures 5.17 and 5.18. The pseudo-densities are equal to:

$$\widehat{\rho}^{(1)} = \rho^{\left(\frac{1}{4}\frac{V_p}{V_{s1}}+\frac{1}{2}\right)}, \tag{5.30}$$

$$\widehat{\rho}^{(2)} = \rho^{\left(\frac{1}{4}\frac{V_p}{V_{s2}}+\frac{1}{2}\right)}. \tag{5.31}$$

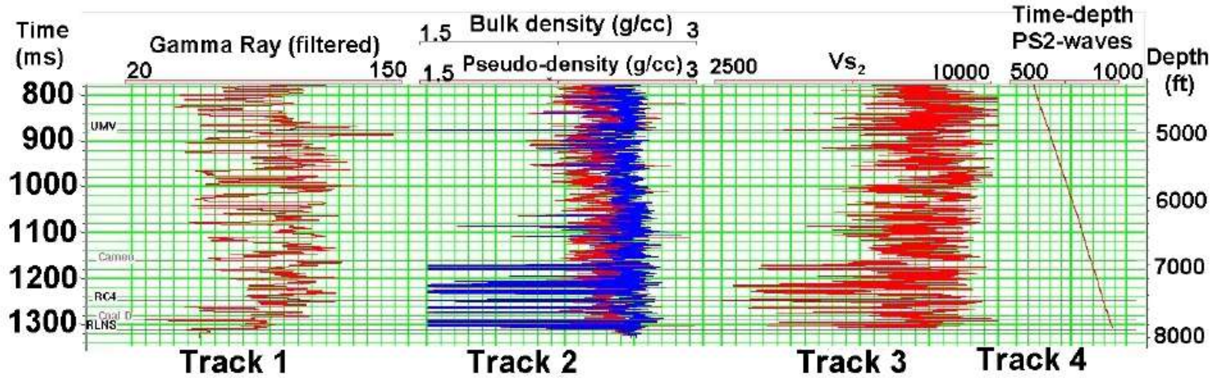

Figure 5.18. Well logs and computed logs at the main reservoir level at the study well RWF 332-21. The gamma-ray is represented at the far left (track 1). Track 2 shows the density log (in blue) and the pseudo-density log related to the slow converted-wave ($\widehat{\rho}^{(2)}$). Track 3 shows the slow shear-wave velocity V_{s2}. Track 4 shows the time-depth conversion function for the $\grave{\mathrm{P}}\acute{\mathrm{S}}_2$-wave.

Pseudo-densities have lower values than the density itself (see Figures 5.17 and 5.18). This is due to the fact that both velocity ratios $\mathrm{Vp/Vs_1}$ and $\mathrm{Vp/Vs_2}$ are less than 2 in most parts of the survey (Figure 3.4). If the velocity ratios were equal to 2, pseudo-density and density would be equal; and if the velocity ratios were greater than two, the pseudo-densitiy would have values greater than those of the density. In the main gas reservoir interval, the vertical velocity ratio is commonly less than two. Therefore, the pseudo-impedances $\widehat{Z_1}$ and $\widehat{Z_2}$ have smaller values than those of the impedances Z_1 and Z_2.

The next step is to build the time-depth relationship. As already shown for pure shear-waves, the inversion of $\grave{\mathrm{P}}\acute{\mathrm{S}}_1$- and $\grave{\mathrm{P}}\acute{\mathrm{S}}_2$-wave data requires a correlation of the relative events in respectively $\grave{\mathrm{P}}\acute{\mathrm{S}}_1$- and $\grave{\mathrm{P}}\acute{\mathrm{S}}_2$-time in order to build a synthetic seismogram. This is done by building a time-depth function for both $\grave{\mathrm{P}}\acute{\mathrm{S}}_1$- and $\grave{\mathrm{P}}\acute{\mathrm{S}}_2$-wave data. An initial model is built with a Vp/Vs ratio equal to two. Then, a visual correlation of seismic events is performed for each mode that modifies the initial time-depth functions. The well-seismic tie of events on the natural domains of both converted-modes can then be performed. The result of this operation is more accurate time-depth functions. The time-depth functions for both modes are represented in track 4 on Figures 5.17 and 5.18.

Wavelet extraction and $\grave{\mathrm{P}}\acute{\mathrm{S}}$-wave synthetic seismogram

As already done for P- and the S-waves, one has to pick the horizons that correspond to prominent geological boundaries on both $\grave{\mathrm{P}}\acute{\mathrm{S}}_1$ and $\grave{\mathrm{P}}\acute{\mathrm{S}}_2$ volumes. The UMV Shale and top Cameo Coal horizons were picked and the time-structure maps for both fast and slow modes are shown in Figures 5.19 and Figures 5.20. These horizons will be used in order to extrapolate the well-log pseudo-impedances over the entire seismic volume in order to build the initial models for the converted shear-wave impedance inversions. The following step is to extract the seismic wavelets from both $\grave{\mathrm{P}}\acute{\mathrm{S}}_1$- and $\grave{\mathrm{P}}\acute{\mathrm{S}}_2$- seismic volumes. The extraction is performed statistically on all traces for the main gas reservoir interval for both $\grave{\mathrm{P}}\acute{\mathrm{S}}_1$- and $\grave{\mathrm{P}}\acute{\mathrm{S}}_2$-wave data. These extracted wavelets are scaled in order for them to have coherent amplitudes after the inversion. In order to use the non-converted shear-wave algorithms that compute the reflection coefficient based on impedance contrasts, one should use the pseudo-impedances instead of the impedances for the inversion, and the $\grave{\mathrm{P}}\acute{\mathrm{S}}$-wavelet should be scaled as already explained in Section 5.1. The scaling factors are computed based on equations (5.26) and (5.27) for a maximum offset of 10,000 ft. The scaled wavelets time and frequency responses for both converted shear-wave volumes are shown in Figure 5.21. The final step is to compute the fast pseudo-impedance and the slow pseudo-impedance at the study well location by respectively multiplying the pseudo-density logs by the fast shear-wave velocity and the slow shear-wave velocity logs. The pseudo-shear impedance results are then convolved with the corresponding extracted and scaled wavelets to give two synthetic seismograms. The correlation coefficients between the synthetic seismograms and the observed converted-wave data reached 87% and 96% for respectively the fast and slow converted-wave seismograms in the reservoir interval

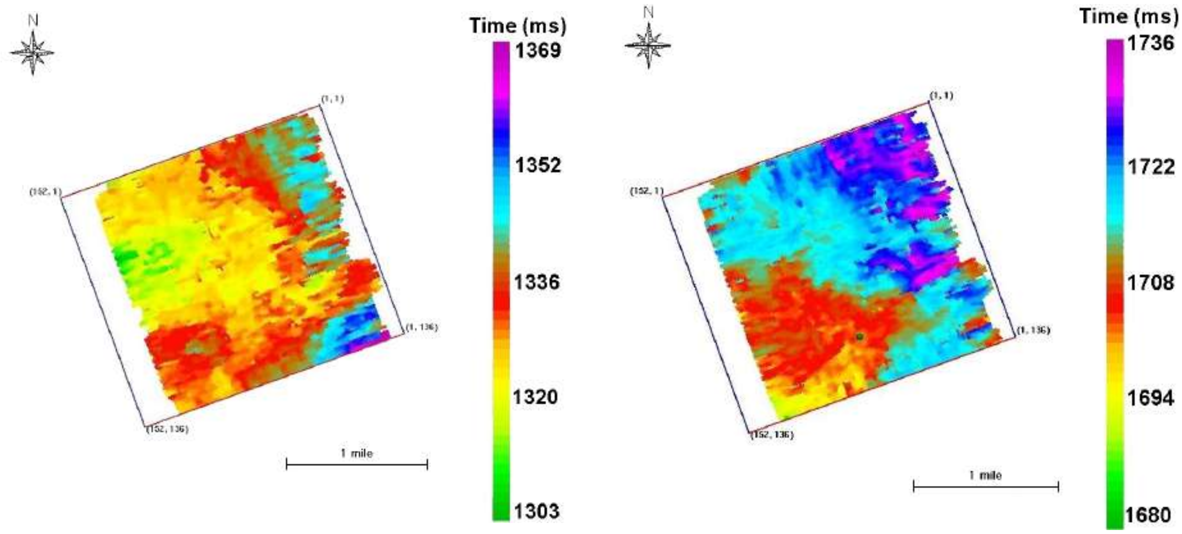

Figure 5.19. $\grave{P}\acute{S}_1$-wave time-structure maps for the UMV Shale horizon (left) and Cameo Coal horizon (right).

(approximately 1,250 ms to 1,750 ms in both $\grave{P}\acute{S}_1$- and $\grave{P}\acute{S}_2$- time). The results are shown on Figures 5.22 and 5.23.

Building the initial model

Both initial fast and slow converted-wave models were built by extrapolating the initial fast and slow pseudo-impedance logs (computed at the study well location) from the UMV Shale and top Cameo Coal horizons. Both $\grave{P}\acute{S}_1$- and $\grave{P}\acute{S}_2$- impedance logs computed using the sonic and density logs were low-pass filtered with a high-cut frequency of 5 Hz. The fast pseudo-impedance initial model (based on the $\grave{P}\acute{S}_1$-wave inversion) is shown in Figure 5.24 and the slow pseudo-impedance initial model (based on the $\grave{P}\acute{S}_2$-wave inversion) is shown in Figure 5.25 .

The $\grave{P}\acute{S}$-wave amplitude inversion

Both initial pseudo-impedance volumes were used to test different inversion parameters at the study well location. The optimum parameter set was found to be identical for both $\grave{P}\acute{S}_1$- and $\grave{P}\acute{S}_2$-wave inversions:

i) number of iterations: 5,

ii) pre-whitening filter: 1%,

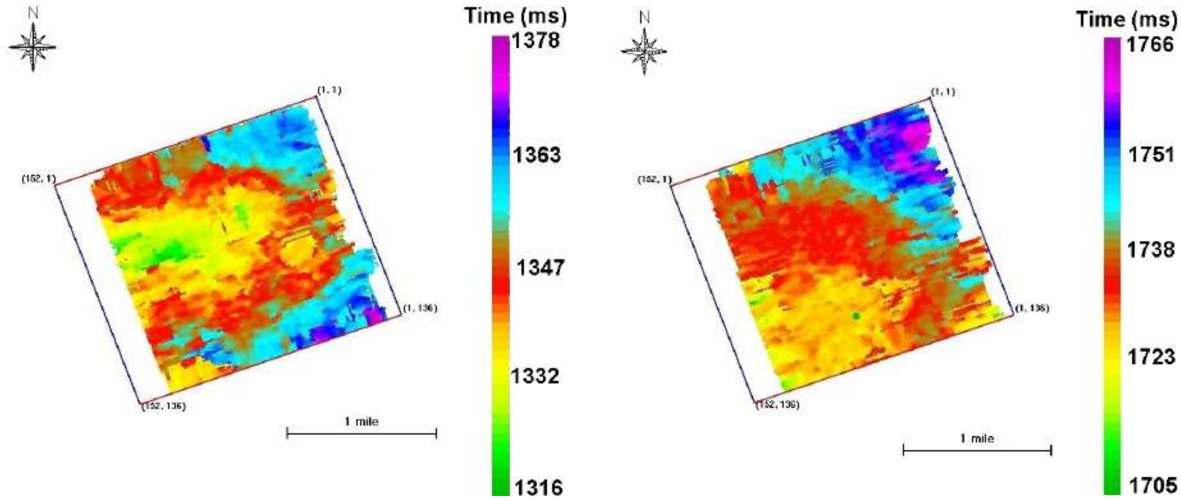

Figure 5.20. $\grave{P}\acute{S}_2$-wave time-structure maps for the UMV Shale horizon (left) and Cameo Coal horizon (right).

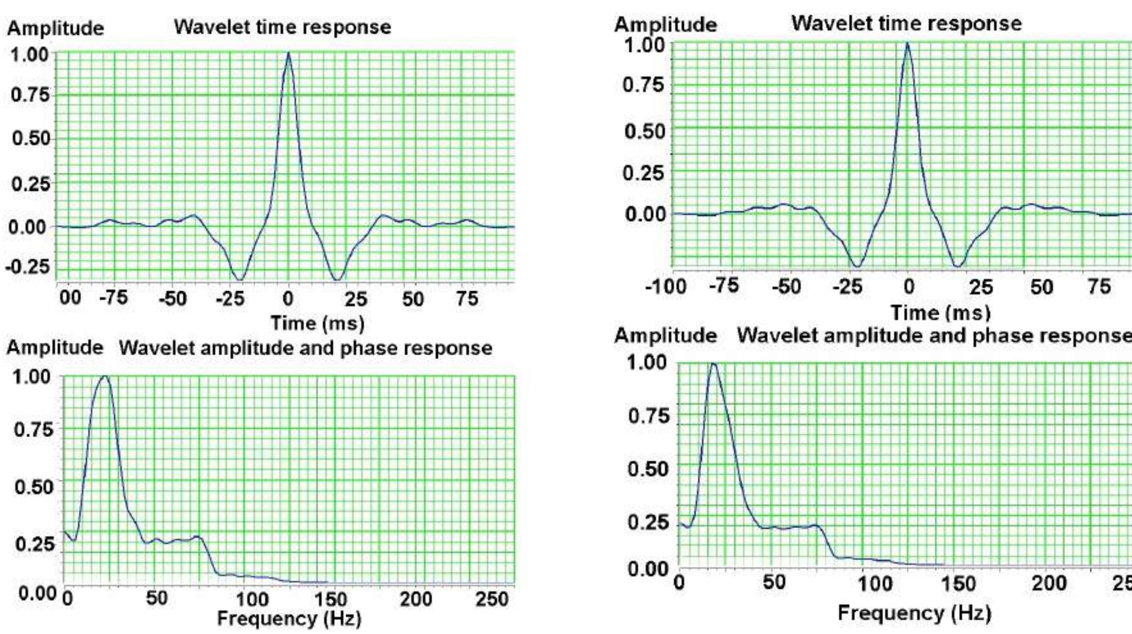

Figure 5.21. Extracted $\grave{P}\acute{S}_1$-wavelet time response (upper left figure) and frequency response (lower left figure) and $\grave{P}\acute{S}_2$-wavelet time response (upper right figure) and frequency response (lower right figure).

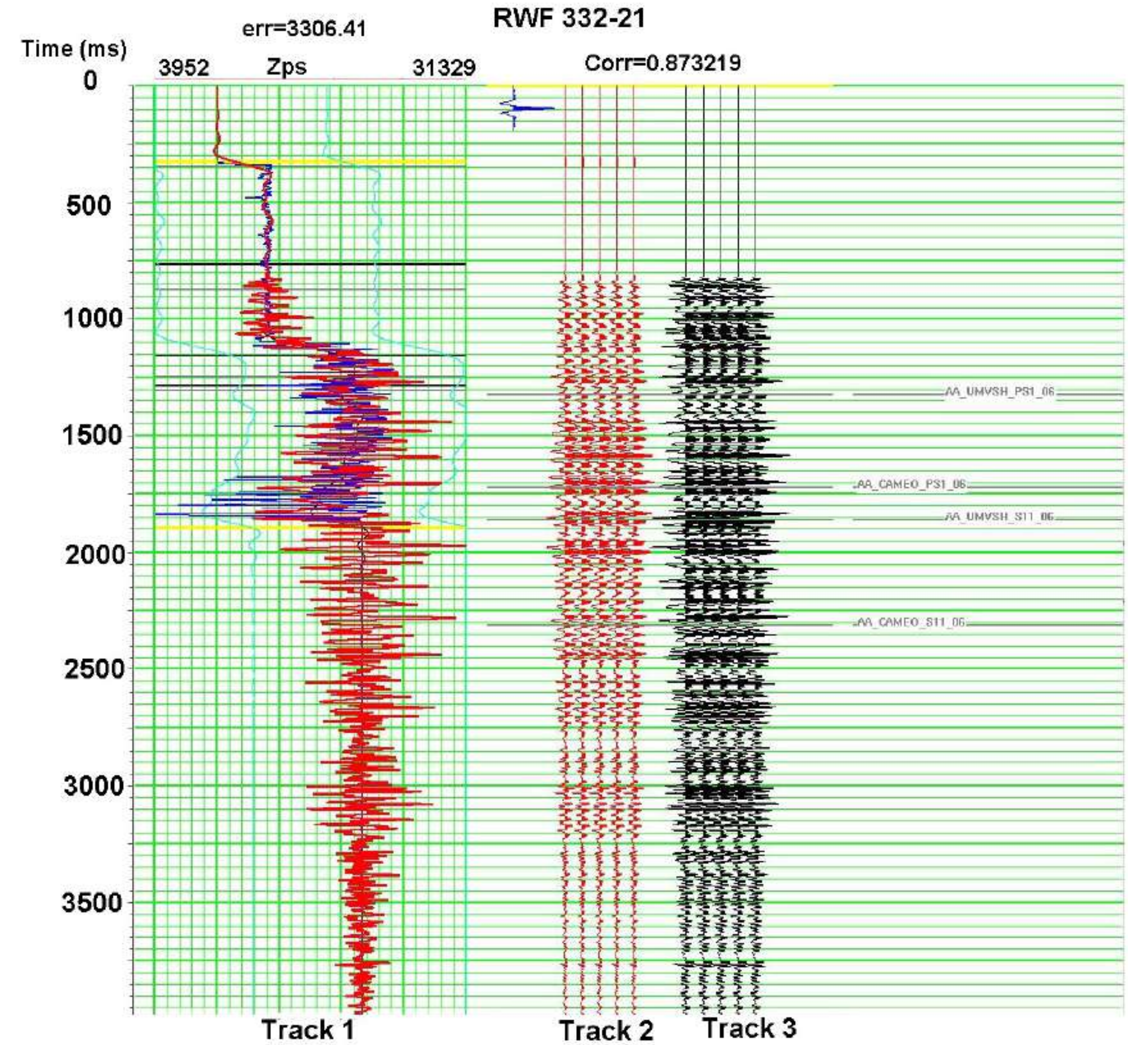

Figure 5.22. Synthetic $\grave{\mathrm{P}}\acute{\mathrm{S}}_1$ -seismogram analysis. Track 1 (left) shows the original fast pseudo-impedance log (in blue) and the inverted fast pseudo-impedance log (in red). Track 2 shows the synthetic $\grave{\mathrm{P}}\acute{\mathrm{S}}_1$-seismogram, and track 3 shows the actual observed $\grave{\mathrm{P}}\acute{\mathrm{S}}_1$-wave data. The correlation coefficient between the observed and synthetic data reached 87% in the reservoir interval (1,250 ms to 1,750 ms in $\grave{\mathrm{P}}\acute{\mathrm{S}}$-time). The extracted and scaled wavelet is represented in blue between tracks 1 and 2.

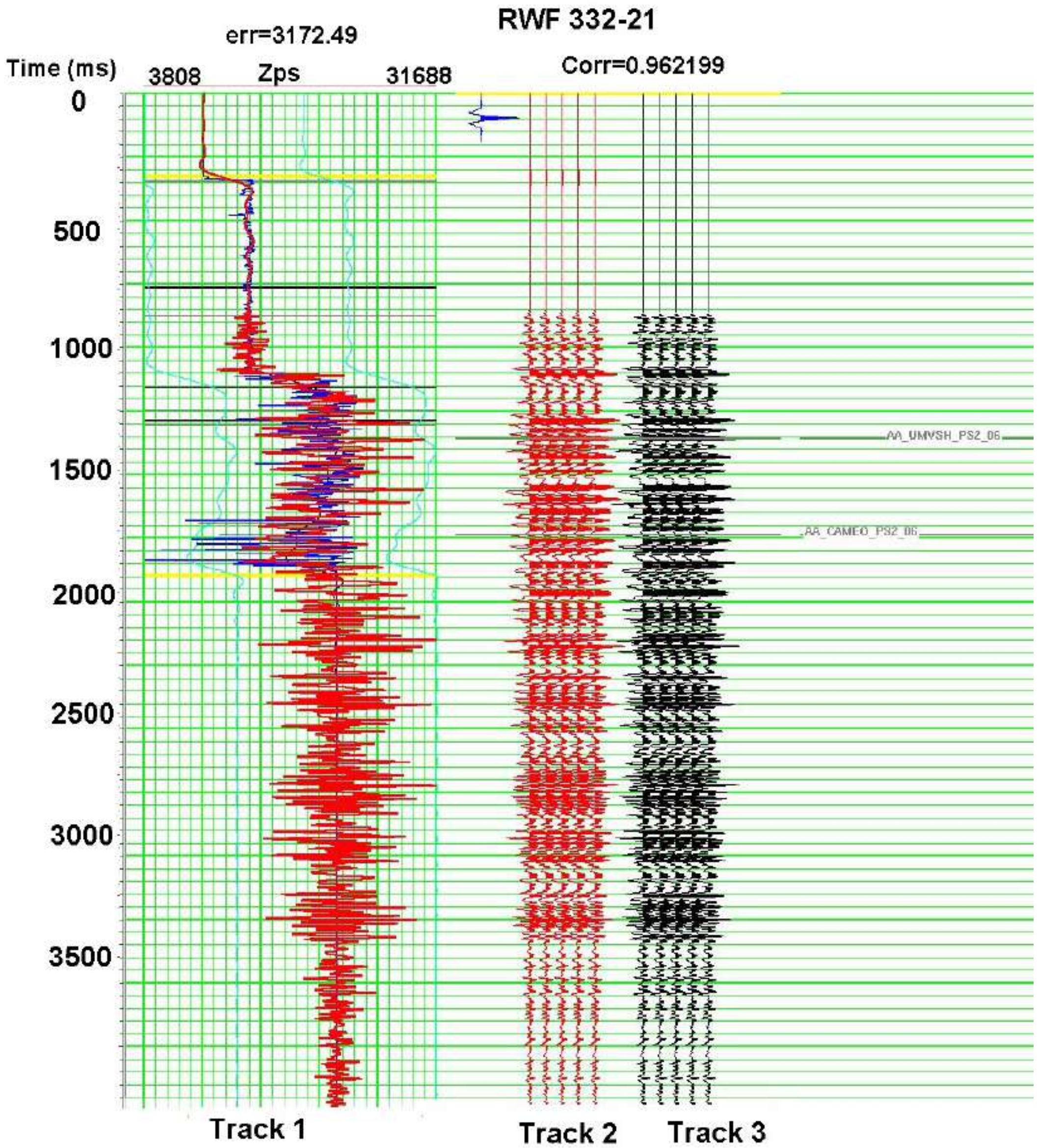

Figure 5.23. Synthetic $\grave{\mathrm{P}}\acute{\mathrm{S}}_2$-seismogram analysis. Track 1 (left) shows the original slow pseudo-impedance log (in blue) and the inverted slow pseudo-impedance log (in red). Track 2 shows the synthetic $\grave{\mathrm{P}}\acute{\mathrm{S}}_2$-seismogram and track 3 shows the actual observed $\grave{\mathrm{P}}\acute{\mathrm{S}}_2$-wave data. The correlation coefficient between the observed and synthetic data reached 96% in the reservoir interval (1,250 ms to 1,750 ms in $\grave{\mathrm{P}}\acute{\mathrm{S}}$-time). The extracted and scaled wavelet is represented in blue between tracks 1 and 2.

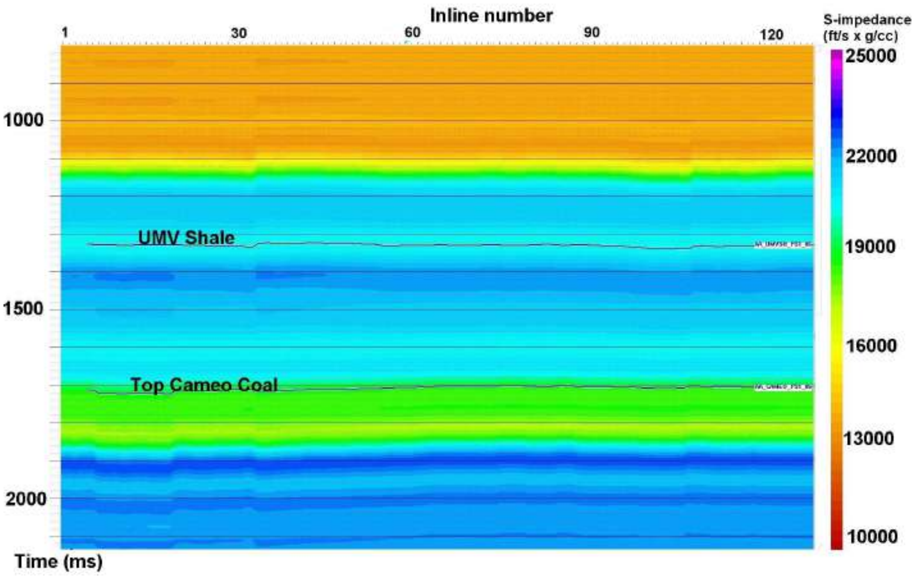

Figure 5.24. Crossline 109 of the low-pass filtered initial $\grave{\mathrm{P}}\acute{\mathrm{S}}_1$ pseudo-impedance model with a high-cut frequency of 5 Hz.

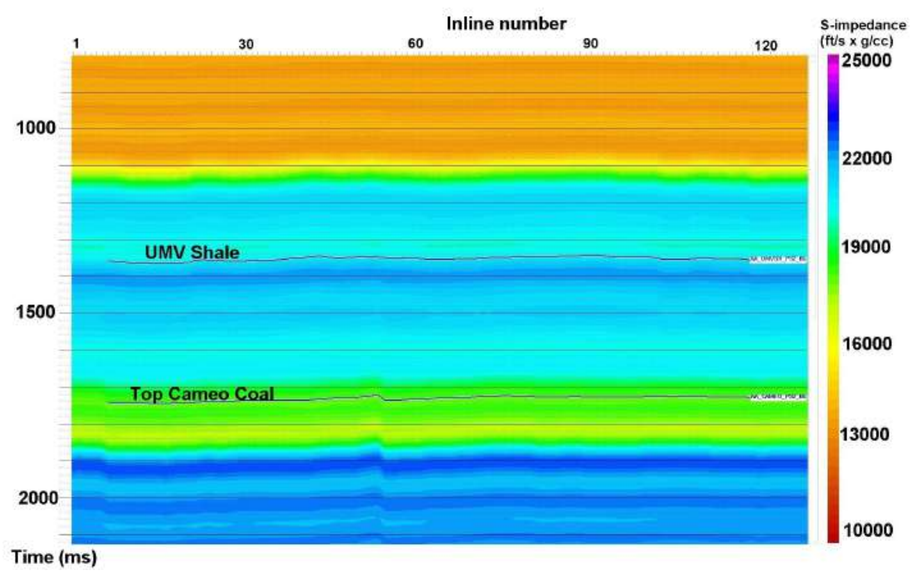

Figure 5.25. Crossline 109 of the low-passed filtered initial $\grave{\mathrm{P}}\acute{\mathrm{S}}_2$ pseudo-impedance model with a high-cut frequency of 5 Hz.

iii) maximum impedance variation from the initial model: ± 35 %,

iv) scalar adjustment factor: 0.5.

The $\grave{\mathrm{P}}\acute{\mathrm{S}}_1$- and $\grave{\mathrm{P}}\acute{\mathrm{S}}_2$-wave amplitude inversions successfully generated impedance models that match respectively the $\grave{\mathrm{P}}\acute{\mathrm{S}}_1$ and $\grave{\mathrm{P}}\acute{\mathrm{S}}_2$ pseudo-impedance logs at the RWF 332-21 location at 0-30 Hz bandwidth (see Figures 5.30 and 5.31). The crossline 109 of the $\grave{\mathrm{P}}\acute{\mathrm{S}}_1$-pseudo-impedance volume is shown in Figure 5.26 and the crossline 109 of the $\grave{\mathrm{P}}\acute{\mathrm{S}}_2$-pseudo-impedance volume is shown in Figure 5.27.

The first observation is that the top and bottom of the reservoir are observable on both volumes. On the other hand, compared to the pure shear-wave inversion, the producing sand bodies in the main gas reservoir have been better imaged. Multiple high impedance intervals that correspond to fluvial sand bodies (all of these high impedance intervals match with low gamma ray intervals on Figures 5.26 and 5.27) have been delineated: at the study well RWF 332-21 location, 11 sand bodies corresponding to low gamma ray values have been detected while the pure shear-wave inversion only resolved only 6 of them; at the well RMV 217-21 location (inline 63; crossline 109), 8 sand bodies have been detected while the pure shear-wave inversion only resolved 5 of them; at the well RMV 211-20 location (inline 114; crossline 107), 6 sand bodies have been detected while the pure shear-wave inversion only resolved 5 of them. The most important part in an exploration point of view is that the lateral extent of these fluvial sand bodies has been imaged. One can now exactly predict which well intersects which sand body, and thereby determine the location of the future wells to drill based on the inversion results.

A horizon-slice was extracted from the $\widehat{\mathrm{Z}}_{s2}$ volume (see Figure 5.28). The location where the horizon-slice was extracted is indicated by a red arrow in Figure 5.27. Two relatively wide geobodies are interpretable as well a clay-filled oxbow and a sand-rich point-bar. Oxbows and point-bars are typical features in meandering channel depositional systems and are now interpretable from pseudo-impedance volumes.

The strong shear impedance contrast between the fluvial sand bodies in Rulison

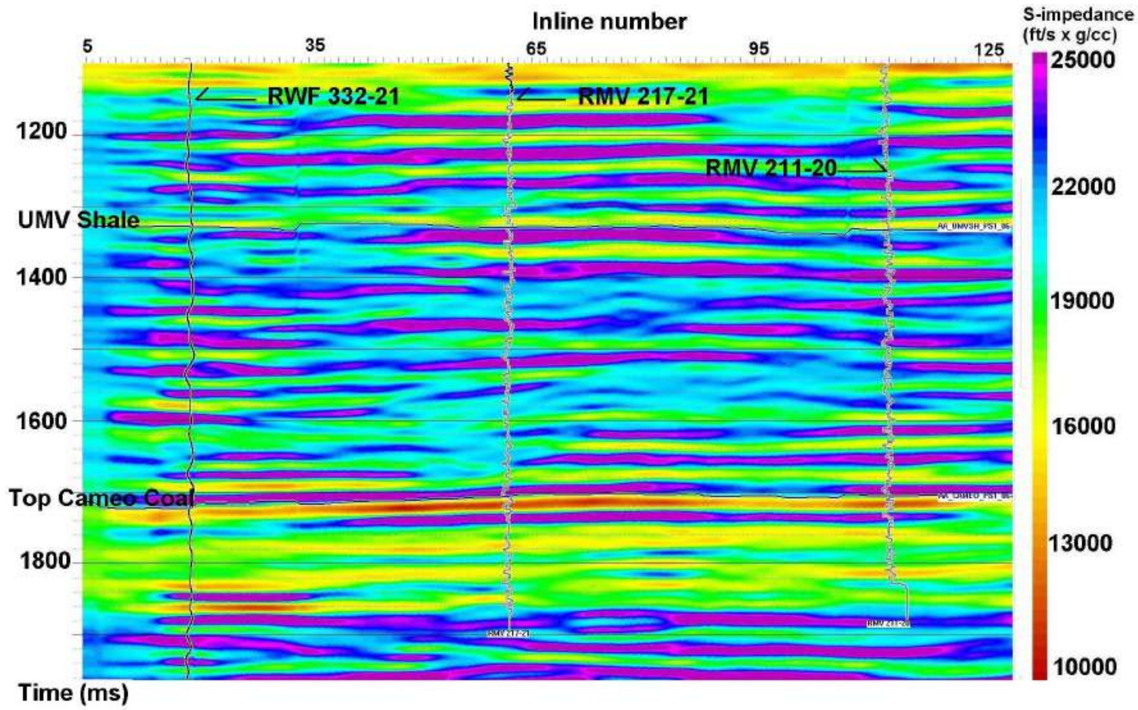

Figure 5.26. Crossline 109 from the $\widehat{Z}_{s1}$ volume: the fast converted-wave ($\grave{\mathrm{P}}\acute{\mathrm{S}}_1$-wave) inversion result with the study well RWF 332-21 low-pass filtered gamma-ray log displayed in black at the leftmost part of the figure. Two other high frequency gamma ray logs, corresponding to wells RMV 217-21 (inline 63; crossline 109) and RMV 211-20 (inline 114; crossline 107), are also displayed on this figure.

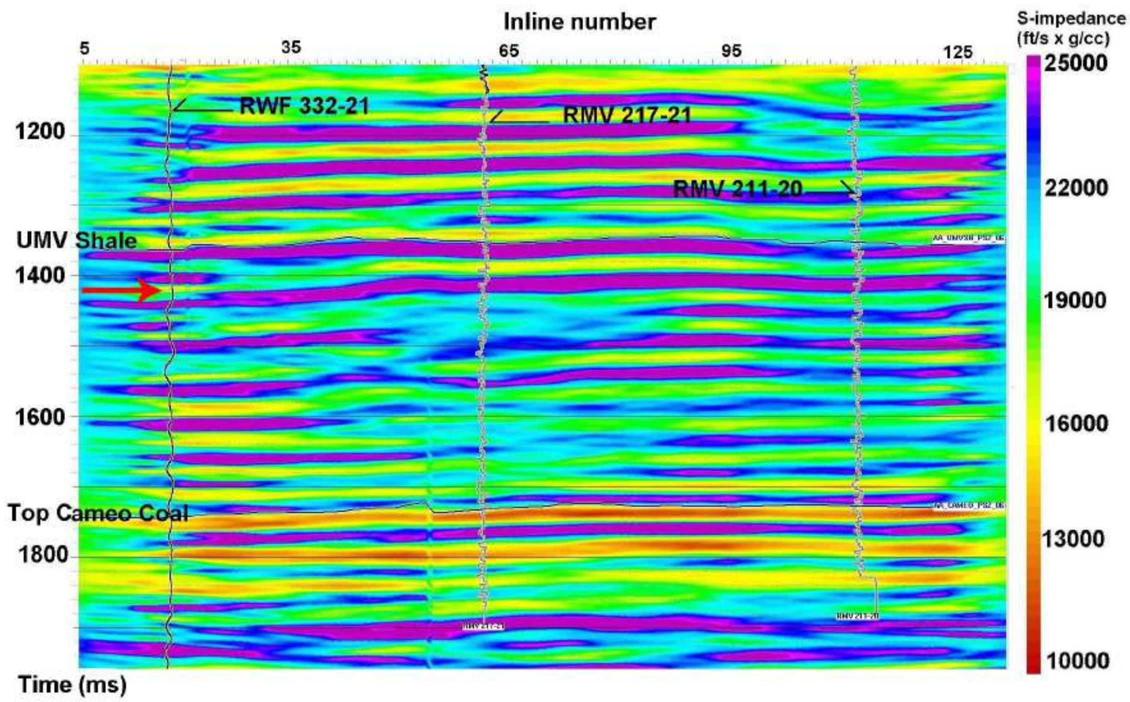

Figure 5.27. Crossline 109 from the $\widehat{Z}_{s2}$ volume: the slow converted-wave ($\grave{\mathrm{P}}\acute{\mathrm{S}}_2$-wave) inversion result with the study well RWF 332-21 low-pass filtered gamma-ray log displayed in black at the leftmost part of the figure. Two other high frequency gamma ray logs, corresponding to wells RMV 217-21 (inline 63; crossline 109) and RMV 211-20 (inline 114; crossline 107), are also displayed on this figure.

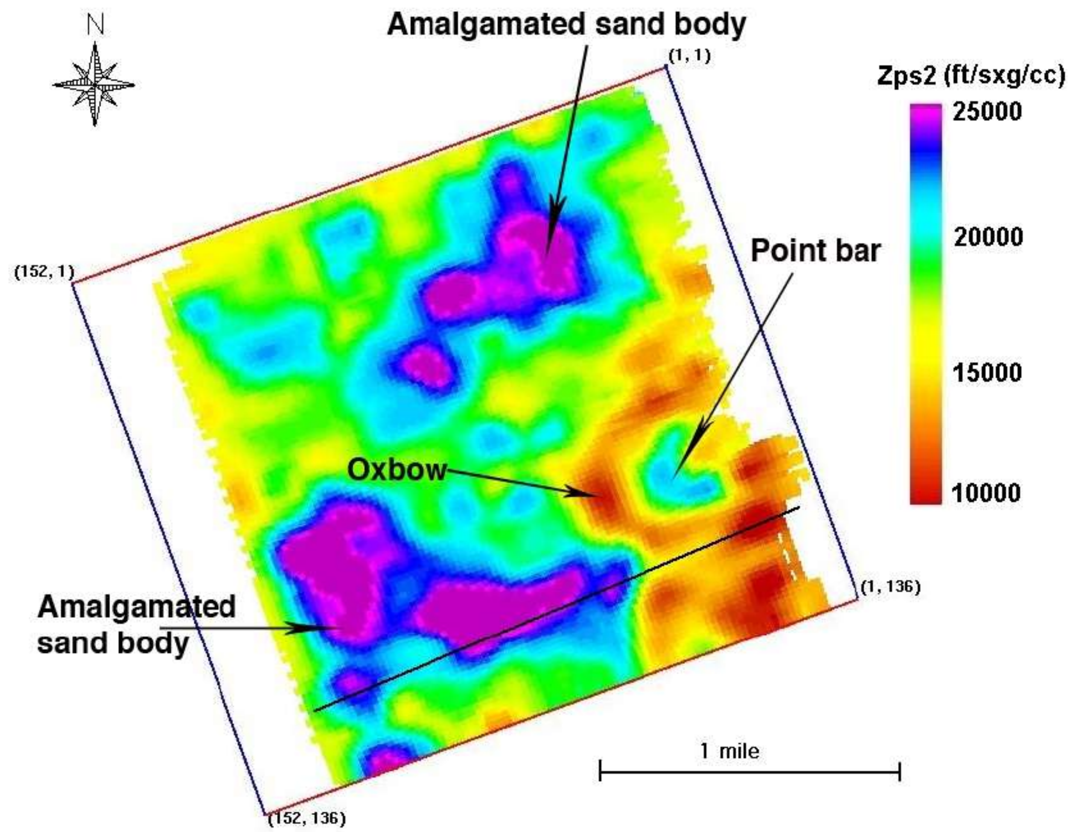

Figure 5.28. Horizon-slice from $\widehat{Z}_{s2}$ volume. The location where the horizon-slice was extracted is indicated by a red arrow in Figure 5.27. The location of crossline 109 is indicated by the black line. Two relatively wide amalgamated sand bodies are interpretable as well an oxbow and a point-bar.

and the adjacent non-marine shales is crucial for sand body delineation but does not explain why the sand bodies are better delineated using converted-waves compared to pure shear-waves. To understand this difference, a simple isotropic AVO modeling study was conducted. The typical elastic parameters for this study are shown in Table 5.1. The reflection coefficients for both converted and non-converted shear-waves are based on the Aki & Richards (1980) expressions:

$$R_{\grave{S}\acute{S}} = 1 - \frac{1}{2}\frac{\Delta\rho}{\overline{\rho}} + \left(\frac{1}{2\,\cos^2\theta_s} - 1\right)\frac{\Delta V_s}{\overline{V_s}}, \tag{5.32}$$

$$\begin{aligned} R_{\grave{P}\acute{S}} = & -\frac{\overline{V_p}}{\overline{V_s}}\frac{\tan\theta_s}{2}\left[\left(1 - 2\,\sin^2\theta_s + 2\,\frac{\overline{V_s}}{\overline{V_p}}\,\cos\theta_p\,\cos\theta_s\right)\frac{\Delta\rho}{\overline{\rho}}\right] \\ & + \frac{\overline{V_p}}{\overline{V_s}}\frac{\tan\theta_s}{2}\left[\left(4\,\sin^2\theta_s - 4\,\frac{\overline{V_s}}{\overline{V_p}}\,\cos\theta_p\;\;cos\theta_s\right)\frac{\Delta V_s}{\overline{V_s}}\right]. \end{aligned} \tag{5.33}$$

The $R_{\grave{P}\acute{S}}$ coefficient is plotted in red on Figure 5.29 and the $R_{\grave{S}\acute{S}}$ coefficient is plotted in blue on that same figure. The main observation is that the $R_{\grave{S}\acute{S}}$ coefficient is larger than the $R_{\grave{P}\acute{S}}$ coefficient (in terms of absolute values) up to an incidence angle of 18°. Therefore, on the poststack gathers, non-converted shear-wave amplitudes reflected from the fluvial sand bodies will be significantly larger than converted-wave amplitudes. Thus, the better results obtained from converted shear-wave inversion cannot be explained by the absolute values of the $R_{\grave{P}\acute{S}}$ coeffcient. The answer might be the frequency bandwidth of the converted-wave data compared to the pure shear-wave data. The P̀Ś-wave data have a larger bandwidth (0-40 Hz) than the S̀Ś-wave data (0-30 Hz) and the peak frequency for the P̀Ś-wave data (23 Hz) is larger than the peak frequency for the S̀Ś-wave data (17 Hz). The larger peak frequency as well as the wider frequency bandwidth for P̀Ś-wave data might explain why the converted-wave inversion leads to better sand body delineation.

In conclusion, the best inversion results are obtained by inverting the converted shear-wave seismic data. The inversion results allowed us to image the sand bodies not only in time but also laterally. Therefore, the shape and the location of the

	P-velocity (m/s)	S-velocity (m/s)	Density (g/cc)
Layer 1	4,590	2,440	2.58
Layer 2	4,710	2,870	2.61

Table 5.1. Elastic parameters for the two-layer isotropic model for the Rulison sand bodies.

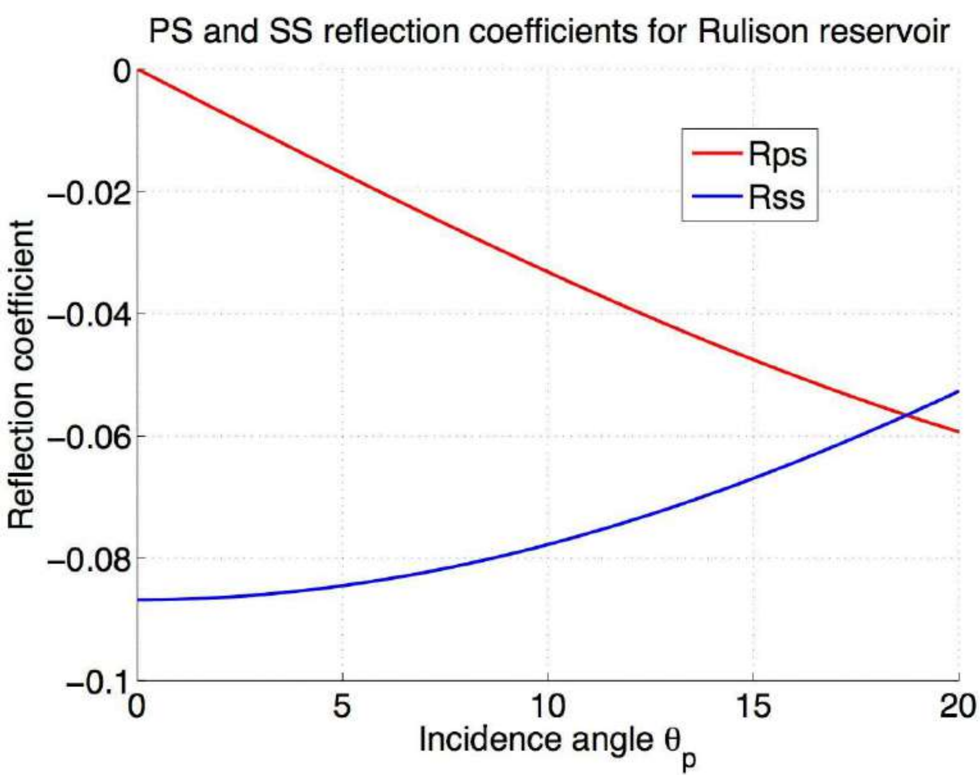

Figure 5.29. $\grave{P}\acute{S}$-wave and $\grave{S}\acute{S}$-wave reflection coefficients in the isotropic model for Rulison sand/shale interface. The elastic parameters for the two-layer isotropic model are given by Table 5.1. On these plots, the $R_{\grave{P}\acute{S}}$ coefficient is shown in red and the $R_{\grave{S}\acute{S}}$ coefficient is shown in blue.

lenticular sand bodies have been successfully determined from the high impedance intervals (in purple on Figures 5.26 and 5.27). This will improve the completion of existing wells and ensure better planning for the drilling of new wells in the area.

$\grave{P}\acute{S}$-wave inversion analysis

The original low-pass filtered $\grave{P}\acute{S}_1$-pseudo-impedance log at the study well location and the inverted $\grave{P}\acute{S}_1$-pseudo-impedance at the study well location extracted from the inverted $\grave{P}\acute{S}_1$-pseudo-impedance volume are represented in track 1 on Figure 5.30, while the original low-pass filtered $\grave{P}\acute{S}_2$-pseudo-impedance log at the study well location and the inverted $\grave{P}\acute{S}_2$-pseudo-impedance at the study well location extracted from the inverted $\grave{P}\acute{S}_2$-pseudo-impedance volume are represented in track 1 on Figure 5.31. These two figures show that at the study well location, for both $\grave{P}\acute{S}_1$- and $\grave{P}\acute{S}_2$-waves, the inverted pseudo-impedance and the low-pass filtered pseudo-impedance computed from the logs at the well location match very well. The correlation coefficient between the inverted pseudo-impedances and the original pseudo-impedances is higher than 92% for both converted-modes. On the other hand, the correlation coefficient between the observed $\grave{P}\acute{S}_1$-wave data and the synthetic $\grave{P}\acute{S}_1$-seismogram at the well location (track 2 on Figure 5.30) is equal to 98%; and the correlation coefficient between the observed $\grave{P}\acute{S}_2$-wave data and the synthetic $\grave{P}\acute{S}_2$-seismogram at the well location (track 2 on Figure 5.31) is equal to 99%. Therefore, compared to the pure-shear inversions, the results of the $\grave{P}\acute{S}$-wave inversions are slightly better: the correlation between the inverted pseudo-impedances and the ground truth (i.e the pseudo-impedance computed from the well log) is higher than 98% for both fast and slow converted-waves and the synthetic seismograms have exceptionally high correlation values with the actual recorded data.

5.3 $\grave{P}\acute{P}$-$\grave{P}\acute{S}$ Registration and Vp/Vs Volumes from Impedance Data

This section focuses on the generation of Vp/Vs volumes that are function of time and space. These volumes are generally referred to in the literature as *high resolution*

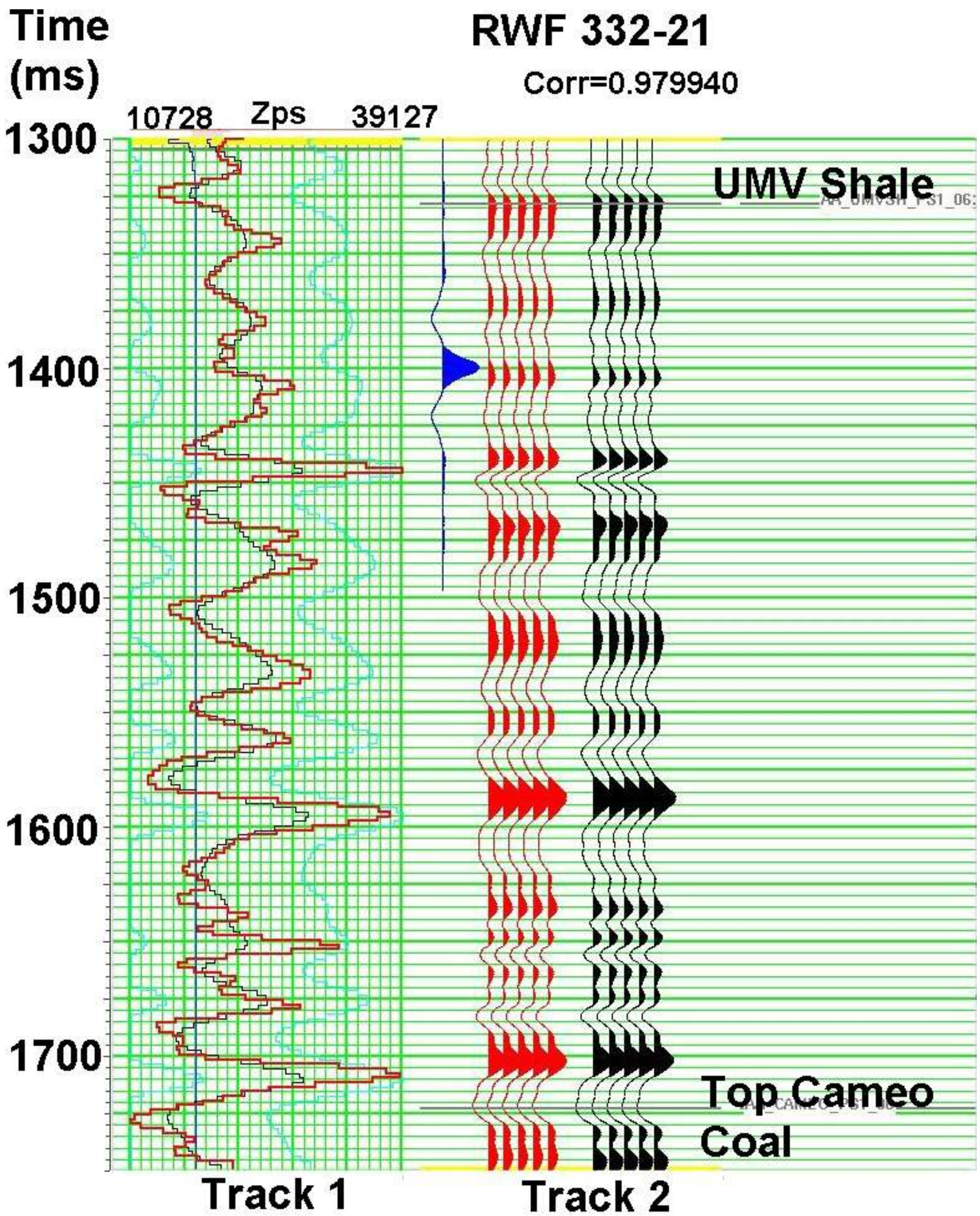

Figure 5.30. $\grave{P}\acute{S}_1$-wave inversion analysis. The ground truth low-pass filtered $\grave{P}\acute{S}_1$-impedance log (in blue) and the inverted $\grave{P}\acute{S}_1$-impedance at the study well location (in red) are represented in track 1. The synthetic $\grave{P}\acute{S}_1$-seismogram (in red) and the observed $\grave{P}\acute{S}_1$-seismic data (in black) at the study well location are represented in track 2; their correlation coefficient is equal to 98%.

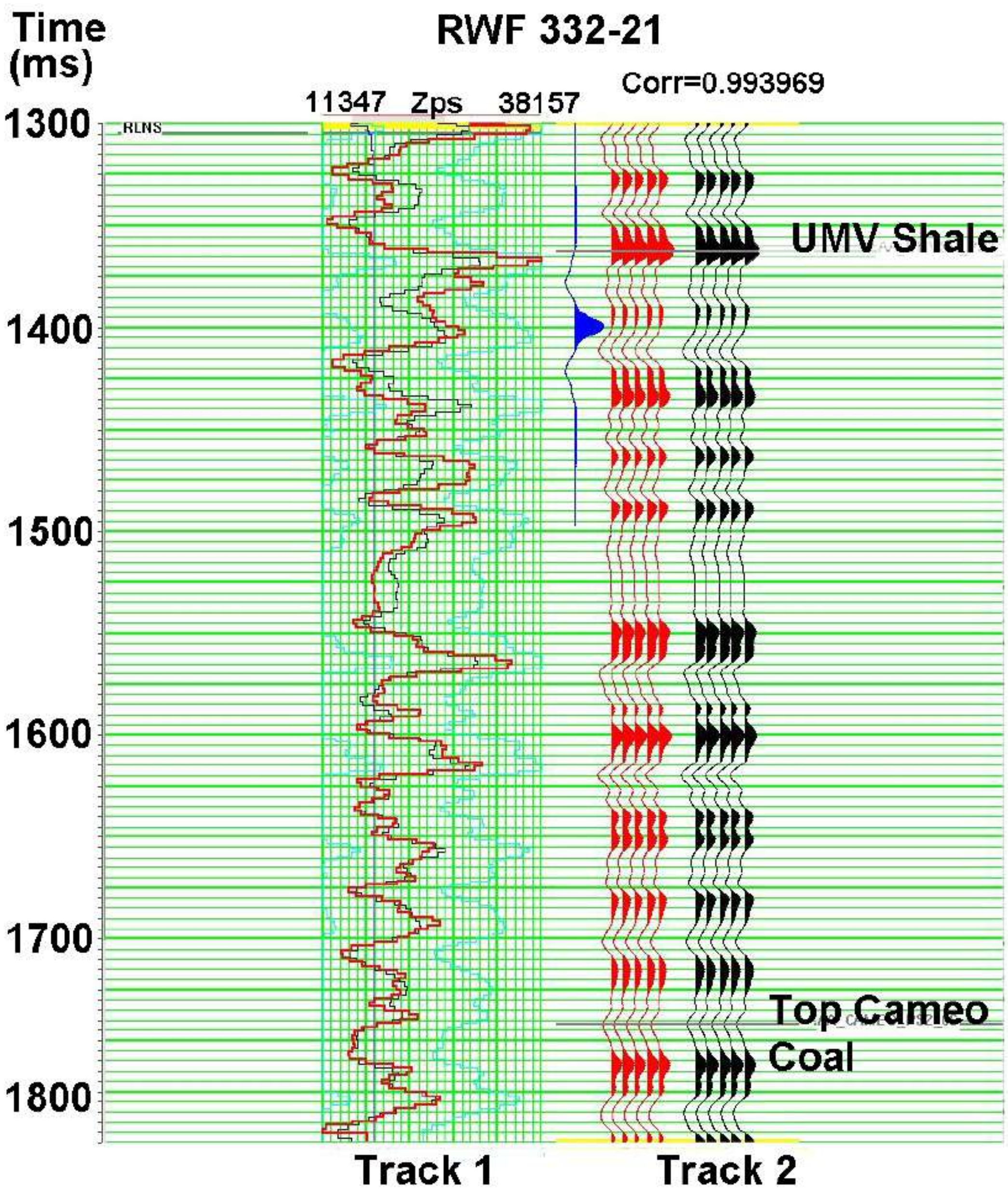

Figure 5.31. $\grave{\mathrm{P}}\acute{\mathrm{S}}_2$-wave inversion analysis. The ground truth low-pass filtered $\grave{\mathrm{P}}\acute{\mathrm{S}}_2$-impedance log (in blue) and the inverted $\grave{\mathrm{P}}\acute{\mathrm{S}}_2$-impedance at the study well location (in red) are represented in track 1. The synthetic $\grave{\mathrm{P}}\acute{\mathrm{S}}_2$-seismogram (in red) and the observed $\grave{\mathrm{P}}\acute{\mathrm{S}}_2$-seismic data (in black) at the study well location are represented in track 2; their correlation coefficient is equal to 99%.

Vp/Vs volumes (Guliyev, 2007).

5.3.1 Vp/Vs and Pseudo-Vp/Vs Volumes

The Vp/Vs volume is an important lithological tool that correlates to pressure regimes (Rojas, 2005): low Vp/Vs values correlate to overpressure regimes, while high Vp/Vs values correlate to underpressure or depletion regimes. The generation of high resolution Vp/Vs volumes is thus of great interest for reservoir characterization in Rulison Field and has been the major topic of different theses and studies (Rojas, 2005; Gulyiev, 2007, Meza, 2008; Davis et al., 2009). Following the work of Rojas (2005), low Vp/Vs values correlate to high sand content, high gas saturation, and high reservoir pressure or a combination of two of these three factors. Therefore, low Vp/Vs values are an indicator of better quality overpressured reservoir sands.

It is important to note that there are two Vp/Vs volumes: a Vp/Vs_1 volume and a Vp/Vs_2 volume, with Vs_1 being the fast shear-wave velocity and Vs_2 the slow shear-wave velocity. For the sake of simplicity, the notation Vp/Vs could refer to either of these two volumes.

The Vp/Vs volumes as a function of time and space can be computed using the P-impedance volume Z_p and the S-impedance volume Z_s:

$$\frac{Z_p}{Z_s}(x,y,t) = \frac{\rho\, V_p(x,y,t)}{\rho\, V_s(x,y,t)} = \frac{V_p}{V_s}(x,y,t), \tag{5.34}$$

where ρ is the density, (x,y) the spatial coordinates, and t the vertical two-way traveltime, which should be the same for both P- and S-impedance volumes. The traveltime t could correspond to $\grave{\mathrm{P}}\acute{\mathrm{P}}$- or $\grave{\mathrm{S}}\acute{\mathrm{S}}$-wave traveltime or even to depth if the time-depth functions for both P-wave and S-wave are available for the time-depth conversion.

On the other hand, high resolution pseudo-Vp/Vs volumes can be computed using the pseudo-impedance volumes defined and computed in the previous section:

$$\frac{Z_p}{\widehat{Z_s}}(x,y,t) = \frac{\rho\, V_p(x,y,t)}{\widehat{\rho}\, V_s(x,y,t)} = \frac{\rho}{\widehat{\rho}}\frac{V_p}{V_s}(x,y,t), \tag{5.35}$$

where $\widehat{\rho}$ is the pseudo-density given by equation (5.16). Vp/Vs and pseudo-Vp/Vs volumes are equal only when Vp/Vs=2. Vp/Vs and pseudo-Vp/Vs volumes have identical behaviors with respect to the vertical-axis and relate to the same lithological variations. Only their actual values differ. For the rest of this study we will be interested in pseudo-Vp/Vs volumes, and for the sake of simplicity, we will just refer to these volumes as Vp/Vs volumes.

5.3.2 Multicomponent Resolution

Vertical resolution

The vertical resolution of seismic data is usually determined from the Rayleigh criterion that states that the minimum resolvable thickness L is approximately equal to one quarter of the seismic wavelength λ given by:

$$\lambda = \frac{V}{f}, \tag{5.36}$$

where V represents the interval velocity and f the dominant frequency of the seismic wave. In order to generate Vp/Vs volumes from P- and $\grave{\text{P}}\acute{\text{S}}$-wave data, the vertical resolution of these two seismic volumes should be similar. For P-wave data, the dominant frequency f_p is equal to 30 Hz. From the traveltime analysis in Chapter 3, the vertical velocity V_{P0} has been shown to be close to 13,000 ft/s for the top of the reservoir at Rulison. For $\grave{\text{P}}\acute{\text{S}}$-wave data, the dominant frequency f_{ps} is equal to 23 Hz; and from the traveltime analysis conducted in Chapter 3, the S-wave vertical velocity V_{s0} has been shown to be close to 6,400 ft/s for the top of the reservoir. Therefore, the $\grave{\text{P}}\acute{\text{S}}$-wave vertical velocity V_{ps0} can be estimated as the arithmetic mean of V_{p0} and V_{s0}. Therefore, V_{ps0} is considered to be equal to 9,700 ft/s. This V_{ps0} value corresponds to the vertical $\grave{\text{P}}\acute{\text{S}}$-wave two-way traveltime at the top of the reservoir

(1,320 ms in Figure 2.3) at 6,000 ft of depth. Therefore, the P-wave wavelength λ_p and the $\grave{\text{P}}\acute{\text{S}}$-wave wavelength λ_{ps} are equal to:

$$\lambda_p = \frac{V_{p0}}{f} \approx \frac{13000}{30} \approx 433ft, \tag{5.37}$$

$$\lambda_{ps} = \frac{V_{ps0}}{f} \approx \frac{9700}{23} \approx 422ft. \tag{5.38}$$

Therefore, $\lambda_p \approx \lambda_{ps}$. This result means that both wave modes have almost the same resolution on their original time domain and bandwidth.

In order to create the Vp/Vs volumes, the $\grave{\text{P}}\acute{\text{S}}$-wave data will be registered to P-wave time. This means that the $\grave{\text{P}}\acute{\text{S}}$-wave volume will be a function of the spatial coordinates x and y, and the P-wave time. This process explained in the next subsection involves squeezing and event matching processes that change the bandwidth of the converted-wave data. After squeezing, both P-wave and $\grave{\text{P}}\acute{\text{S}}$-wave data will have comparable dominant frequency (≈30 Hz), and after the event matching, the P-wave and $\grave{\text{P}}\acute{\text{S}}$-wave arrival times will be identical (Meza, 2008). Therefore even after registration, $\lambda_p \approx \lambda_{ps}$. Considering the Rayleigh criterion stated in the beginning of this subsection, the minimum resolvable thickness L in this case is equal to:

$$L \approx \frac{\lambda_p}{4} \approx \frac{\lambda_{ps}}{4} \approx 105ft. \tag{5.39}$$

The average sand body thickness in the Rulison reservoir is close to 10 ft. Imaging the Rulison sand bodies using 3D seismic data is therefore an unrealistic task since the minimum resolvable thickness is equal to 105 ft. Nevertheless, it is possible to identify layers thiner than the wavelength, but the amplitude response may be distorted by tuning. In case of impedance data derived from seismic amplitude data, the tuning thickness is one third of that for amplitude data (Hill, 2005). Therefore, the vertical resolution of the impedance data is close to 35 ft and some of the stacked amalgamated sand bodies can therefore be imaged from impedance data.

Lateral resolution

The Fresnel-zone concept, borrowed from optics, is often used to estimate the lateral resolution of unmigrated stacked P-wave data. This concept can be extended in oder to estimate the lateral resolution of P̀Ś-wave data (Eaton et al., 1991).

For a layer of thickness z, and a dominant wavelength λ_p, the Fresnel-zone can be expressed as:

$$R_{Fp} = \left(\frac{\lambda_p z}{\gamma}\right)^{1/2}, \tag{5.40}$$

where λ_p/γ expresses the limiting two-way path length difference. Following the Sheriff (1980) criterion, γ is set to 2. Therefore,

$$R_{Fp} = (\lambda_p z)^{1/2}. \tag{5.41}$$

For the Rulison reservoir case, $\lambda_p \approx 430$ ft as previously shown, and the thickness of the reservoir z is approximately equal to 2,000 ft. Therefore, $R_{Fp} \approx 927$ ft.

Following the work of Eaton et al. (1991), the Fresnel-zone for P̀Ś-waves can be expressed as:

$$R_{Fps} = \left(\frac{V_p\, V_s\, z\, k}{f_{ps}(V_p\, z + V_s\, k)}\right)^{1/2}, \tag{5.42}$$

where V_p is the P-wave vertical velocity, V_s is the S-wave vertical velocity, z is the layer thickness, k is the distance from the receiver to the base of the layer, and f_{ps} is the P̀Ś-wave dominant frequency.

For the main gas reservoir, $V_p \approx 13{,}000$ ft/s, $V_s \approx 6{,}500$ ft/s, $z \approx 2{,}000$ ft, $k \approx 8{,}000$ ft, and $f_{ps} \approx 23$ Hz. Therefore, $R_{Fps} \approx 868$ ft. Therefore, $R_{Fp} \approx R_{Fps}$ and both unmigrated and stacked P-wave and P̀Ś-wave data have similar lateral resolution. Furthermore, in the case of ideal migrated datasets, one would expect to have $R_F \approx \lambda/4$ (Lines & Newrick, 2004). Ideally, migration would reduce the Fresnel zone from 868 ft to 105 ft. Since $\lambda_p \approx \lambda_{ps}$, therefore, even for migrated datasets, the approximation $R_{Fp} \approx R_{Fps}$ still holds.

Conclusion

In conclusion, unregistered P- and P̀Ś-wave datasets have similar vertical resolution. This is also true for registered datasets. Furthermore, unmigrated and migrated P- and P̀Ś-wave datasets have similar lateral resolutions. Therefore, both P- and P̀Ś-wave volumes, and by extension the impedance volumes inverted from these seismic datasets, are suitable to be jointly processed in order to build the Vp/Vs volumes.

5.3.3 P̀Ṕ-P̀Ś Registration

In order to properly compare P- and P̀Ś-wave volumes, one should have a common vertical scale for both datasets. This is a crucial step in order to properly build the Vp/Vs volumes by dividing the P-impedance by the pseudo-S-impedance.

The registration of the P-impedance and the pseudo-S-impedance volumes was done using the Transfrom TerraMorph software which allows 3D interactive registration of seismic events (Meza, 2008). The P̀Ṕ- and P̀Ś-wave volumes to be registered must have the same grid spacing. The P̀Ṕ- and P̀Ś-wave volumes can either be seismic data volumes or inverted impedance volumes. Since the vertical sampling for the P̀Ś-wave data is larger because of its slower velocities and longer traveltimes, subsets of both P̀Ṕ- and P̀Ś-wave volumes corresponding to their common area were generated. If the volumes that are dealt with are actual seismic data, another step is necessary before starting the registration process. This step is to create the envelope amplitude of both P̀Ṕ- and P̀Ś-wave data and to use these envelopes in the building of the gamma function that is necessary for the registration. This step removes the problem of correlating two datasets with different phase properties.

The next step was to register the $\grave{P}\acute{S}_1$-wave data to P̀Ṕ-time by stretching and squeezing the $\grave{P}\acute{S}_1$-wave data to find likely correlations between P̀Ṕ-wave data and $\grave{P}\acute{S}_1$-wave data. This process generated a Vp/Vs volume denoted in this case as $\gamma_1 = \mathrm{Vp/Vs}_1$. The $\grave{P}\acute{S}_2$-wave data were also registered to P̀Ṕ-time by stretching and squeezing the $\grave{P}\acute{S}_2$-wave data to find likely correlations between P̀Ṕ-wave data and $\grave{P}\acute{S}_2$-wave data. This process generated another Vp/Vs volume denoted in this case as $\gamma_2 = \mathrm{Vp}/\mathrm{Vs}_2$.

The γ_1 and γ_2 functions are built by an iterative process. Both γ_1 and γ_2 have an initial value of two everywhere in time and space. We will first deal with the γ_1 function. The γ_2 function will be built exactly in the same way by using the $\grave{\mathrm{P}}\acute{\mathrm{S}}_2$ impedance data. The registration and the gamma function building will be performed exclusively on the inverted impedance data because the final aim of this process is the generation of high resolution Vp/Vs volumes. Therefore, by $\grave{\mathrm{P}}\acute{\mathrm{P}}$ data we mean the impedance volume Z_p and by $\grave{\mathrm{P}}\acute{\mathrm{S}}$ data we mean the pseudo-S-impedance volume $\widehat{Z_s}$.

An automated picking process starts by picking an event in the $\grave{\mathrm{P}}\acute{\mathrm{S}}_1$-data volume on its natural time domain and then the $\grave{\mathrm{P}}\acute{\mathrm{S}}_1$-dataset is squeezed vertically until an event on the $\grave{\mathrm{P}}\acute{\mathrm{P}}$-data is found that visually correlates the picked event on $\grave{\mathrm{P}}\acute{\mathrm{S}}_1$-data. Then iteratively, few common seismic events will be picked generating at each iteration a finer squeeze of the $\grave{\mathrm{P}}\acute{\mathrm{S}}_1$-data volume. The final amount of vertical squeezing defines the γ_1 function (Meza, 2008). In the left panel of Figure 5.32, the $\grave{\mathrm{P}}\acute{\mathrm{P}}$-data are displayed as an inline and the $\grave{\mathrm{P}}\acute{\mathrm{S}}_1$-data are displayed as a crossline both on their natural time domain. In the middle panel are displayed the $\grave{\mathrm{P}}\acute{\mathrm{P}}$-data as an inline and the registered $\grave{\mathrm{P}}\acute{\mathrm{S}}_1$-data as a crossline. In other words, the $\grave{\mathrm{P}}\acute{\mathrm{S}}_1$-data is displayed in $\grave{\mathrm{P}}\acute{\mathrm{P}}$-time. Finally, in the left panel on Figure 5.32, is represented the γ_1 function that was used for the registration of the $\grave{\mathrm{P}}\acute{\mathrm{S}}_1$-data to $\grave{\mathrm{P}}\acute{\mathrm{P}}$-time. On Figure 5.33 are represented the exact same displays as on Figure 5.32 for the registration of the $\grave{\mathrm{P}}\acute{\mathrm{S}}_2$-data to $\grave{\mathrm{P}}\acute{\mathrm{P}}$-time.

From Figures 5.32 and 5.33 we can conclude that:

i) the impedance volumes, as stated before, were comparable in term of wavelength and were suitable for a registration process,

ii) the registration successfully mapped the $\grave{\mathrm{P}}\acute{\mathrm{S}}$-data into $\grave{\mathrm{P}}\acute{\mathrm{P}}$-time,

iii) as one would have expected from previous geological and geophysical studies done in Rulison (Rojas, 2005), both gamma functions (γ_1 and γ_2) have their values included in the interval 1.80-1.95.

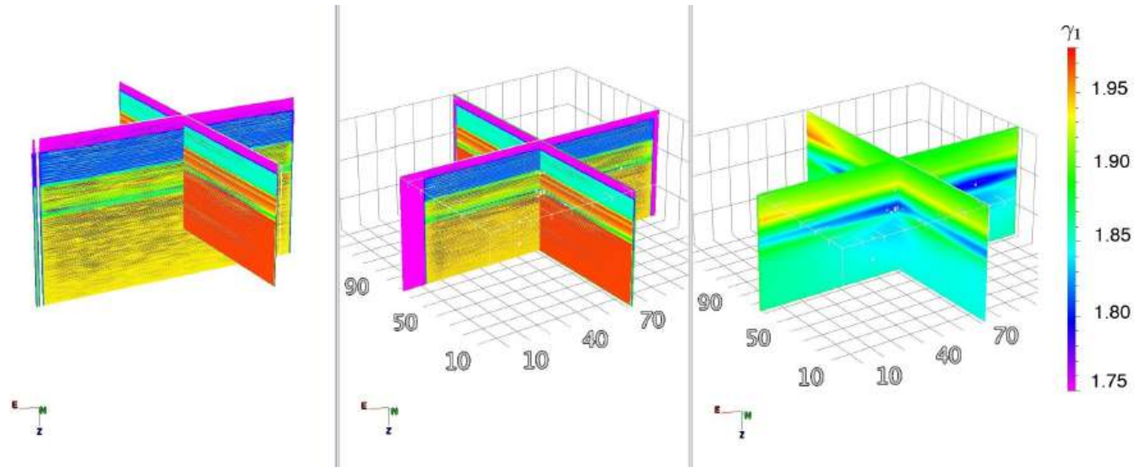

Figure 5.32. Registering the $\widehat{Z}_{s1}$ volume. In the left panel, the $\grave{\mathrm{P}}\acute{\mathrm{P}}$-impedance data are displayed as an inline, and the $\grave{\mathrm{P}}\acute{\mathrm{S}}_1$-impedance data are displayed as a crossline both on their natural time domain. In the middle panel are displayed the $\grave{\mathrm{P}}\acute{\mathrm{P}}$-data as an inline and the registered $\grave{\mathrm{P}}\acute{\mathrm{S}}_1$-data as a function of $\grave{\mathrm{P}}\acute{\mathrm{P}}$-time as a crossline. On the right panel is shown the $\gamma_1 = Vp/Vs_1$ function that was used in order to perform the registration of the $\grave{\mathrm{P}}\acute{\mathrm{S}}_1$-data to $\grave{\mathrm{P}}\acute{\mathrm{P}}$-time.

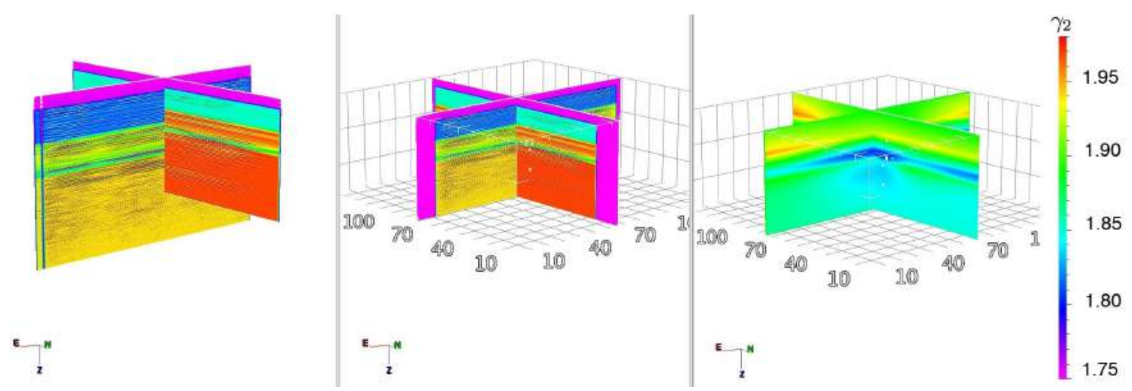

Figure 5.33. Registering the $\widehat{Z}_{s2}$ volume. In the left panel, the $\grave{\mathrm{P}}\acute{\mathrm{P}}$-impedance data are displayed as an inline and the $\grave{\mathrm{P}}\acute{\mathrm{S}}_2$-impedance data are displayed as a crossline both on their natural time domain. In the middle panel are displayed the $\grave{\mathrm{P}}\acute{\mathrm{P}}$-data as an inline and the registered $\grave{\mathrm{P}}\acute{\mathrm{S}}_2$-data as a function of $\grave{\mathrm{P}}\acute{\mathrm{P}}$-time as a crossline. On the right panel is shown the $\gamma_2 = Vp/Vs_2$ function that was used in order to perform the registration of the $\grave{\mathrm{P}}\acute{\mathrm{S}}_2$-data to $\grave{\mathrm{P}}\acute{\mathrm{P}}$-time.

5.3.4 High-resolution Vp/Vs Volumes

Now that the $\grave{P}\acute{S}$-data volumes have been registered to $\grave{P}\acute{P}$ time, the division of the P-impedance volume by the registered pseudo-S-impedance volumes will be performed. The crossline 109 of the Vp/Vs_1 volume is shown in Figure 5.34, and the crossline 109 of the Vp/Vs_2 volume is shown in Figure 5.35. The low frequency filtered gamma ray at the study well location is shown on both figures (the leftmost curve), while the two other gamma-ray curves represented on both figures correspond to wells RMV 217-21 and RMV 210-20. It is important to note that the absolute Vp/Vs values are not interpretable. As mentioned before, these are not actual Vp/Vs volumes but pseudo-Vp/Vs volumes. From these pseudo-volumes, one can draw several conclusions:

i) Low gamma ray values correspond to low Vp/Vs values; and the low Vp/Vs values correlate well with the high pseudo-S-impedance beds obtained from the $\grave{P}\acute{S}$-wave inversion. Therefore, the low Vp/Vs intervals correspond to better quality overpressured clay-free gas-bearing sand bodies.

ii) The Vp/Vs volumes are effective indicators of lithology: low Vp/Vs intervals correlate with the best sandstone reservoir quality and high Vp/Vs intervals correlate with shale intervals.

iii) The impedance inversion combined with the high resolution Vp/Vs volumes give us more confidence about the relative location and the lateral extent of the gas-bearing lenticular fluvial sand bodies in Rulison.

iv) The wavy shape of some of the low and high Vp/Vs intervals as well as most of the structure and faulting seen on these Vp/Vs volumes are fictitious. These phenomena are due to the registration process that is largely based on a manual picking and correlation of events. The way to get rid of these fictitious phenomena is to build a fully automated registering and warping algorithm.

v) Meza (2008) generated Vp/Vs volumes based on the inversion of pure shear-wave data from the 2003, 2004, and 2006 surveys. He then performed a time-lapse analysis on these Vp/Vs volumes and linked the observed changes to the reservoir depletion (Meza, 2008; Davis et al., 2009). In this thesis, Vp/Vs volumes were generated based on converted-wave inversion because converted-waves are more widely used in the industry, and because the converted-wave inversion gave better results than the pure shear-wave inversion: the number of imaged sand bodies in the vicinity of the study well location increased by 40% using the converted-wave inversion. Finally, a time-lapse study was not performed on the different pseudo-Vp/Vs volumes corresponding to the three available surveys because of the problems encountered during the registration process. As already mentioned, the registration process introduces errors due to manual correlation of seismic events between the $\grave{\mathrm{P}}\acute{\mathrm{P}}$- and $\grave{\mathrm{P}}\acute{\mathrm{S}}$-impedance volumes, and therefore, the discrimination between Vp/Vs time-lapse anomalies due to reservoir depletion, and anomalies due to uncorrelated manual errors in the registration of the different impedance volumes over the three surveys will be hard to achieve without other additional data (production data, pressure data...).

5.4 Instantaneous Anisotropy

Another topic that can be investigated using the inverted pseudo-S-impedance volumes, or equivalently the Vp/Vs$_1$ and Vp/Vs$_2$ volumes, is the anisotropy based on the shear-wave splitting denoted as $\gamma^{(S)}$ in Chapter 3. Now that we have two volumes $\widehat{Z_{s1}}$ and $\widehat{Z_{s2}}$ as a function of time and the spatial coordinates, the fractional difference between these two volumes (or equivalently the fractional difference between the Vp/Vs$_1$ and Vp/Vs$_2$ volumes) corresponds to the instantaneous shear-wave splitting: shear-wave splitting affects the amplitude of the converted-waves and, therefore, the impedance volumes derived from the $\grave{\mathrm{P}}\acute{\mathrm{S}}$-wave amplitude inversion. Thus, this is a technique for determining in space and vertical propagation time the location of high azimuthal shear-wave anisotropy and high fracture density. The subtraction was first performed on the pseudo-S-impedance volumes instead of the Vp/Vs volumes because of some of the fictitious phenomena observed on the velocity ratio volumes. These

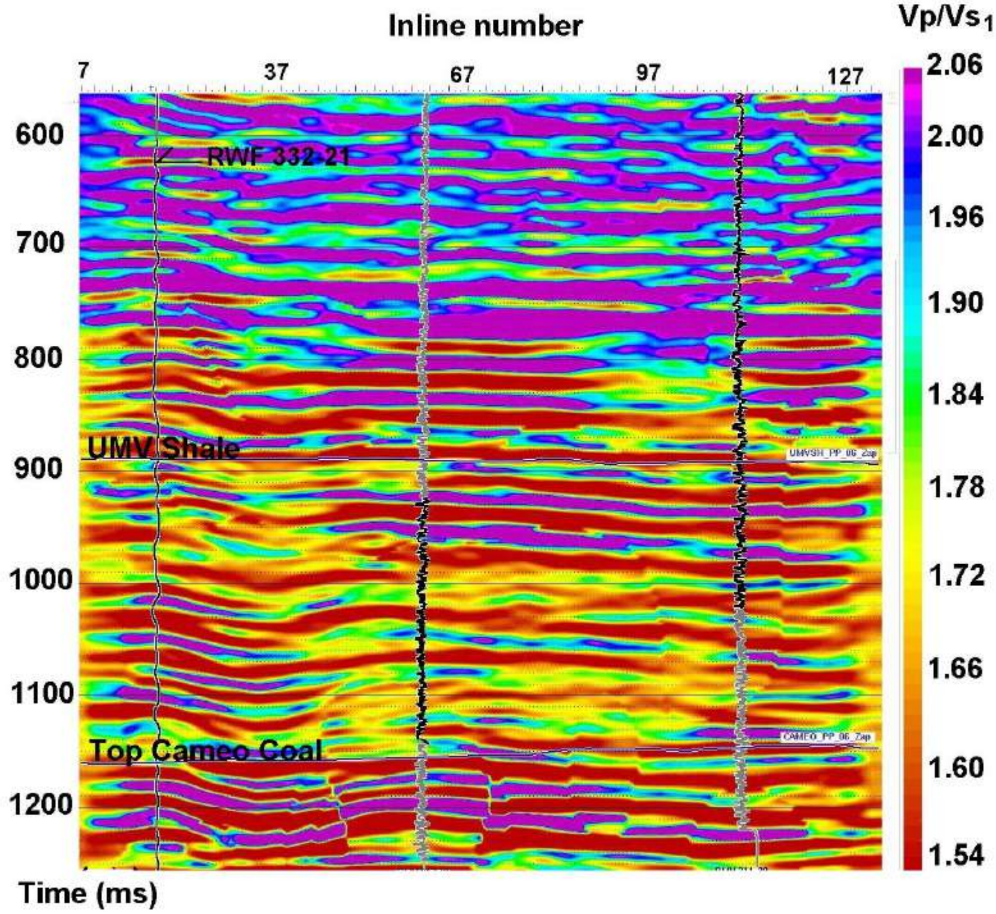

Figure 5.34. Crossline 109 of the high resolution $V_p/V_{s1}(x, y, t)$ volume. This volume is generated from the division of the P-impedance volume (Z_p) by the inverted fast pseudo-S-impedance volume ($\widehat{Z_{s1}}$).

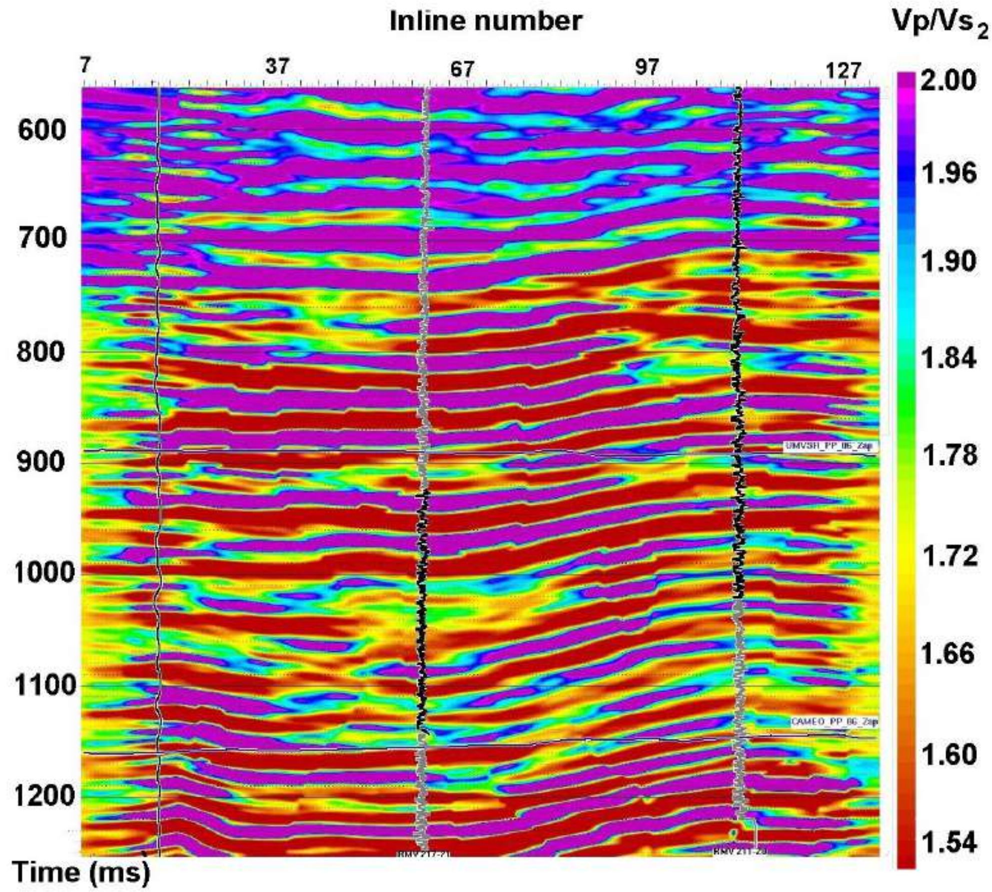

Figure 5.35. Crossline 109 of the high resolution $V_p/V_{s2}(x, y, t)$ volume. This volume is generated from the division of the P-impedance volume (Z_p) by the inverted slow pseudo-S-impedance volume ($\widehat{Z_{s2}}$).

fictitious phenomena are not coherent between Vp/Vs$_1$ and Vp/Vs$_2$ volumes because they are due to the manual picking and correlation of events between $\grave{P}\acute{P}$- and $\grave{P}\acute{S}$-wave data. Nevertheless, the fractional difference between the Vp/Vs$_1$ and Vp/Vs$_2$ volumes was performed and only the most important anomalies were qualitatively interpreted.

The fractional difference between $\widehat{Z_{s1}}$ and $\widehat{Z_{s2}}$ was performed and the crossline 109 of the subtraction volume is shown on Figure 5.36. The purple and red intervals indicate highly anisotropic beds, while the yellowish and greenish intervals indicate an absence or a very low degree of anisotropy. The purple intervals are related to positive instantaneous anisotropy ($\widehat{Z_{s1}}$ being greater than $\widehat{Z_{s2}}$) and the red intervals are related to negative instantaneous anisotropy ($\widehat{Z_{s1}}$ being smaller than $\widehat{Z_{s2}}$). The first observation is that the high anisotropy intervals correspond to the interpreted sand bodies on the impedance volumes. This is coherent with the Rulison geology. The Rulison main gas reservoir is a tight-gas reservoir. The main permeability is a fracture-induced permeability, rather than a matrix permeability. Therefore, the producing sand bodies are fractured and thus anisotropic.

The dipole anisotropy log at the study well location is superposed over the impedance anisotropy volume on Figure 5.36. The correlation between the impedance anisotropy data and the dipole anisotropy log is satisfactory given all the assumptions behind the seismic amplitude inversion: among the 12 high-anisotropy units identified on the anisotropy volume between the UMV Shale horizon and the bottom Cameo Coal horizon, 10 correspond to anisotropy peaks on the dipole anisotropy log (black circles on Figure 5.37). In other words, only two high-anisotropy beds did not correspond to any peak in the dipole anisotropy log (red arrows on Figure 5.37). This might be due to fractures away from the well-bore. On the other hand, only two anisotropy peaks on the dipole anisotropy log did not correspond to any high anisotropy interval on the derived anisotropy volume.

A horizon-slice was extracted from the instantaneous anisotropy volume (see Figure 5.38) and was then normalized by $\widehat{Z_{s2}}$. The result is an instantaneous shear-wave splitting parameter $\gamma^{(S)}$ map for a given sand body. The location where the horizon-slice was extracted is indicated by a red arrow in Figure 5.37. The aperture of the VSP survey (Mazumdar, 2009) is shown by the red circle. The red areas correspond to high $\gamma^{(S)}$ values, and therefore, to fractured zones. The high $\gamma^{(S)}$ zones inside the red circle correspond to the high anisotropy regions observed by Mazumdar (2009).

The fractional difference between the $\mathrm{Vp/Vs}_1$ and $\mathrm{Vp/Vs}_2$ volumes was then performed and only important anomalies were highlighted in red and white (Figure 5.39). These red and white intervals are the intervals of maximum anisotropy. Two important observations can be made. The first observation is that along the study well RWF 332-21, the maximum anisotropy intervals correspond to interpreted sand bodies on the impedance volumes. This observation is similar to the one made for the impedance anisotropy volumes. The second observation is that the highest anisotropic bed (in red under the UMV Shale) is located 250 ms below the UVM Shale horizon. This corresponds to the top gas boundary in the main gas reservoir interval. This gas-bearing interval is thus fractured and should be drilled.

The dipole anisotropy log at the study well location is also superposed over the anisotropy volume derived from Vp/Vs volumes on Figure 5.39. Some of the anisotropy beds corresponds to peaks on the dipole anisotropy log (yellow circles on Figure 5.40) but some of them are slightly misplaced (red arrows on Figure 5.40). This might be due to errors in the registration process. The errors in the registration process are also responsible of some of the fictitious fault blocks seen on the anisotropy volume on Figures 5.39 and 5.40.

5.5 Conclusions

The converted-wave amplitude inversion led to a successful static anisotropic reservoir characterization. The gas-bearing lenticular fluvial sand bodies were imaged with a vertical resolution of 35 ft using pseudo-S-impedance volumes (Figures

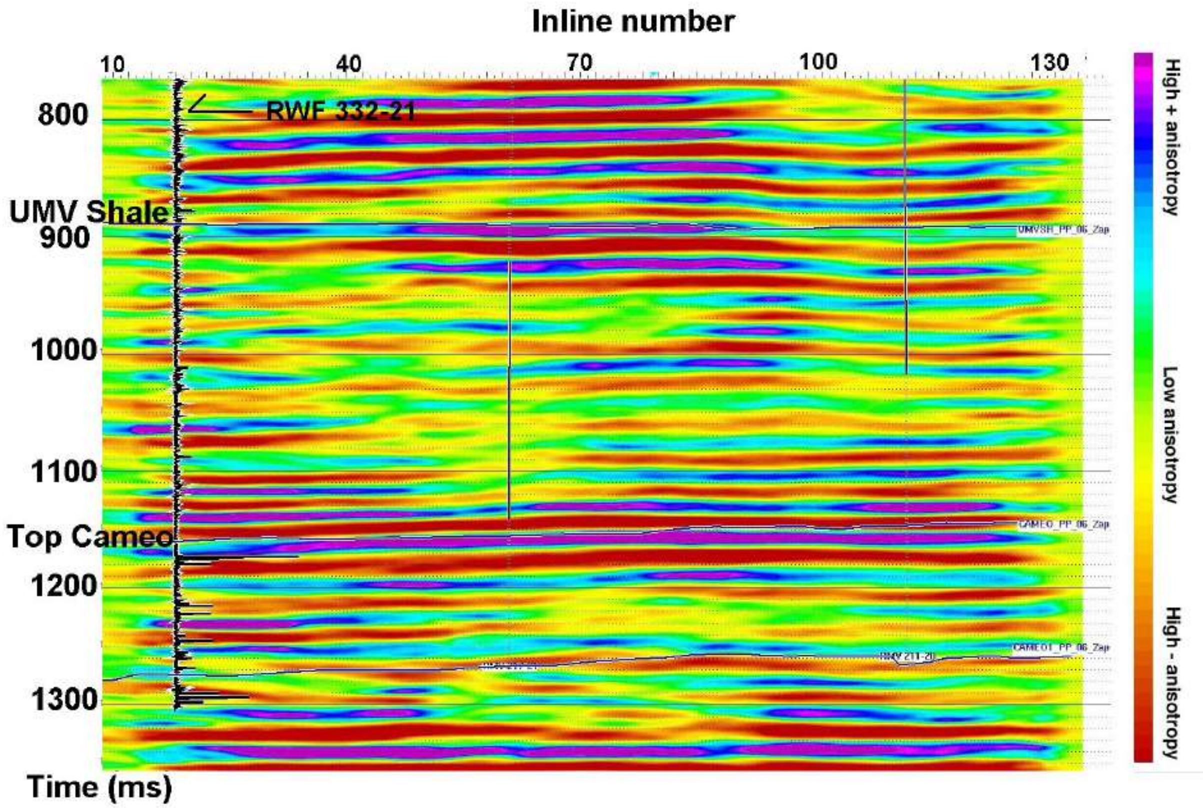

Figure 5.36. Crossline 109 of the P̀Ś-wave splitting volume ($\gamma^{(S)}(x, y, t)$ volume) computed from the difference between the fast and slow inverted pseudo-S-impedance volumes $\widehat{Z_{s1}}$ and $\widehat{Z_{s2}}$. The purple and red intervals indicate highly anisotropic beds, while the yellowish and greenish intervals indicate an absence or a very low degree of anisotropy. The purple intervals are related to positive impedance anisotropy ($\widehat{Z_{s1}}$ being greater than $\widehat{Z_{s2}}$) and the red intervals are related to negative impedance anisotropy ($\widehat{Z_{s1}}$ being smaller than $\widehat{Z_{s2}}$). The dipole anisotropy log is plotted at the study well location. Peaks in the dipole anisotropy log correspond to highly anisotropic beds.

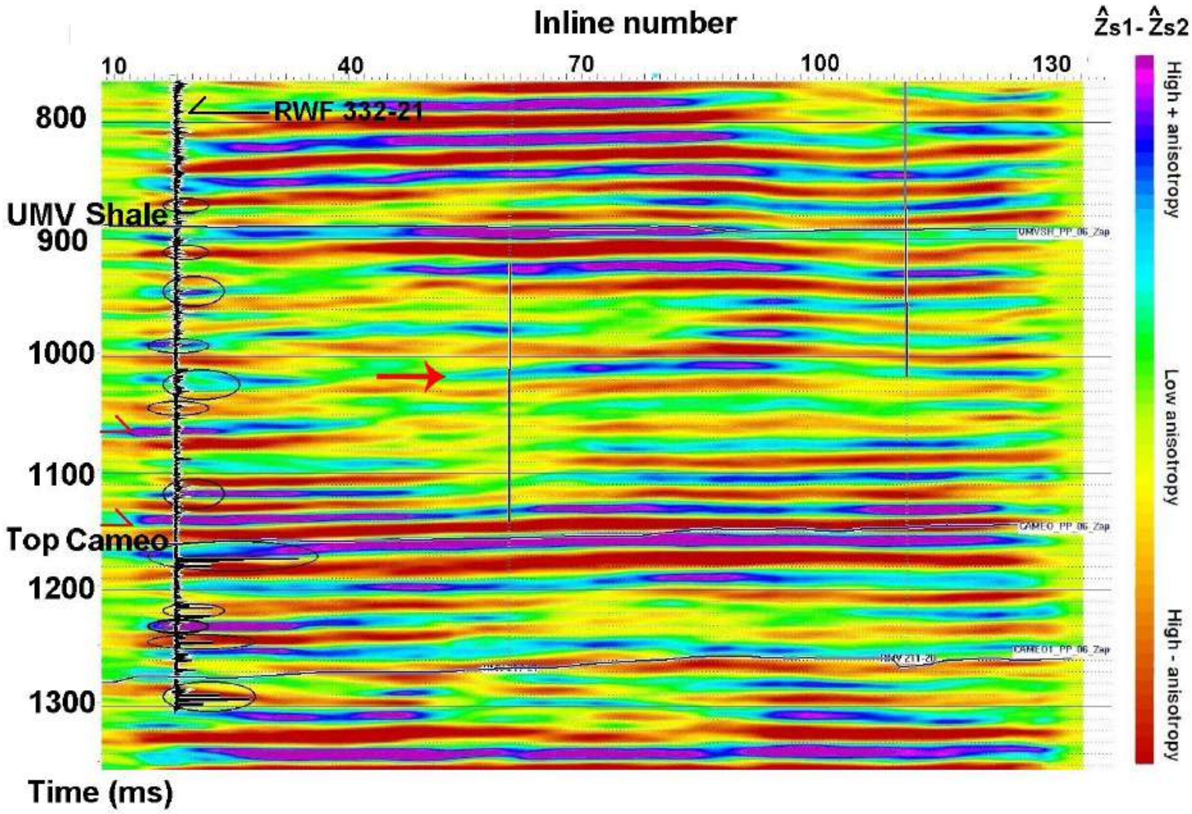

Figure 5.37. Same display as for Figure 5.36. The black circles indicate the anisotropy intervals that correspond to peaks in the dipole anisotropy log, and the red arrows correspond to anisotropy beds that do not correspond to peaks in the dipole anisotropy log.

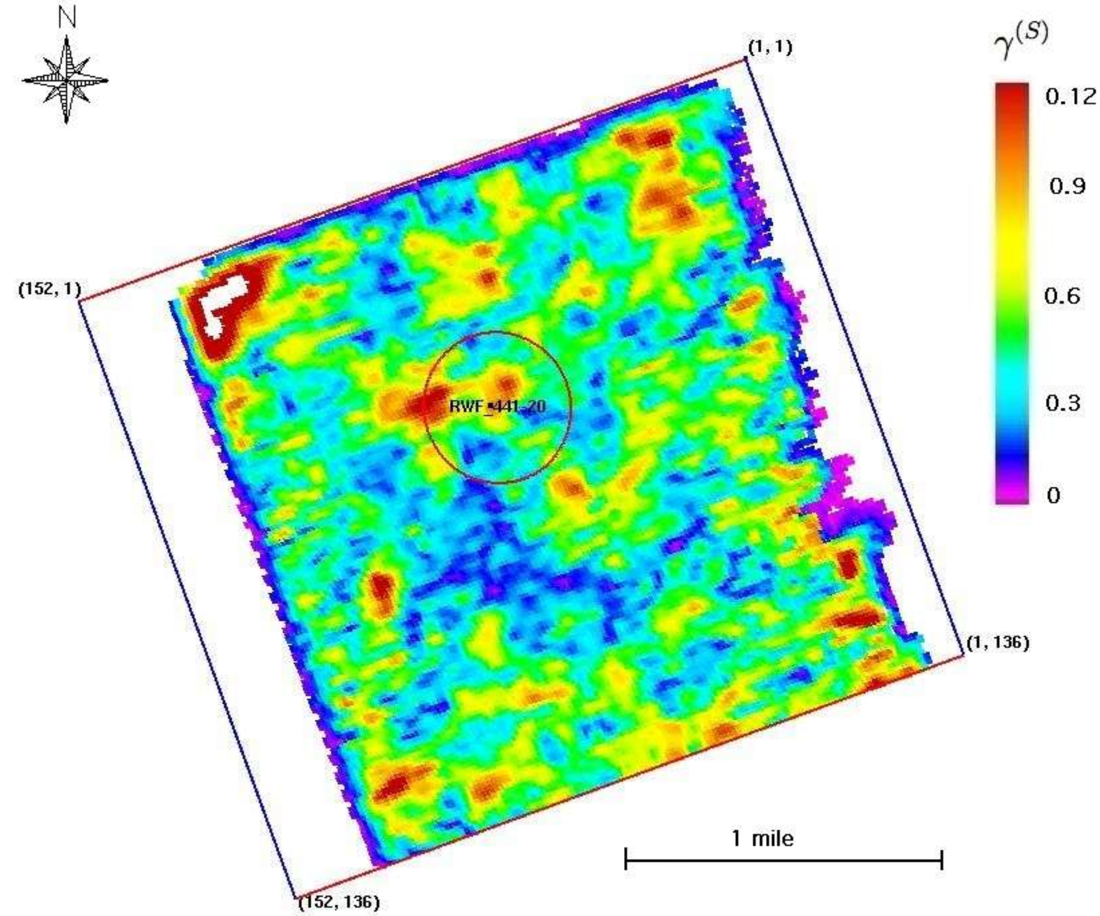

Figure 5.38. Horizon-slice from the shear-wave splitting volume normalized by $\widehat{Z_{s2}}$. The result is an instantaneous shear-wave splitting ($\gamma^{(S)}$) map for a given sand body. The location where the horizon-slice was extracted is indicated by a red arrow in Figure 5.37. The aperture of the VSP survey (Mazumdar, 2009) is shown by the red circle.

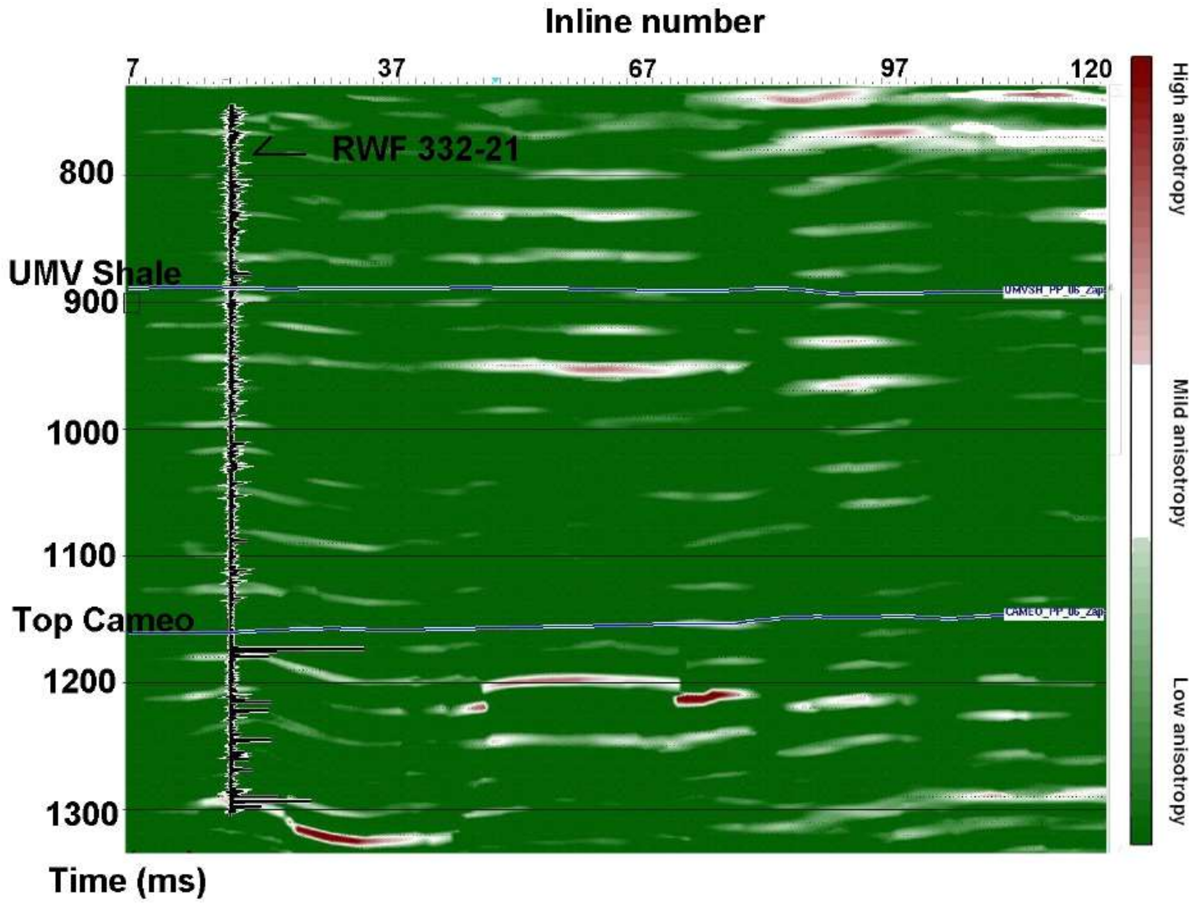

Figure 5.39. Crossline 109 of the P̀Ś-wave splitting volume computed from the difference between the Vp/Vs$_1$ and Vp/Vs$_2$ volumes. Only the important anomalies are highlighted in red and white. The white intervals correspond to highly anisotropic intervals and the red intervals correspond to very highly anisotropic intervals. The dipole anisotropy log is plotted at the study well location. Peaks in the dipole anisotropy log correspond to highly anisotropic beds.

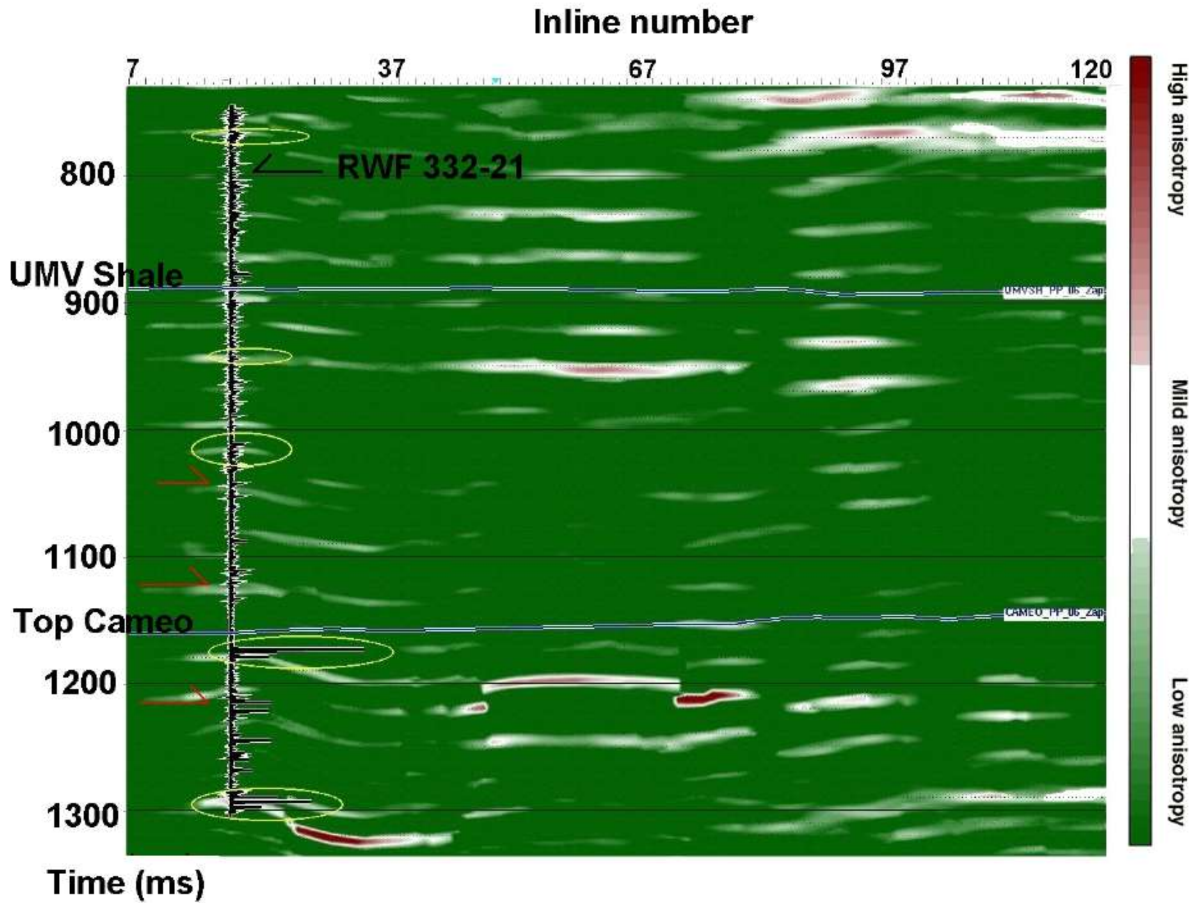

Figure 5.40. Same display as for Figure 5.39. The yellow circles indicate the anisotropy intervals that correspond to peaks in the dipole anisotropy log and the red arrows correspond to anisotropy beds that are misplaced compared to the peaks of the dipole anisotropy log.

5.26 and 5.27). Their position and lateral extent were successfully determined. The good quality overpressured sand bodies were identified from high-resolution Vp/Vs volumes (Figures 5.34 and 5.35). Finally, the high fracture density intervals were determined using the influence of shear-wave splitting on converted-wave amplitudes and, therefore, on the impedance volumes (Figure 5.36).

Chapter 6

CONCLUSIONS AND FUTURE WORK

6.1 Conclusions

In this thesis, I proposed a workflow for joint inversion of $\grave{P}\acute{P}$- and $\grave{P}\acute{S}$-waves. $\grave{P}\acute{P}$- and $\grave{P}\acute{S}$-wave traveltime data were jointly inverted in order to build an anisotropic model for the UMV Shale and generate fracture density maps. Using the amplitude data, the gas-bearing lenticular fluvial sand bodies were imaged with a minimum vertical resolution of 35 ft. The high quality overpressured producing sand bodies were discriminated from the low quality underpressured or depleted sandstones using Vp/Vs volumes generated from impedance volumes. The high fracture density intervals were identified from the effects of shear-wave splitting on the amplitude responses of converted-wave data.

The main workflow steps are summarized below:

1) Structural imaging (see Figures 2.6 and 2.7) and fracture density mapping (see Figures 2.16 and 2.17) of the reservoir using poststack $\grave{P}\acute{S}$-wave traveltime data.

2) Inversion for the Thomsen anisotropy parameters in the UMV Shale layer assuming a VTI model (see Figure 3.9). In the presence of wide-azimuth prestack 3-C data, more complicated anisotropic models, such as orthorhombic media, can be considered. The Thomsen parameters at the reservoir level can then be obtained using Dix-type differentiation.

3) Elastic anisotropic AVO modeling based on the Thomsen parameters extracted from the traveltime inversion in order to quantify the effects of anisotropy and polar angle on the reflection coefficients of $\grave{P}\acute{P}$- and $\grave{P}\acute{S}$-waves (see Figures 4.14 and 4.16).

4) Inversion of the $\grave{P}\acute{P}$- and $\grave{P}\acute{S}$-wave amplitude data. The output of the $\grave{P}\acute{S}$-wave

amplitude inversions is two pseudo-S-impedance volumes (see Figures 5.26, 5.27 and 5.28). The sand bodies correspond to the high pseudo-S-impedance intervals.

5) Generation of the Vp/Vs volumes after registration of the pseudo-S-impedance volumes to $\grave{\mathrm{P}}\acute{\mathrm{P}}$-wave time scale (see Figures 5.34 and 5.35). Low Vp/Vs intervals correlate to good quality overpressured sand bodies, while high Vp/Vs values correlate to underpressured or depleted sandstones.

6) Mapping of high fracture density intervals using the effects of shear-wave splitting anisotropy on $\grave{\mathrm{P}}\acute{\mathrm{S}}$-wave reflectivity. Subtraction of the fast and slow pseudo-S-impedance volumes leads to instantaneous anisotropy volume (see Figures 5.37 and 5.38). The intervals of high anisotropy are related to high fracture density.

Poststack $\grave{\mathrm{P}}\acute{\mathrm{S}}$-wave traveltime data were first used for structural mapping. The main wrench fault located at the base of the Cameo Coal was successfully imaged using $\grave{P}\acute{S}_2$-wave traveltime data. On the other hand, the normalized difference between the traveltimes of the S-waves polarized in orthogonal directions is a practical measure of the shear-wave splitting parameter $\gamma^{(S)}$ related to potentially high fracture density. Density fracture maps were generated from pure shear- and converted-wave data for the main gas reservoir. The maps were found to be similar and agreed with previous shear-wave studies conducted in Rulison (Rumon, 2006; Jackson, 2007).

The Thomsen parameters were estimated in the UMV Shale Formation using the vertical and NMO P-wave and S-wave velocities. At the vicinity of the study well, δ was found to be equal to -0.11 and ϵ to 0.07. These values of δ and ϵ were then combined with the elastic properties extracted from log data at the study well location in order to build the VTI model for the UMV Shale. The main gas reservoir was modeled as an HTI medium. The Thomsen parameters were taken from the work of Vasconcelos & Grechka (2007) assuming that the anisotropy parameters in one of the symmetry planes were equal to zero. A 3-C anisotropic AVO modeling study for the VTI-over-HTI medium was then conducted at the vicinity of the study well location. The study showed that for $\grave{\mathrm{P}}\acute{\mathrm{P}}$-offsets not exceeding 7,000 ft and $\grave{\mathrm{P}}\acute{\mathrm{S}}$-offsets not exceeding 5,000 ft, the reflection coefficients in the VTI-over-HTI model of the upper gas reservoir can be approximated by the small-offset reflection coefficients in isotropic media. For $\grave{\text{P}}\acute{\text{S}}_1$-waves, an amplitude scaling by a factor of 5/7 should be applied in order for the approximation to hold. For $\grave{\text{P}}\acute{\text{S}}_2$-waves, the amplitude scaling factor is equal to 1/2.

A model-based inversion was conducted on the multicomponent data under the isotropic small-offset approximation. The validity of this approximation has been verified by the AVO modeling. Inversion of the converted-wave data required two additional processing steps: the generation of a pseudo-density and a pseudo-impedance log at the study well location and the scaling of the amplitude data. The converted-wave amplitude inversion generated two pseudo-S-impedance volumes $\widehat{Z}_{s1}$ and $\widehat{Z}_{s2}$. The lenticular fluvial sand bodies were successfully imaged on the pseudo-S-impedance volumes as high impedance intervals with a vertical resolution of 35 ft.

The pseudo-S-impedance volumes were then registered to compressional-wave time scale in order to generate Vp/Vs volumes. The Vp/Vs volumes successfully discriminated between overpressured good quality reservoir sandstones characterized by low Vp/Vs values and depleted sand bodies characterized by high Vp/Vs values. Finally, the fractional difference between the $\widehat{Z}_{s1}$ and $\widehat{Z}_{s2}$ impedance volumes highlighted the intervals affected by shear-wave splitting. The anisotropy zones matched the data from the dipole anisotropy log at the study well location. The fractured intervals were hence successfully imaged from the impedance volumes.

6.2 Future work

This thesis should be followed up by studies related to AVO analysis, correlation and registration of $\grave{\text{P}}\acute{\text{P}}$- and $\grave{\text{P}}\acute{\text{S}}$-wave data, and multicomponent time-lapse studies. Interval anisotropy was qualitatively described using impedance volumes but was not quantified. A proper quantification of anisotropy will require the study of the azimuthal dependence of the $R_{\grave{P}\acute{S}}$ coefficients given the elastic properties of the Rulison reservoir. This study can be conducted based on the work of Jílek (2002). The modeling results should then be compared to the P̀Ś-wave AVO response of the reservoir in order to carry out anisotropic inversion of the P̀Ś-wave amplitude data.

In this thesis, the registration process relied partially on manual interpretation. An algorithm proposed by Fomel et al. (2003) can help us improve the registration process and, therefore, improve the accuracy of the Vp/Vs volumes. The proposed algorithm is based on a non-stationary spectral balancing method that takes into account the differences in the frequency content of the P̀Ṕ- and P̀Ś-wave data. One of the additional advantages of this algorithm is the direct extraction of the interval Poisson's ratio from the warping function.

Finally, the workflow proposed in this thesis should be applied to the RCP 2003 and 2004 surveys in order to generate pseudo-Vp/Vs volumes for both surveys. A time-lapse analysis has been conducted by Meza (2008) based on pure shear-wave data. Meza (2008) correlated the time-lapse anomalies observed on the different Vp/Vs volumes with the depletion in the reservoir. A similar approach can be applied to the Vp/Vs volumes derived from P̀Ś-wave data. Integrating pressure log data with Vp/Vs time-lapse anomalies should help us delineate the depleted zones in the reservoir and, therefore, help in dynamic reservoir characterization.

REFERENCES CITED

Aki, K., & Richards, P. G. 1980. *Quantitative seismology.* second edn. University Science books.

Al-Dajani, A. F., & Tsvankin, I. 1998a. Non hyperbolic reflection moveout for horizontal transverse isotropy. *Geophysics*, **63**(5), 1738–1753.

Al-Dajani, A. F., & Tsvankin, I. 1998b. Nonhyperbolic reflection moveout for orthorhombic media. *60th EAGE Conference & Exhibition, Expanded Abstracts.*

Al-Dajani, A. F., Tsvankin, I., & Toksöz, M. N. 1996. Non hyperbolic reflection moveout for horizontal transverse isotropy. *58th EAGE Conference & Exhibition, Expanded Abstracts.*

Alford, R. M. 1986. Shear data in the presence of azimuthal anisotropy: Dilley, Texas. *56th Annual Internat. Mtg., Soc. Expl. Geophys., Expanded Abstracts*, **5**, 476.

Alkhalifah, T. 1997. Vertical velocity analysis using nonhyperbolic moveout in transversely isotropic media. *Geophysics*, **62**(6), 1839–1854.

Alkhalifah, T., & Tsvankin, I. 1995. Velocity analysis for transversely isotropic media. *Geophysics*, **60**(5), 1550–1566.

Alkhalifah, T., Tsvankin, I., Larner, K., & Toldi, J. 1996. Velocity analysis and imaging in transversely isotropic media: methodology and a case study. *The Leading Edge*, **15**(5), 371–378.

Araman, A., & Davis, T. L. 2009a. Converted-wave analysis applied to Rulison Field, Colorado. *71st EAGE Conference & Exhibition Expended Abstract.*

Araman, A., & Davis, T. L. 2009b. Joint PP-PS traveltime and amplitude inversions for reservoir characterization at Rulison Field, Colorado. *79th Annual Internat. Mtg., Soc. Expl. Geophys., Expanded Abstracts.*

Araman, A., Hoffman, M., & Davis, T. L. 2008a. Thief zone identification through seismic monitoring of a CO_2 flood, Weyburn Field, Saskatchewan. *78th Annual Internat. Mtg., Soc. Expl. Geophys., Expanded Abstracts.*

Araman, A., Hoffman, M., & Davis, T. L. 2008b. Thief zone identification through seismic monitoring of a CO_2 flood, Weyburn Field, Saskatchewan. *Nafta*, **59**(11), 529–535.

Artola, F. A. V., Leiderman, R., Fontoura, S. A. B., & Silva, M. B. C. 2004. PS converted wave: conversion point and zero offset energy in anisotropic media. *Journal of applied geophysics*, **56**, 155–163.

Atkins, D. R., Wilson, M., & Sams, M. S. 2001. Sequence stratigraphy and seismic impedance: a new approach to reservoir characterization. *63rd EAGE Conference & Exhibition Expended Abstract.*

Bakulin, A., & Calvert, R. 2006. The Virtual Source method: theory and case study. *Geophysics*, **71**(4), SI139–SI150.

Bancroft, J. C., Geiger, H. D., & Margrave, G. F. 1998. The equivalent offset method of prestack time migration. *Geophysics*, **63**(6), 2042–2053.

Behura, J., & Tsvankin, I. 2006. Small angle AVO response of PS-wave in tilted transversely isotropic media. *Geophysics*, **71**(5), 69–79.

Behura, J., & Tsvankin, I. 2008. Reflection coefficients in attenuative anisotropic media. *78th Annual Internat. Mtg., Soc. Expl. Geophys., Expanded Abstracts*, **27**, 260.

Bostick, N. H., & Freeman, V. L. 1984. Tests of vitrinite reflectance and paleotemperature models at the Multiwell Experimental Site, Piceance Creek Basin, Colorado. *Open File Report - U. S. Geological Survey (in Geologic studies in support of the U. S. Department of Energy Multiwell Experiment, Garfield County, Colorado)*, 110–120.

Bryan, D., Davis, T. L., Tsvankin, I., Verm, R., & Hilterman, R. 2002. Multicomponent AVO analysis, Vacuum Field, New Mexico. *Geophysics*, **67**(3), 701–710.

Carazzone, J. J. 1986. Inversion of P-SV seismic data. *Geophysics*, **51**(5), 1056–1068.

Cary, P. W. 1994. 3-D Converted-wave seismic processing. *CREWES Research Report*, **6**.

Cole, R. 2005. Characterization of fluvial sand bodies in the Lower Williams Fork Formation (Campanian), Coal Canyon area, Colorado. *Rocky Mountain Section - 57th Annual Meeting, Paper No. 19-1.*

Cole, R., & Cumella, S. P. 2003. Stratigraphic architecture and reservoir characteristics of the Mesaverde Group, southern Piceance Basin, Colorado. *in K. M. Peterson, T. M. Olsen, and D. S. Anderson, eds., Piceance Basin 2003 guidebook: Rocky Mountain Association of Geologists*, 385–442.

Contreras, P., Grechka, V., & Tsvankin, I. 1999. Moveout inversion of P-wave data for horizontal transverse isotropy. *Geophysics*, **64**(4), 1219–1229.

Cumella, S. P., & Scheevel, J. 2008. The influence of stratigraphy and rock mechanics on Mesaverde gas distribution, Piceance Basin, Colorado. *in S. P. Cumella, K. W. Shanley, and W. K. Camp, eds., Understanding, exploring, and developing tight-gas sands – 2005 Vail Hedberg Conference: AAPG Hedberg Series*, 137–155.

Davis, T. L. 2006. Pushing the limits in a fractured reservoir. *Hart's E &P*, **79**(9).

Davis, T. L. 2007. Let's go cracking. *The Leading Edge*, **26**(2), 160–161.

Davis, T. L., & Benson, R. D. 2007. Multicomponent 4-D Seismic Reservoir Characterization of Tight Gas Sands, Rulison Field, Colorado. *69th EAGE Conference & Exhibition, Expended Abstracts.*

Davis, T. L., & Benson, R. D. 2009. Tight gas seismic monitoring, Rulison Fied, Colorado. *The Leading Edge*, **28**(4), 408–411.

Davis, T. L., Meza, R. G., & Benson, R. D. 2009. Multi-component seismic analysis of high resolution Vp/Vs ratio for tight gas pressure detection and monitoring, Rulison Field, Colorado. *First Break*, **27**(4).

Eaton, D. W. S., & Lawton, D. C. 1992. P-SV stacking charts and binning periodicity. *Geophysics*, **57**(5), 745–748.

Eaton, D. W. S., Stewart, R. R., & Harrison, M. P. 1991. The Fresnel zone for P-SV waves. *Geophysics*, **56**(3), 360–364.

Fomel, S., Backus, M. M., DeAngelo, M. V., Murray, P. E., & Hardage, B. A. 2003. Multicomponent seismic data registration for subsurface characterization in the shallow Gulf of Mexico. *2003 Offshore Technology Conference, paper 15117.*

Franco, G. 2007. *Seismic anisotropy in tight gas sandstones, Rulison Field, Piceance Basin, Colorado.* M.Phil. thesis, Colorado School of Mines.

Gaiser, J. E. 2004. PS-Wave Azimuthal Anisotropy: Benefits for Fractured Reservoir*. *Search and Discovery Article ♯40120.*

Gaiser, J. E., & Jackson, A. R. 2000. Accuracy and limitations of PS-wave conversion-point computations: How effective is γ_{eff}? *70th Annual Internat. Mtg., Soc. Expl. Geophys., Expanded Abstracts*, 1138–1141.

Grechka, V., & Tsvankin, I. 1998. 3-D description of normal moveout in anisotropic inhomogeneous media. *Geophysics*, **63**(3), 1079–1092.

Grechka, V., & Tsvankin, I. 1999. 3-D moveout inversion in azimuthally anisotropic media with lateral velocity variation: Theory and a case study. *Geophysics*, **64**(4), 1202–1218.

Grechka, V., & Tsvankin, I. 2002. PP+PS=SS. *Geophysics*, **67**(6), 1961–1971.

Grechka, V., Tsvankin, I., & Cohen, J. 1999a. Generalized Dix equation and analytical treatment of normal-moveout velocity for anisotropic media. *Geophysical Prospecting*, **47**(2), 117–148.

Grechka, V., Theophanis, S., & Tsvankin, I. 1999b. Joint inversion of P- and PS-waves in orthorhombic media: Theory and a physical modeling study. *Geophysics*, **64**(1), 146–161.

Grechka, V., Tsvankin, I., Bakulin, A., & Hansen, J.O. 2002a. Anisotropic inversion and imaging of PP and PS reflection data in the North Sea. *The Leading Edge*, **21**(1), 90–97.

Grechka, V., Tsvankin, I., Bakulin, A., Hansen, J. O., & Signe, C. 2002b. Joint inversion of PP and PS reflection data for VTI media: A North Sea case study. *Geophysics*, **67**(5), 1382–1395.

Guliyev, E. 2007. *Vp/Vs estimation from multicomponent seismic data for improved characterization of a tight sandstone reservoir, Rulison Field, Colorado*. M.Phil. thesis, Colorado School of Mines.

Hemborg, H. T. 2000. Gas production characteristics of the Rulison, Grand Valley, Mamm Creek, and Parachute Fields, Garfield County, Colorado: Turning marginally economic basin-centered tight-gas sands into profitable reservoirs in the southern Piceance Basin. *Colorado Geological Survey, Ressource series*, **39**, 1–30.

Hill, S. J. 2005. Inversion-based thickness determination. *The Leading Edge*, **24**(5), 477–480.

Hood, K. C., & Yurewicz, D. A. 2008. Assessing the Mesaverde basin-centered gas play, Piceance Basin, Colorado. *in S. P. Cumella, K. W. Shanley, and W. K. Camp, eds., Understanding, exploring, and developing tight-gas sands – 2005 Vail Hedberg Conference: AAPG Hedberg Series*, 87–104.

Jackson, J. 2007. *Fracture modeling and fault zone characteristics applied to reservoir characterization of the Rulison Gas Field, Garfield County, Colorado*. M.Phil. thesis, Colorado School of Mines.

Jansen, K. 2005. *Seismic investigation of wrench faulting and fracturing at Rulison Field, Colorado*. M.Phil. thesis, Colorado School of Mines.

Jiaming, T., Yue, H., Xiangrong, X., Tinnin, J., & Hallin, J. 2009. Application of converted-wave 3D/3-C data for fracture detection in a deep tight-gas reservoir. *The Leading Edge*, **28**(7), 826–838.

Jílek, P. 2002a. Converted PS-wave reflection coefficients in weakly anisotropic media. *Pure and Applied Geophysics*, **159**, 1527–1562.

Jílek, P. 2002b. *Modeling and inversion of converted-wave reflection coefficients in anisotropic media: a tool for quantitative analysis*. Ph.D. thesis, Colorado School of Mines.

Keighley, D. 2006. *P-wave time-lapse seismic data interpretation at Rulison Field, Piceance Basin, Colorado*. M.Phil. thesis, Colorado School of Mines.

Korneev, V., & Bakulin, A. 2006. On the fundamentals of the Virtual Source method. *Geophysics*, **71**(3), A13–A17.

Kusuma, M. 2005. *Analysis of time-lapse P-wave seismic data from Rulison Field, Colorado.* M.Phil. thesis, Colorado School of Mines.

Kuuskraa, V. A., Campagna, D., & Decker, D. 1997. Application of High Fold, Multi-Azimuth 3-D P-Wave Seismic to Characterize Natural Fractures in the Rulison Field, Piceance Basin. *Innovative Applications of Petroleum Technology Guidebook, Rocky Mountain Association of Geologists, Denver, CO*, 73–86.

LaBarre, E. A., Davis, T. L., & Benson, R. D. 2008. Finding the sweet spot. *Hart's E & P*, **81**(3), 73–74.

LaBarre, L. 2008. *Reservoir Prediction from Multicomponent seismic data, Rulison Field, Piceance Basin, Colorado*. M.Phil. thesis, Colorado School of Mines.

Li, X., Wang, L., Dai, H., & Sun, X. 2008. Estimating anisotropic parameters from PS converted-wave data: a case sutdy. *Journal of seismic exploration*, **17**(2), 147–158.

Lines, L., & Newrick, R. 2004. *Fundamentals of Geophysical Interpretation*. Society of Exploration Geophysicists, Geophysical Monograph Series.

Lorenz, J. C., Heinze, D. M., Clark, J. A., & Searls, C. A. 1985. Determination of widths of meander-belt sandstone reservoirs from vertical downhole data. Mesaverde Group, Piceance Creek Basin, Colorado. *AAPG Bulletin*, **69**, 710–721.

Lynn, H. B., Bates, C., & Dok, R. Van. 1999. The effects of azimuthal anisotropy in P-wave 3-D seismic. *69th Annual Internat. Mtg., Soc. Expl. Geophys., Expanded Abstracts*, 727–720.

Magoon, L. B., & Dow, W. G. 1994. The petroleum system - from source to trap. *AAPG Memoir*, **60**, 3–24.

Mazumdar, P. 2009. *VSP imaging of tight sandstones in Rulison Field, Colorado*. Ph.D. thesis, Colorado School of Mines.

Mazumdar, P., Mateeva, A., & Bakulin, A. 2008. Azimuthal Anisotropy Characterization with Multicomponent virtual shear sources at Rulison Field, Colorado. *78th Annual Internat. Mtg., Soc. Expl. Geophys., Expanded Abstracts*.

Meza, R. G. 2008. *Time-lapse Vp/Vs analysis for reservoir characterization, Rulison Field, Colorado*. M.Phil. thesis, Colorado School of Mines.

Pšenčík, I. 1998. Green's function for inhomogeneous weakly anisotropic media. *Geophysical Journal International*, **135**, 279–288.

Qian, Z., Li, X., & Chapman, M. 2007. Azimuthal variation of PP- and PS-wave attributes: a synthetic study. *77st Annual Internat. Mtg., Soc. Expl. Geophys., Expanded Abstracts*, **26**, 184.

Qiankun, L., Liguo, H., Enli, W., & Gangyi, S. 2008. Reflection coefficients of P-SV waves in weak anisotropy media. *Applied Geophysics*, **5**(1), 18–23.

Rojas, N. 2005. *Elastic rock properties of tight gas sandstones for reservoir characterization at Rulison Field, Colorado.* M.Phil. thesis, Colorado School of Mines.

Rüger, A. 1996. *Reflection coefficients and azimuthal AVO analysis in anisotropic media.* Ph.D. thesis, Colorado School of Mines.

Rüger, A. 1997. P-wave reflection coefficients for transversely isotropic models with vertical and horizontal axis of symmetry. *Geophysics*, **62**, 713–722.

Rüger, A. 2001. *Reflection coefficients and azimuthal AVO analysis in anisotropic media.* Society of Exploration Geophysicists, Geophysical Monograph Series.

Rumon, M. 2006. *Shear-wave time-lapse monitoring of a tight gas reservoir, Rulison Field, Colorado.* M.Phil. thesis, Colorado School of Mines.

Selley, R. C. 1982. *Elements of Petroleum Geology.* second edn. Academic Press.

Shaw, R. K., & Sen, M. K. 2004. Born integral, stationary phase and linearized reflection coefficients in weak anisotropic media. *Geophysical Journal International*, **158**, 225–238.

Sheriff, R. E. 1980. Nomogram for Fresnel-zone calculation. *Geophysics*, **45**(5), 968–972.

Sheriff, R. E., & P.Geldart, L. 1982. *Exploration Seismology.* Cambridge University Press.

Stewart, R. R. 1991. Rapid map and inversion of P-SV waves. *Geophysics*, **56**(6), 859–862.

Stewart, R. R., Henry, C. B., & Xu, C. 1998. What is a P-S zero-offset section? *CREWES Research Report*, **10**.

Stewart, R. R., Gaiser, J. E., Brown, R. J., & Lawton, D. C. 1999. Converted-wave seismic exploration: a tutorial. *CREWES Research Report*, **11**.

Tessmer, G., & Behle, A. 1988. Common reflection point data stacking technique for converted waves. *Geophysical Prospecting*, **36**(7), 671–688.

Thomsen, L. 1986. Weak elastic anisotropy. *Geophysics*, **51**(10), 1954–1966.

Thomsen, L. 1988. Reflection seismology over azimuthally anisotropic media. *Geophysics*, **53**(3), 304–313.

Thomsen, L. 1999. Converted-wave reflection seismology over inhomogeneous, anisotropic media. *Geophysics*, **64**(3), 678–690.

Topper, R., Spray, K. L., Bellis, W. H., Hamilton, J. L., & Barkman, P. E. 2003. *Ground water of Colorado.* Colorado Geological Survey Special Publication 53.

Tsvankin, I. 1997a. Anisotropic parameters and P-wave velocity for orthorhombic media. *Geophysics*, **62**(4), 1292–1309.

Tsvankin, I. 1997b. Reflection moveout and parameter estimation for horizontal transverse isotropy. *Geophysics*, **62**(10), 614–629.

Tsvankin, I. 2001. *Seismic signatures and analysis of reflection data in anisotropic media*. first edn. Elsevier Science.

Tsvankin, I., & Grechka, V. 2002. 3D description and inversion of reflection moveout of PS-waves in anisotropic media. *Geophysical Prospecting*, **50**(3), 301–316.

Tsvankin, I., & Thomsen, L. 1994. Nonhyperbolic reflection moveout in anisotropic media. *Geophysics*, **59**(8), 1290–1304.

Valenciano, A. A., & Michelena, R. J. 2000. Stratigraphic inversion of poststack PS converted waves data. *70th Annual Internat. Mtg., Soc. Expl. Geophys., Expanded Abstracts*.

Vasconcelos, I., & Grechka, V. 2007. Seismic characterization of multiple fracture sets at Rulison Field, Colorado. *Geophysics*, **72**(2), 19–30.

Wang, W., & Tsingas, C. 2002a. Converted-wave pre-stack imaging and velocity analysis by pseudo-offset migration. *First Break*, **20**(11), 704–714.

Wang, W., & Tsingas, C. 2002b. Converted-wave prestack imaging and velocity analysis by pseudo-offset migration. *PGS publications*.

Winarsky, R., & Kendall, R. 2004a. *RCP Rulison 3D/9C processing review: Breakout session*. Tech. rept. Veritas Geoservices, Calgary, Alberta.

Winarsky, R., & Kendall, R. 2004b. *RCP Rulison 9C processing review*. Tech. rept. Veritas Geoservices, Calgary, Alberta.

Xu, X., & Tsvankin, I. 2007. A case study of azimuthal AVO analysis with anisotropic spreading correction. *The Leading Edge*, **26**(12), 1552–1561.

Xu, X., & Tsvankin, I. 2008. Moveout-based geometrical-spreading correction for PS-waves in layered anisotropic media. *Journal of Geophysics and Engineering*, **5**, 195–202.

Yilmaz, Ö. 2001. *Seismic data analysis*. Society of Exploration Geophysicists.

Yuan, J., & Li, X. 2001. PS-wave conversion-point equation in layered anisotropic media. *71st Annual Internat. Mtg., Soc. Expl. Geophys., Expanded Abstracts*, 157–160.

Yuan, J., Li, X., & Ziolkowski, A. 2001. Converted-wave moveout analysis in layered anisotropic media: a case study. *63rd EAGE Conference & Exhibition Expended Abstract*.

Yurewicz, D. A., Kronmueller, K., Bohacs, K. M., Klimentidis, R. E., Meurer, K. E., Yeakel, J. D., Ryan, T. C., & Kendall, J. 2008. Controls on gas and water distributions, Mesaverde basin-centered gas play, Piceance Basin, Colorado. *in S. P. Cumella, K. W. Shanley, and W. K. Camp, eds., Understanding, exploring, and developing tight-gas sands – 2005 Vail Hedberg Conference: AAPG Hedberg Series*, 105–135.

Zhang, E., Hill, R. J., Katz, B. J., & Tang, Y. 2008. Modeling of gas generation from the Cameo Coal zone in the Piceance Basin, Colorado. *AAPG Bulletin*, **92**(8), 1077–1106.

APPENDIX A

CONVERTED-WAVE SEISMOLOGY IN LAYERED VTI MEDIA

P̀Ś-wave moveout analysis in layered VTI media

In layered VTI media, the P̀Ś-wave traveltime for a ray converted at the nth layered and emerging at offset x can be written as a modified Taylor series expansion (Tsvankin & Thomsen, 1994):

$$t_{\grave{p}\acute{s}}^2 = t_{\grave{p}\acute{s},0}^2 + \frac{x^2}{V_{\grave{p}\acute{s},2}^2} + \frac{A_4\, x^4}{1 + A_5\, x^2} + \cdots\,, \tag{A.1}$$

where $t_{\grave{p}\acute{s},0}$ is the vertical two-way P̀Ś-wave traveltime,

$$t_{\grave{p}\acute{s},0} = t_{p0} + t_{s0} = t_{p0}(1 + \kappa_0), \tag{A.2}$$

and $V_{\grave{p}\acute{s},2}$ is the P̀Ś-wave moveout given by Thomsen (1999) as:

$$V_{\grave{p}\acute{s},2}^2 = \frac{V_{p2}^2}{1+\kappa_0} + \frac{V_{s2}^2}{1+1/\kappa_0} = \frac{V_{p2}^2}{1+\kappa_0}(1 + 1/\kappa_{eff}), \tag{A.3}$$

with κ_0 and κ_{eff} given respectively by equations (3.18) and (3.22). The quartic term A_4 was first derived by Tsvankin & Thomsen (1994). A simplified from was published by Thomsen (1999), but that expression is only valid for offset-to-depth ratios of 1. A more accurate expression for A_4 was derived by Yuan et al. (2001). The expressions for A_4 and the correction term A_5 are:

$$A_4 = -\frac{(\kappa_0\, \kappa_{eff} - 1)^2 + 8\,(1+\kappa_0)(\eta_{eff}\, \kappa_0\, \kappa_{eff}^2 - \zeta_{eff})}{4\, t_{\grave{p}\,\acute{s},0}^2\, V_{\grave{p}\acute{s},2}^4\, \kappa_0\, \left(1 + \kappa_{eff}\right)^2}, \tag{A.4}$$

$$A_5 = \frac{A_4}{1/V_{p_h}^2 - 1/V_{\grave{p}\acute{s},2}^2}, \tag{A.5}$$

where η_{eff} is an effective anisotropy parameter introduced by Alkhalifah (1997) and ζ_{eff} is another effective anisotropic parameter introduced by Yuan et al. (2001):

$$\eta_{eff} = \frac{1}{8\, t_{p0}\, V_{p2}^2} \left[\sum_{i=1}^{n} V_{p2,i}^4 \Delta t_{p0,i} (1 + 8\eta_i) - t_{p0} V_{p2}^4 \right], \tag{A.6}$$

$$\zeta_{eff} = \frac{-1}{8\, t_{s0}\, V_{s2}^2} \left[\sum_{i=1}^{n} V_{s2,i}^4 \Delta t_{s0,i} (1 + 8\zeta_i) - t_{s0} V_{s2}^4 \right], \tag{A.7}$$

with

$$\eta_i = \frac{\epsilon_i - \delta_i}{1 + 2\, \delta_i}, \tag{A.8}$$

$$\zeta_i = \frac{\kappa_{2,i}^4}{\kappa_{0,i}^2} \eta_i = \kappa_{eff,i}^2 \eta_i, \tag{A.9}$$

$$\kappa_{0,i} = \frac{V_{p0,i}}{V_{s0,i}}, \tag{A.10}$$

$$\kappa_{2,i} = \frac{V_{p2,i}}{V_{s2,i}}, \tag{A.11}$$

$$\kappa_{eff,i} = \frac{\kappa_{2,i}^2}{\kappa_{0,i}^2}, \tag{A.12}$$

where V_{p2} and V_{s2} are respectively the P-wave and S-wave NMO velocities, κ_0 is the vertical velocity ratio, κ_2 is the NMO velocity ratio, ϵ and δ are the Thomsen (1986) anisotropy parameters, η is the Alkhalifah & Tsvankin (1995) anellipticity parameter, V_{ph} is the P-wave horizontal velocity, and the subscript i refers to the ith layer. Therefore,

$$t_{p0} = \sum_{i=1}^{n} \Delta t_{p0,i}, \tag{A.13}$$

$$t_{s0} = \sum_{i=1}^{n} \Delta t_{s0,i}, \tag{A.14}$$

$$t_{\grave{p}\acute{s},0} = t_{p0} + t_{s0}, \tag{A.15}$$

$$V_{p2} = \frac{1}{t_{p0}} \sum_{i=1}^{n} V_{p2,i}^2 \Delta t_{p0,i}, \tag{A.16}$$

$$V_{s2} = \frac{1}{t_{s0}} \sum_{i=1}^{n} V_{s2,i}^2 \Delta t_{s0,i}, \tag{A.17}$$

$$V_{\grave{p}\acute{s},2} = \frac{1}{t_{\grave{p}\acute{s},0}} (t_{p0}\, V_{p2}^2 + t_{s0}\, V_{s2}^2). \tag{A.18}$$

The P-wave moveout velocity is controlled only by two parameters: the moveout velocity V_{p2} and the Alkhalifah & Tsvankin (1995) anellipticity η. On the other hand, the P̀Ś-wave moveout velocity will be controlled by 4 parameters: $V_{\grave{p}\acute{s},2}$, κ_0, κ_{eff} and χ_{eff}, with χ_{eff} defined as a combination of η_{eff}, κ_0, κ_{eff}, and ζ_{eff}:

$$\chi_{eff} = \eta_{eff}\, \kappa_0\, \kappa_{eff} - \zeta_{eff}. \tag{A.19}$$

κ_0 is obtained by correlating similar events on P-wave and converted-wave poststack data, $V_{\grave{p}\acute{s},2}$ is obtained by normal moveout analysis on the converted-wave prestack data, κ_{eff} is obtained by the following expression:

$$\kappa_{eff} = \frac{V_{p,2}}{V_{\grave{p}\acute{s},2}^2 (1 + \kappa_0) - V_{p,2}^2}, \tag{A.20}$$

and χ_{eff} is obtained by equation (A.19), with the anellipticity parameter η derived from a nonhyperbolic analysis on the converted-wave data. For completeness, we should note that the horizontal velocity V_{ph} can be estimated by the following empirical formulae given by Yuan et al. (2001):

$$V_{ph} = V_{p2} \sqrt{1 + 2\eta}. \tag{A.21}$$

$\grave{\mathrm{P}}\acute{\mathrm{S}}$-wave conversion point in layered VTI media

The conversion point in a n-layered VTI media is still given by the general Thomsen (1999) expression for conversion points in layered media,

$$x_c = x \left(c_0 + \frac{c_2\, x^2}{1 + c_3\, x^2} \right), \tag{A.22}$$

where the coefficients c_0 and c_2 have been derived by Yuan & Li (2001), and the coefficient c_3 is a combination of c_0 and c_2 ($c_3 = c_2/(1 - c_0)$):

$$c_0 = \frac{\sum_{i=1}^{n} V_{p2,i}^2 \Delta t_{p0,i}}{\sum_{i=1}^{n} V_{p2,i}^2 \Delta t_{p0,i} + \sum_{i=1}^{n} V_{s2,i}^2 \Delta ts0, i}, \tag{A.23}$$

$$c_2 = \frac{\left[\sum_{i=1}^{n} V_{s2,i}^2 \Delta t_{s0,i}\right] \left[\sum_{i=1}^{n} V_{p2,i}^4 \Delta t_{p0,i} (1 + 8\eta_i)\right]}{2\left[\sum_{i=1}^{n} V_{p2,i}^2 \Delta t_{p0,i} + \sum_{i=1}^{n} V_{s2,i}^2 \Delta t_{s0,i}\right]^2}$$

$$- \frac{\left[\sum_{i=1}^{n} V_{p2,i}^2 \Delta t_{p0,i}\right] \left[\sum_{i=1}^{n} V_{s2,i}^4 \Delta t_{s0,i} (1 + 8\zeta_i)\right]}{2\left[\sum_{i=1}^{n} V_{p2,i}^2 \Delta t_{p0,i} + \sum_{i=1}^{n} V_{s2,i}^2 \Delta t_{s0,i}\right]^2}. \tag{A.24}$$

Finally, using the definitions of the Alkhalifah (1997) effective parameter η_{eff} and the Yuan et al. (2001) effective parameter ζ_{eff} given respectively by equations (A.6) and (A.7), the coefficients c_0 and c_2 become:

$$c_0 = \frac{\kappa_{eff}}{1 + \kappa_{eff}}, \tag{A.25}$$

$$c_2 = \frac{\kappa_{eff}(1 + \kappa_0)}{2\, t_{\grave{p}\acute{s},0}\, V_{\grave{p}\acute{s},2}^2\, \kappa_0\, (1 + \kappa_{eff}^3)} \left[(\kappa_0\, \kappa_{eff} - 1) + 8\, (\eta_{eff}\, \kappa_0\, \kappa_{eff} - \zeta_{eff}) \right]. \tag{A.26}$$

.

The coefficient c_0 for layered VTI media has the exact same expression as the coefficient c_0 for the multilayer isotropic case given by equation (3.26), while the coefficient c_2 is more complicate in the layered VTI case than in the multilayer isotropic case of Chapter 3. In fact, in the multilayer VTI case there is an extra residual term $[8(\eta_{eff}\kappa_0\kappa_{eff} - \zeta_{eff})]$ compared to the multilayer isotropic case. This residual term is in the order of $[\kappa_0\kappa_{eff} - 1]$ (Yuan et al., 2001) and hence cannot be discarded. A numerical analysis published by Gaiser & Jackson (2000) showed that the multilayer isotropic coefficient c_2 given in Chapter 3 by equation (3.26) is not sufficient to account for the anisotropy effects, and thus the residual term $[8(\eta_{eff}\kappa_0\kappa_{eff} - \zeta_{eff})]$ should be taken into account. This result was also confirmed by Artola et al. (2004).